



# UNIVERSITY OF CAMBRIDGE

## Investigating small-molecule inhibitors of platelet aggregation



**Roxanna Hajbabaie**

Darwin College

August 2022

This thesis is submitted for the degree of  
Doctor of Philosophy

Department of Pharmacology  
University of Cambridge



## Declaration

This thesis is the result of my own work and includes nothing which is the outcome of work done in collaboration except as declared in the Preface and specified in the text. It is not substantially the same as any that I have submitted or is being concurrently submitted for a degree or diploma or other qualification at the University of Cambridge or any other University or similar institution except as declared in the Preface and specified in the text. I further state that no substantial part of my thesis has already been submitted, or is being concurrently submitted for any such degree, diploma, or other qualification at the University of Cambridge or any other University or similar institution except as declared in the Preface and specified in the text. It does not exceed the prescribed word limit of 60,000 words, excluding bibliography, figure legends, and appendices.

Roxanna Hajbabaie

August 2022



# Abstract

## Investigating small-molecule inhibitors of platelet aggregation

Roxanna Hajbabaie

Cardiovascular disease, including myocardial infarction, remains the number one cause of worldwide morbidity and mortality. The major cause of myocardial infarction is arterial thrombosis, driven by platelet aggregation. Adenosine diphosphate (ADP)-induced platelet aggregation is mediated by the G<sub>i</sub>-protein-coupled receptor (GPCR), P2Y<sub>12</sub>. Therefore, P2Y<sub>12</sub> antagonists are clinically used to prevent thrombotic events. However, current antiplatelet drugs have several drawbacks such as the increased risk of bleeding, difficulty in fine-tuning the antiplatelet effects of irreversible antagonists, and variability in patient response. Furthermore, the nucleoside-based, reversible drug ticagrelor has been reported to cause dyspnoea due to off-target effects. Additionally, the binding modes of the P2Y<sub>12</sub> ligands are not fully known. Interestingly, the recently solved crystal structure of P2Y<sub>12</sub> has revealed that the orthosteric site is composed of two sub-pockets. This thesis had two complementary aims: 1) to further understand the mechanism of action of cangrelor – the most recently approved, and only intravenously acting P2Y<sub>12</sub> antagonist; and 2) to discover novel, competitively acting, non-nucleotide-based reversible inhibitor(s) of ADP-induced platelet aggregation.

A plate-based aggregometry assay and platelet-rich plasma (PRP) isolated from the blood of human donors were used to show that cangrelor (in nM and μM concentrations) may act in a non-competitive manner to ADP (up to mM concentrations). This is in contrast with reports in the literature that cangrelor is a competitive antagonist of the P2Y<sub>12</sub> receptor. Interestingly, it acted in a competitive manner when the P2Y<sub>12</sub> receptor was stimulated with the synthetic and more potent agonist, 2-methylthio-ADP (2MeSADP). The cangrelor analogue, AR-C66096, acted in a competitive manner with both agonists. Subsequently, a multiplexed flow cytometric assay assessing phosphorylated platelet vasodilator-stimulating phosphoprotein (pVASP) levels in platelets was successfully optimised. For this assay, a technique called barcoding was used with a novel combination of dye and fluorophore-conjugated antibody, opening a new avenue for barcoding. This assay further showed that ADP (up to 1mM) + cangrelor (100nM) E<sub>max</sub> did not reach that of ADP (1mM) + vehicle, whereas AR-C66096 did. Electrostatic field potential analysis of the two compounds revealed that AR-C66096 had a field of negative electrostatic potential that was missing in cangrelor. Additionally, these results suggested that there may be mechanistic differences in the activation of the receptor by ADP and 2MeSADP.

To achieve the second aim, ligand-based *in silico* tools were used to virtually screen over 440,000 molecules to identify novel scaffolds possessing reasonable similarities in 3D shape and electrostatic properties in reference to the experimental P2Y<sub>12</sub> antagonist, AZD1283.

Docking of the best hits was performed against the recently solved crystal structure of P2Y<sub>12</sub>. Following the meticulous inspection of docked poses, as well as similarity indices with the query ligand, 33 compounds were purchased for *in vitro* validation. From these, two competitively acting, novel scaffolds (namely compound B6 and B11) were identified, which showed consistent inhibition of ADP-induced aggregation of platelets from human blood donors. These compounds were predicted to have comparable interactions with the receptor to the co-crystallised antagonist, AZD1283. Of these two best hits, compound B6, which is a 2-aryl benzoxazole derivative, was chosen for further investigation. To establish the structure-activity relationship (SAR) analysis around the B6 scaffold, nine analogues of this compound were purchased and experimentally tested using the assays described above. This led to the identification of another novel inhibitor of ADP-induced platelet aggregation, namely compound S8. However, despite good docking profiles of the compounds against the crystal structure of P2Y<sub>12</sub>, the latter could not be confirmed as their target upon analysis of pVASP levels. Further work is required to confirm the mechanism by which these compounds inhibit platelet aggregation. To summarise, this thesis has increased our understanding of cangrelor's mechanism of action, and several 2-aryl benzoxazole derivatives are described as competitive and reversibly acting inhibitors of ADP-induced platelet aggregation.

## Acknowledgments

First and foremost, I would like to thank God for the opportunities I have been given, the blessings in my life, and for giving me the strength to persevere through challenging times.

I would like to express my deepest thanks and gratitude to my supervisors, Dr Matthew Harper and Dr Taufiq Rahman. It has been an honour to have the opportunity to learn from you and work in your labs. Thank you for your time, patience, and everything you have taught me over the past 4 years. I will always treasure the valuable knowledge and skills I gained from you. I would like to thank members of the Harper and Rahman Labs, past and present, who made my time at Cambridge so memorable: Jess Berry, Sarah Millington-Burgess, Jess Davies, Joanna-Marie Dear, Jack Greenhalgh, Maria Eznarriaga, Dora Lopresto, Rebecca Riddle, Venkat Vadlamani, Saifur Rahman, and Rory Triniman. We were faced with many challenges during the pandemic, but the teamwork everyone showed was amazing. Special thanks to friends in the office and department: Charity Bhebhe, Wanna Chen, Melissa Irvine, Charlotte Jones, Ollie King, Cynthia Okoye, Dewi Safitri, Holly Smith, and Ayla Wahid. Thank you to my labmate and dear friend, Sinayat Mahzabeen, for always being so kind and supportive.

Thank you to Dr Graham Ladds for use and guidance of his lab's cAMP assay kit. Thank you to members of the Department of Pharmacology, especially those who volunteered to give blood, without whom experiments would not have been possible. Also, others for administrative or lab safety advice: Barney Leeke, Ian Saunders, Sergio Tomey, Sofia Travassos. I would like to express my deepest thanks to Dr Lucia Pereira Giraldez (MRC Toxicology) for allowing me to use her flow cytometer when our instrument was not functioning at a critical point in my experiments. Special thanks for helping me to read samples. I would also like to acknowledge Cresset and OpenEye Scientific for granting academic licenses to use their respective software.

I would like to thank my amazing parents. Thank you, Mum, for being my best friend, for inspiring me to study a Ph.D., and for always giving me hope. Thank you, Dad, for all your kindness and unwavering support. I will always be grateful to you both. Thank you to my incredible grandparents for teaching me the value of books from a young age, and for all you have done for me. Thanks to my friend Brooke for our wonderful friendship. I would also like to thank my previous mentors at St. John's University, New York, for inspiring me to continue to study pharmacology and setting the foundation of my knowledge in the field: Dr Michael Barletta, Dr Zhe-Sheng Chen, Dr Vikas Dukhande, Dr Raymond Ochs, Dr Jeanette Perron, Dr Sandra Reznik, Dr Louis Trombetta, & Dr John Wurpel. Thank you to the University of Cambridge and Darwin College who made this project possible, and who continuously inspire their students and people around the world with the academic opportunities they make available.



## Presentations and publications

### Presentations

**Winner of the Early Career Poster Prize:** British Pharmacological Society conference, Pharmacology 2020 (December 2020) ‘Toward novel modes of action for cangrelor’ (abstract selected for publication in the British Journal of Pharmacology).

<https://pharmacology2020.ipostersessions.com/default.aspx?s=E1-2F-D6-B0-72-7B-FC-65-CC-AC-AD-E0-6B-80-7D-8D>

### Publications

**Selected abstract (first-author):** Hajbabaie, R., Harper, M. and Rahman, T., 2021, January. Toward unveiling novel modes of action for cangrelor. In *British Journal of Pharmacology* (Vol. 178, No. 2, pp. 387-388). USA: Wiley.

*During this Ph.D., the following papers were published relating to the coronavirus pandemic, the findings of which are not presented in this thesis:*

**Original article (first-author):** Hajbabaie, R., Harper, M. T., & Rahman, T. (2021).

Establishing an Analogue Based in Silico Pipeline in the Pursuit of Novel Inhibitory Scaffolds against the SARS Coronavirus 2 Papain-Like Protease. *Molecules*, 26(4), 1134.

**Original article, journal cover story (joint first-author):** Augustin, T. L., Hajbabaie, R., Harper, M. T., & Rahman, T. (2020). Novel small-molecule scaffolds as candidates against the SARS coronavirus 2 main protease: a fragment-guided in silico approach. *Molecules*, 25(23), 5501.



# Table of contents

List of figures.....	XVII
List of tables.....	XXV
Nomenclature.....	XXVII
<b>Chapter 1. Introduction.....</b>	<b>1</b>
<b>1.1. Platelet structure.....</b>	<b>3</b>
<b>1.2. Role of platelets in haemostasis.....</b>	<b>6</b>
<b>1.3. Pathological role of platelets in arterial thrombosis.....</b>	<b>7</b>
1.3.1. Arterial plaque formation and rupture.....	7
1.3.2. Molecular insights into thrombus formation.....	9
1.3.2.1. Prevention of platelet activation in a healthy vessel.....	9
1.3.2.2. Platelet adherence and activation.....	10
1.3.2.3. Release of secondary mediators and platelet aggregation.....	13
1.3.2.4. The blood coagulation cascade.....	18
<b>1.4. P2Y<sub>12</sub>: structure and pharmacology.....</b>	<b>19</b>
1.4.1. Overview.....	19
1.4.2. Pharmacology of the P2Y <sub>12</sub> receptor.....	21
1.4.2.1. Irreversible P2Y <sub>12</sub> antagonists.....	24
1.4.2.2. Reversible P2Y <sub>12</sub> antagonists.....	26
1.4.3. Structural insights.....	30
1.4.3.1. Overview.....	30
1.4.3.2. The open vs. closed-lid models of P2Y <sub>12</sub> .....	35
1.4.3.3. Mechanisms of P2Y <sub>12</sub> activation.....	39
1.4.3.4. Binding of the reversible P2Y <sub>12</sub> antagonists.....	47

1.4.3.5. Binding of the irreversible P2Y <sub>12</sub> antagonists.....	55
<b>1.5. Principles of computer-aided drug discovery.....</b>	<b>58</b>
<b>1.6. Aims and objectives.....</b>	<b>62</b>
<b>Chapter 2. Materials and methods.....</b>	<b>67</b>
<b>2.1. <i>In silico</i> methods.....</b>	<b>68</b>
2.1.1. Chemical libraries.....	69
2.1.2. Ligand structure preparation.....	70
2.1.3. Ligand-based virtual screening.....	70
2.1.4. Molecular field-based alignment.....	70
2.1.5. Protein structure preparation.....	71
2.1.6. Molecular docking.....	71
2.1.7. Analogue search.....	73
2.1.8. Analysis of protein-ligand interactions.....	73
2.1.9. Exploring compound properties.....	73
2.1.10. Molecular visualisation.....	73
<b>2.2. <i>In vitro</i> methods.....</b>	<b>74</b>
2.2.1. Isolation of platelet-rich plasma from human blood.....	74
2.2.2. Platelet-rich plasma purity analysis.....	75
2.2.3. Preparation of washed platelets.....	76
2.2.4. Plate-based aggregometry.....	77
2.2.5. LANCE cAMP assay.....	79
2.2.6. Development of a multiplexed pVASP assay.....	83
2.2.7. Calcium assay.....	93

2.2.8. General data analysis with GraphPad Prism.....	95
2.2.9. Chemical preparations and sources.....	95
<b>Chapter 3. Unveiling a novel mode of action for cangrelor.....</b>	<b>101</b>
3.1. Aim of the study and approach taken.....	102
3.2. Establishing a plate-based platelet aggregation assay.....	102
3.2.1. PRP purity analysis.....	104
3.2.2. Aggregometry assay validations.....	107
3.3. Cangrelor may act in a non-competitive manner to ADP.....	116
3.4. Cangrelor and AR-C66096 act in a competitive manner to 2MeSADP.....	120
3.5. Cangrelor (10nM) acts in a competitive manner to ADP.....	123
3.6. Cangrelor's electrostatic profile reveals a missing field of negative potential compared to AR-C66096.....	124
3.7. Establishing an assay of P2Y <sub>12</sub> activity.....	127
3.7.1. The LANCE cAMP assay is not compatible with P2Y <sub>12</sub> .....	127
3.7.2. Setting up a multiplexed VASP phosphorylation assay for platelets.....	130
3.8. pVASP assay shows ADP is unable to overcome the effects of cangrelor (10µM) or AR-C66096 (10µM).....	141
3.9. pVASP assay shows ADP is unable to overcome the effects of cangrelor (100nM) but not AR-C66096 (100nM).....	142
3.10. pVASP assay shows AR-C66096 (10nM) acts in a competitive manner to ADP.....	144
3.11. Cangrelor affects calcium signalling.....	146
3.12. Cangrelor achieves a different time vs. % inhibition profile to vehicle in the aggregometry.....	150
3.13. Discussion.....	152

<b>Chapter 4. Discovering compounds B6 and B11 as novel inhibitors of platelet aggregation.....</b>	<b>159</b>
4.1. Aim of the study.....	160
4.2. <i>In vitro</i> validations of the positive control, AZD1283.....	160
4.3. Initial trials: testing some FDA-approved drugs and special studies .....	163
4.4. <i>In silico</i> validations of the positive control, AZD1283.....	170
4.5. <i>In vitro</i> screens lead to the discovery of two novel inhibitors of platelet aggregation.....	176
4.6. Discussion.....	204
<b>Chapter 5. Analogue search: using the B6 scaffold to discover novel antiplatelet agent S8.....</b>	<b>211</b>
5.1. Aim of the study.....	212
5.2. B6 analogue search leads to the discovery of novel antiplatelet agent S8.....	212
5.3. Compounds B6 and S8 did not affect pVASP levels significantly.....	223
5.4. Compound B6 significantly enhances cytosolic Ca <sup>2+</sup> levels.....	228
5.5. Compounds B6 and S8 do not significantly affect TRAP-6 amide-induced platelet aggregation.....	230
5.6. Scaffold novelty.....	232
5.7. Discussion.....	233
<b>Chapter 6. General discussion.....</b>	<b>239</b>
6.1. Summary of results.....	240
6.1.1. Cangrelor may act in a non-competitive manner to ADP.....	240
6.1.2. 2-aryl benzoxazole derivatives as novel inhibitors of platelet aggregation.....	245

6.2. Limitations and future directions.....	248
6.2.1. Limitations of the <i>in vitro</i> methods.....	248
6.2.1.1. Phenotypic assay: 96-well aggregometry.....	248
6.2.1.2. Molecular assays.....	252
6.2.2. Limitations of the <i>in silico</i> methods.....	254
6.2.3. Limitations of the findings.....	256
6.2.3.1. Cangrelor may act in a non-competitive manner to ADP.....	256
6.2.3.2. 2-aryl benzoxazole derivatives as novel inhibitors of platelet aggregation.....	259
6.2.4. Future work.....	261
6.2.4.1. For groups interested in the mode of action of cangrelor or structural biology.....	261
6.2.4.2. For groups interested in novel inhibitors of platelet aggregation.....	263
<b>References.....</b>	<b>267</b>
<b>Appendix.....</b>	<b>297</b>



## List of figures

### Chapter 1. Introduction

<b>Figure 1:</b> A schematic diagram showing the structure of a platelet.....	5
<b>Figure 2:</b> A schematic diagram showing the formation of a thrombus .....	8
<b>Figure 3:</b> A schematic diagram showing the mechanisms of platelet activation.....	11
<b>Figure 4:</b> The P2Y <sub>1</sub> and P2Y <sub>12</sub> signalling pathways.....	15
<b>Figure 5:</b> Modulators of P2Y <sub>12</sub> .....	22
<b>Figure 6:</b> The structure of P2Y <sub>12</sub> .....	30
<b>Figure 7:</b> Cartoon representations of the crystal structures of P2Y <sub>12</sub> .....	32
<b>Figure 8:</b> The orthosteric binding site for the co-crystallised antagonist, AZD1283, on the human P2Y <sub>12</sub> receptor.....	34
<b>Figure 9:</b> Surface representations of the structures of P2Y <sub>12</sub> at various putative states.....	38
<b>Figure 10:</b> Amino acid residues surrounding the agonist and antagonist-bound pockets of the P2Y <sub>12</sub> receptor.....	43
<b>Figure 11:</b> Close-up view of the binding pose of the co-crystallised agonist, 2MeSADP, at the orthosteric site of the human P2Y <sub>12</sub> receptor.....	44
<b>Figure 12:</b> Key residues surrounding the agonist and antagonist-bound pockets of the P2Y <sub>12</sub> receptor.....	45
<b>Figure 13:</b> The ring moiety of AZD1283 and ticagrelor lodges in between helices 6 and 7, preventing their inward shift.....	50

<b>Figure 14:</b> Surface representation of the 2MeSADP-bound pocket of P2Y <sub>12</sub> .....	51
<b>Figure 15:</b> A summary diagram showing how the P2Y <sub>12</sub> crystal structures facilitate the understanding of ligand binding.....	57
<b>Figure 16:</b> A summary of how structure-based docking and ligand-based virtual screening are performed.....	59

## Chapter 2. Materials and methods

<b>Figure 17:</b> Isolation of platelets from whole blood.....	75
<b>Figure 18:</b> Concept behind how the LANCE cAMP assay works.....	80
<b>Figure 19:</b> A basic outline of the pVASP assay.....	85

## Chapter 3. Unveiling a novel mode of action for cangrelor

<b>Figure 20:</b> Representative forward scatter-area vs. side scatter-area plot for platelets in plasma (platelet-rich plasma).....	105
<b>Figure 21:</b> PRP purity analysis.....	106
<b>Figure 22:</b> Validation of the aggregometry assay using eptifibatide.....	109
<b>Figure 23:</b> Validation of the aggregometry assay using forskolin.....	110
<b>Figure 24:</b> Validation of the aggregometry assay using PGE <sub>1</sub> .....	111
<b>Figure 25:</b> Validation of the aggregometry assay using MRS 2179.....	112
<b>Figure 26:</b> Validation of the aggregometry assay using the weak inhibitor of platelet aggregation, AMP.....	114

<b>Figure 27:</b> Cangrelor may act in a non-competitive manner to ADP.....	117
<b>Figure 28:</b> AR-C66096 acts in a competitive manner to ADP.....	119
<b>Figure 29:</b> Cangrelor acts in a competitive manner to 2MeSADP.....	121
<b>Figure 30:</b> AR-C66096 acts in a competitive manner to 2MeSADP.....	122
<b>Figure 31:</b> Cangrelor (10nM) and AR-C66096 (10nM) act in a competitive manner to ADP.....	123
<b>Figure 32:</b> The structures and electrostatic potential field comparisons of cangrelor and AR-C66096.....	126
<b>Figure 33:</b> Finding the optimal concentration (EC <sub>80</sub> ) of forskolin to stimulate adenylyl cyclase in platelets.....	128
<b>Figure 34:</b> P2Y <sub>12</sub> agonists, ADP and 2MeSADP, are picked up as cAMP by the anti-cAMP antibody.....	129
<b>Figure 35:</b> Representative forward scatter-area (FSC-A) vs. side scatter-area (SSC-A) plot for washed platelets.....	130
<b>Figure 36:</b> Validation of phospho-VASP (serine 157) rabbit monoclonal primary antibody and anti-rabbit IgG (H+L), F(ab') <sub>2</sub> fragment, Alexa Fluor 647 conjugate.....	131
<b>Figure 37:</b> Testing stains with intracellular targets for barcoding in washed platelets.....	133
<b>Figure 38:</b> Testing stains with extracellular targets for barcoding in washed platelets.....	134
<b>Figure 39:</b> A schematic diagram summarising the barcoding layers achieved for each stain, with the target location and binding type specified.....	135

<b>Figure 40:</b> Non-covalent binding dye, DiOC <sub>6</sub> , barcodes were lost and did not survive pooling in PRP or washed platelets.....	136
<b>Figure 41:</b> Barcodes achieved for fixable viability dye eFluor 520.....	137
<b>Figure 42:</b> Barcodes achieved for CD41a monoclonal antibody conjugated to PE-Cy7.....	138
<b>Figure 43:</b> Testing various concentrations of PGE <sub>1</sub> with 30μM ADP.....	139
<b>Figure 44:</b> Testing various concentrations of ADP with 100nM PGE <sub>1</sub> .....	140
<b>Figure 45:</b> pVASP assay shows ADP is unable to overcome the effects of cangrelor or AR-C66096 (10μM).....	141
<b>Figure 46:</b> pVASP assay shows ADP is unable to overcome the effects of cangrelor (100nM), but not AR-C66096 (100nM).....	143
<b>Figure 47:</b> pVASP assay shows AR-C66096 (10nM) acts in a competitive manner to ADP.....	145
<b>Figure 48:</b> Calcium levels can be measured using the calcium-sensitive dye, Cal-520.....	146
<b>Figure 49:</b> Calcium assay shows cangrelor affects calcium signalling.....	147
<b>Figure 50:</b> Cangrelor (10μM) but not AR-C66096 (10μM) has a significantly different effect on Cal-520 fluorescence compared to vehicle.....	148
<b>Figure 51:</b> Cangrelor (10nM) and AR-C66096 (10nM) do not have a significantly different effect on Cal-520 fluorescence compared to vehicle.....	149
<b>Figure 52:</b> Cangrelor achieves a different time vs. inhibition profile to vehicle in the aggregometry.....	151

## Chapter 4. Discovering compounds B6 and B11 as novel inhibitors of platelet aggregation

<b>Figure 53:</b> Experimental validation of the positive control, AZD1283 (10 $\mu$ M), against platelet aggregation using varying concentrations of ADP.....	161
<b>Figure 54:</b> Experimental validation of the positive control, AZD1283 (10 $\mu$ M), against platelet aggregation using varying concentrations of 2MeSADP.....	162
<b>Figure 55:</b> Structures of some FDA-approved drugs (and two experimental drugs) and a natural compound used to trial the aggregometry assay.....	164
<b>Figure 56:</b> Experimental evaluation of some FDA-approved drugs (and two experimental drugs) used to trial the aggregometry assay.....	165
<b>Figure 57:</b> Experimental evaluation of remdesivir's active metabolite, GS-441524 (10 $\mu$ M), against platelet aggregation .....	166
<b>Figure 58:</b> Experimental evaluation of para-topolin riboside (10 $\mu$ M) against platelet aggregation.....	167
<b>Figure 59:</b> Effect of para-topolin riboside (10 $\mu$ M) on platelet aggregation with varying concentrations of ADP.....	169
<b>Figure 60:</b> Structure and key pharmacophore features of AZD1283.....	170
<b>Figure 61:</b> Validation of blind docking of the positive control, AZD1283, against the human P2Y <sub>12</sub> structure.....	171
<b>Figure 62:</b> Validation of focused docking of the positive control, AZD1283, against the human P2Y <sub>12</sub> structure.....	173
<b>Figure 63:</b> Recognition of the co-crystallised AZD1283 within the orthosteric ligand binding pocket of the human P2Y <sub>12</sub> structure.....	175

<b>Figure 64:</b> 2D structures of 15 compounds purchased from Enamine for subsequent experimental testing.....	177
<b>Figure 65:</b> Experimental evaluation of the purchased Enamine molecules (50µM) against platelet aggregation.....	178
<b>Figure 66:</b> Experimental evaluation of the purchased Enamine molecules (10µM) against platelet aggregation.....	179
<b>Figure 67:</b> 2D structures of five compounds purchased from Vitas for subsequent experimental evaluation.....	180
<b>Figure 68:</b> Experimental evaluation of the purchased Vitas molecules against platelet aggregation.....	181
<b>Figure 69:</b> 2D structures of 14 compounds purchased from Specs for subsequent experimental evaluation.....	182
<b>Figure 70:</b> Experimental evaluation of the purchased Specs molecules (100µM) against platelet aggregation.....	183
<b>Figure 71:</b> Experimental evaluation of the purchased Specs molecules (10µM or 50µM) against platelet aggregation.....	185
<b>Figure 72:</b> Effect of compound B6 (10µM) on platelet aggregation using varying concentrations of ADP.....	187
<b>Figure 73:</b> Effect of compound B11 (10µM) on platelet aggregation using varying concentrations of ADP.....	189
<b>Figure 74:</b> Similarity indices for compounds B6 and B11 with respect to AZD1283.....	191

<b>Figure 75:</b> Molecular field-based alignment of compounds B6 and B11 with respect to AZD1283.....	193
<b>Figure 76:</b> Possible binding modes of compound B6 against the human P2Y <sub>12</sub> structure predicted through blind docking.....	195
<b>Figure 77:</b> Possible binding mode of compound B6 against the human P2Y <sub>12</sub> structure predicted through focused docking.....	196
<b>Figure 78:</b> Recognition of compound B6 within the orthosteric ligand binding pocket of the human P2Y <sub>12</sub> structure .....	198
<b>Figure 79:</b> Possible binding modes of compound B11 against the human P2Y <sub>12</sub> structure predicted through blind docking.....	200
<b>Figure 80:</b> Possible binding mode of compound B11 against the human P2Y <sub>12</sub> structure predicted through focused docking.....	201
<b>Figure 81:</b> Recognition of compound B11 within the orthosteric ligand binding pocket of the human P2Y <sub>12</sub> structure.....	203

## **Chapter 5. Analogue search: using the B6 scaffold to discover novel antiplatelet agent S8**

<b>Figure 82:</b> 2D structures of the B6 analogues (S compounds) purchased from MolPort for subsequent experimental evaluation.....	212
<b>Figure 83:</b> Experimental evaluation of the purchased S compounds (10µM) against platelet aggregation.....	214
<b>Figure 84:</b> Further experimental evaluation of compounds B6 and S8 (10µM) against platelet aggregation.....	215

<b>Figure 85:</b> Possible binding modes of compound S8 against the human P2Y <sub>12</sub> structure predicted through blind docking.....	219
<b>Figure 86:</b> Possible binding mode of compound S8 against the human P2Y <sub>12</sub> structure predicted through focused docking.....	220
<b>Figure 87:</b> Recognition of compound S8 within the orthosteric ligand binding pocket of the human P2Y <sub>12</sub> structure and similarity indices with respect to AZD1283.....	222
<b>Figure 88:</b> A schematic diagram showing various molecular pathways that were probed using AZD1283, B6, and S8.....	223
<b>Figure 89:</b> Assessing the effect of AZD1283, B6, and S8 on platelet pVASP levels.....	225
<b>Figure 90:</b> Assessing the effect of AZD1283 and compound S8 on pVASP levels using varying concentrations of ADP.....	227
<b>Figure 91:</b> Experimental evaluation of AZD1283, S8, and B6 in a platelet calcium assay.....	229
<b>Figure 92:</b> Assessing the effect of AZD1283, S8, and B6 on TRAP-6 amide-induced platelet aggregation.....	231

## Chapter 6. General discussion

<b>Figure 93:</b> Proposed cangrelor binding pocket.....	241
<b>Figure 94:</b> SAR analysis around the 2-aryl benzoxazole scaffold based on experimental evaluation of nine analogues of compound B6.....	247

## List of tables

### Chapter 1. Introduction

**Table 1a:** Marketed P2Y<sub>12</sub> antagonists.....23

**Table 1b:** Reported binding affinity values for the P2Y<sub>12</sub> ligands under study in this work.....23

### Chapter 2. Materials and methods

**Table 2:** List of *in silico* tools used.....68

**Table 3:** List of chemicals/reagents used.....96

**Table 4:** List of screening compounds used. ....98

**Table 5:** List of antibodies used.....100

### Chapter 4. Discovering compounds B6 and B11 as novel inhibitors of platelet aggregation

**Table 6:** Mechanisms of some FDA-approved drugs (and two experimental drugs) and a natural compound used to trial the aggregometry assay .....164

### Chapter 5. Analogue search: using the B6 scaffold to discover novel antiplatelet agent S8

**Table 7:** Predicted physicochemical properties of AZD1283, B6, and S8.....217



# Nomenclature

## Abbreviations

2MeSADP: 2-methylthio-adenosine-5'-diphosphate

2MeSAMP: 2-methylthioadenosine 5'-monophosphate

2MeSATP: 2-methylthioadenosine 5'-triphosphate

5-HT: 5-hydroxytryptamine i.e., serotonin

AA: arachidonic acid

ACD: acid citrate dextrose

ACS: acute coronary syndrome

ADME: absorption, distribution, metabolism, excretion

ADP: adenosine 5'-diphosphate

AMP: adenosine 5'-monophosphate

ANOVA: analysis of variance

Ap<sub>4</sub>A: di-adenosine tetraphosphate

APC: allophycocyanin

ATP: adenosine 5'-triphosphate

AUC: area under the curve

AZD1283: AstraZeneca drug 1283

BMI: body mass index

BSA: bovine serum albumin

Ca<sup>2+</sup>: calcium ion

CaCl<sub>2</sub>: calcium chloride

CADD: computer-aided drug discovery

CalDAG-GEFI: calcium and 1,2-diacylglycerol-regulated guanine exchange factor 1

CAM: cell adhesion molecule

cAMP: 3',5'-cyclic adenosine monophosphate

CD: cluster of differentiation

cGMP: cyclic guanosine monophosphate

CHAMPION-PHOENIX: Effect of platelet inhibition with cangrelor during PCI on ischemic events (clinical trial)

CHO cells: Chinese hamster ovary cells

COVID-19: coronavirus disease 2019

CYP: cytochrome P450

Cryo-EM: cryogenic electron microscopy

DAG: 1,2-diacylglycerol

dH<sub>2</sub>O: distilled water

DiOC<sub>6</sub>: 3,3'-dihexyloxacarbocyanine, iodide

DM: diabetes mellitus

DMSO: dimethyl sulfoxide

DRY motif: Asp (D)-Arg (R)-Tyr (Y) motif

DTS: dense tubular system

EC<sub>50</sub>: half-maximal effective concentration

EC<sub>80</sub>: effective concentration of drug that produces 80% of the maximal response

ECL: extracellular loop

E<sub>max</sub>: maximum effect

ENT1: equilibrative nucleoside transporter 1

EtOH: ethanol

Eu-SA: streptavidin labelled with Europium-W8044 chelate

F: fluorescence

FACS: fluorescence-activated cell sorting

Factor I: fibrinogen

Factor VII: proconvertin

Factor Xa: Stuart-Prower factor

Factor XII: Hageman factor

FDA: Food and Drug Administration

FITC: fluorescein isothiocyanate

FL: fluorescence channel

FRET: fluorescence resonance energy transfer

FSC: forward scatter

G-protein: guanine nucleotide-binding protein

GAP: GTPase-activating protein

GDP: guanosine diphosphate

GEF: guanine exchange factor

G<sub>i</sub>: inhibitory G protein

GOLD: genetic optimisation for ligand docking

GPIb: glycoprotein Ib

GPIIb/IIIa: glycoprotein IIb/IIIa (integrin  $\alpha_{IIb}\beta_3$ )

GPCR: G-protein-coupled receptor

GPVI: glycoprotein VI

G<sub>q</sub>: stimulatory G protein

G<sub>s</sub>: stimulatory G protein

GS-441524: active metabolite of remdesivir

GTP: guanosine triphosphate

GTPase: guanosine triphosphatase

H: hydrogen

HBS: HEPES-buffered saline

HEPES: hydroxyl-ethyl-piperazine-ethane-sulfonic acid

HIV: human immunodeficiency virus

HTS: high-throughput screening

IBMX: 3-isobutyl-1-methylxanthine

ICL: intracellular loop

IgG: immunoglobulin G

IgG (H+L): immunoglobulin G heavy and light chains

iLOGP: implicit LOGP

IP<sub>3</sub>: inositol trisphosphate

IP<sub>3</sub>R: inositol trisphosphate receptor

IP receptor: prostanoid receptor

K<sub>D</sub>: dissociation constant

K<sub>i</sub>: inhibitory constant

LDLs: low-density lipoproteins

Log: logarithm

LogEC<sub>50</sub>: logarithm of the EC<sub>50</sub>

LTA: light transmission aggregometry

MD simulations: molecular dynamic simulations

Me: methyl

MFI: median fluorescence intensity

MMFF94: Merck Molecular Force Field

MMV: Molegro Molecular Viewer

mRNA: messenger RNA

NO: nitric oxide

ns: not significant

NSAID: non-steroidal anti-inflammatory drug

NTPDase: ectonucleoside triphosphate diphosphohydrolase

OCS: open canalicular system

P2Y<sub>1</sub>: purinergic 2Y<sub>1</sub> receptor

P2Y<sub>12</sub>: purinergic 2Y<sub>12</sub> receptor

PAINS: pan-assay interference compounds

PAR: protease-activated receptor

Para-topolin riboside: N6-(4-hydroxybenzyl)adenosine)

PBS: phosphate-buffered saline

PCI: percutaneous coronary intervention

PCI-CURE: Effects of pre-treatment with clopidogrel and aspirin followed by long-term therapy in patients undergoing percutaneous coronary intervention (clinical trial)

pCMBS: *p*-chloromercuribenzene sulphonate

PDB: Protein Data Bank

PE: phycoerythrin

PE-Cy7: phycoerythrin-cyanine 7

PFA: paraformaldehyde

PGE<sub>1</sub>: prostaglandin E<sub>1</sub>

PGI<sub>2</sub>: prostaglandin I<sub>2</sub>, prostacyclin

PI3K: phosphoinositide 3-kinase

IC<sub>50</sub>: negative log of the half-maximal inhibitory concentration (IC<sub>50</sub>)

PK<sub>i</sub>: negative log of the inhibitory constant (K<sub>i</sub>)

PIP<sub>2</sub>: phosphatidylinositol 4,5-bisphosphate

PKA: protein kinase A

PKC: protein kinase C

PKG: protein kinase G or cGMP-dependent protein kinase

PLA<sub>2</sub>: phospholipase A<sub>2</sub>

PLATO: Ticagrelor versus clopidogrel in patients with acute coronary syndromes  
(clinical trial)

PLC: phospholipase C

PLCβ<sub>2</sub>: phospholipase C β<sub>2</sub>

PLCγ<sub>2</sub>: phospholipase C γ<sub>2</sub>

PLIP: Protein-Ligand Interaction Profiler

POPC: 1-palmitoyl-2-oleoyl-sn-glycero-3-phosphocholine

PPP: platelet-poor plasma

PRP: platelet-rich plasma

PSGL-1: P-selectin glycoprotein ligand-1

pVASP: phosphorylated vasodilator-stimulated phosphoprotein

RAP1B: Ras-related protein B

RASA3: Ras-GTPase-activating protein 3

ROS: Reactive oxygen species

RMSD: root-mean-square-deviation

RNA: ribonucleic acid

ROCS: Rapid Overlay of Chemical Structures

rpm: rotations per minute

RT: room temperature

SAR: structure-activity relationship

S1P<sub>1</sub>: sphingosine-1-phosphate receptor 1

Sdf: structure data file

SEM: standard error of the mean

s.f.: significant figures

SSC: side scatter

SMARTS: SMILES arbitrary target specification

SMILES: Simplified Molecular Input Line Entry System

SNPs: single nucleotide polymorphisms

TF: tissue factor

TLRs: toll-like receptors

TM: transmembrane

TPSA: total polar surface area

TRAP: thrombin receptor-activating peptide

TR-FRET: time-resolved fluorescence resonance energy transfer

TRITON-TIMI 38: Prasugrel versus clopidogrel in patients with acute coronary syndromes (clinical trial)

TWILIGHT: Ticagrelor with or without aspirin after PCI: the TWILIGHT platelet substudy

TxA<sub>2</sub>: thromboxane A<sub>2</sub>

UCSF Chimera: University of California, San Francisco Chimera (software)

VASP: vasodilator-stimulated phosphoprotein

vWF: von Willebrand factor

WHO: World Health Organisation



## Symbols and units

$\alpha$ : alpha

$\delta$ : delta

$\lambda$ : lambda

$\text{\AA}$ : angstrom

$\Delta G$ : Gibb's free energy (in kcal/mol)

$\pm$ : plus-minus

$\pi$ : pi

%: percent

$^{\circ}\text{C}$ : degrees Celsius

g: gram

$g$ : relative centrifugal force

g/mol: gram per mol

Kcal/mol: kilocalorie per mole

L: litre

mL: millilitre

M: molar

mM: millimolar

nM: nanomolar

nm: nanometre

n: sample size

$\mu\text{L}$ : microlitre

$\mu\text{g}$ : microgram

$\mu\text{M}$ : micromolar

## Amino acids

<b>Amino acid</b>	<b>3-letter abbreviation</b>	<b>1-letter symbol</b>
Alanine	Ala	A
Arginine	Arg	R
Asparagine	Asn	N
Aspartic acid	Asp	D
Cysteine	Cys	C
Glutamine	Gln	Q
Glutamic acid	Glu	E
Glycine	Gly	G
Histidine	His	H
Isoleucine	Ile	I
Leucine	Leu	L
Lysine	Lys	K
Methionine	Met	M
Phenylalanine	Phe	F
Proline	Pro	P
Serine	Ser	S
Threonine	Thr	T
Tryptophan	Trp	W
Tyrosine	Tyr	Y
Valine	Val	V



# **Chapter 1.**

## **Introduction**

"The problem with heart disease is...  
the first symptom is often fatal".

-Michael Phelps

As the world continues to fight the coronavirus disease 2019 (COVID-19) pandemic, another pandemic is silently boiling over. Cardiovascular disease remains the number one cause of worldwide morbidity and mortality, as reported by the World Health Organisation (WHO)<sup>1-4</sup>. Within cardiovascular diseases, myocardial infarction is the most common cause of death. Arterial thrombosis, or the formation of a clot in an artery, is a significant underlying cause of myocardial infarction. Such a clot will form when an atherosclerotic plaque ruptures, recruiting platelets to the site. Platelets essentially recognise this region as a site of vascular injury and carry out their physiological haemostatic functions to form a platelet plug, where none is required. This results in the formation of platelet aggregates, which narrow the diameter of the blood vessel, impeding blood flow to major organs. Although arterial thrombosis can occur throughout the arterial tree, it can result in catastrophic cardiovascular events such as myocardial infarction when the thrombus forms in the coronary circulation<sup>2</sup>. Acute coronary syndrome (ACS) encompasses a range of conditions caused because of inadequate blood flow to the heart. If formed in the cerebral circulation, the thrombus can limit blood flow to the brain, causing ischemic stroke. The primary cause of either of these distressing and often life-threatening events is the formed thrombus impeding oxygen-rich blood flow to major organs.

The purinergic  $P2Y_{12}$  ( $P2Y_{12}$ ) receptor is a key player in thrombosis, and antagonists of  $P2Y_{12}$  are routinely administered to minimise the likelihood of secondary thrombotic events in patients with ACS<sup>5,6</sup>. However, the currently available  $P2Y_{12}$  antagonists have several major drawbacks. For example, it is difficult to control and fine-tune the antiplatelet effects of the covalently binding antagonists clopidogrel and prasugrel. In addition, the nucleoside-based, reversibly acting antagonist ticagrelor has been reported to cause dyspnoea<sup>7-15</sup>. To date, there is no approved non-nucleotide-based, reversibly acting  $P2Y_{12}$  antagonist. In this thesis, computer-aided drug discovery

(CADD) tools will be used in the search for a novel scaffold to aid drug development. The crystal structures of P2Y<sub>12</sub> were recently solved, which can be used to explore structure-activity relationships of the known ligands, as well as facilitate the discovery of novel ligands<sup>16-18</sup>. Importantly, a novel scaffold may also be used as a tool to further understand P2Y<sub>12</sub> structure and pharmacology. Additionally, in a complementary aim, the most recently approved and only intravenously acting P2Y<sub>12</sub> antagonist, cangrelor, will be studied to further understand its mode of action.

This section will introduce platelet structure and function, haemostasis and arterial thrombosis, P2Y<sub>12</sub> structure and pharmacology, and finally, the principles of computer-aided drug discovery.

## 1.1. Platelet structure

Platelets, or thrombocytes, are specialised, anucleate blood cells that play an important role in preventing bleeding in mammals. Each microliter (μL) of human blood contains between 150,000-450,000 platelets, which have a lifespan of approximately 10 days<sup>19</sup>. Platelets are formed in a process called haematopoiesis, which takes place in the bone marrow<sup>20,21</sup>. As the young platelets begin their lives and enter the circulation, they will embark upon a protective and vigilant mission to prevent bleeding.

Resting platelets circulate in the blood as irregularly shaped, discoid structures, measuring approximately 2-4μm in diameter. They are off-white, or cream, in colour. In their active form, they will change shape to form extending finger-like projections called filopodia. As platelets are formed from fragments of megakaryocyte cytoplasm, they do not contain a nucleus. Therefore, they are not considered true cells but are commonly referred to as a type of blood cell in the literature and the haematopoiesis model. Platelets are, in fact, cytoplasts. However, their sophisticated structure and complex interior organelle system enable them to carry out an extraordinary number of

specialised cellular functions. For example, even though lacking a nucleus, platelets contain the translational machinery required to synthesise certain proteins. They achieve this through the translation of remnant messenger ribonucleic acid (mRNA) from the parent megakaryocyte<sup>22-28</sup>. This is usually in response to activation signals.

Like cells, platelets possess a plasma membrane composed of a phospholipid bilayer (**Figure 1**). Embedded throughout the bilayer is a range of protein receptors, crucial to signalling transduction pathways and platelet activity. Connected to the surface membrane is the open canalicular system (OCS), which is an internal network of membrane channels, or tunnels, formed from invaginations of the plasma membrane<sup>29</sup>. The OCS increases the surface area of the platelet and supports the entry of extracellular substances deep into the cytosol, as well as the secretion of platelet granule contents (discussed later). The OCS also serves an important role in aiding membrane remodelling during platelet spreading and shape change by providing the additional membrane required. Platelets also contain a dense tubular system (DTS), which is a membrane network originating from the endoplasmic reticulum of the parent megakaryocyte<sup>30,31</sup>. The DTS sequesters calcium ions ( $\text{Ca}^{2+}$ ), which are released into the cytosol upon platelet activation<sup>30,32</sup>. The DTS is also the site where prostaglandins are synthesised<sup>33</sup>.

A platelet's discoid, biconvex shape is supported by its cytoskeleton, which is composed of numerous components, including microtubule filaments<sup>34-36</sup>. Microtubules are found beneath the membrane, spanning the circumference of the platelet. They are primarily composed of the protein tubulin<sup>37</sup>. Smaller filaments composed of actin form networks within the cytoplasm<sup>38</sup>. Additionally, strands of spectrin are connected to the membrane, forming the membrane skeleton<sup>39,40</sup>. Other components, such as filamin and talin, serve as scaffolds that support the intracellular portion of certain membrane

proteins<sup>41</sup>. The platelet cytoskeleton plays a crucial role in facilitating the shape changes that the platelet will undergo upon activation.

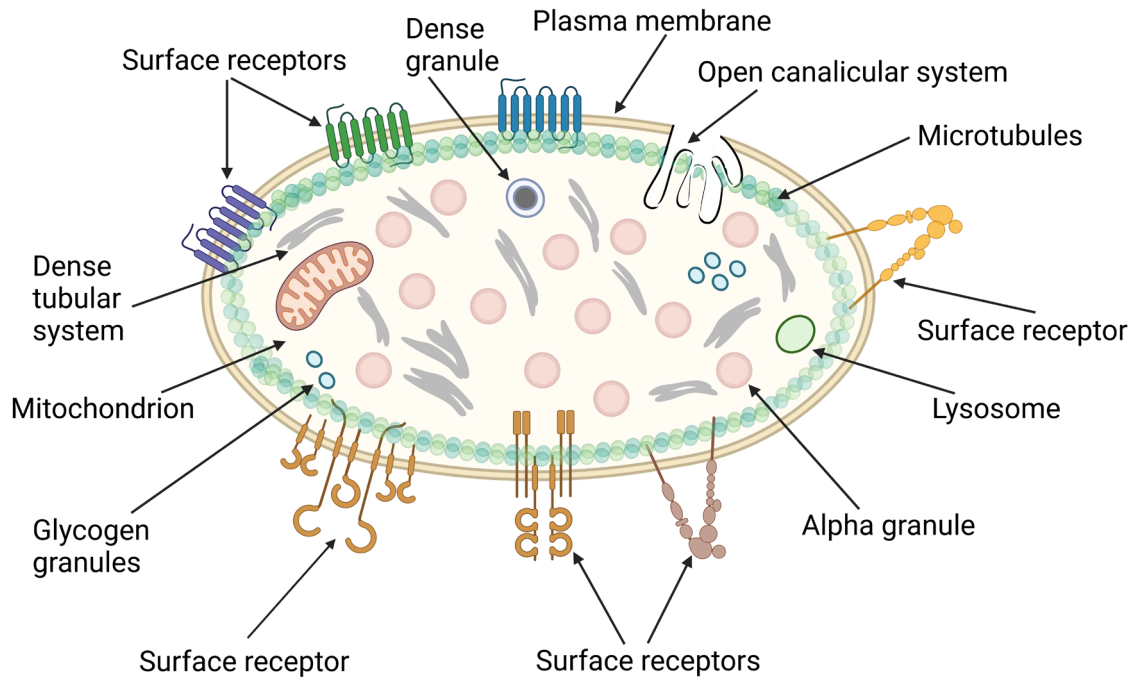


**Figure 1: A schematic diagram showing the structure of a platelet.** Platelets are composed of a plasma membrane containing surface receptors crucial for pro-aggregatory signalling pathways. Additionally, an abundance of intracellular features is important for platelet function. The image was created using BioRender.

Furthermore, the platelet cytosol is packed with granules, namely the alpha ( $\alpha$ ) granules, and dense-core ( $\delta$ ) granules, which are important secretory organelles<sup>42-44</sup>. Alpha granules are tube-like structures, measuring approximately 200nm-500nm in diameter, with a single membrane. They contain a range of proteins important to platelet activity, including coagulation factors, such as von Willebrand factor (vWF), and fibrinogen (factor I)<sup>43</sup>. The cell adhesion molecule (CAM), P-selectin (CD62P) can be found expressed on the alpha granule membrane. Approximately 40-80 alpha granules are found distributed within each platelet, making them the most abundant platelet organelle<sup>45</sup>.

In contrast to alpha granules, dense granules are smaller tube-like structures, measuring approximately 150nm in diameter. They are also less abundant, with each platelet containing around 3-8 dense granules<sup>45</sup>. These granules obtain their name from the appearance of their electron-dense core upon viewing in electron microscopy. Dense granules contain a range of small-molecules and cations as their cargo<sup>43</sup>. These include the adenine nucleotides adenosine diphosphate (ADP), adenosine triphosphate (ATP), serotonin (5-hydroxytryptamine), as well as Ca<sup>2+</sup> ions, and polyphosphates.

Additionally, platelets contain numerous other structures, such as respiring mitochondria, rough endoplasmic reticulum for protein synthesis, glycogen granules for energy storage, and lysosomes containing degradative enzymes<sup>46</sup>. Each platelet may contain up to three lysosomes.

## **1.2. Role of platelets in haemostasis**

Platelets are necessary to prevent bleeding after injury and ensure the survival of an organism. In the event of an injury, vascular endothelium damage exposes the sub-endothelial matrix, as well as vascular smooth muscle cells, to the circulating blood. This will cause spasm of the vascular smooth muscle cells, and the vessel will constrict ('vasoconstriction'), becoming narrow<sup>47</sup>. This serves as a physiological response to prevent blood loss. However, this response is short-lived, and further mechanisms are required to prevent blood loss. Platelets function to form a haemostatic plug at the site of injury in primary haemostasis. Primary haemostasis is followed by secondary haemostasis, where blood coagulation occurs, with the formation of a meshwork of fibrin stabilising the clot. The process of haemostasis is highly dynamic. Although primary and secondary haemostasis may be considered independently for simplicity, many key events are occurring simultaneously, with substantial crosstalk between the two pathways.

## 1.3. Pathological role of platelets in arterial thrombosis

### 1.3.1. Arterial plaque formation and rupture

Arterial thrombosis is preceded by the formation of an atherosclerotic plaque in the inner lining of the artery wall<sup>2</sup>. This can be caused by a range of factors. Primarily, it is due to the presence of high levels of low-density lipoproteins (LDLs) in the blood (often referred to as ‘bad’ cholesterol in popular press)<sup>48,49</sup>. This is often caused by an unhealthy diet and a lack of exercise. Other risk factors for atherosclerotic plaque formation include smoking, pollution, diabetes, obesity, and high blood pressure<sup>49,50</sup>. LDLs are passively transported from the blood into the inner layer of the artery wall (tunica intima), becoming oxidised. As LDLs accumulate here, they are engulfed by macrophages, a type of white blood cell<sup>51</sup>. The macrophages will enlarge, and in this state are often referred to as foam cells<sup>52</sup>. Foam cells promote local inflammation and promote the growth of the plaque. The plaque will harden due to calcification, which is a response to inflammatory cytokines in the area<sup>53-55</sup>.

The formation of a subendothelial plaque in the artery wall may take years to develop and can often cause stable angina<sup>56</sup>. The growth of the plaque, and its hardening, will cause changes to the architecture of the artery wall, thickening it. This is often shown as a lesion protruding into the lumen, causing partial occlusion of the blood vessel. When an atherosclerotic plaque becomes unstable, it can rupture. This results in damage to the blood vessel wall, exposing collagen in the sub-endothelial matrix to the blood<sup>2</sup>. Additionally, tissue factor at the necrotic core of the plaque is revealed to coagulation factors in the blood. Collagen and tissue factor are highly thrombogenic<sup>2,52,57-60</sup>. The blood coagulation cascade will be triggered due to the exposed tissue factor in the plaque. As the thrombus grows and is propagated further into the lumen of the artery, the blood shear rate in this environment will increase

**(Figure 2).** As platelets are subjected to this pathological high shear, they become highly dependent on the formation of integrin receptor links between each other to form stable aggregates<sup>2</sup>. This results in the formation of ‘white thrombi’, rich in platelets, which is typical of an arterial thrombus<sup>61</sup>. In contrast to primary haemostasis, thrombus formation is a highly uncontrolled process.

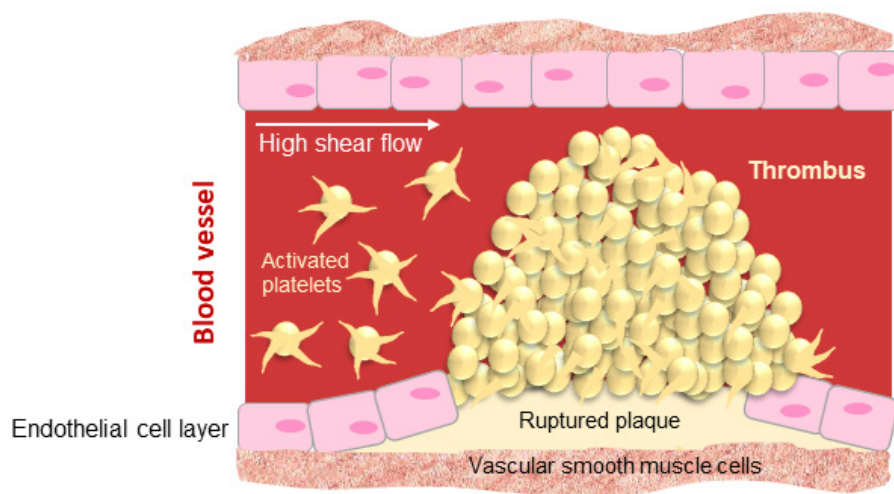


**Figure 2: A schematic diagram showing the formation of a thrombus.** As a plaque ruptures, tissue factor and collagen are exposed, which are highly thrombogenic. Platelets adhere to the site and activate. Activated platelets also release pro-aggregatory molecules, establishing a positive feedback loop for platelet activation. As they aggregate, a thrombus forms, resulting in pathological high shear. This further propagates thrombus growth. The thrombus is stabilised by a fibrin mesh (not shown), where the fibrin is a product of the coagulation cascade. The diagram was created using Microsoft PowerPoint.

Another major difference between the aggregates forming in arterial thrombus, and the aggregates forming in primary haemostasis is the location where they form<sup>2</sup>. In arterial thrombosis, the aggregates will propagate into the lumen of the artery, whereas in primary haemostasis, the aggregates will form within the vessel wall to stem blood

loss. Furthermore, the platelet plug formed in haemostasis varies in architecture to a thrombus<sup>62</sup>. The core of a platelet plug formed in haemostasis is platelet-rich, but the shell is composed of fibrin strands. Red blood cells will often become trapped in these strands, giving the clot at the site of injury a red appearance. In a large, occlusive, coronary thrombus, there is a lack of red blood cells trapped by fibrin. This is related to the blood shear rate in the local area. Specifically, increased shear rate promotes an increase in platelets nearer the vessel wall<sup>63-65</sup>. In contrast, red blood cells will flow away from the vessel wall during an increased shear rate. The effect of shear rate, and the resulting changes to the microenvironment, play a significant role in arterial thrombus formation.

### *1.3.2. Molecular insights into thrombus formation*

#### 1.3.2.1. Prevention of platelet activation in a healthy vessel

In a healthy vessel, platelet activation is prevented due to the release of prostacyclin (prostaglandin I<sub>2</sub> or PGI<sub>2</sub>) and nitric oxide (NO) from endothelial cells of the vessel wall. Prostacyclin binds to prostanoid (IP) receptors on platelets. IP receptors are a type of G<sub>s</sub>-protein-coupled receptor (GPCR), which stimulate the activity of the membrane-bound enzyme adenylyl cyclase. This enzyme is responsible for converting ATP to the second messenger 3',5'-cyclic adenosine monophosphate (cAMP). This leads to increased levels of cAMP. Downstream events in this pathway, which will be discussed in detail later, prevent platelet aggregation. Additionally, NO secreted from endothelial cells will cross the platelet plasma membrane and activate soluble guanylyl cyclase<sup>66</sup>. Guanylyl cyclase catalyses the conversion of guanosine triphosphate (GTP) to cyclic guanosine monophosphate (cGMP). cGMP activates cGMP-dependent protein kinase

(protein kinase G or PKG), which in turn will inhibit the activity of phospholipase C (PLC), an important enzyme in platelet activation.

#### 1.3.2.2. Platelet adherence and activation

Initially, circulating vWF in the plasma will bind to collagen<sup>67,68</sup>. vWF is constitutively secreted by the liver<sup>69</sup>. Upon vascular injury, vWF is also released from the Weibel-Palade bodies within endothelial cells, as well as the alpha granules of activated platelets. As platelets circulate and encounter the site of plaque rupture, they will roll over the surface of the plaque, and adhere to the exposed collagen matrix. The platelet glycoprotein Ib (GPIb) receptor (**Figure 3**) can bind to immobilised vWF under high shear through the A1 domain<sup>67,68</sup>. This triggers a weak intracellular signalling cascade which results in some activation of the integrin receptors. Secretion of platelet granular contents also begins to occur. Furthermore, the binding of vWF to GPIb anchors the platelet to the plaque surface, such that other surface receptors can interact with collagen.

As further shown in **Figure 3**, the glycoprotein VI (GPVI) receptor on the surface of the resting platelet will bind directly to exposed collagen in the subendothelial matrix<sup>70,71</sup>. Even though this interaction occurs with low affinity, it leads to strong intracellular signalling within the platelet<sup>71</sup>. The activation of GPVI leads to phosphorylation of the associated Fc receptor gamma chain, initiating a tyrosine kinase-based signalling cascade that culminates in the activation of phospholipase C gamma 2 (PLC $\gamma$ 2)<sup>72,73</sup>.

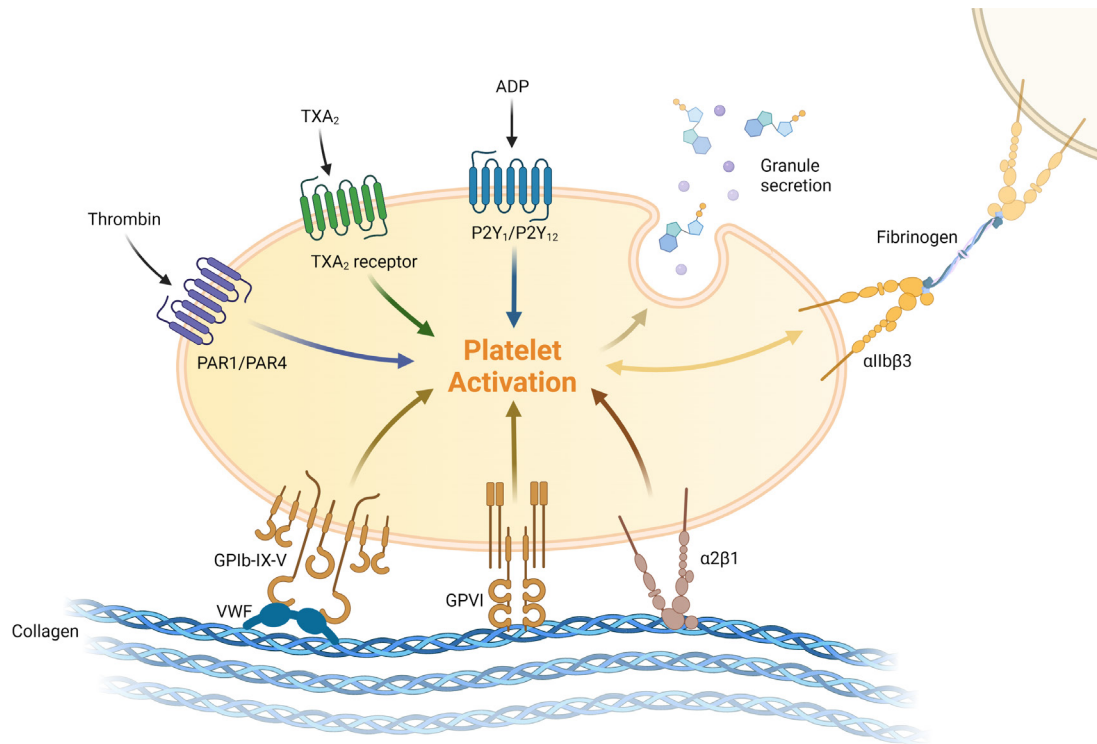


**Figure 3: A schematic diagram showing the mechanisms of platelet activation.**

Platelets initially adhere to the site of injury. GPIb binds to vWF, whereas the GPVI receptor and  $\alpha 2\beta 1$  bind directly to exposed collagen in the subendothelial matrix. This triggers inside-out signalling cascades and the release of secondary mediators from granules. Various agonists are involved in platelet activation (such as thrombin,  $\text{TxA}_2$ , and ADP). ADP activates the  $\text{P2Y}_1/\text{P2Y}_{12}$  receptors, which are crucial for platelet aggregation. Platelets will aggregate with one another through fibrinogen bridges linking their  $\alpha_{\text{IIb}}\beta_3$  integrins. The image was created using BioRender.

PLC $\gamma 2$  cleaves and hydrolyses membrane-bound phosphatidylinositol 4,5-bisphosphate (PIP $_2$ ), to the second messengers 1,2-diacylglycerol (DAG) and inositol 1,4,5-trisphosphate (IP $_3$ )<sup>74</sup>. DAG will activate protein kinase C (PKC), which is important in facilitating platelet granule secretion. Granules contain potent platelet receptor agonists, which further promote activation in a positive feedback loop. DAG also stimulates phospholipase A2 (PLA2) activity<sup>75,76</sup>. PLA2 facilitates the synthesis of thromboxane A2 ( $\text{TxA}_2$ ) from arachidonic acid (AA), a lipid that is liberated from the membrane due to the hydrolytic effects of activated PLA2 on phospholipids<sup>77,78</sup>. In turn, increased synthesis, and secretion of  $\text{TxA}_2$  from platelets results in further platelet

activation, as TxA<sub>2</sub> is an agonist (**Figure 3**) at the TxA<sub>2</sub> receptor<sup>79</sup>. The TxA<sub>2</sub> receptor is a G<sub>i</sub>-coupled protein, and its activation further drives pro-aggregatory events.

IP<sub>3</sub> will bind to and activate the inositol trisphosphate receptor (IP<sub>3</sub>R), a Ca<sup>2+</sup> channel embedded in the DTS. The DTS serves as an intracellular Ca<sup>2+</sup> store, and activation of the IP<sub>3</sub>R will lead to Ca<sup>2+</sup> mobilisation and increased cytosolic Ca<sup>2+</sup> levels. Ca<sup>2+</sup> is an important second messenger and facilitates platelet shape change to the active state, as well as granule content release. It will also facilitate conformational changes in the platelet integrins. Increases in cytosolic Ca<sup>2+</sup> and TxA<sub>2</sub> synthesis are also driven by thrombin-induced activation of protease-activated receptor 1 (PAR1) (**Figure 3**) and, at higher concentrations of thrombin, PAR4<sup>80</sup>. Thrombin is the most potent platelet activator. Thrombin-induced activation of the PARs is facilitated through proteolytic cleavage of the N-terminus<sup>81,82</sup>. PAR1 is coupled to a G<sub>q</sub> protein. The G<sub>q</sub> activated pathway facilitates the mobilisation of Ca<sup>2+</sup> through activation of phospholipase C beta 2 (PLCβ2)<sup>83</sup>. Thrombin-induced PAR activation requires P2Y<sub>12</sub> receptor activity (discussed in the next section) to potentiate and sustain the pro-aggregatory signal, and P2Y<sub>12</sub> antagonism will suppress PAR-mediated effects, such as TxA<sub>2</sub> production<sup>84</sup>.

As shown in **Figure 3**, the α2β1 integrin also activates, and binds directly to collagen<sup>85</sup>. Unlike GPVI and GPIb, this receptor's interaction with collagen is dependent on previously established intracellular signals, termed 'inside-out signalling'. This is because α2β1 requires activation signals to switch from its 'closed' inactive state to its 'open' active state, revealing binding sites for collagen. It will form high affinity and stable interactions with collagen, and this in turn will lead to the activation of additional intracellular signalling within the platelet. Additionally, integrin α<sub>IIB</sub>β<sub>3</sub> (glycoprotein IIb/IIIa or GPIIb/IIIa), which also requires inside-out signalling to exist in its active state, will also indirectly bind to collagen<sup>86,87</sup>. This interaction is facilitated by vWF, as described above.

As platelets activate, their shape changes, leading to the formation of finger-like projections called filopodia, and sheet-like protrusions called lamellipodia. This enables platelets to establish increased contact with the vessel wall<sup>88,89</sup>. The formation of filopodia is dependent on the reorganisation and elongation of actin filaments within the cytoskeleton, a process that is dependent on increased cytosolic  $\text{Ca}^{2+}$ <sup>38</sup>. The OCS provides the extra membrane required for platelet spreading.

#### 1.3.2.3. Release of secondary mediators and platelet aggregation

In an intact endothelium, endothelial ectonucleoside triphosphate diphosphohydrolase (NTPDase), also known as ecto-ATPase, degrades trace amounts of ADP, which is a platelet activator<sup>90-93</sup>. As platelets adhere to the damaged endothelium and activate, they will secrete ADP from their dense granules, in a process known as degranulation. ADP stimulates the GPCRs P2Y<sub>1</sub>, and P2Y<sub>12</sub>, which play a critical role in facilitating platelet aggregation<sup>94,95</sup>. As shown in **Figure 3** and **Figure 4**, ADP activates the receptors through binding to a site in their extracellular domain. This causes a dynamic change in the conformation of the proteins' helices, which is transmitted to the protein's intracellular domains<sup>96</sup>. This conformational change produces a powerful effect on the coupled trimeric G-protein, causing it to exchange guanosine diphosphate (GDP) for GTP. This allows the trimeric G-protein's  $\alpha$  subunit to dissociate from the  $\beta\gamma$  dimer. The subunits can then act on downstream proteins.

Upon stimulation with ADP, platelets experience two waves of aggregation. The first wave is rapid, transient, and reversible<sup>97</sup>. It is the result of the activation of the P2Y<sub>1</sub> receptor, which is a G<sub>q</sub>-coupled protein. As shown in **Figure 4**, activation of P2Y<sub>1</sub> initiates a cascade increasing the activity of the PLC $\beta$  enzyme, which cleaves and hydrolyses PIP<sub>2</sub> into the second messengers DAG and IP<sub>3</sub><sup>98</sup>. As previously mentioned, DAG will act on PKC. PKC activity is necessary for further granule secretion, resulting

in the secretion of more ADP to further act on the platelet, as well as on neighbouring platelets<sup>99</sup>. As IP<sub>3</sub> facilitates Ca<sup>2+</sup> mobilisation from intracellular Ca<sup>2+</sup> stores, this results in the rapid and transient increase in cytosolic Ca<sup>2+</sup> levels, facilitating shape change<sup>100</sup>. This Ca<sup>2+</sup> signal is not sustained, likely due to desensitisation of the receptor. Ca<sup>2+</sup> and DAG increase the activity of calcium and diacylglycerol-regulated guanine exchange factor 1 (CalDAG-GEFI), which stimulates the Ras-related protein RAP1B, allowing it to bind GTP<sup>101,102</sup>. RAP1B is a small guanosine triphosphatase (GTPase), and its stimulation leads to downstream events resulting in integrin  $\alpha_{IIb}\beta_3$  activation. When bound to GTP, RAP1B can bind to talin, a cytoskeletal protein<sup>103</sup>. This will initiate a process whereby talin is recruited to the plasma membrane, and tethered there, binding to the cytoplasmic domain of the integrin  $\alpha_{IIb}\beta_3$ <sup>104</sup>. This promotes conformational changes in the integrin, which switch it into its open, active state.

The integrin  $\alpha_{IIb}\beta_3$  is composed of an  $\alpha$  chain ( $\alpha_{IIb}$ ) and a  $\beta$  chain ( $\beta_3$ )<sup>105</sup>. These chains are composed of multiple extracellular domains, a transmembrane domain, and a cytoplasmic domain. In the inactive state, the extracellular portions of these chains are ‘bent’ and exist in a closed conformation. However, in their activated conformation, these chains are open, exposing the ‘headpieces’ of the receptor (**Figure 3**), where binding sites exist for fibrinogen<sup>106</sup>. Fibrinogen is a soluble blood protein that is necessary for platelet aggregation to occur<sup>107</sup>. It is a glycoprotein with a rod-like structure and is composed of three chains ( $\alpha_2\beta_2\lambda_2$ ), each existing as homodimers<sup>108-110</sup>. The homodimers are connected through a central domain. Thus, at each end of the fibrinogen protein exists identical C-terminals from each of the chains. The C-terminal of the  $\lambda$  chain contains a unique sequence that can bind to ligand binding sites present in the active conformation of the  $\alpha_{IIb}\beta_3$  ectodomain<sup>111-114</sup>. Fibrinogen is an important

endogenous ligand for the integrin  $\alpha_{IIb}\beta_3$ , and serves as a vital bridging molecule, facilitating platelet-platelet adherence (**Figure 3**).

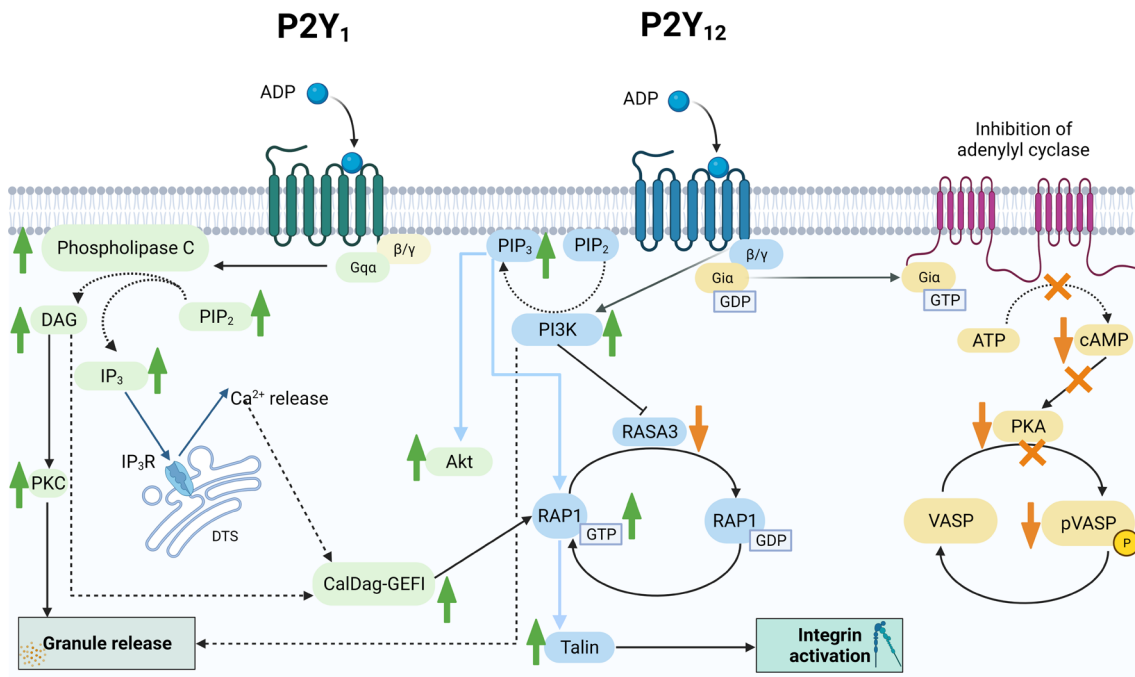


**Figure 4: The P2Y<sub>1</sub> and P2Y<sub>12</sub> signalling pathways.** P2Y<sub>1</sub> is a G<sub>q</sub>-coupled receptor, and its activation leads to an increase in phospholipase C activity. In turn, phospholipase C hydrolyses PIP<sub>2</sub> into the second messengers DAG and IP<sub>3</sub>. IP<sub>3</sub> acts on IP<sub>3</sub> receptors (IP<sub>3</sub>Rs) embedded in the dense tubular system (DTS), leading to Ca<sup>2+</sup> mobilisation. DAG will activate protein kinase C, which is important for granule release. DAG and Ca<sup>2+</sup> increase CalDAG-GEFI activity, which stimulates RAP1B. Conversely, P2Y<sub>12</sub> is a G<sub>i</sub>-coupled receptor. Activation of the G<sub>i</sub> β/γ signalling pathway will lead to an increase in phosphoinositide 3-kinase (PI3K) activity. PI3K phosphorylates PIP<sub>2</sub>, leading to an increase in PIP<sub>3</sub> levels. PIP<sub>3</sub> prevents the Ras-GTPase-activating protein 3 (RASA3)-induced deactivation of RAP1B (in its GDP-bound form). RAP1B interacts with talin, which is crucial for integrin activation. Activation of the P2Y<sub>12</sub> receptor's G<sub>i</sub> α signalling pathway will lead to inhibition of adenylyl cyclase, and a decrease in cAMP levels. This leads to a decrease in PKA (protein kinase A) activity and VASP cannot be phosphorylated. Note that in this schematic, dotted arrows denote an increase in the level of a substance, whereas full arrows denote an increase in the activity of a protein. Green arrows denote an increase in protein activity, whereas orange arrows denote a decrease in protein activity. The image was created using BioRender.

The second wave of platelet aggregation is irreversible and sustained, occurring slower than the first wave. It is the result of the activation of the P2Y<sub>12</sub> receptor by ADP<sup>2,115-119</sup>. The P2Y<sub>12</sub> G<sub>i</sub>-protein's βγ subunit will activate phosphoinositide 3-kinase (PI3K). PI3K will inhibit the GTPase-activating protein (GAP) Ras-GTPase-activating protein 3 (RASA3)<sup>120</sup>. In circumstances where RASA3 is not inhibited by PI3K, it regulates RAP1B, by promoting its inactive GDP-bound form (RAP1B-GDP). The P2Y<sub>12</sub>→PI3K signalling pathway leads to an increase in PIP<sub>3</sub>, and this sustains downstream RAP1B activation initiated by P2Y<sub>1</sub>, by preventing its RASA3 induced deactivation<sup>101</sup>. Therefore, P2Y<sub>12</sub> activation is required to inactivate RASA3 and maintain RAP1B in its active GTP-bound form. This reinforces the P2Y<sub>1</sub>→CalDAG-GEFI→RAP1B induced pro-aggregatory signal<sup>99,102,121</sup>. Thus, integrins on neighbouring platelets continue to bind together as the result of the amplifying pro-aggregatory signals from P2Y<sub>12</sub>. The PI3K→PIP<sub>3</sub>→RASA3 pathway is key in fulfilling P2Y<sub>12</sub>'s biological activity.

Additionally, once PI3K is activated by the G-protein's βγ subunit, it can also go on to cause increased degranulation from platelet dense granules, which contain ADP. This further reinforces the pro-aggregatory signal in a self-perpetuating manner and facilitates the recruitment of additional platelets to the site of injury. As well as this, potentiation of the PI3K pathway enhances platelet alpha granule secretion. This leads to the expression of the protein P-selectin on the surface of platelets. As previously mentioned, P-selectin is found embedded in the membranes of platelet alpha granules and its translocation to the surface membrane serves as a marker of platelet activation. P-selectin expressed on the surface of activated platelets will bind to the P-selectin glycoprotein ligand-1 (PSGL-1), which is present on white blood cells<sup>122-124</sup>. This facilitates platelet-neutrophil and platelet-monocyte interactions<sup>125</sup>. Platelets also express PSGL-1, albeit at lower levels than white blood cells. Studies have suggested

that P-selectin expression also plays an important role in mediating platelet-platelet interactions, in a mechanism occurring independently from that of the integrin  $\alpha_{IIb}\beta_3$  receptors<sup>123,126,127</sup>. As additional platelets are recruited to the site, the aggregates will build beyond a monolayer.

Lastly, P2Y<sub>12</sub> agonism will also cause the G<sub>i</sub>-protein  $\alpha$  subunit to bind to the membrane-bound enzyme, adenylyl cyclase, reducing the enzyme's activity (**Figure 4**). The enzyme can no longer catalyse the conversion of ATP to cAMP. This, in turn, reduces levels of the second messenger cAMP<sup>95</sup>. Where there are insufficient levels of cAMP to bind to and activate downstream protein kinase A (PKA), PKA is also unable to phosphorylate its substrates, including vasodilator-stimulated phosphoprotein (VASP)<sup>128</sup>. Whilst integrin activation is not particularly affected by loss of VASP, phosphorylated VASP (pVASP) is studied as an important marker in assessing P2Y<sub>12</sub> antagonism and serves as a read-out of cAMP $\rightarrow$ PKA signalling<sup>129</sup>.

#### 1.3.2.4. The blood coagulation cascade

Although the blood coagulation cascade was not the primary focus of this work, it is important to understand how it contributes to thrombus formation. The cascade is composed of two independent pathways - the extrinsic pathway and the intrinsic pathway. These pathways are composed of a sequence of interactions between blood coagulation factors, denoted by Roman numerals, each of which activates the next.

The extrinsic pathway is triggered by blood coagulation factor VII (proconvertin) forming a complex with tissue factor. The intrinsic pathway (also known as the ‘contact pathway’) is triggered upon blood coagulation factor XII (Hageman factor) achieving contact with collagen. In either case, the resulting event of each of these pathways is the formation of the enzyme thrombin. Thrombin cleaves the blood protein fibrinogen into fibrin monomers. These undergo polymerisation to form long strands which will deposit at the site of injury to form a mesh to stabilise the platelet plug<sup>62,112</sup>. Thrombin’s role in PAR activation has previously been described (**Figure 4**).

## 1.4. P2Y<sub>12</sub>: structure and pharmacology

### 1.4.1. Overview

An orphan platelet GPCR was identified in 1999 (named SP1999, also HORK3, P2CYC, P2T<sub>AC</sub>)<sup>130</sup>. In 2001, the receptor was cloned, and its cognate ligand was identified as ADP<sup>131</sup>. During this time, new names began to emerge for the receptor, including P2Y<sub>ADP</sub> and P2Y<sub>12</sub>. The receptor was found to belong to the purinergic 2Y (P2Y) family of receptors, which are activated by nucleotides<sup>132,133</sup>.

P2Y<sub>12</sub> is a class A (rhodopsin-like) GPCR expressed on the surface of platelets that can be stimulated by the endogenous agonist, ADP, and the synthetic (and more potent) agonist, 2-(methylthio)adenosine 5'-diphosphate (2MeSADP) (**Figure 5, Table 1b**). As shown in **Table 1b**, 2MeSADP has greater binding affinity for the receptor than ADP. The PK<sub>i</sub> values for 2MeSADP and ADP are reported to be 5.9 and 9.2, respectively<sup>134</sup>. However, ADP is more biologically relevant as it is the only agonist that can act on P2Y<sub>12</sub> *in vivo*.

As previously described, P2Y<sub>12</sub> plays a crucial role in the formation and stabilisation of platelet aggregates. P2Y<sub>12</sub> is essential to prevent bleeding in mammals and ensure survival. Inherited P2Y<sub>12</sub> deficiency or dysfunction can cause lifelong bleeding disorders<sup>121,135</sup>. Importantly, P2Y<sub>12</sub> is a member of the GPCR superfamily, which is the largest class of proteins in the human genome, and the leading protein targets for marketed drugs<sup>136-138</sup>. Due to the key role P2Y<sub>12</sub> plays in thrombus formation, it is an attractive pharmacological target<sup>139,140</sup>. It is targeted by the covalently acting antagonists, clopidogrel and prasugrel, and the reversibly acting antagonists, ticagrelor and cangrelor.

The key reasons to develop novel P2Y<sub>12</sub> modulators can be broadly divided into five areas, which will be discussed in detail in this section. 1) The covalent antagonists have a slow onset and offset of action, and their effects are difficult to fine-tune and control<sup>141,142</sup>; 2) 30-50% of the population respond poorly to clopidogrel therapy because of polymorphisms in the cytochrome P450 enzyme 2C19 (CYP2C19), thus it cannot be converted to its active metabolite<sup>141-144</sup>; 3) The reversibly acting drug, ticagrelor, causes dyspnoea which may limit some daily activities and/or lower patient adherence<sup>8-10,14,15,145-147</sup>; 4) All of the P2Y<sub>12</sub> antagonists increase the risk of bleeding in patients<sup>141,142,148,149</sup>; 5) The recently solved P2Y<sub>12</sub> crystal structures have not previously been used in the development of novel modulators.

Novel scaffolds with better pharmacokinetic profiles and reduced likelihood of causing dyspnoea are required. Additionally, whilst a P2Y<sub>12</sub> antagonist with 0% bleeding risk is impossible to find, scaffolds which carry a lower bleeding risk than the current inhibitors may still be possible to find. Accumulation of novel P2Y<sub>12</sub> inhibitory scaffolds may broaden the pharmacological space for the receptor and facilitate future drug discovery efforts. Little is known about how the P2Y<sub>12</sub> ligands bind to P2Y<sub>12</sub>. Interestingly, P2Y<sub>12</sub> has a bifurcated orthosteric site, making both competitive and non-competitive antagonism possible<sup>17,18</sup>. This section explores the pharmacology of the receptor, its structure, and structure-function relationships.

### *1.4.2. Pharmacology of the P2Y<sub>12</sub> receptor*

Inhibition of P2Y<sub>12</sub> is important in patient populations where there is an increased risk of arterial thrombosis. There are currently four approved drugs on the market designated as the P2Y<sub>12</sub> antagonists (**Figure 5, Table 1**): clopidogrel (Plavix™, manufactured by Bristol-Myers Squibb and Sanofi Pharmaceuticals), prasugrel (Effient™, manufactured by Eli Lilly and Company), ticagrelor (Brilinta™, manufactured by AstraZeneca), and cangrelor (Kengreal™, manufactured by The Medicines Company).

The orally active drugs clopidogrel, and ticlopidine (now discontinued), were approved by the Food and Drug Administration (FDA) for medical use in 1997, and 1999, respectively<sup>134</sup>. In 2009, prasugrel was approved. The active metabolites of these thienopyridine drugs bind covalently to P2Y<sub>12</sub>. In 2010, a direct and reversibly acting drug, ticagrelor, was approved<sup>150,151</sup>. Ticagrelor is also orally active. Cangrelor (AR-C69931MX), which is also direct and reversibly acting, was approved in 2015<sup>152</sup>. It is the only P2Y<sub>12</sub> antagonist that can be administered intravenously. Cangrelor is administered in patients undergoing percutaneous coronary intervention (PCI) to reduce the likelihood of thrombotic events occurring during or immediately after the procedure. In the same year, ticlopidine was withdrawn from the market due to toxicity concerns. The P2Y<sub>12</sub> antagonists are an important class of drugs as they have been shown to prevent secondary thrombotic events occurring in cardiovascular patients with ACS<sup>5,6,95,153-157</sup>. The orally active drugs are usually prescribed in dual antiplatelet therapy with the non-steroidal anti-inflammatory drug (NSAID) aspirin<sup>156,158-161</sup>.

All currently marketed P2Y<sub>12</sub> antagonists were discovered in the absence of the P2Y<sub>12</sub> structure. Furthermore, ticlopidine, clopidogrel, prasugrel and cangrelor were all discovered before the P2Y<sub>12</sub> receptor was cloned. Thus, their target was unidentified at the time.

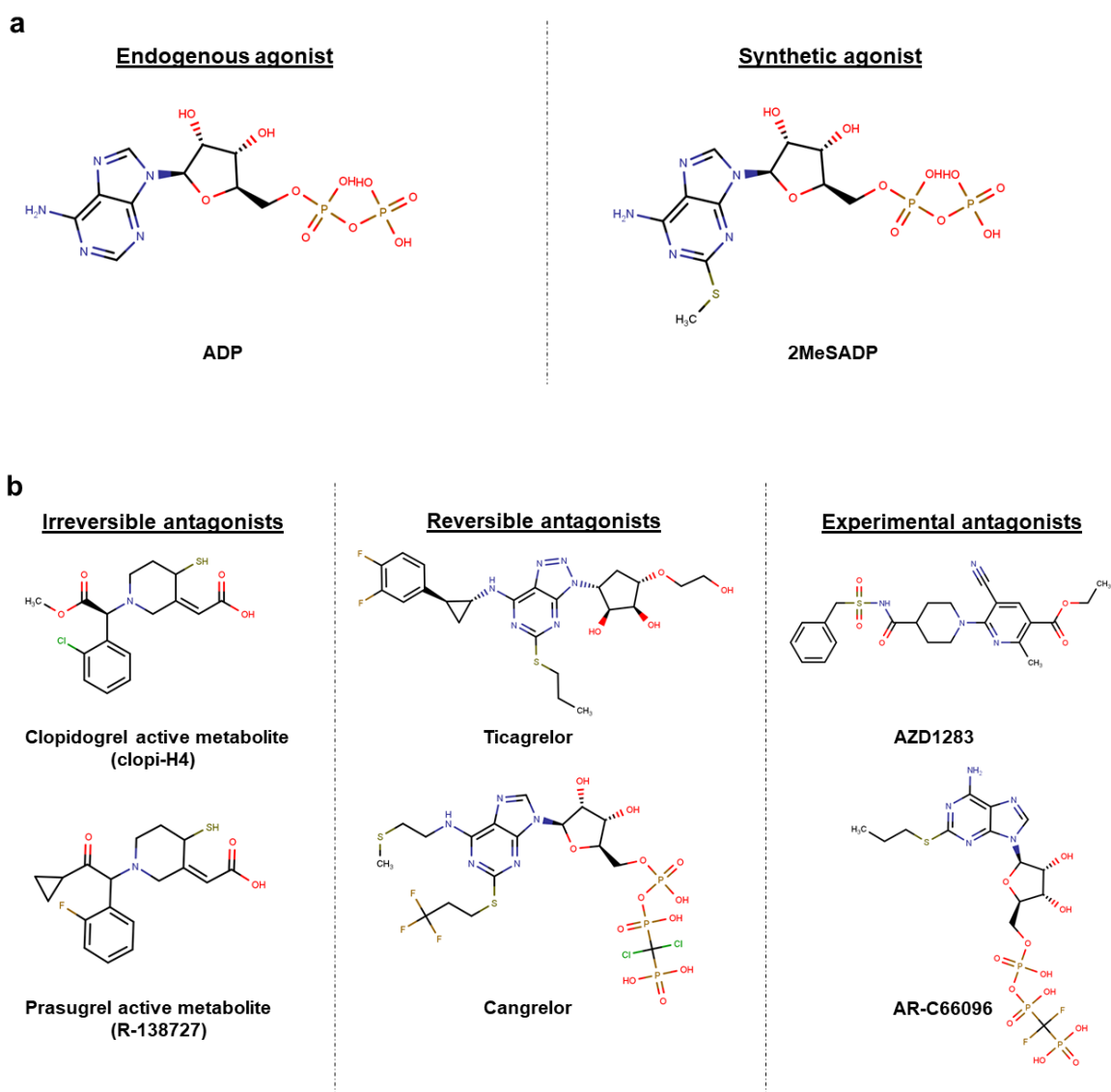


**Figure 5: Modulators of P2Y<sub>12</sub>.** **a)** The 2D chemical structures of the P2Y<sub>12</sub> agonists. **b)** The 2D chemical structures of the marketed irreversible and reversible antagonists, as well as the experimental antagonists (both reversible). The structures were drawn using MarvinSketch.

**Table 1a: Marketed P2Y<sub>12</sub> antagonists.**

<b>Drug</b>	<b>Description</b>	<b>Route of administration</b>	<b>Metabolism</b>
<b>Clopidogrel</b>	Thienopyridine	Oral	Pro-drug; Metabolised by CYP2C19 in the liver to active metabolite clopi-H4.
<b>Prasugrel</b>	Thienopyridine	Oral	Pro-drug; Metabolised by esterases in the intestines, as well as by CYP3A and CYP2B6 in the liver to active metabolite R-138727.
<b>Ticagrelor</b>	Nucleoside-based	Oral	Direct-acting, but also has an equipotent metabolite AR-C124910XX (metabolised by CYP3A4 and CYP3A5 in the liver).
<b>Cangrelor</b>	Nucleotide-based; ATP analogue	Intravenous	Direct-acting.

**Table 1b: Reported binding affinity values for the P2Y<sub>12</sub> ligands under study in this work.**

<b>Compound</b>	<b>Reported parameter</b>	<b>Value</b>	<b>Reference(s)</b>
<b>ADP</b>	PK <sub>i</sub>	5.9	[134]
<b>2MeSADP</b>	PK <sub>i</sub>	9.2	[134]
<b>Cangrelor</b>	PK <sub>D</sub>	8.6-9.2	[208], [346], [347]
<b>AR-C66096</b>	PK <sub>D</sub>	7.6-8.7	[344], [345]
<b>AZD1283</b>	PK <sub>D</sub>	8.0-8.2	[16], [17]

### 1.4.2.1. Irreversible P2Y<sub>12</sub> antagonists

The first P2Y<sub>12</sub> antagonist, ticlopidine, was found by chance (1972) when searching for anti-inflammatory drugs related to the drug tinoridine<sup>151,162</sup>. Although not found to manifest any anti-inflammatory property, ticlopidine displayed antiplatelet activity in rats orally administered the drug. The structure of the second antagonist in this class, clopidogrel, was reported in 1987<sup>151,163</sup>. Its scaffold was based directly on ticlopidine, with minor additions of some chemical groups. Clopidogrel has an improved side effect profile in contrast to ticlopidine<sup>164</sup>. Its effects were demonstrated in the PCI-CURE trial, where it was found to be highly effective at preventing thrombotic events in patients post-PCI<sup>165</sup>. Although its target and molecular mechanisms were unknown when it was discovered, it went on to become a blockbuster drug, and one of the best-selling of all time<sup>166-168</sup>.

The third thienopyridine-based drug, prasugrel, was discovered in 2000 through an analogue-based approach, with modifications to the clopidogrel structure<sup>169</sup>. Prasugrel was found to be superior to clopidogrel in the TRITON-TIMI 38 trial<sup>170</sup>. It displays a more rapid onset of action, increased potency, and less variability in response between patients<sup>154,171-175</sup>. The discovery of the thienopyridine class of P2Y<sub>12</sub> antagonists was based a great deal on a serendipitous observation. The drugs were approved for market based on their inhibitory effects on ADP-induced platelet aggregation, and inhibition of a receptor, designated 'P2T<sub>AC</sub>' (later named P2Y<sub>12</sub>), which had not yet been molecularly identified.

Prasugrel has a greater number of associated side effects than clopidogrel, due to the increased likelihood of bleeding risk<sup>155,176</sup>. This was also found during the TRITON TIMI 38 trial<sup>170</sup>. However, some studies have suggested there is no difference in bleeding risk between clopidogrel and prasugrel<sup>153,177</sup>. Prasugrel is prescribed as a

substitute for clopidogrel in patients with resistance to treatment with clopidogrel<sup>178,179</sup>. Clopidogrel resistance is primarily associated with problems metabolising the drug into its active form, but other factors can also lead to resistance, such as single nucleotide polymorphisms (SNPs) at P2Y<sub>12</sub>, or increased platelet responsiveness to ADP<sup>172,179-182</sup>. Regarding the latter, inter-individual variability in clopidogrel response may be due to varying platelet response to ADP, rather than varying platelet responsiveness to clopidogrel.

Polymorphisms in CYP2C19 are a major reason why clopidogrel metabolism is highly variable<sup>143,144</sup>. It has been suggested that 30-50% of those treated with clopidogrel are non-responders or exhibit an unsatisfactory response<sup>141</sup>. Prasugrel is initially metabolised by esterases in the intestines, and its metabolism is not affected by CYP2C19 polymorphisms (**Table 1**)<sup>183</sup>. It may be possible that prasugrel's superiority over clopidogrel may be due to its more consistent metabolism and effect in patients. However, both drugs have similar drawbacks<sup>181</sup>. For example, they have a slow onset of action due to being pro-drugs that require metabolism. They also have a long duration of action due to their covalent mode of binding, making it difficult to control their antiplatelet effects.

### 1.4.2.2. Reversible P2Y<sub>12</sub> antagonists

Reversible P2Y<sub>12</sub> antagonists are an attractive alternative to the irreversible antagonists due to their faster offset of action. The discovery of the reversible antagonists was more intuitive, in that a lead scaffold was used. Cangrelor (**Figure 5, Table 1**) was based on the structure of ATP, a weak inhibitor of platelet aggregation and a proposed antagonist of the P2T<sub>AC</sub> receptor<sup>151,152,184-187</sup>. Given the only difference between the agonist ADP and the antagonist ATP is their terminal  $\gamma$ -phosphate group, this clue was important in the rationale to use ATP as a starting point in developing a novel P2T<sub>AC</sub> antagonist. The cangrelor structure was then used to develop ticagrelor, which has a nucleoside-based scaffold. Ticagrelor has an equipotent active metabolite, AR-C124910XX<sup>188,189</sup>. In the PLATO trial, ticagrelor was found to be superior to clopidogrel in preventing adverse cardiovascular events<sup>148,157,176,190-193</sup>. Additionally, although P2Y<sub>12</sub> antagonists are usually given in conjunction with aspirin (dual antiplatelet therapy), the TWILIGHT trial suggested that ticagrelor monotherapy provides the same protection against thrombotic events<sup>194</sup>. Reduced risk of bleeding was observed than with a dual ticagrelor + aspirin regimen.

However, a major problem with ticagrelor is the off-target effects that are caused by its nucleoside-based scaffold, due to its inhibition of the equilibrative nucleoside transporter 1 (ENT1) on platelets and erythrocytes<sup>7-13,189,195</sup>. This causes an increase in extracellular adenosine levels<sup>9,145</sup>. Patients have been reported to experience dyspnoea, which has also been reported as a side effect of the reversible, nucleotide-based drugs cangrelor, and elinogrel, the latter of which did not complete clinical trials due to administrative reasons<sup>8,9,14,15,145-147</sup>. Furthermore, ticagrelor has been reported to trigger ventricular pauses<sup>8,196</sup>. It also causes dyspnoea in healthy subjects<sup>10</sup>. Interestingly, no evidence has been found that either cangrelor or elinogrel antagonise ENT1. This

suggests that dyspnoea caused by these reversible nucleotide-based antagonists may be mediated by a mechanism related to P2Y<sub>12</sub> inhibition<sup>197</sup>.

In randomised trials, dyspnoea has not been indicated to be a side effect of the irreversible P2Y<sub>12</sub> antagonists, or other antiplatelet drugs, such as aspirin or the integrin antagonist, eptifibatide<sup>14,15</sup>. Another reversible drug, selatogrel, which is structurally like ticagrelor as it contains a pyrimidine core, entered Phase 1 clinical trials in 2020<sup>198-200</sup>. Although highly potent and reported to have a lower bleeding risk than ticagrelor, it has also been indicated to cause dyspnoea<sup>197,198</sup>. However, like cangrelor, this drug can only be administered intravenously. It has not been reported whether a non-nucleotide reversible antagonist of P2Y<sub>12</sub> (such as AZD1283) can cause dyspnoea. Whilst ticagrelor's off-target effects on the ENT1 receptor may be undesired due to the resulting dyspnoea, this dual-action (on P2Y<sub>12</sub> and ENT1) increases the overall inhibition of platelet aggregation levels<sup>7,11</sup>. It has also been reported that its effects on ENT1 may lead to further inhibitory effects on platelet activation by affecting the activity of the toll-like receptors (TLRs), and PAR1<sup>12,13,189</sup>.

Moreover, some *in vitro* evidence has suggested that ticagrelor exhibits inverse agonism at the P2Y<sub>12</sub> receptor<sup>7,201</sup>. It was found to reduce basal activity levels of the receptor. However, these experiments were conducted in cell lines where P2Y<sub>12</sub> was overexpressed. Whether or not this scenario will be true in an *in vivo* system is debatable, as there is no evidence that P2Y<sub>12</sub> is a constitutively active GPCR. It is also difficult to decipher how the inactive conformation of P2Y<sub>12</sub> is stabilised in comparison to known constitutively active GPCRs, as the P2Y<sub>12</sub> crystal structures are all ligand-bound.

Whilst ticagrelor is a nucleoside analogue, and its [1,2,3]triazolo[4,5-d]pyrimidine ring mimics adenine, cangrelor (reported PK<sub>DS</sub>: 8.6-9.2 (**Table 1b**)) is a nucleotide analogue (**Figure 5**) containing a core adenosine scaffold and three

phosphate groups<sup>150,152,202</sup>. Cangrelor has a fast onset of action (2 minutes), and a fast offset of action (30-60 minutes), making it ideal for use in a hospital setting<sup>203</sup>. Its fast offset of action is due to it being rapidly hydrolysed by phosphatases in the blood. Cangrelor cannot be administered orally because it is poorly absorbed due to the presence of its negatively charged phosphate groups. In the CHAMPION-PHOENIX trial, cangrelor was found to be effective at preventing thrombotic events in patients undergoing PCI, with no significantly increased risk of bleeding<sup>204</sup>. Cangrelor has an experimental analogue, AR-C66096, with reported PK<sub>D</sub> values of 7.6-8.7 (**Figure 5, Table 1b**).

Another reversibly acting P2Y<sub>12</sub> antagonist, AZD1283 (**Figure 5**), was also discovered by AstraZeneca through an iterative medicinal chemistry process<sup>151,205-207</sup>. AZD1283 has a non-nucleotide scaffold and is a high affinity P2Y<sub>12</sub> antagonist (PK<sub>D</sub>: 8.0-8.2) *in vitro*. However, it failed clinical trials due to the presence of its metabolically unstable ester group, as well as poor absorption *in vivo*<sup>151,207</sup>. Structure-activity relationship (SAR) around novel scaffolds must be carefully analysed in tackling this problem and exploring other group options. Although not approved for use in humans, AZD1283 still serves as an important experimental compound as it is the only antagonist co-crystallised with P2Y<sub>12</sub><sup>17</sup>.

Additionally, several groups of medicinal chemistry have already reported a few other reversibly acting, non-nucleotide scaffolds: BX-667, compound 4, and PSB-0739<sup>182,208-211</sup>. Despite existing in the literature for over a decade, none of these compounds has yet been further developed or approved as P2Y<sub>12</sub> antagonists. The precise reasons for this remain unknown, but there could be unfavourable pharmacokinetic, toxicological, or selectivity issues. Importantly, these scaffolds were reported before the X-ray crystal structure of P2Y<sub>12</sub> was solved. The use of the protein structure to explore binding modes of hit molecules is pivotal to the work in this thesis.

This is testified by the fact that, to date, no P2Y<sub>12</sub> antagonists have been reported from *in silico* screening against the published crystal structure of P2Y<sub>12</sub>. Novel antagonists may also enable us to gain a further mechanistic understanding of P2Y<sub>12</sub> pharmacology.

### 1.4.3. Structural insights

#### 1.4.3.1. Overview

In humans, P2Y<sub>12</sub> is composed of 342 amino acid residues (**Figure 6**), which form a bundle of seven transmembrane  $\alpha$ -helices (TM1-7), connected by three extracellular loops (ECLs), and three intracellular loops (ICLs). An eighth helix (TM8) is found parallel to the lipid membrane.

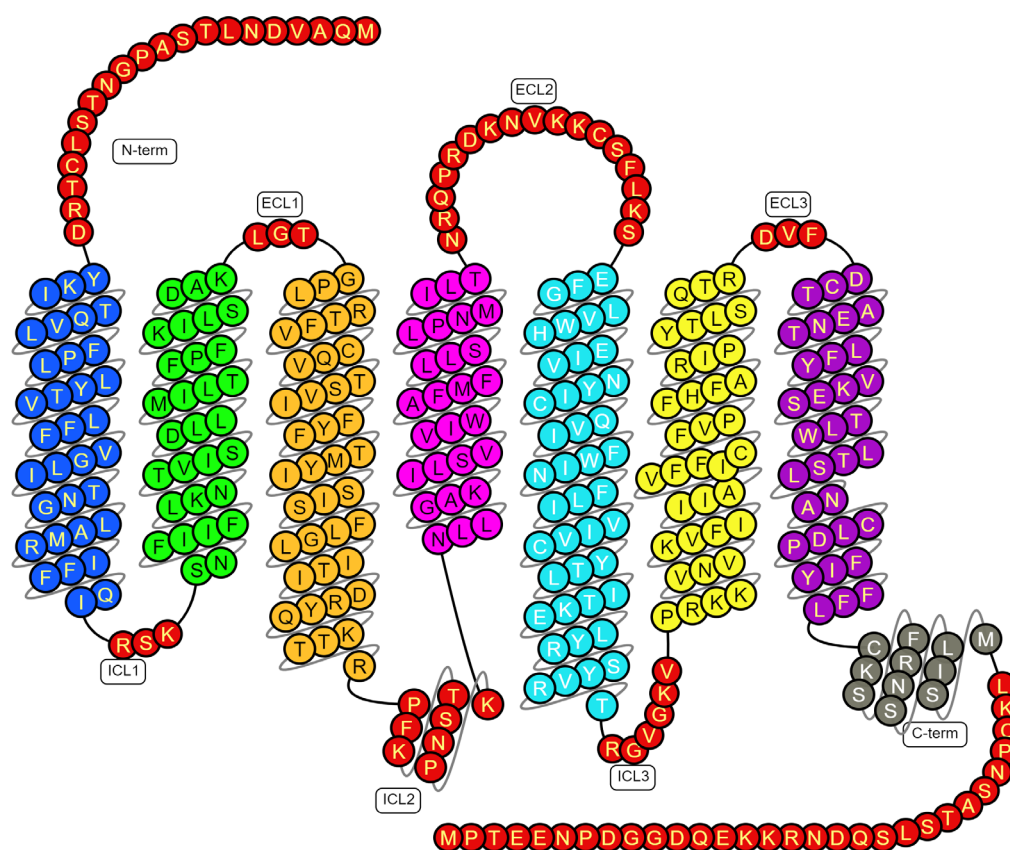


**Figure 6: The structure of P2Y<sub>12</sub>.** P2Y<sub>12</sub> is a class A GPCR composed of seven transmembrane helices, three extracellular loops (ECLs), and three intracellular loops (ICLs). It also possesses an eighth helix (dark grey) adjacent to the C-terminal domain. N-term: N-terminus, C-term: C-terminus. The figure (‘snakeplot’) was created in the GPCRDB (gpcrdb.org).

The first series of P2Y<sub>12</sub> crystal structures were published in 2014<sup>16,17</sup>. There are three available structures: antagonist-bound, agonist-bound, and partial agonist-bound. The structures make it possible to further explore ligand-binding modes. The

antagonist-bound crystal structure (Protein Data Bank (PDB) ID: 4NTJ; **Figure 7a-b**) is co-crystallised with the non-nucleotide ligand, AZD1283<sup>17</sup>. This structure was used in molecular docking in this work. The agonist-bound crystal structure (PDB ID: 4PXZ; **Figure 7c-d**) is co-crystallised with the nucleotide, 2MeSADP<sup>16</sup>. There is no ADP-bound structure available to date. The partial agonist-bound crystal structure (PDB ID: 4PY0; not shown) is co-crystallised with 2-(methylthio)adenosine 5'-triphosphate (2MeSATP). In this thesis, the agonist-bound structure and the antagonist-bound structure will also be referred to as the 'nucleotide-bound structure', and the 'non-nucleotide-bound structure', respectively. Furthermore, the Ballesteros-Weinstein numbering system will be used to denote amino acid residue positioning in superscript format, for example: 'Lys-280<sup>7.35</sup>' (where the first number represents the transmembrane helix that the residue belongs to, and the second number represents the position of the residue relative to the most conserved residue, 50)<sup>212,213</sup>.

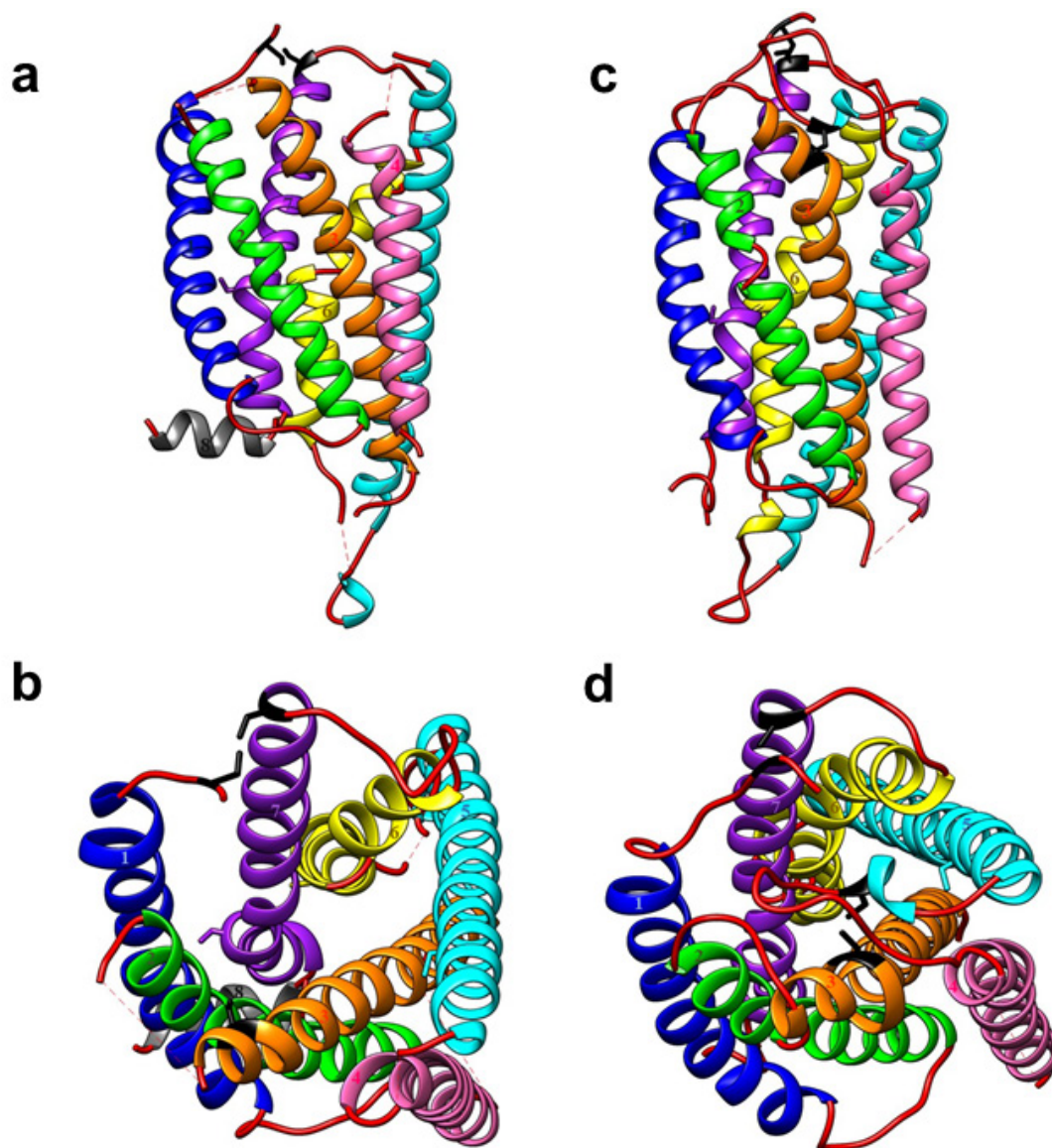


**Figure 7: Cartoon representations of the crystal structures of P2Y<sub>12</sub>.** **a)** side view of the antagonist-bound structure (ligand not shown), PDB ID: 4NTJ. **b)** Top view of the antagonist-bound structure. **c)** side view of the agonist bound structure (ligand not shown), PDB ID: 4PXZ. **d)** Top view of the agonist-bound structure. Blue: helix 1, green: helix 2, orange: helix 3, pink: helix 4, cyan: helix 5, yellow: helix 6, purple: helix 7. Loops are shown in red. Extracellular cysteines are shown in black. A disulfide bond forms between Cys-97<sup>3,25</sup> and Cys-175<sup>45,50</sup> in the agonist-bound structure. Hydrogen bonds are shown as red dashes. The figure was created using UCSF Chimera (University of California, San Francisco).

Several key differences exist between the nucleotide-bound and non-nucleotide-bound structures of P2Y<sub>12</sub>. In the nucleotide-bound structure (PDB ID: 4PXZ), a disulphide bond (**Figure 7c-d**) is found between Cys-97<sup>3,25</sup>, which belongs to the extracellular region of the third helix, and Cys-175<sup>45,50</sup>, which belongs to ECL 2<sup>16,18</sup>. The disulphide bond between residue 3.25 and ECL 2 is highly conserved amongst all class A GPCR structures that have been solved so far, except for the sphingosine-1-phosphate receptor 1 (S1P<sub>1</sub>)<sup>136,214-216</sup>. Interestingly, ECL 2 is missing in the non-nucleotide-bound structure of P2Y<sub>12</sub> (PDB ID: 4NTJ), and the previously mentioned disulphide bond is not observed<sup>16-18</sup>. Thus, this disulphide bond may be dynamic or labile in P2Y<sub>12</sub>, which may be important for receptor function<sup>17</sup>. Additionally, an eighth helix is found in the non-nucleotide-bound structure of P2Y<sub>12</sub>, whereas it is only partially resolved in the nucleotide-bound structure<sup>16,17</sup>.

The non-nucleotide-bound structure contains a cavity spanning two sub-pockets ('pocket 1', and 'pocket 2'), where AZD1283 is co-crystallised in pocket 1 (**Figure 8**) and spans over 17Å. Zhang et al. (2014) stated that the AZD1283 binding pocket is 'distinct in shape and location' compared to ligand binding pockets observed in other solved crystal structures<sup>17</sup>. The two pockets are separated by a barrier comprising of two bulky residues, namely Tyr-105<sup>3,33</sup> and Lys-280<sup>7,35</sup>. However, the agonist (2MeSADP) pocket is smaller in size, contracted, and confined to a buried region (shown later). This change in pocket shape arises due to the movement of helices 6 and 7 upon 2MeSADP binding, which does not occur upon AZD1283 binding<sup>16,17</sup>. Therefore, the structural rearrangements caused by agonist binding to shift helices 6 and 7 inward are likely the underlying reason it can activate the receptor, whereas the antagonist cannot.

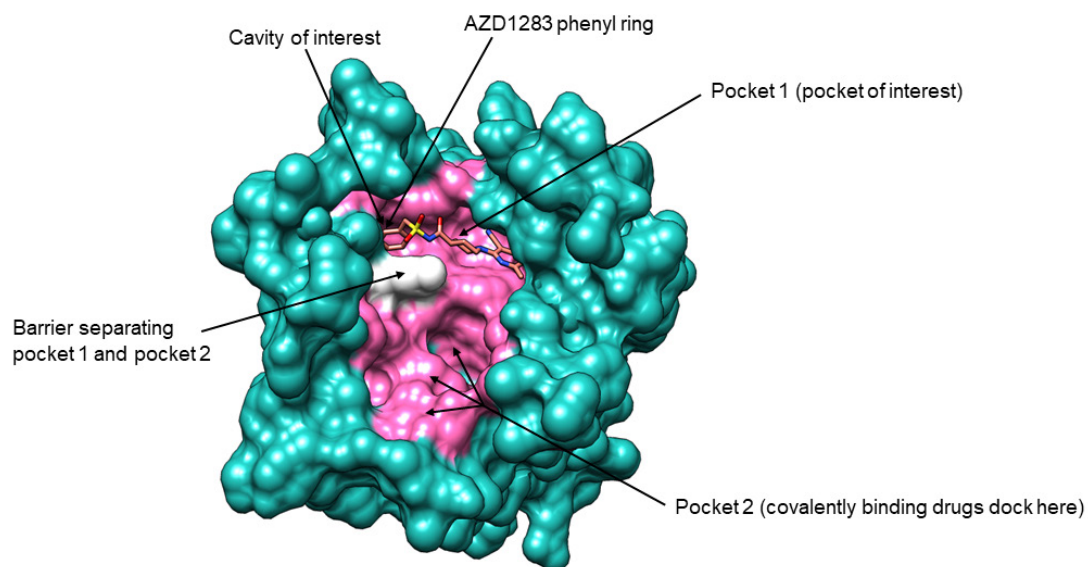


**Figure 8: The orthosteric binding site for the co-crystallised antagonist, AZD1283, on the human P2Y<sub>12</sub> receptor.** AZD1283 is shown in pocket 1 of the antagonist-bound P2Y<sub>12</sub> structure (PDB ID: 4NTJ). The phenyl ring of AZD1283 lodges between helices 6 and 7 (cavity of interest), preventing their inward shift. The protein structure is shown in surface representation and coloured teal. The general area of the orthosteric site is coloured pink. Pockets 1 and 2 are separated by a barrier (Tyr-105<sup>3.33</sup> and Lys-280<sup>7.35</sup>), coloured white. The active metabolites of the covalently binding drugs, clopidogrel and prasugrel, have been predicted to bind in pocket 2, where Cys-97<sup>3.25</sup> is found<sup>17,18</sup>. The image was created using PyMOL (Schrödinger Inc., New York, NY, USA).

### 1.4.3.2. The open vs. closed-lid models of P2Y<sub>12</sub>

The antagonist-bound state of P2Y<sub>12</sub> forms an open ‘lid’, whilst agonist binding causes ‘lid’ closure. The ‘lid’ is formed by the N-terminus and ECLs, which Zhang et al. (2014) described as ‘unusually cationic’<sup>16</sup>. The ECLs are mostly positively charged<sup>217</sup>. Molecular docking has shown that the reason helices 6 and 7 do not shift upon AZD1283 binding is because the phenyl ring of the compound lodges in between the helices, preventing their inward movement. In this case, the receptor’s ‘lid’ remains open (**Figure 8, Figure 9**). SAR analysis around the AZD1283 scaffold has revealed this phenyl ring to be crucial for its activity<sup>205</sup>.

However, upon agonist binding, the movement of helices 6 and 7 causes the receptor’s ‘lid’ to snap shut (**Figure 9**). The ‘lid’ plays a central role in P2Y<sub>12</sub>’s activation mechanism. A ‘lid’ has not been described for other GPCRs in the P2Y family, including P2Y<sub>1</sub>. However, rhodopsin has been described to possess  $\beta$ -hairpin loops which form a ‘lid’ at the extracellular domain<sup>218</sup>. Another paper suggested that, upon ligand binding, the ECL 2 in rhodopsin forms a ‘lid’ over the binding site which protects and restrains the bound ligand<sup>216</sup>. This paper also proposed that the shape of the lid is dependent on the ligand’s efficacy.

Comparisons between the non-nucleotide-bound (open-lid, PDB ID: 4NTJ) and nucleotide-bound (closed-lid, PDB ID: 4PXZ) crystal structures of P2Y<sub>12</sub> allow a better understanding of critical residues for ligand recognition, as well as receptor function. Additional insights for the activation and inhibition mechanisms of P2Y<sub>12</sub> could stem from having a 3D structure (ideally with good i.e.,  $\leq 2\text{\AA}$  resolution) solved in its *apo* state. The latter hitherto remains unavailable, and it may be the case that the unliganded or *apo* version of this receptor is too dynamic to lend itself to crystallisation or any other structural biology methods. However, if possible, this would be a valuable tool in

exploring how the antagonist affects the natural state of the receptor, and how that structure is then affected by the agonist. Furthermore, it would allow us to begin to understand how the receptor's structure may change during *in vitro* experiments. Although P2Y<sub>12</sub>, like other GPCRs, exists in an array of states, and is highly dynamic, at least one *apo* state of the receptor may be a key starting point, and possible 'control' structure, for any following comparisons involving ligand-bound structural changes<sup>96,136,219</sup>.

The non-liganded structure of the receptor (**Figure 9**) has previously been alluded to in the literature and described by one group in detail using simulations<sup>18</sup>. Paoletta et al. (2015) used molecular dynamics (MD) to generate a hybrid model of P2Y<sub>12</sub> using the nucleotide and non-nucleotide-bound structures, in a membrane-like environment. Through this method, some interaction details were predicted that had previously not been shown in the ligand-bound crystal structures. For example, at the residue level, a salt bridge was found between Arg-256<sup>6.55</sup> and Glu-188<sup>5.37</sup>, which linked helices 5 and 6. The polar side chains of Gln-195<sup>5.44</sup> and Thr-260<sup>6.59</sup> further stabilised the interaction between neighbouring helices 6 and 7, through a network of hydrogen bonds with water molecules and membrane 1-palmitoyl-2-oleoyl-sn-glycero-3-phosphocholine (POPC) lipids.

Furthermore, clusters of water molecules were found to bridge residues in helices 1, 2 and 7. These residues included Lys-80<sup>2.60</sup>, Asp-84<sup>2.64</sup>, Arg-93<sup>3.21</sup>, and Glu-281<sup>7.36</sup>, as well as Arg-19 (N-terminal domain), Tyr-21<sup>1.28</sup>, Lys-174 (ECL 2), and Glu-273<sup>7.28</sup>. Chloride ions also appeared to play a role in stabilising interactions between residues, found in close vicinity to Arg-93<sup>3.21</sup>. This is also identified in the ligand-bound crystal structures.

The *apo* state of P2Y<sub>12</sub> has been predicted to possess an open 'lid' conformation (**Figure 9**), which is also in agreement with work by Zhang et al. (2014)<sup>16,18</sup>. The non-nucleotide-bound structure also has an open 'lid', whereas the nucleotide-bound structure has a closed 'lid'. Piecing together these clues, it is possible to build up a chronological picture of the dynamic changes that occur in the architecture of the receptor in its different states. Beginning with an open 'lid' in its resting state, followed by the binding of the antagonist, which maintains this open 'lid' conformation, and finally, the 'lid' closing upon binding of the agonist, at which point the receptor will activate. It is unknown what the implications of a closed 'lid' are for agonist dissociation.

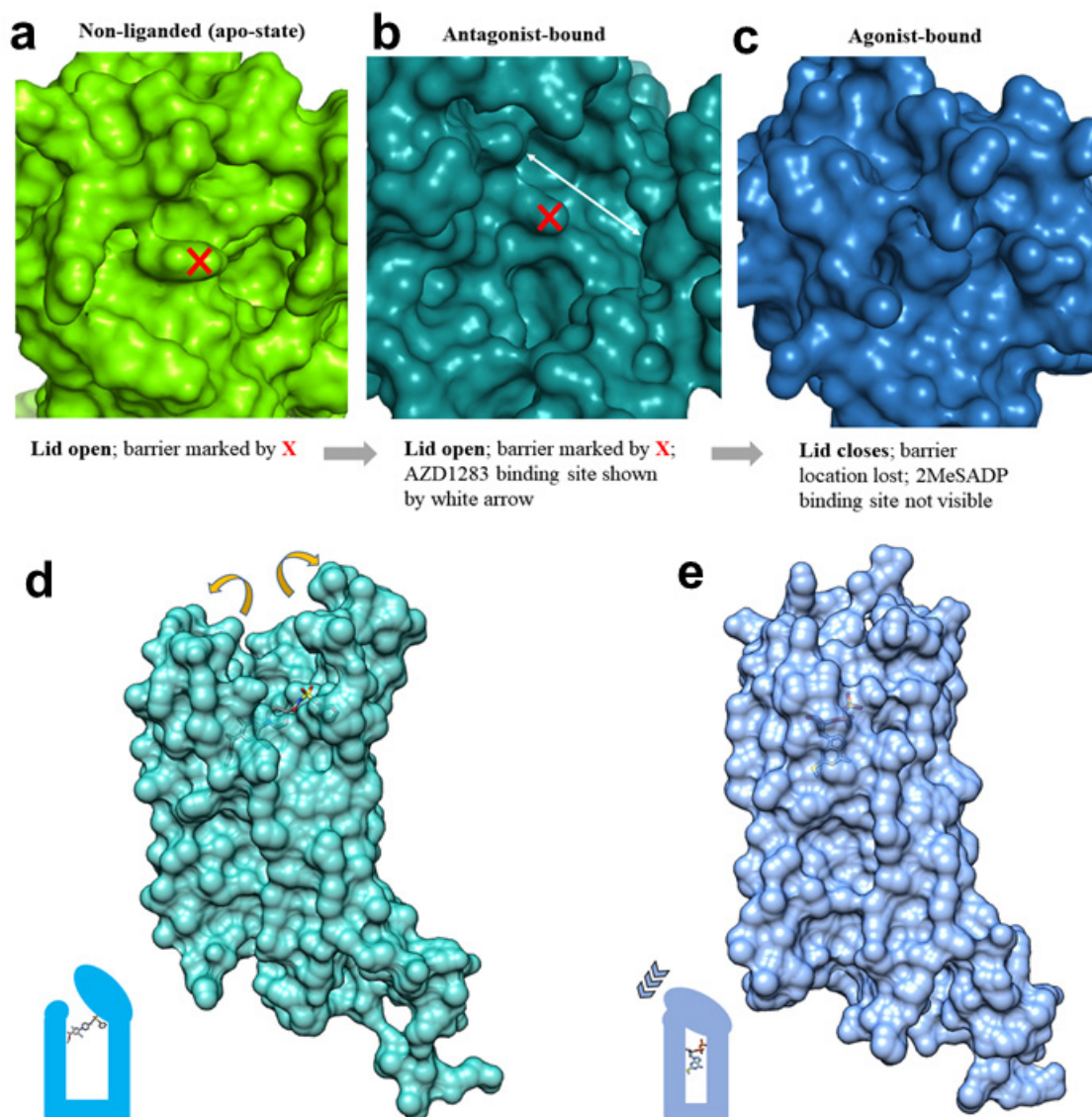


**Figure 9: Surface representations of the structures of P2Y<sub>12</sub> at various putative states.** **a)** The *apo* state of the protein was obtained from a PyMOL session of molecular dynamic simulations, performed by Paoletta et al. (2015)<sup>18</sup>. The protein is coloured green. The barrier separating pockets 1 and 2 is marked by a red X (Tyr-105<sup>3,33</sup> and Lys-280<sup>7,35</sup>). Note that this is not a real crystal structure, but a predicted model. **b)** Antagonist-bound crystal structure (PDB ID: 4NTJ), barrier marked by X, the protein is coloured dark cyan. **c)** Agonist-bound crystal structure (PDB ID: 4PXZ), barrier no longer visible, the protein is coloured blue. **d)** Side view of the antagonist-bound structure (AZD1283 shown as sticks), with an open-lid conformation, the protein is coloured cyan. **e)** Side view of the agonist-bound structure (2MeSADP shown as sticks), with a closed-lid conformation, the protein is coloured blue. The images were created using PyMOL and Microsoft PowerPoint.

### 1.4.3.3. Mechanisms of P2Y<sub>12</sub> activation

The inward shift of helices 6 and 7 serves as a ‘macro-switch’ for P2Y<sub>12</sub> activation. Upon agonist binding, helix 6 shifts over 10Å inward, and helix 7 shifts over 5Å inward, compared to the antagonist-bound structure<sup>16</sup>. This is consistent with the activation mechanism of other class A GPCRs, where rearrangements in helices 5-7 play a pivotal role in the transmission of the signal to the cytosolic domain<sup>96,218,220,221</sup>. This movement results in the structural rearrangement of a crevice which will accommodate the G-protein. The movement of helix 6 is found to be a hallmark activation ‘switch’ throughout the GPCR family, as it enables G-protein coupling<sup>96,218,220,221</sup>. However, this is often described as an outward shift and not an inward shift as with P2Y<sub>12</sub>. In contrast to other GPCRs, the extracellular domain of P2Y<sub>12</sub> undergoes substantial structural changes upon agonist binding and is highly plastic<sup>16</sup>.

GPCR activation commonly results in subtle changes in the extracellular domain, which lead to large structural rearrangements in the intracellular domain. In P2Y<sub>12</sub>, the conformational changes in the intracellular domain are not as prominent as those in the extracellular domain. However, this is likely because the structure captures the 2MeSADP-bound inactive state (no G-protein bound) with regard to the intracellular domain, as stated by Zhang et al.<sup>16</sup>.

The ‘micro-switches’ (residue contacts) that trigger helix movement and P2Y<sub>12</sub> activation are less clear. Micro-switches may be considered at two levels: 1) direct - the immediate contacts that the agonist forms with the receptor, and 2) indirect - the effect on other residues because of (1), i.e., the residues involved in agonist binding which do not form direct contact with the ligand. With regards to point (1), although class A GPCRs tend to undergo similar structural changes at the macro level to couple to the G-

protein, their micro-switches vary. GPCRs have evolved to respond to a repertoire of structurally diverse ligands, and it is expected that immediate residue contacts widely vary between ligands acting on different GPCRs<sup>96,222</sup>. Upon ligand binding, there is no single residue contact that shows conserved rearrangement between class A GPCRs<sup>221</sup>.

However, with regards to point (2) a universal ‘transmission switch’ exists in residues 3.40, 5.51, 6.44, and 6.48, which possess hydrophobic side chains<sup>96,218,220,221</sup>. This has previously been found through analyses and comparisons of GPCR crystal structures in their active and inactive states. It is suggested that repacking of intrahelical contacts occurs between the residues 6.44 and 6.48<sup>218</sup>. Residue 3.40 will move toward 6.48, and 5.51 will move toward 6.44. These residues are highly conserved and play an important role in facilitating the movement of helix 6. In P2Y<sub>12</sub>, these residues are: Ile-112<sup>3.40</sup>, Phe-202<sup>5.51</sup>, Phe-245<sup>6.44</sup>, and Phe-249<sup>6.48</sup>. Furthermore, residues Lys-174 (ECL 2) and Arg-265 (ECL 3) are suggested to play an important role in receptor activation even though they do not form direct contact with 2MeSADP<sup>16</sup>.

Additionally, P2Y<sub>12</sub> contains a DRY motif (Asp-121<sup>3.49</sup>, Arg-122<sup>3.50</sup>, and Tyr-123<sup>3.51</sup>) in helix 3 (**Figure 6**), which is a common motif amongst class A GPCRs<sup>223</sup>. In class A GPCRs, the conserved residue, Arg-122<sup>3.50</sup>, in the DRY motif forms an ionic intrahelical ‘lock’ with residue 6.30 or 6.34. Upon ligand binding, the DRY motif will ‘swing’ to interact with the G-protein<sup>220</sup>. However, this ionic lock between the DRY motif and helix 6 is lacking in P2Y<sub>12</sub>, which may reflect the protein’s high basal activity<sup>17,224,225</sup>. Importantly, a mutation in the DRY motif (Arg-122<sup>3.50</sup> to Cys) has been shown to result in reduced aggregation and a chronic bleeding disorder<sup>226-228</sup>. Furthermore, helix 3 has been suggested to serve as a structural ‘hub’ in class A GPCRs and plays a central role in the stabilisation of distinct conformational states<sup>218,220</sup>.

Although the residue level changes that occur upon P2Y<sub>12</sub> activation have not been described, some clues can be delineated from 2MeSADP-P2Y<sub>12</sub> interactions. Several key differences exist between 2MeSADP and AZD1283 in their interactions with their protein, which may shed light on why 2MeSADP causes a shift in helices 6 and 7 upon binding, whereas AZD1283 does not (**Figure 10, 11, and 12**)<sup>16-18</sup>. The 2D protein-ligand interaction maps for 2MeSADP and AZD1283 seem to vary between papers, as different 2D protein-ligand interaction profiler software tend to generate slightly different maps. **Figure 12** shows the residues surrounding the binding pocket, and the ligand interactions figure created using the 2D protein-ligand interaction profiler, PoseView (Centre for Bioinformatics, University of Hamburg (<https://proteins.plus/>)). The original 2D protein-ligand interaction map figures could not be shown here due to copyright reasons. However, the reader may refer to the two original crystal structure papers to view these figures<sup>16,17</sup>. The interaction maps generated by Paoletta et al. may also be referred to<sup>18</sup>.

In the 2MeSADP-bound structure, Phe-106<sup>3,34</sup>, Leu-155<sup>4,56</sup>, Ser-156<sup>4,57</sup> and Asn-159<sup>4,60</sup> form a small hydrophobic cavity (**Figure 10, 11, and 12**) between helices 3 and 5. The -SCH<sub>3</sub> group of 2MeSADP has been shown to bind in this region at the C2 position<sup>16,18</sup>. Given that this -SCH<sub>3</sub> group is the only difference between 2MeSADP and the less potent agonist ADP, this region may be important in determining agonist potency. It has been suggested that the -SCH<sub>3</sub> group serves as an anchor, increasing the binding complementarity of 2MeSADP<sup>16</sup>. This explains the greater affinity of 2MeSADP for the receptor, compared to ADP. Computational predictions have shown that linear groups are well-tolerated within this region, whereas bulky substituents are not. Interestingly, the antagonists AZD1283, cangrelor, AR-C66096, AR-C67085, and AR-C68511 are all predicted to have a linear chain extending into this hydrophobic cavity when docked against the agonist-bound structure<sup>17,18</sup>.

Furthermore, 2MeSADP's phosphate groups also appear to be important for its potency (**Figures 10, 11, and 12**). They bind in a region composed of a polar network of residues: Arg-93<sup>3,21</sup>, Arg-256<sup>6,55</sup>, Tyr-259<sup>6,58</sup>, Gln-263<sup>6,62</sup>, Lys-280<sup>7,35</sup> (**Figure 12**). Mutagenesis studies have shown that some of these residues are important for receptor function and/or ligand binding<sup>229,230</sup>. For example, the cationic residues Arg-256<sup>6,55</sup> and Lys-280<sup>7,35</sup> have been reported as essential for agonist binding<sup>16,17</sup>. However, mutations in Lys-280<sup>7,35</sup> and Arg-256<sup>6,55</sup> do not affect the binding of the reversible antagonist ticagrelor<sup>18</sup>. MD simulations have shown that Arg-256<sup>6,55</sup> forms a salt bridge with Glu-188<sup>5,37</sup>, which links helices 5 and 6<sup>18</sup>. Furthermore, Tyr-259<sup>6,58</sup> is conserved within the P2Y family and plays an important role in coordinating the phosphate moieties. The positively charged ECLs have been suggested to fold around 2MeSADP through charge complementarity with the negatively charged phosphate moieties<sup>217</sup>. The additional  $\gamma$ -phosphate group in 2MeSATP results in a loss of agonist potency<sup>16</sup>. Similarly, ATP acts as an antagonist at the receptor due to its additional phosphate group, compared to the full agonist ADP<sup>231</sup>.

Moreover, 2MeSADP (but not AZD1283) interacts with the disulphide bond formed between Cys-97<sup>3,25</sup> and Cys-175<sup>45,50</sup>, which is only resolved in the nucleotide-bound structure (**Figure 7**). As shown in **Figure 12**, 2MeSADP forms hydrogen bonds with these residues. Mutations to either Cys-97<sup>3,25</sup> or Cys-175<sup>45,50</sup> significantly reduce agonist binding<sup>16</sup>. The movement of the ECLs in concert with helical movements is suggested to be important in GPCR activation and termed the 'global toggle switch model'<sup>232</sup>. ECL 2 has been suggested to play a critical role in ligand binding<sup>233</sup>. Disrupting contacts between the helical bundle and ECL 2 may play a role in GPCR activation. As explained in the previous section, ECL 2 may have a significant role in 'lid' closure upon agonist binding<sup>216,233</sup>. ECL 2 is not resolved in the antagonist-bound structure.

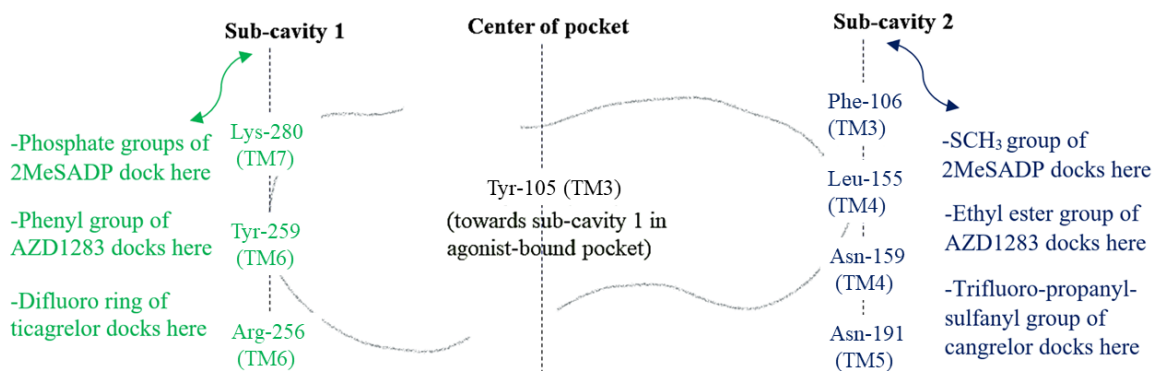


**Figure 10: Amino acid residues surrounding the agonist and antagonist-bound pockets of the P2Y<sub>12</sub> receptor.** The 2MeSADP and AZD1283 binding pockets of the P2Y<sub>12</sub> receptor partially overlap. The interactions within the orthosteric ligand binding site of P2Y<sub>12</sub> that are common to both 2MeSADP and AZD1283 are shown. Common residues in sub-cavity 1 are shown, where the phenyl group of AZD1283 and the difluoro ring of ticagrelor dock against the antagonist-bound structure<sup>17,18</sup>. The phosphate groups of 2MeSADP dock in this small sub-cavity against the agonist-bound structure<sup>16,18</sup>. Tyr-105<sup>3,33</sup> is at the center of the pocket in the AZD1283-bound pocket, but towards sub-cavity 1 in the 2MeSADP-bound pocket. Common residues in the small sub-cavity 2 are shown, where the -SCH<sub>3</sub> group of 2MeSADP, the ethyl ester group of AZD1283, and the tri-fluoro-sulfanyl group of cangrelor dock. Note that 2MeSADP and AZD1283 are reported to stabilise different conformations of P2Y<sub>12</sub>, and the diagram only shows a simplified representation of the orthosteric binding pocket based on common residue interactions<sup>16-18</sup>. The image was created using Microsoft PowerPoint.

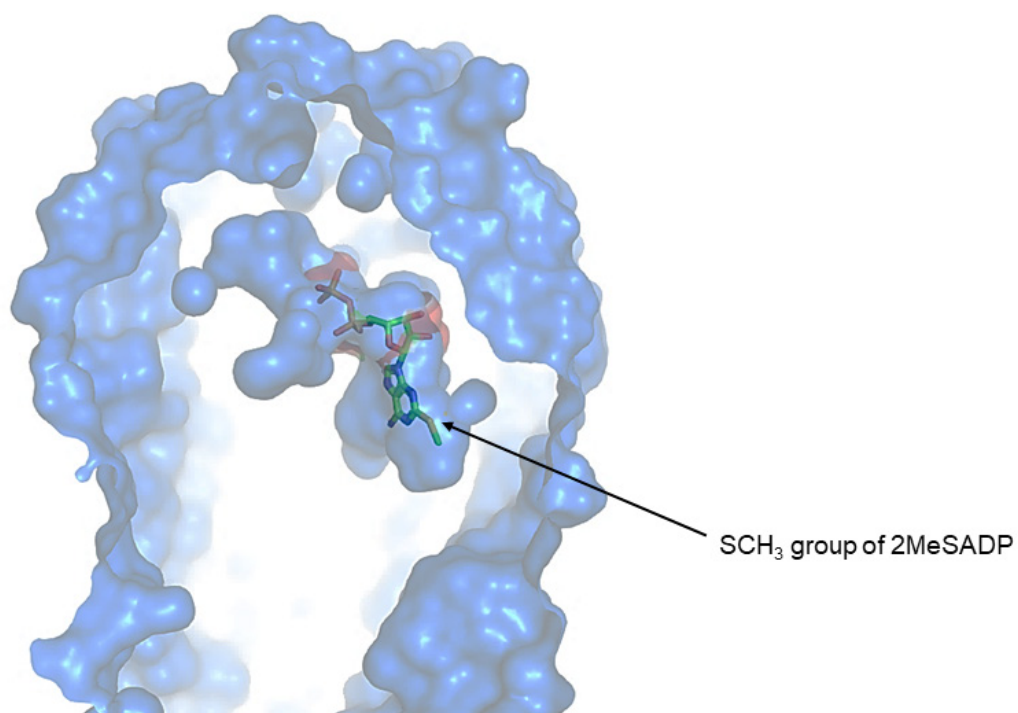


**Figure 11: Close-up view of the binding pose of the co-crystallised agonist, 2MeSADP, at the orthosteric site of the human P2Y<sub>12</sub> receptor.** 2MeSADP is shown as sticks in its respective pocket in the closed ‘lid’ agonist-bound structure of the human P2Y<sub>12</sub> receptor (PDB ID: 4PXZ). The protein is shown in surface representation and coloured blue. The 2MeSADP binding site is in a buried region, unlike AZD1283. The -SCH<sub>3</sub> group of 2MeSADP, which is important for its potency, is labelled. The image was created using PyMOL.

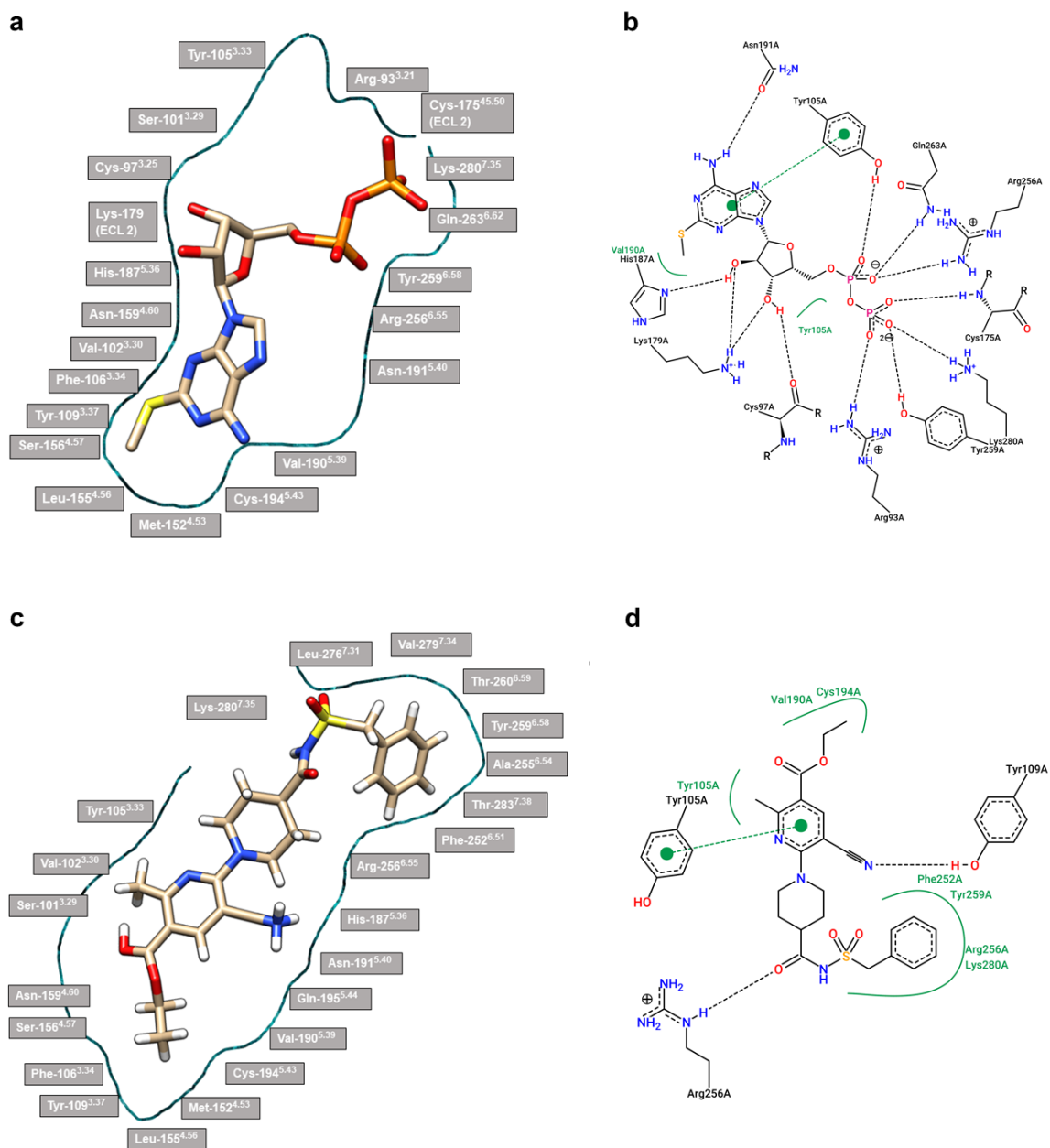


**Figure 12: Key residues surrounding the agonist and antagonist-bound pockets of the P2Y<sub>12</sub> receptor. a)** Key residues surrounding the contracted 2MeSADP-bound pocket (pocket outline in blue). Residues are shown in grey. The biggest shift upon agonist binding takes place in helices and 7, which move inward. The figure was created using UCSF Chimera (University of California, San Francisco) and Microsoft PowerPoint. **b)** 2MeSADP interaction map, generated using PoseView<sup>234-236</sup> (Centre for Bioinformatics, University of Hamburg) using the crystal structure (PDB ID: 4PXZ). **c)** Key residues surrounding the larger AZD1283-bound pocket. The figure was created as described in (a). **d)** AZD1283 interaction map, generated in PoseView using the crystal structure (PDB ID: 4NTJ). Green: hydrophobic residues, green dashes:  $\pi$ - $\pi$  stacking, black dashes: hydrogen bonds.

When 2MeSADP is docked *in silico* against the non-nucleotide-bound structure (PDB ID: 4NTJ), it can successfully dock against the AZD1283 binding site, but it can also dock against pocket 2<sup>17</sup>. Furthermore, mutagenesis data has shown that mutations in certain residues in pocket 2 lower the affinity of [<sup>3</sup>H]2MeSADP for the receptor<sup>17</sup>. The second pocket is not technically allosteric but is part of the orthosteric binding pocket that AZD1283 binds. However, it has its own distinct space due to the branched shape of the orthosteric site. Given their similarity in structure to 2MeSADP, this may hint that the nucleotide-derived antagonists may potentially bind in a region of the pocket distinct from the AZD1283 binding site. It may be inferred, then, that the nucleotide-derived antagonists, such as cangrelor, may not exhibit antagonistic effects through directly preventing inward shifting of helices 6 and 7, but through some other unknown, but perhaps related mechanism.

#### 1.4.3.4. Binding of the reversible P2Y<sub>12</sub> antagonists

The binding modes that will be described in this section are hypothetical and have not been fully proven, except for the co-crystallised antagonist AZD1283. Based on computational studies, the nucleotide (agonist)-bound structure was found to be best suited to understanding the binding of the nucleotide antagonists including cangrelor, AR-C66096, and AR-C67085<sup>16,18</sup>. These antagonists are all more similar in structure to the co-crystallised agonist 2MeSADP, and not the co-crystallised antagonist AZD1283. Their structures contain a bulky purine group and ribose ring. Therefore, the non-nucleotide (antagonist)-bound structure may not be ideal to predict their docking modes, as it is based on an antagonist with a dramatically different structure that does not have a nucleotide scaffold<sup>206</sup>. The non-nucleotide-bound structure may be more appropriate to predict the binding modes of ligands with more agreeable structures to AZD1283 (non-nucleotide scaffolds).

However, the ‘closed-lid’ model is representative of the receptor in its activated state. Thus, questions remain as to how a nucleotide-based antagonist, like cangrelor, would act to keep the nucleotide-bound receptor’s ‘lid’ open, which is described as necessary for P2Y<sub>12</sub> antagonism<sup>17</sup>. As previously mentioned, when the nucleotide ligand, 2MeSADP, was docked against the non-nucleotide (antagonist)-bound structure (PDB ID: 4NTJ), it produced inconsistent docking poses, which could be due to the larger size of the orthosteric site pocket and more available space for binding<sup>17</sup>.

Moreover, a hybrid structure was found to be most suited to predicting the binding mode of the reversible antagonist ticagrelor<sup>18</sup>. Despite obvious differences in structure between the non-nucleotide AZD1283 and the nucleoside-based ligand ticagrelor, they both show similar modes of binding<sup>17,18</sup>. MD simulations have predicted that ticagrelor’s difluoro phenyl ring (**Figure 5**) docks in between helices 6 and 7,

preventing their inward movement, as is the case with AZD1283's phenyl ring (**Figure 13**). Ticagrelor's difluoro phenyl ring also increases its affinity by 10-fold<sup>150</sup>. The hydrophobic groove where ticagrelor and AZD1283's ring moieties dock may be an important region for the discovery of novel modulators. This hydrophobic groove is composed of the residues Phe-252<sup>6,51</sup>, Arg-256<sup>6,55</sup>, Tyr-259<sup>6,58</sup>, and Lys-280<sup>7,35</sup> (**Figure 10, Figure 12**). As previously described, this region is important for ligand binding.

However, ticagrelor has a complicated docking profile. Previous studies have shown that it could not successfully dock against the 2MeSADP pocket of the P2Y<sub>12</sub> agonist-bound structure with similar conformation to nucleotide analogues<sup>16</sup>. This was due to ticagrelor's bulky difluoro phenyl ring. Studies have suggested that successful docking of ticagrelor would require a rearrangement of helix 6<sup>17</sup>. Even though it is based on a nucleoside scaffold, ticagrelor may have a more similar mode of binding to the non-nucleotide AZD1283, rather than the nucleotide analogues, such as cangrelor, or the agonists.

The AZD1283 scaffold is composed of multiple building blocks that are important for its inhibitory effects. The presence of the sulfonyl group increases the compound's affinity<sup>205,206</sup>. Furthermore, it has been found that replacing the -NH group with a methyl group reduces potency 5-11-fold, depending on the assay<sup>205</sup>. This could be due to increased hydrophobicity not being tolerated well in this specific region of the protein, or the increase in chain length causing steric hindrance (the 'barrier' [Tyr-105<sup>3,33</sup> and Lys-280<sup>7,35</sup>]) from the protein exists in immediate proximity to this region). A similar sulfonyl group is found in the P2Y<sub>12</sub> antagonist, elinogrel<sup>151</sup>.

Additionally, the pyridine moiety in AZD1283 is predicted to form  $\pi$ - $\pi$  interactions with the benzene ring in Tyr-105<sup>3,33</sup> (**Figure 12**), as in 2MeSADP<sup>17,18,217</sup>. Tyr-105<sup>3,33</sup> plays an important role in stabilising ligand binding, through  $\pi$ - $\pi$  stacking

interactions<sup>229,230</sup>. The aromatic group of several antagonists has been shown to interact with Tyr-105<sup>3,33,17,18</sup>. Moreover, the AZD1283 pyridine moiety accommodates a juxtaposed hydrophobic group and electronegative group. Lack of -CH<sub>3</sub> or -CF<sub>3</sub> in the hydrophobic region reduces affinity<sup>205</sup>. Similarly, the lack of a cyano or chloro group in the electronegative region reduces affinity, and bromine or hydrogen groups are not tolerated well in this region<sup>205</sup>. The cyano group forms a hydrogen bond with Tyr-109<sup>3,37</sup> (**Figure 12**). Mutational studies have shown that the Tyr-109<sup>3,37</sup> mutant construct of the receptor results in significantly reduced agonistic (ADP) activity<sup>237</sup>. 2MeSADP was not stated to interact with Tyr-109<sup>3,37</sup> in the original crystal structure paper, but this residue is found in the same pocket that accommodates 2MeSADP's -SCH<sub>3</sub> group<sup>16,17</sup>. The ethyl ester group of AZD1283 (**Figure 5**) forms hydrophobic contacts with Val-190<sup>5,39</sup> and Cys-194<sup>5,43</sup> in a small sub-cavity (**Figure 10, Figure 12**)<sup>17,18</sup>. Substitution of this ethyl ester group with an *i*-propyl or methyl group reduces potency<sup>18,205,207</sup>. From these details, we can delineate the key pharmacophore features or 'fingerprint' required for a non-nucleotide P2Y<sub>12</sub> antagonist.

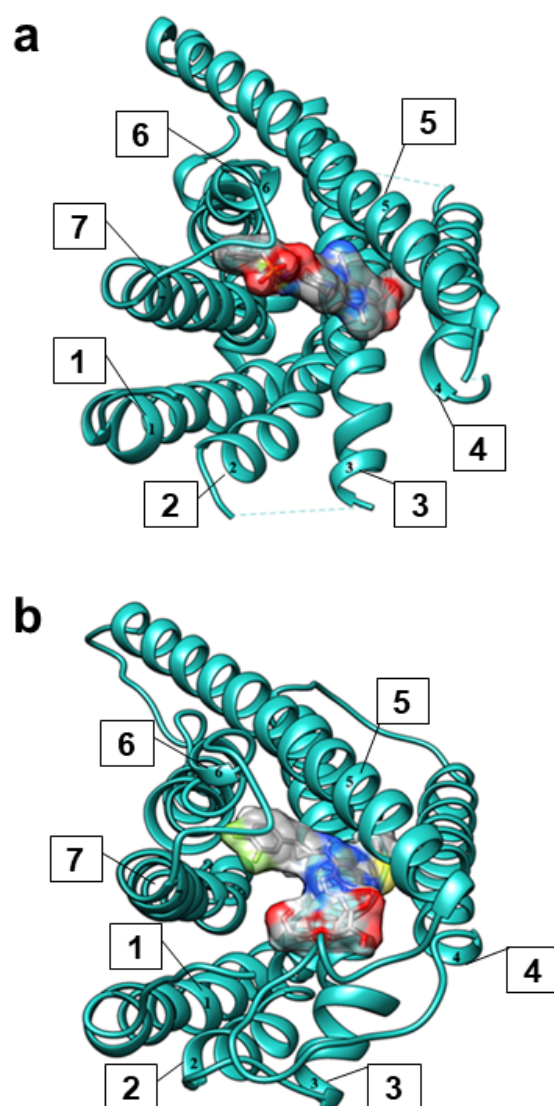


**Figure 13: The ring moiety of AZD1283 and ticagrelor lodges in between helices 6 and 7, preventing their inward shift. a)** AZD1283's phenyl ring is shown in between helices 6 and 7. The P2Y<sub>12</sub> antagonist-bound crystal structure is coloured cyan (PDB ID: 4NTJ). **b)** The difluoro phenyl ring of ticagrelor is shown between helices 6 and 7. The image was created using a PyMOL session showing the results of MD simulations performed by Paoletta et al. (2015)<sup>18</sup>. Ligand surfaces are shown and coloured by element. Helices are numbered in black.

In contrast, a different docking profile has been predicted for cangrelor. Cangrelor (**Figure 5**) is predicted to dock against the same pocket as the agonist, 2MeSADP, in the nucleotide-bound structure of P2Y<sub>12</sub> (**Figure 14**), and with a similar conformation to 2MeSADP, ADP, ATP, 2MeSATP, AR-C66096, and AR-C67085<sup>16,18</sup>.

The -SCH<sub>3</sub> group of 2MeSADP falls into the same hydrophobic cavity as the trifluoro-propyl-sulfanyl group of cangrelor. However, cangrelor's trifluoro-propyl-sulfanyl group is extended further into this cavity, which may facilitate its antagonistic activity.

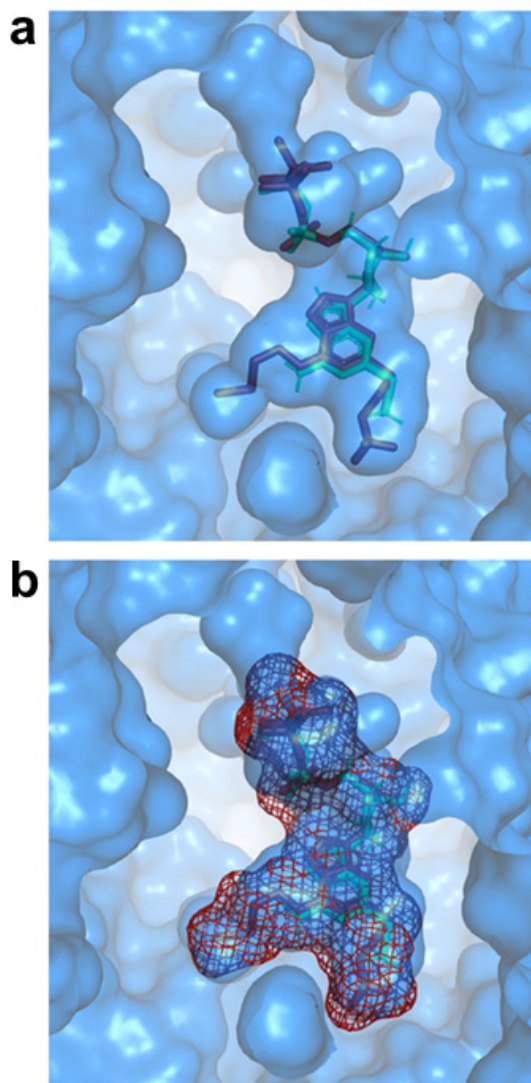


**Figure 14: Surface representation of the 2MeSADP-bound pocket of P2Y<sub>12</sub>.**

**a)** The 2MeSADP co-crystallised pose is shown in green and cangrelor (docked pose) in red. The agonist-bound structure is coloured blue (PDB ID: 4PXZ). The -SCH<sub>3</sub> group of 2MeSADP binds in a small hydrophobic sub-cavity formed by Asn-159<sup>4,60</sup>, Phe-106<sup>3,34</sup>, Leu-155<sup>4,56</sup>, and Asn-191<sup>5,40</sup> (see **Figure 10 and 12**). This cavity also accommodates the trifluoro-propyl-sulfanyl group of cangrelor, as well as linear groups from other antagonists, such as AR-C66096 and AR-C67095 (not shown). **b)** Mesh showing the general architecture of the pocket. The image was created using PyMOL.

Cangrelor also has an additional (methylthio)ethyl group, which 2MeSADP does not possess (**Figure 5**). This (methylthio)ethyl group may not be vital for cangrelor's inhibitory effects, as the antagonist AR-C66096, which is structurally similar (**Figure 5**) to cangrelor, is missing this group. Additionally, AR-C66096 has a (methylthio)ethyl group in the same position as cangrelor's trifluoro-propyl-sulfanyl group. AR-C66096's (methylthio)ethyl group docks in the same position as 2MeSADP's methylthio group, and, like cangrelor, this group is further extended into the hydrophobic cavity than 2MeSADP's methylthio group<sup>16</sup>. As previously mentioned, this cavity may be important for determining agonist potency. However, this cavity may also be important to explore in understanding the activity of the nucleotide-derived antagonists.

Unlike AZD1283, there is no evidence that cangrelor or AR-C66096 dock in such a conformation that they prevent the inward movement of helices 6 and 7. It may also be possible that the AZD1283 binding site may accommodate cangrelor, albeit with quite a different conformation to AZD1283 due to its bulky groups. But, in this case, it would be possible for cangrelor's (methylthio)ethyl group or tri-fluoro-propyl-sulfanyl group to dock against the same region as the phenyl ring of AZD1283, preventing the inward shift of helices 6 and 7. Another potential scenario may be that cangrelor could dock partially in pocket 1 and partially in pocket 2, given that the dinucleotide antagonist Ap<sub>4</sub>A docks in this way<sup>17,18</sup>. It is also possible that cangrelor may dock in pocket 2.

To explore this, it may be significant to further understand pocket 2. It appears that pocket 2 has been, for the most part, overlooked in the literature due to the primary focus being on the AZD1283 binding site. This sub-pocket can only be observed in the non-nucleotide (antagonist)-bound structure, and not in the nucleotide (agonist)-bound structure. Therefore, it may be an important space to consider in antagonist binding.

P2Y<sub>12</sub> is unique in that this shape of pocket has not been observed in any other GPCR. Pocket 2 is formed by helices 1, 2, 3, and 7<sup>17</sup>.

Interestingly, cangrelor binding precludes clopidogrel or prasugrel binding<sup>238</sup>. This may be due to steric hindrance of Cys-97<sup>3,25</sup> by cangrelor fully or partially occupying pocket 2. It has been suggested that the reason a conclusion has not been reached on the conformation of the nucleotide-derived compounds in the antagonist-bound structure, is due to the highly plastic nature of the binding site<sup>17</sup>. This means it is unknown how the nucleotide antagonists dock against the open 'lid' structure of the receptor, which significantly limits our understanding of how these ligands bind to the receptor *in vitro* or *in vivo*. The agonist-bound structure, or a hybrid structure of the receptor, appear to be safer options in providing unambiguous answers to the binding modes of the nucleotide-derived antagonists.

However, it should be noted that the nucleotide (agonist)-bound structure only provides an artificial encapsulation of nucleotide antagonist docking, as in a biological setting these ligands would bind in the open 'lid' antagonist-bound structure of the receptor, and not the closed 'lid' agonist-bound structure, where the agonist has stabilised the active state of P2Y<sub>12</sub>. Likely, the non-nucleotide-bound structure is not suited to show accurate docking of agonists. A successful docking method used previously was to first dock ligands against both the nucleotide-bound and non-nucleotide-bound structures, to predict binding modes<sup>18</sup>. The most appropriate structure was then chosen for each family of ligands tested. This included building a hybrid structure, using a combination of the nucleotide and non-nucleotide-bound structures.

According to Zhang et al. (2014), the contracted nucleotide-bound pocket will not allow competitive antagonist AZD1283 to bind<sup>16</sup>. Additionally, the P2Y<sub>12</sub> receptor desensitises in the prolonged presence of micromolar concentrations of ADP and will

not re-sensitise unless the agonist is removed completely<sup>239-241</sup>. Although desensitisation is typical in GPCRs upon prolonged exposure to an agonist, it is not known how the presence of the receptor's 'lid' will affect its desensitisation<sup>242</sup>. Regarding the closed 'lid' model, it would also be challenging to test the effects of AZD1283 on P2Y<sub>12</sub> after the addition of ADP.

The assumption that the contracted agonist-bound pocket will not accommodate antagonists also raises questions about the effects of the antagonists in an *in vitro* system where platelets have already been activated by ADP. In such a model, the receptor would have supposedly already adopted a closed 'lid' conformation, and this can be further confirmed if the competitive antagonists do not exert any inhibitory effects. In a previous study, when an additional disulphide bond was engineered between ECL 2 and TM7 in the M2 muscarinic acetylcholine receptor, this impaired the binding of orthosteric and allosteric-binding ligands. It was suggested that this additional disulphide bond resulted in 'lid' closure, preventing access to the binding crevice<sup>216,233</sup>.

#### 1.4.3.5. Binding of the irreversible P2Y<sub>12</sub> antagonists

The predicted binding modes of clopidogrel and prasugrel to P2Y<sub>12</sub> have been difficult to decipher, due to their covalent nature. This is because most commonly docking tools are not designed to explore covalent docking<sup>18</sup>. However, docking has successfully been used to show that the active metabolite of prasugrel docks against pocket 2 (**Figure 8**) of the non-nucleotide-bound structure<sup>17</sup>. Pocket 2 is where Cys-97<sup>3,25</sup> is located.

Clopidogrel's active metabolite, clopi-H4, contains a thiol group and has been reported to bind irreversibly to two of the four cysteines found in the extracellular domain of the protein: Cys-97<sup>3,25</sup> and Cys-175<sup>45,50</sup>, through the formation of a disulfide bond<sup>17,243,244</sup>. However, some papers have suggested it binds to Cys-17 (N-terminal domain) and Cys-270<sup>7,25,245,246</sup>. The active metabolite of prasugrel, R-138727, has also been suggested to bind either Cys-97<sup>3,25</sup> and Cys-175<sup>45,50</sup>, or Cys-17 (N-terminal domain) and Cys-270<sup>7,25</sup>.

The irreversible antagonists may bind such that they prevent the disulphide bond between Cys-97<sup>3,25</sup> and Cys-175<sup>45,50</sup> from forming. Preventing the formation of this disulphide bond may be important for keeping the receptor in its 'open-lid' state and may be the reason why the disulphide bond is not observed in the antagonist-bound structure, and why ECL 2 is only partially resolved. It is unknown how AZD1283 binding may prevent the formation of the disulphide bond since it does not bind the cysteine residues, although it may be through an indirect mechanism. Interestingly, the thiol-reactive reagent *p*-chloromercuribenzenesulphonate (pCMBS) also inhibits P2Y<sub>12</sub> activation (but not P2Y<sub>1</sub> activation)<sup>17,247</sup>.

It may be possible that the AZD1283 sub-pocket accommodates reversible antagonists, and the second pocket, where prasugrel docks, accommodates covalent acting molecules. Of course, such generalisations must be taken with caution, and these rules may not apply to every ligand. Questions remain as to which structure is more

suitable to perform docking against for each ligand class. From the available data in the literature, the ideal structures to understand the predicted binding modes of each ligand class are summarised in **Figure 15**.

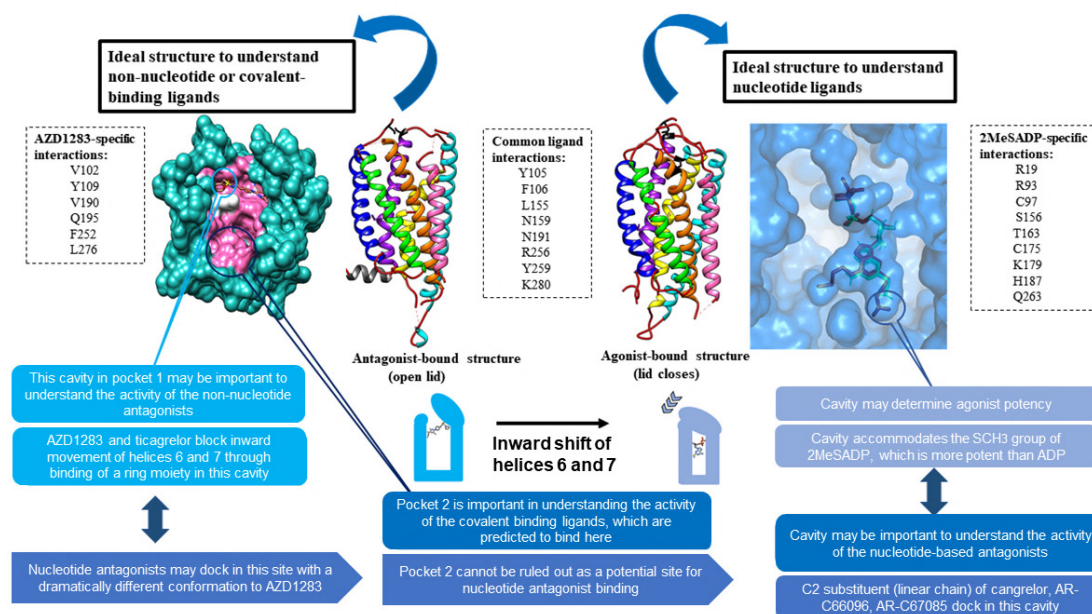


**Figure 15: A summary diagram showing how the P2Y<sub>12</sub> crystal structures facilitate the understanding of ligand binding.** The antagonist-bound structure (open-lid), or the non-nucleotide bound structure, is ideal for understanding the mode of binding of the non-nucleotide antagonist, AZD1283, and the covalent-binding ligands. The phenyl ring of AZD1283 binds in a sub-cavity in pocket 1 (phenyl ring circled in blue) and prevents the inward shift of helices 6 and 7. Ticagrelor is a nucleoside-based ligand, however, its ring moiety has also been suggested to block the inward movement of helices 6 and 7. The docking of nucleotide-based antagonists against this structure results in ambiguous and variable poses. Pocket 2 in the non-nucleotide bound structure is important for understanding how the covalent antagonists bind at the receptor. These ligands form a covalent bond with Cys-97<sup>3,25</sup>, which is found in pocket 2. Conversely, the binding of the agonist results in the inward shift of helices 6 and 7, and a closed-lid receptor conformation. The agonist-bound structure (closed-lid), or the nucleotide-bound structure, is ideal for understanding the binding of the nucleotide-based agonist 2MeSADP and the nucleotide-based antagonists. In this structure, the agonist-binding cavity is buried. A sub-cavity (circled in navy) accommodates the -SCH<sub>3</sub> group of 2MeSADP, which is the only structural difference between 2MeSADP, and the less potent agonist ADP. The C2 substituent of various nucleotide-based antagonists has been predicted to bind in this cavity, which may be important for their antagonism. The key protein-ligand interactions of the co-crystallised ligands and common interactions between them are listed.

## 1.5. Principles of computer-aided drug discovery

Computer-aided drug discovery (CADD) is a method that is employed to virtually predict ‘hits’ for *in vitro* testing<sup>248</sup>. It is more time-efficient and cost-effective than empirical high-throughput screening (HTS) methods, where hundreds or thousands of small-molecules are tested daily to find an effective scaffold<sup>249</sup>. Although HTS is an important tool to obtain *in vitro* data for many compounds within a reasonable time frame, *in silico* methods can complement HTS. As thousands or millions of molecules can first be screened in a computer to filter out unwanted compounds and to generate a sub-set of potential binders, this can aid the early stages of the drug discovery process in finding hits<sup>250,251</sup>. CADD methods have previously proven to be successful, resulting in several bio-active molecules<sup>252-264</sup>.

As shown in **Figure 16**, CADD may be divided into two main categories: structure-based screening (molecular docking) and ligand-based virtual screening<sup>248</sup>. In ligand-based virtual screening, a reference or query ligand with proven activity is used to find hits with similar shape and electrostatic profiles<sup>265</sup>. For shape or electrostatic similarity to the reference ligand, compounds can be scored using the Tanimoto coefficient<sup>266</sup>. Analysis of a ligand’s shape and electrostatic profile is useful for pharmacophore analysis. Understanding the basic components of the ideal pharmacophore, or ‘fingerprint’, for a known ligand is important in the search for novel ligands<sup>267</sup>.

In structure-based virtual screening, the 3D chemical structures of compounds are docked against the binding site of the target protein. The purpose of this is to predict which compounds are likely to bind to the target protein and the binding mode of the compound within the protein’s binding pocket. Docking is often performed against a solved X-ray crystal structure of the target protein<sup>18,268-270</sup>. Where this is unavailable, homology modelling is performed to obtain a predicted structure of the receptor<sup>271</sup>. A

known ligand of the receptor is first docked against the protein to validate the docking protocol<sup>272,273</sup>. This is performed in multiple programs and docking poses are compared to the binding mode of the known ligand against the protein binding pocket. Based on this, the program which predicts the binding pose of the known ligand most accurately is chosen for further *in silico* experiments.

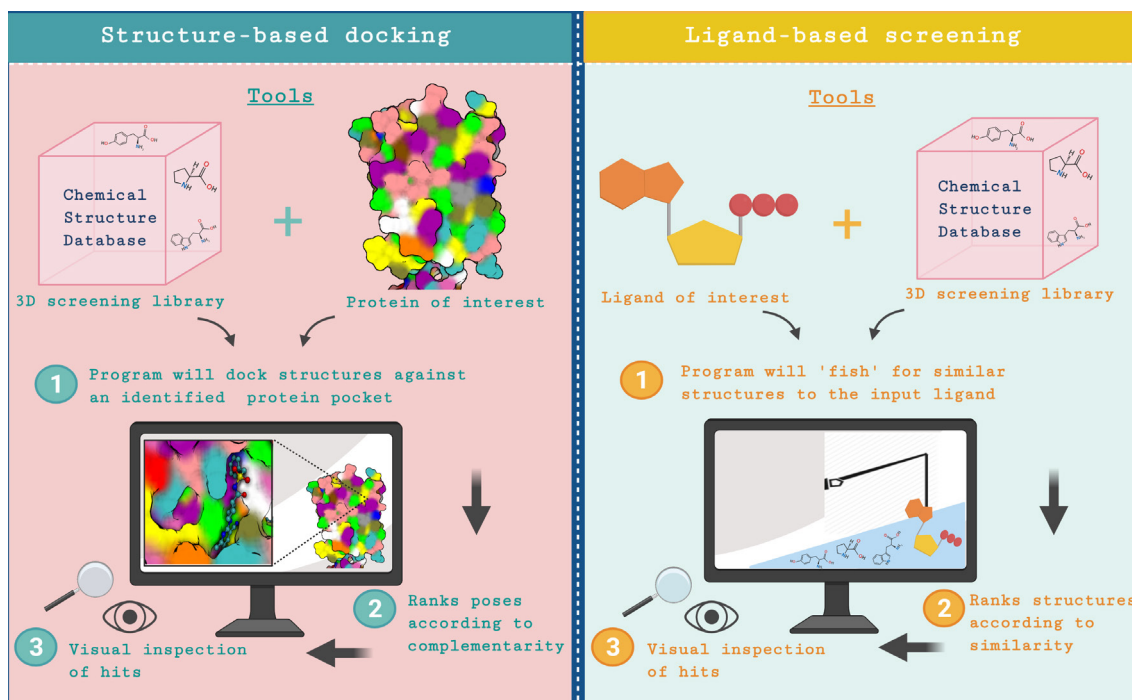


**Figure 16: A summary of how structure-based docking and ligand-based virtual screening are performed.** Structure-based virtual screening, which is effectively docking in its large scale, requires a 3D screening library of energy-minimised structures and a 3D protein structure. The program will bind each compound in the library against a binding pocket. Poses are then ranked, and protein-ligand interactions can be visually inspected. In ligand-based screening, a ligand of interest (query molecule) and a 3D screening library are required. The program will search for compounds with structural and group similarities to the query molecule. Chemical structures are ranked according to the Tanimoto coefficient. The image was created using BioRender.

Molecular docking can further be divided into two categories: blind docking and focused docking<sup>272,273</sup>. In blind docking, the entire protein is defined as search space for docking. If the ligand is docked in any location other than the known binding cavity, then the poses and scores from blind docking are considered meaningless. Conversely, in focused docking, the binding site for docking is explicitly defined. In focused docking, the software first generates a grid of the binding cavity, with consideration to its shape and electrostatic profile. In either case, the ligand is often treated as flexible, and multiple low-energy conformations of the ligand are docked against the rigid binding cavity<sup>274</sup>. Treating the binding cavity as rigid reduces the search space for docking, and results in fewer false-positive hits<sup>275</sup>. Other CADD methods, such as MD simulations, take into account the plasticity of the receptor, and the conformational changes that occur upon ligand binding.

The program will then rank the generated ligand conformations using a scoring function. Many different programs are available for docking, each adopting subtly different scoring functions. Often, an empirical scoring function is adopted, where different types of interactions between the ligand and protein are considered<sup>276,277</sup>. Hydrophobic contacts are often awarded, whereas hydrophilic contacts are penalised. Hydrogen bonds are regarded as important for affinity and are often awarded. The number of rotatable bonds present in the ligand is important in determining how many different conformations can be adopted in the binding site and shape complementarity. The lowest energy poses (most negative values) are the ‘best’ ranking.

Finding that a consensus is reached in the predicted binding mode of a ligand in different docking programs is often regarded as the ‘gold’ standard for choosing hit molecules. In addition to scores, protein-ligand interactions are also visually inspected with reference to the known ligand’s interactions with the protein, which are important for determining structure-activity relationships<sup>278-280</sup>. Ligand-based screening and

molecular docking are often performed together to use as much information available regarding a known ligand and its biological target, which results in a more powerful approach to finding hits for *in vitro* validation. Currently marketed P2Y<sub>12</sub> antagonists were all discovered in the absence of the protein's structure. The recently solved structure may now be used to search for and establish SAR for novel leads in the search for a new generation of P2Y<sub>12</sub> antagonists.

## 1.6. Aims and objectives

The aims of this thesis were as follows:

**1) To explore whether any novel information could be obtained regarding the pharmacological profile of the most recently approved, and only intravenously acting P2Y<sub>12</sub> antagonist, cangrelor<sup>281</sup>.**

Cangrelor (AR-C69931MX), which is reported to be a competitively acting, reversible antagonist, has been shown to prevent the active metabolites of clopidogrel and prasugrel from binding to P2Y<sub>12</sub> *in vitro*<sup>238,282,283</sup>. Clinical guidelines state that thienopyridine therapy should be stopped before cangrelor administration due to a possible negative pharmacodynamic interaction<sup>284</sup>. Interestingly, the binding of ticagrelor is not compromised in the presence of cangrelor<sup>285-287</sup>. This may point to a model where cangrelor and the covalent-binding antagonists bind in a separate pocket to that of ticagrelor and AZD1283. Little is known about the binding mode of cangrelor at P2Y<sub>12</sub>. An important part of this aim was to investigate and compare the pharmacological profile of cangrelor to its analogue AR-C66096 using a phenotypic aggregometry and molecular assay. This was to gain mechanistic insight into how their structural differences may affect their activity.

**2) To use the recently solved P2Y<sub>12</sub> crystal structure and computational drug discovery tools to find novel non-nucleotide inhibitor(s) of ADP-induced platelet aggregation.**

Initially, the non-nucleotide scaffold of the known P2Y<sub>12</sub> antagonist AZD1283 was to be used to perform pharmacophore analysis in the pursuit of novel non-nucleotide

scaffolds with shape and electrostatic similarity. However, this ligand-based approach was not to be a medicinal chemistry campaign to improve upon or modify the AZD1283 scaffold, which has already been performed<sup>207</sup>. It was to use AZD1283's most important shape and electrostatic features as clues to understand the key building blocks required for a reversible antagonist and facilitate the search for an entirely novel class of antagonists. This stage served as a 'filter' to narrow down the thousands of compounds that were obtained from virtual screening libraries before further refinement in docking.

The recently solved X-ray crystal structure of the P2Y<sub>12</sub> receptor co-crystallised with the non-nucleotide antagonist AZD1283 was then to be used to perform molecular docking of hit scaffolds. This would be followed by the screening of molecules using a phenotypic aggregation assay and blood from human donors. A recently developed 96-well aggregometry method was to be used to enable the screening of large numbers of compounds efficiently, as well as to generate concentration-response curves<sup>288-293</sup>.

Pharmacologic screening of the most effective hits from the phenotypic screen would then be performed using a P2Y<sub>12</sub> molecular assay. There are no reports where the P2Y<sub>12</sub> crystal structures have been used in *in silico* work to pursue the search for novel modulators, thus the approach used here was novel. Previous pursuits for P2Y<sub>12</sub> antagonists have often involved pharmaceutical companies using medicinal chemistry approaches, large and expensive screening libraries, as well as specialised high-throughput screening equipment<sup>150-152,205</sup>.

Therefore, the work involved in achieving this aim was to be just as much a validation of the X-ray crystal structures and approach, as it was about using them to discover a novel antagonist. Importantly, in the advent of the crystal structure of the human P2Y<sub>12</sub> receptor, it is now possible to understand how a known, reversible antagonist, AZD1283, engages at the target site. These details can be used to inform SAR and explorative variations around hit molecules with comparison to the

interactions of the reference ligand. This is crucial to establish key amino acid residue contacts required for affinity.

Furthermore, the specific scaffold sought after was to be competitive, reversibly acting, and not nucleotide derived. The rationale for pursuing such a scaffold was, 1) the available antagonist-bound X-ray crystal structure to be used in this work exists in a conformation stabilised by a reversibly acting, competitive non-nucleotide; 2) the only orally available and reversible P2Y<sub>12</sub> antagonist, ticagrelor, is based on a nucleoside scaffold and has been found to cause dyspnoea in patients. This is due to its unwanted off-target actions and subsequent effects on adenosine levels; 3) there are currently no approved, reversibly acting P2Y<sub>12</sub> antagonists that are based on a non-nucleotide scaffold. Furthermore, a major aim of antiplatelet drug discovery is to prevent arterial thrombosis without affecting haemostasis. Thus, a novel class of P2Y<sub>12</sub> antagonists would be desired to carry a lower bleeding risk.

To facilitate experiments planned for Aim 1 and Aim 2, an assay was to be developed where levels of phosphorylated VASP were to be measured in platelets pre-treated with a test compound and then ADP. Phosphorylated VASP levels increase upon P2Y<sub>12</sub> antagonism. Currently, there are no existing concentration-response curves in the literature showing in detail how varying levels of the agonist ADP affect pVASP levels. Although diagnostic assays kits exist where pVASP levels can be measured in response to single concentrations of the agonist, (multiple) concentration-response curves cannot be created easily. This is due to the high pricing of kits, and limitations in kit contents (e.g., enough reagent for a limited number of samples).

To enable more freedom in testing a larger number of samples in flow cytometry, an approach called barcoding has recently been described<sup>294-296</sup>. In this approach, samples are labelled with one or two fluorescent dyes to assign them unique barcode signatures. These samples can then be pooled together into one, with a primary

antibody added to the pooled sample, instead of multiple individual samples. Due to the high pricing of the pVASP primary antibody, this multiplexed approach was to be adopted to develop a flow cytometric assay. To further advance this approach, a novel combination of fluorescent dye and fluorophore-conjugated antibodies were to be used to create signature barcodes.

To summarise this section, new information is sought after for the mode of action of the newest and only intravenously administered P2Y<sub>12</sub> antagonist, cangrelor, which may inform its clinical use. Additionally, no inhibitors of ADP-induced platelet aggregation have been reported as a direct consequence of structure-guided drug discovery using the protein's crystal structure. This is important because novel ligands found using this approach may validate the crystal structures and serve as tools to expand our knowledge of P2Y<sub>12</sub> pharmacology. Furthermore, although highly effective, the nucleotide-based P2Y<sub>12</sub> antagonists have been found to cause dyspnoea. Importantly, antiplatelet drugs increase bleeding risk, and there is an unmet clinical need for improved scaffolds. No reversibly acting, non-nucleotide P2Y<sub>12</sub> antagonists have been approved to date, highlighting a gap in the market and a need for new scaffolds to guide drug development.



# **Chapter 2.**

## **Materials and methods**

## 2.1. *In silico* methods

The *in silico* tools employed throughout the project are listed in **Table 2**. *In silico* experiments were performed using a Dell desktop with a Windows 64-bit operating system and Intel® Core™ i5-8500 CPU (3.00 GHz), and 8.00GB RAM.

**Table 2: List of *in silico* tools used.** Purpose and vendor (including uniform resource location (URL)) of the software is specified. The table is continued on page 69.

Programme	Purpose	Vendor/(URL)
<b>AutoDock 4.0</b>	Molecular docking.	The Scripps Research Institute, San Diego (autodock.scripps.edu)
<b>AutoDock Vina</b>	Molecular docking.	The Scripps Research Institute, San Diego (vina.scripps.edu)
<b>DockRMSD</b>	Calculation of RMSD between two poses of a molecule docked against a protein.	Zhang Lab, University of Michigan (zhanggroup.org/DockRMSD/)
<b>Forge</b>	Electrostatic field potential analysis.	Cresset Group (cresset-group.com/software/)
<b>GlideXP</b>	Molecular docking.	Schrödinger Inc. (schrodinger.com)
<b>GOLD</b>	Molecular docking.	Cambridge Crystallographic Data Centre (ccdc.cam.ac.uk)
<b>ICM-Pro</b>	Preparation of 3D protein structure for docking.	Molsoft L.L.C. (molsoft.com)
<b>Maestro</b>	Interface used to run GlideXP.	Schrödinger Inc. (schrodinger.com)
<b>MarvinSketch</b>	To draw 2D diagrams of chemical structures.	ChemAxon (chemaxon.com)
<b>MMV</b>	Processing files downloaded from the Protein Data Bank.	Molexus (molexus.io)
<b>MOE</b>	Energy minimisation of 3D chemical structures.	Chemical Computing Group (chemcomp.com)
<b>NotePad++</b>	Code editor used to view scores from GOLD.	Microsoft (notepad-plus-plus.org/)
<b>OMEGA</b>	Conformer generation software.	OpenEye Scientific (eyesopen.com/omega)
<b>Open Babel</b>	Energy minimisation of chemical structures.	Open Babel (openbabel.org)

<b>PLIP</b>	Analysis of protein-ligand interactions from docking.	Biotec ( <a href="http://plip-tool.biotec.tu-dresden.de/plip-web/plip/index">plip-tool.biotec.tu-dresden.de/plip-web/plip/index</a> )
<b>PoseView</b>	Analysis of protein-ligand interactions from docking.	University of Hamburg, Center for Bioinformatics ( <a href="http://proteins.plus">proteins.plus</a> )
<b>PyMOL</b>	Molecular viewer.	Schrödinger Inc. ( <a href="http://schrodinger.com">schrodinger.com</a> )
<b>PyRX</b>	Interface used to run Open Babel, AutoDock Vina, and AutoDock 4.0.	PyRX ( <a href="http://pyrx.sourceforge.io/">pyrx.sourceforge.io/</a> )
<b>ROCS</b>	Ligand-based virtual screening.	OpenEye Scientific ( <a href="http://eyesopen.com/rocs">eyesopen.com/rocs</a> )
<b>SwissDock</b>	Molecular docking.	Swiss Institute of Bioinformatics ( <a href="http://swissdock.ch">swissdock.ch</a> )
<b>UCSF Chimera</b>	Molecular viewer.	University of California, San Francisco ( <a href="http://cgl.ucsf.edu/chimera">cgl.ucsf.edu/chimera</a> )
<b>ZINCPharmer</b>	To generate a pharmacophore model for a ligand.	University of Pittsburgh ( <a href="http://zincpharmer.csb.pitt.edu/">zincpharmer.csb.pitt.edu/</a> )

### *2.1.1. Chemical libraries*

Chemical libraries containing three-dimensional structures of compounds were sourced for virtual screening. Libraries containing a diverse range of commercially available compounds were chosen. This included the Enamine Hit Locator library (200,000 compounds), the Vitas Broadway library (32,600 compounds), and the Specs library (208,670 compounds). For use in ligand-based screening tools or docking programs where the ligand is considered ‘rigid’, OMEGA, version 4.2.0.1 (OpenEye Scientific, Santa Fe, NM), was operated via the OpenEye command line ([docs.eyesopen.com/applications/index.html](http://docs.eyesopen.com/applications/index.html)) to generate multiple conformers for each compound in the input chemical library<sup>297</sup>. However, in docking programs where the ligand is considered ‘flexible’, the conformer library was not required because the program itself calculated multiple conformers for each input ligand.

### *2.1.2. Ligand structure preparation*

The three-dimensional structure of the reference P2Y<sub>12</sub> antagonist, AZD1283, was obtained from PubChem (pubchem.ncbi.nlm.nih.gov/). Where 3D chemical structures were not available on PubChem (e.g., cangrelor), they were manually drawn using MarvinSketch, version 20.16 (ChemAxon Ltd., Budapest, Hungary)<sup>298</sup>. All chemical structures, including those from the chemical screening libraries, were energy-minimised in Open Babel, version 2.4.0., using the Merck Molecular Force Field 94 (MMFF94)<sup>299-301</sup>.

### *2.1.3. Ligand-based virtual screening*

The three-dimensional structure of AZD1283 was used as a query molecule in Rapid Overlay of Chemical Structures (ROCS), version 3.4.1.0 (OpenEye Scientific Software, Santa Fe, NM, USA)<sup>302</sup>. Chemical libraries were virtually screened for similarity indices to AZD1283, specifically analysing shape and colour<sup>256,259,272,273</sup>. The OpenEye command line was used to generate a ROCS report, which detailed the results. The Shape Tanimoto score denoted structural similarity to the reference ligand, AZD1283, and the Color Tanimoto score denoted chemical group similarity. Each of the scoring functions had a maximum obtainable score of 1.

### *2.1.4. Molecular field-based alignment*

Forge, version 10.4.2. (Cresset, Litlington, Cambridgeshire, UK) was used to align the highest-scoring hits to AZD1283 to manually inspect electrostatic field similarity and field score<sup>303</sup>. Based on these two criteria, a chosen subset of compounds proceeded to the subsequent molecular docking stages for further filtering.

### *2.1.5. Protein structure preparation*

The three-dimensional X-ray crystal structure of P2Y<sub>12</sub> bound to the antagonist, AZD1283, was obtained from the Protein Data Bank ([www.rcsb.org](http://www.rcsb.org)) (PDB ID: 4NTJ). ICM-Pro, version 3.8 (Molsoft, L.L.C., San Diego, CA, USA) was used to prepare the protein structure for docking<sup>304</sup>. These preparations involved the removal of water groups, which interfere with docking calculations, and the addition of hydrogens. The co-crystallised ligand (AZD1283) was also removed from the structure.

### *2.1.6. Molecular docking*

#### *Blind docking*

A variety of different docking software was first used to perform validation blind docking using the control ligand, AZD1283. This was performed to find the program that could best reproduce the control ligand's co-crystallised pose. Software tested (details in **Table 2**) included Glide XP, version 6.7, AutoDock Vina (or 'Vina'), version 1.1.2, AutoDock 4.2, version 4.2.6, and the SwissDock server. Glide XP was run using the Maestro graphical interface, version 11<sup>305-308</sup>. AutoDock Vina and AutoDock 4.2 were run using the PyRx interface, version 0.8.

To run AutoDock Vina or AutoDock 4, input ligands were first converted to AutoDock Ligand in Open Babel, also in the PyRx interface. This step involved energy-minimisation of the ligand using the MMFF94<sup>309</sup>. The protein structure was imported into PyRx and converted to AutoDock Macromolecule for docking in AutoDock Vina or AutoDock 4.2<sup>310</sup>. For AutoDock Vina, the AutoGrid was maximised to encapsulate the entire P2Y<sub>12</sub> X-ray crystal structure as possible search space for docking. An exhaustiveness value of 24 was used. The exhaustiveness parameter is used to instruct the software how many times calculations should be repeated. In AutoDock 4.2, the

AutoGrid was also maximised to capture the entire protein, and the Lamarckian genetic algorithm was selected for docking.

Programs ranked poses according to the predicted free energy of binding, where more negative scores indicated lower predicted free energy and therefore 'better' poses. The scoring functions used by the various programs were as follows: Glide XP: GlideScore, which is a proprietary scoring function belonging to Schrödinger Inc. (Schrödinger, LLC, New York, NY, USA), AutoDock Vina, and AutoDock 4.2: Gibbs free energy ( $\Delta G$ ) (in kcal/mol) score, and SwissDock: also,  $\Delta G$ . Docking programs often measure the predicted free energy of binding ( $\Delta G$ ). However, this is often reported as 'binding affinity' in the literature. Therefore, ' $\Delta G$ ' and 'binding affinity' are used interchangeably throughout this text.

The highest rank pose from each program was superimposed against the AZD1283 co-crystallised pose to calculate a root-mean-square-deviation (RMSD) value in the DockRMSD server, version 1.1. Smaller RMSD values indicated better alignment of the docked AZD1283 poses to the co-crystallised AZD1283 pose. For visualisation purposes, the highest-ranking docked pose for AZD1283 was superimposed against the co-crystallised pose in UCSF Chimera, version 1.14 (University of California, San Francisco)<sup>311</sup>. Scores are presented in this text as mean  $\pm$  SEM, for five independent docking runs. Any presented docking poses are indicative of the highest-ranked pose.

#### *Pose refinement using focused docking*

The Genetic Optimisation for Ligand Docking (GOLD) suite, version 5.8.0 (The Cambridge Crystallographic Data Centre (CCDC), Cambridge, UK), was used for focused docking<sup>312</sup>. In GOLD, the binding site was defined using x, y, and z, coordinates (x: 16.5840, y: 103.8940, z: 51.0410), which referred to the centre mass of the bound AZD1283. Atoms within a 5Å radius of this defined region were analysed by

the program as search space for docking. In GOLD, the generated poses are ranked by ChemPLP score (which was viewed in NotePad++). The poses can be visually inspected in other software.

#### *2.1.7. Analogue search*

To explore SAR around a hit scaffold, available analogues were searched for in MolPort. Chosen analogues were limited to possessing minimal group differences, making them easier to compare to the parent scaffold. This search was performed using the MolPort SMILES search tool (<https://molport.com/shop/find-chemicals-by-smiles>), using a 2D Tanimoto cut-off of 0.7, where structures were visually inspected to find desirable analogues. Analogues were prepared and docked, as detailed above.

#### *2.1.8. Analysis of protein-ligand interactions*

To analyse interactions in 3D, the Protein-Ligand Interaction Profiler (PLIP) (BIOTEC, Tatzberg, Dresden ([www.plip-tool.biotec.tu-dresden.de/plip-web/plip/index](http://www.plip-tool.biotec.tu-dresden.de/plip-web/plip/index))) was used.

#### *2.1.9. Exploring compound properties*

The SwissADME tool (<http://www.swissadme.ch/>) was used to explore compound properties. The SMILES for each compound was entered into the program.

#### *2.1.10. Molecular visualisation*

PyMOL, version 2.4. (Schrödinger, LLC, New York, NY, USA), and UCSF Chimera (University of California, San Francisco) were used to visualise the protein X-ray crystal structure, the co-crystallised ligand's pose, as well as poses of compounds docked against the protein. Docking files were processed using Molegro Molecular Viewer (MMV), version 7.0 (Molexus IVS, Odder, Denmark), and Open Babel<sup>313</sup>. To

draw 2D chemical structures, MarvinSketch, version 20.16 (ChemAxon Ltd., Budapest, Hungary), was used<sup>298</sup>. To generate a 3D pharmacophore model for a ligand, ZINCPharmer (<http://zincpharmer.csb.pitt.edu/>; University of Pittsburgh, USA) was used<sup>314,315</sup>.

## **2.2. In vitro methods**

### *2.2.1. Isolation of platelet-rich plasma from human blood*

Blood was obtained from healthy volunteers who were drug-free for at least 10 days before blood collection. Blood use from human subjects was approved by the University of Cambridge, Human Biology Research Ethics Committee. Written, informed consent was obtained from donors before blood collection, in accordance with the Declaration of Helsinki. Blood was drawn into vacutainers containing the anti-coagulant sodium citrate (3.2% v/v). Citrate chelates  $\text{Ca}^{2+}$ , which makes  $\text{Ca}^{2+}$  unavailable for coagulation proteins, inhibiting the coagulation cascade. As shown in **Figure 17**, platelet-rich plasma (PRP) was isolated from whole blood by centrifugation (Thermo Scientific Heraeus Megafuge 16R Centrifuge; 200 g, 10 minutes, room temperature (RT), no brake). PRP is a yellow aqueous solution (pH: 7.4) containing proteins, such as albumins and globulins, mineral ions, and clotting factors, such as fibrinogen. PRP was aspirated and transferred to a new tube.

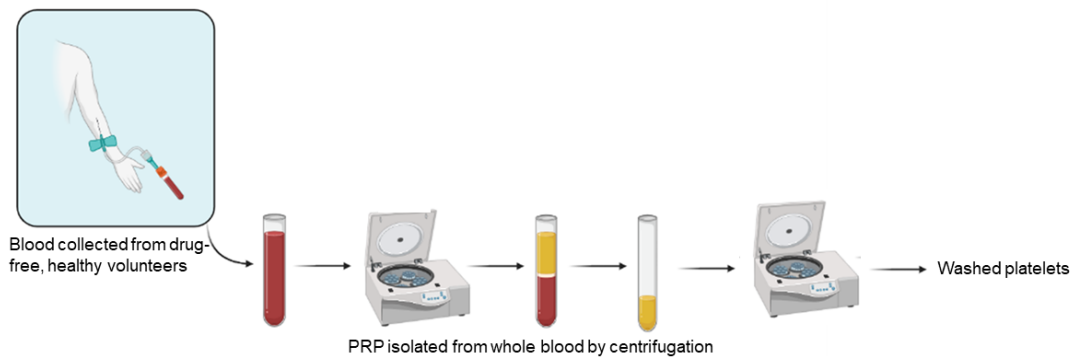


**Figure 17: Isolation of platelets from whole blood.** Blood is collected from drug-free, healthy volunteers and centrifuged to isolate platelet-rich plasma (PRP). The PRP can be further centrifuged to obtain a platelet pellet that can be resuspended (washed platelets). The image was created using BioRender.

### 2.2.2. Platelet-rich plasma purity analysis

PRP purity was determined by flow cytometry (BD Accuri C6), using fluorophore-conjugated antibodies to specific surface markers to identify platelets, contaminating leukocytes, and red blood cells. Mouse anti-human CD41a monoclonal antibody conjugated to fluorescein isothiocyanate (FITC) or mouse anti-human CD41a monoclonal antibody conjugated to allophycocyanin (APC) were used to detect CD41a (integrin  $\alpha_{IIb}\beta_3$ ) expressed on platelets. Mouse anti-human CD45 monoclonal antibody conjugated to APC, mouse anti-human CD14 monoclonal antibody conjugated to APC, and mouse anti-human CD15 monoclonal antibody conjugated to FITC, were used to detect the leukocyte antigens CD45, CD14, or CD15, respectively.

Mouse anti-human CD235 monoclonal antibody conjugated to phycoerythrin (PE) was used to detect the red blood cell marker, CD235 (glycophorin A). Antibodies were incubated with PRP using a 1:100 dilution for 5 minutes (RT). 15 $\mu$ L of the sample was collected by the BD Accuri C6 flow cytometer for analysis. The threshold was set

to 20,000 on forward scatter-height (FSC-H), and a fast flow rate was used. Using the controller BD Accuri™ C6 Software, density plots with logarithmic scales were created to show forward scatter-area vs. side scatter-area (FSC-A vs. SSC-A; FSC-A being representative of cell size, and SSC-A being representative of cell complexity/granularity), and FSC-A vs. FL (fluorescence). Histograms were created to show FL vs. count (number of platelets containing dye emitting fluorescence at a particular wavelength), with a logarithmic scale used for FL. The median fluorescence intensity (MFI) was recorded for each sample (see section '*Flow cytometry*' on page 91 for more information on the individual fluorescence channels). Grid positions on plots in the BD Accuri C6 software were adjusted around cell populations to obtain percentage values of cells in the sample.

### *2.2.3. Preparation of washed platelets*

Blood was collected as described in section 2.2.1. (**Figure 17**). Acid citrate dextrose (ACD; 85mM tri-sodium citrate, 71mM citric acid, 111mM D-glucose) was added to freshly drawn blood (1:7 v/v). ACD had been warmed in a water bath at 30°C. PRP was isolated from whole blood, as previously described. PRP was diluted 1:1 with 4-(2-hydroxyethyl)-1-piperazineethanesulfonic acid (HEPES)-buffered saline (135mM NaCl, 3mM KCl, 10mM HEPES free acid, 1mM MgCl<sub>2</sub>·6H<sub>2</sub>O, 0.34mM Na<sub>2</sub>HPO<sub>4</sub>, 12mM NaHCO<sub>3</sub>; pH 7.4) supplemented with D-glucose (9mg/10mL). The HBS-glucose had been warmed in a water bath at 30°C. Apyrase grade VII (0.02 U/mL) was added to the diluted PRP. Apyrase catalyses the hydrolysis of trace amounts of ADP in the blood to AMP, preventing ADP-induced platelet aggregation and desensitisation of the P2Y<sub>1</sub>/P2Y<sub>12</sub> receptors. A platelet pellet was formed by further centrifugation (600 g, 10 minutes, RT). The supernatant was aspirated, and the platelet pellet was resuspended in

1mL HBS. A platelet count was performed on the BD Accuri C6 Flow Cytometer using a 1:100 dilution of platelets to HBS. The washed platelets were diluted to a concentration of  $1 \times 10^8$  platelets/mL.

#### *2.2.4. Plate-based aggregometry*

Platelet aggregation can be determined *in vitro* using platelet-rich plasma isolated from whole blood. This phenotypic assay served as the primary starting point for screening compounds.

#### *Blocking wells*

The experiment began immediately after PRP preparation. The required number of wells in 96-well plates (white flat bottom; Greiner Bio-One; catalogue number 655983) had already been blocked with 0.75% gelatin for 90 minutes, at 4°C. The gelatin was then discarded and any liquid remaining in the wells was further aspirated by pipetting.

#### *Plate preparation*

The volume of vehicle or test compound dispensed in each well was 9µL. PRP, which had been dispensed into a separate plate, was transferred to the main plate using a multichannel pipette at a volume of 81µL, giving a total volume of compound and PRP of 90µL. PRP was incubated with the compound for 30 minutes at RT.

### *Preparation of controls*

Unstimulated PRP and platelet-poor plasma (PPP) were used as controls. PPP was prepared by transferring PRP to eight Eppendorf tubes (400 $\mu$ L/tube), which was pelleted using the Thermo Scientific Heraeus Fresco 17 Centrifuge (17 g, 10 minutes, RT). The PPP was then transferred to fresh Eppendorf tubes and pelleted again. The resulting PPP was transferred to fresh Eppendorf tubes and double filtered using Millex-GP filters, 0.22 $\mu$ M (Merck Millipore, catalogue number: SLGP033RS). 81 $\mu$ L PRP or PPP was transferred to the wells. Wells were made up to 90 $\mu$ L using HBS.

### *Microplate reader settings*

The FLUOstar Omega microplate reader (BMG LABTECH) was prepared for subsequent steps. The Omega software was used for plate reader control. Plate reader injectors were cleaned with 70% EtOH and dH<sub>2</sub>O using the primer function (3000 $\mu$ L was primed at a pump speed of 430 $\mu$ L/second). The pumps were then primed with the appropriate concentration of the agonist. After the 30 minutes incubation period, wells were made up to the required volume with HBS before the injection of varying volumes of the agonist.

Wells were injected with agonist, to a final volume of 100 $\mu$ L and shaken for 5 minutes (double orbital, 700 rotations per minute (rpm)) after the injection cycle. Control wells were not injected with the agonist, and instead were made up to the final volume of 100 $\mu$ L using HBS. Shaking or stirring of samples was required to ensure platelets would encounter each other and form contacts. The kinetic window was composed of three cycles, with 22 flashes per well and cycle. The injection took place in cycle 2. The pump speed was set to 430 $\mu$ L, with the 'Smart dispensing' option selected. Absorbance was measured at 595nm (excitation filter) in plate mode, at RT.

## *Data analysis*

As in previous work, the percentage of platelet aggregation was determined from the raw data (absorbance readings)<sup>288-293</sup>. The PRP controls corresponded with 100% light absorbance in the sample, and the PPP controls corresponded with 0% light absorbance in the sample. The following equation was used to convert absorbance values to % aggregation values:

$$\% \text{ Aggregation: } \frac{\text{PRP control absorbance} - \text{Test well absorbance}}{\text{PRP control absorbance} - \text{PPP control absorbance}} \times 100$$

### *2.2.5. LANCE cAMP assay*

The LANCE-cAMP 384 kit (Perkin Elmer) is an immunoassay used to measure intracellular cAMP levels. cAMP is a second messenger, and its levels decrease upon activation of the P2Y<sub>12</sub> signalling pathway due to the inhibition of adenylyl cyclase by the G<sub>i</sub>α subunit. Thus, the assay can measure compounds' effect on P2Y<sub>12</sub>-mediated adenylyl cyclase inhibition. This kit is normally used for cells, and the protocol had to be specially optimised for platelets, which have a lower volume than most cells.

Forskolin, which is a potent activator of adenylyl cyclase, was used to stimulate cAMP production in platelets. The purpose of this was to increase basal cAMP levels to levels detectable in the assay, which could then be decreased in subsequent P2Y<sub>12</sub> agonism experiments.

The kit is a Fluorescence Resonance Energy Transfer (FRET) immunoassay. As shown in **Figure 18**, competition exists between sample cAMP, and a europium-labelled cAMP tracer complex, for binding to anti-cAMP antibodies (labelled with Alexa Fluor 647). Where there are high levels of sample cAMP, the Alexa Fluor does not become excited, and there is decreased response. However, in low levels of sample

cAMP, the cAMP tracer complex is more likely to bind to anti-cAMP antibodies, and energy from the europium chelate (excited by 315nm light) is transferred to the Alexa Fluor. This fluorophore will emit fluorescence at 665nm, which is the measured TR-FRET signal.

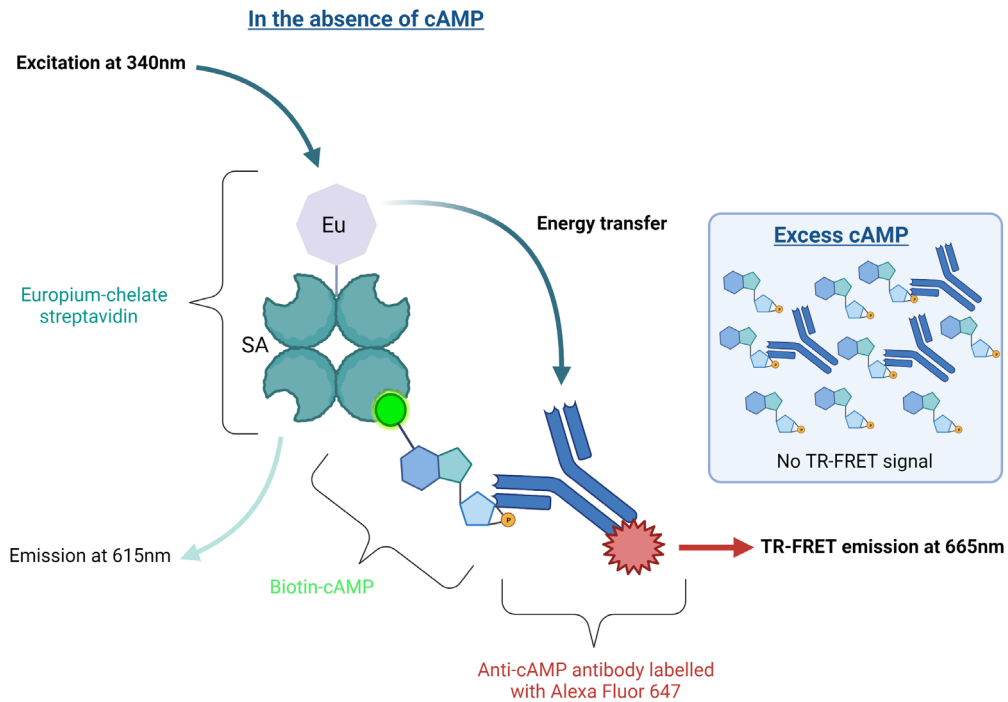


**Figure 18: Concept behind how the LANCE cAMP assay works.** In the absence of sample cAMP, the tracer complex (composed of europium-chelate streptavidin and biotin-cAMP) will bind to anti-cAMP antibodies labelled with Alexa Fluor 647. Upon excitation with a light pulse at 340nm, energy is transferred from the europium-chelate to the anti-cAMP antibody labelled with Alexa Fluor 647. The TR-FRET signal can be detected at 665nm. In the presence of excess sample cAMP, anti-cAMP antibodies will bind to sample cAMP instead of the tracer complex, resulting in no (or lower) TR-FRET signal than in the absence of sample cAMP where the tracer complex did not have to compete with sample cAMP for binding to the anti-cAMP antibody. The image was created using BioRender.

### Preparations

The following is a protocol adapted from the LANCE-cAMP 384 kit manual for use with platelets. BSA 0.1% (referred to as ‘stimulation buffer’ in the kit manual) was warmed in a water bath at 30°C. Isobutylmethylxanthine (IBMX) (1M), which required

a heat block to fully thaw, was added to the warmed stimulation buffer at a volume of 10 $\mu$ L. The final concentration of IBMX in the stimulation buffer was 500 $\mu$ M. IBMX is a non-selective phosphodiesterase inhibitor and was present in the buffer to prevent the breakdown of the cAMP in samples (as suggested in the kit protocol).

### *Plate preparation*

In a 96-well plate, the cAMP Standard solution (50 $\mu$ mol/L) was serially diluted to desired working concentrations of cAMP using stimulation buffer. This was performed to create a cAMP standard curve. Row A1 contained 92 $\mu$ L stimulation buffer, and rows B1-H1 contained 90 $\mu$ L HBS. cAMP Standard (8 $\mu$ L) was added to Row A1 to achieve a final volume of 100 $\mu$ L. 10 $\mu$ L of this solution was transferred to Row B1, and so on to perform serial dilutions. This was done such that the wells in Rows A1-G1 contained 2 x 10<sup>-6</sup> M, 2 x 10<sup>-7</sup> M, 2 x 10<sup>-8</sup> M, 2 x 10<sup>-9</sup> M, 2 x 10<sup>-10</sup> M, 2 x 10<sup>-11</sup> M, 2 x 10<sup>-12</sup> M cAMP, respectively. The control wells (HBS only) did not contain cAMP Standard solution. In the second column of the 96-well plate, serial dilutions were made for forskolin, as the aim of initial experiments involving this assay was to construct concentration-response curves showing changes in cAMP in response to varying concentrations of forskolin. The EC<sub>80</sub> of forskolin could then be obtained, which would be used in subsequent experiments where P2Y<sub>12</sub> agonism and antagonism would be tested.

In well A2 of the 96-well plate, 98 $\mu$ L of stimulation buffer was added. Wells B2-H2 contained 90 $\mu$ L stimulation buffer. Forskolin (10mM) was added to well A2 at a volume of 2 $\mu$ L, and serially diluted (transferring 10 $\mu$ L) to well B2, and so on, to achieve the following concentrations: 2 x 10<sup>-4</sup> M, 2 x 10<sup>-5</sup> M, 2 x 10<sup>-6</sup> M, 2 x 10<sup>-7</sup> M, 2 x 10<sup>-8</sup> M in wells A2-E2, respectively. The control well (HBS only) did not contain forskolin.

### *Addition of anti-cAMP antibody*

Washed platelets were prepared as previously described. The platelet pellet obtained was resuspended in stimulation buffer to achieve the desired initial stock concentration of platelets. A diluted stock of  $1.8 \times 10^6$  platelets/mL was required. Platelets (99 $\mu$ L) were then transferred to an Eppendorf tube (tube 'A'), to which Alexa Fluor 647 anti-cAMP antibody (1 $\mu$ L) was added. The platelets were incubated with anti-cAMP antibody for 10 minutes at RT. A white, opaque 384-well OptiPlate (catalogue number: 6007290, Perkin Elmer) was used for the final stage of the experiment. In this plate, column 1 would accommodate samples for the cAMP standard curve, and column 2 would accommodate samples for the forskolin concentration-response curve. Platelets (5 $\mu$ L) from tube 'A' were transferred to the wells in column 2 (wells A2-P2) of the 384-well plate.

The wells in column 1 (standard curve) did not contain platelets. For this column, anti-cAMP antibody was prepared by diluting 2 $\mu$ L Alexa Fluor 647 anti-cAMP antibody with 198 $\mu$ L stimulation buffer in an Eppendorf tube. From this, 5 $\mu$ L was dispensed into each well in column 1 (wells A1-P1). Samples (5 $\mu$ L) from the 96-well plate were transferred to their respective column in the 384-well plate in duplicate and incubated for 5 minutes at RT, avoiding exposure to light.

### *Addition of detection mixture*

The detection mixture was prepared, as follows. Streptavidin labelled with Europium-W8044 chelate (Eu-SA) (1 $\mu$ L; concentration not stated) was diluted in 35 $\mu$ L of the kit-supplied cAMP detection buffer (pH: 7.4) and mixed gently. 20 $\mu$ L of this was transferred to a foil-wrapped Falcon tube containing 2460 $\mu$ L detection buffer. The detection buffer contained Triton (0.35%) which would permeabilise platelet membranes in subsequent steps.

Biotin-cAMP tracer (2 $\mu$ L; concentration not stated) was added to 22 $\mu$ L detection buffer and mixed gently. 20 $\mu$ L of this mixture was added to the Falcon tube containing Eu-SA and detection buffer. The detection mixture (10 $\mu$ L) was distributed into a 96-well plate and dispensed into every sample well in the 384-well OptiPlate, for a total assay volume of 20 $\mu$ L. Samples were incubated with detection mixture for 1 hour at RT, avoiding exposure to light.

#### *Microplate reader*

Responses were measured using the LB Mithras 940 plate reader to measure time-resolved fluorescence at 665nm. MikroWin 2000 software was used for reader control.

#### *2.2.6. Development of a multiplexed pVASP assay*

##### *Platelet incubation with compounds*

The pVASP assay (**Figure 19**) began immediately after washed platelet preparation. 96-well plates were used to incubate platelets with compounds. All compounds were diluted to the desired working concentration using filtered HBS. Where agonist response curves were desired, the test compound (10 $\mu$ L) was dispensed in the wells belonging to row A, labelled 'drug incubation', and incubated with 90 $\mu$ L of washed platelets (1 x 10<sup>8</sup> platelets/mL) (30 minutes, RT) to achieve a final concentration of 10 $\mu$ M. A maximum of eight samples could be tested for each response curve, the reasons for which are explained in the section below entitled, '*Barcoding procedures*'. Platelets were dispensed in all wells in Row 1 at the same time.

Row 2 of wells, labelled 'Platelets active', contained 10 $\mu$ L prostaglandin E<sub>1</sub> (PGE<sub>1</sub>), dissolved in pure ethanol, (100nM final concentration), and 10 $\mu$ L of the P2Y<sub>12</sub> agonist, ADP, dissolved in filtered distilled water (varying final concentrations). PGE<sub>1</sub>

was used to stimulate adenylyl cyclase, increasing levels of cAMP and, hence, pVASP above baseline to detectable levels. In contrast, ADP reduces pVASP levels through activation of the P2Y<sub>12</sub> pathway, and subsequent inhibition of adenylyl cyclase.

Platelets (80µL) from Row 1 were transferred to Row 2, and PGE<sub>1</sub>/ADP were incubated simultaneously with pre-treated platelets for 10 minutes at RT. Each response curve required two rows (drug incubation and platelet activation) as described above (i.e., vehicle: 2 rows, drug A: 2 rows, drug B: 2 rows, etc.). In cases where screens were performed with a single concentration of agonist that did not require response curves, the same methodology as above was adopted. Additionally, a stimulated control was required, which contained PGE<sub>1</sub> (no ADP), and an unstimulated control was required, which contained HBS (no PGE<sub>1</sub> or ADP).

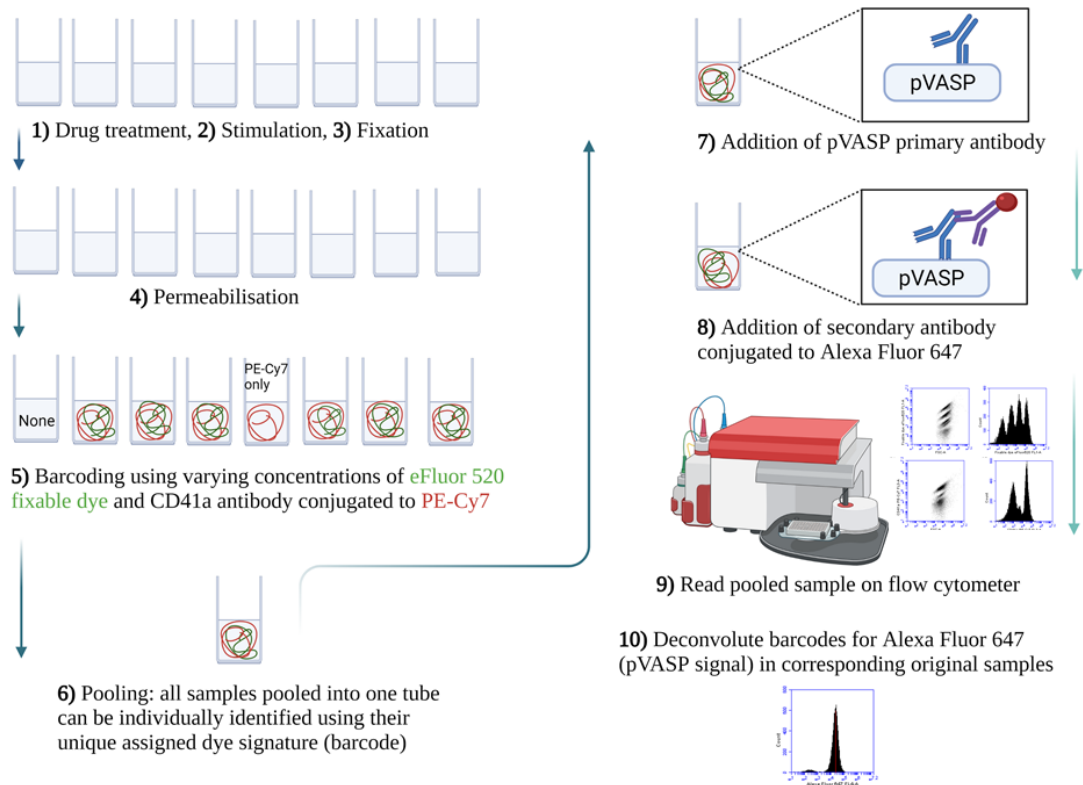


**Figure 19: A basic outline of the pVASP assay.** These steps were performed using washed platelets or PRP. Platelets were treated with the drug, stimulated, and fixed. They were then permeabilised. Samples were uniquely barcoded using varying concentrations of two dyes. All samples were pooled into one tube. Each pooled sample could accommodate eight barcoded samples. Primary antibody against pVASP was added to the pooled sample, followed by a secondary antibody conjugated to Alexa Fluor 647. The pooled sample was read using flow cytometry. The barcodes could be deconvoluted for Alexa Fluor 647 (pVASP signal) in the original samples. These stages are explained in detail in the text. The image was created using BioRender.

### *Fixation*

Eppendorf tubes were labelled A1-A8, B1-B8, and C1-C8, where each set of 8 accommodated samples for the eight points of one response curve. Samples from Row 2 of each set were transferred to the appropriate test tubes at a volume of 62.4µL, ensuring to time-match samples. Paraformaldehyde (PFA) (4%; methanol free) was added to the tubes in each row at a volume of 37.6µL and mixed (ensuring that corresponding tubes were time-matched) to achieve a final concentration of 1.5%. Samples were fixed with PFA for 10 minutes at RT. Following fixation, samples were washed with 1% bovine serum albumin (BSA), 100µL. BSA prevents platelets sticking to the walls of the tubes and the platelets will also adhere to the BSA, making the pellet more visible (see **Troubleshooting Tips for the pVASP assay** in the **Appendix**). Platelets were then pelleted (Thermo Scientific Heraeus Fresco 17 Centrifuge; 1.2 g, 10 minutes, 4°C). This centrifuge could accommodate a maximum of 24 samples (i.e., three sets of eight samples: vehicle group, test drug 1 group, and test drug 2 group, to produce a maximum of 3 response curves). The samples were kept on ice from hereon.

### *Permeabilisation*

The supernatant in each sample was aspirated, and the pellet was resuspended in 190µL, ice-cold, filtered, PBS. Triton (2%; in PBS) was added to each sample at a volume of 10µL to achieve a final concentration of 0.1%, ensuring to time-match samples that would later be corresponding points on the response curves. Samples were incubated on ice for 10 minutes to permeabilise the platelet plasma membranes. Samples were then washed with 300µL ice-cold BSA (1%), and pelleted (1.2 g, 10 minutes, 4°C). The supernatant was aspirated, and the pellet was resuspended in the appropriate volume of PBS required before the addition of barcoding dye.

## *Barcoding procedures*

**1) Choosing stains and optimisation stages** (*this section was not a part of the final protocol - the reader may skip to point (2) for the next step in the protocol*).

Fluorescent stains were chosen which could be analysed by flow cytometer channels (fluorescence emission wavelengths: FL1: 533/30nm (green); FL2: 585/40nm (yellow); FL3 > 670nm (red)) other than FL4 (FL4: 675/25nm (far-red)). This was because FL4 was used to read Alexa Fluor 647 fluorescence, which was the fluorophore-conjugated to the secondary antibody. Additionally, the barcode fluorophores read on channels FL1 and FL3 were excited at 488nm by laser 1 (solid-state blue argon ion laser), whereas the Alexa Fluor 647, correlating with pVASP levels, was excited at 640nm by laser 2 (diode red helium-neon laser).

Furthermore, in the initial optimisation stages, three stains with extracellular targets were tested: mouse anti-human CD41a monoclonal antibody conjugated to phycoerythrin-cyanine 7 (PE-Cy7) (read on FL3), mouse anti-human CD42a monoclonal antibody conjugated to FITC (read on FL1), and mouse anti-human CD42b monoclonal antibody conjugated to FITC (read on FL1). Additionally, two stains with intracellular targets were tested: a hydrophilic binding dye, 3,3'-dihexyloxacarbocyanine iodide, DiOC<sub>6</sub>, (read on FL3), and a covalent binding fixable viability dye conjugated to eFluor 520 (read on FL1).

Following permeabilisation and pelleting, the supernatant was aspirated, and the platelet pellet was resuspended in varying volumes of 1% BSA, depending on the desired final concentration of barcoding stains. The stains were tested at the desired final concentrations or dilutions with washed platelets resuspended in HBS (varying volumes) to a final volume of 100µL: mouse anti-human CD41a monoclonal antibody conjugated to PE-Cy7: none (PBS), 0.025µg (1µL (1:100)), 0.050µg (2µL (1:5)),

0.075 $\mu$ g (3 $\mu$ L (1:33)), 0.100 $\mu$ g (4 $\mu$ L (1:25)), 0.125 $\mu$ g (5 $\mu$ L (1:20)); mouse anti-human CD42a monoclonal antibody conjugated to FITC: none (PBS), 1:20 (5 $\mu$ L), 1:10 (10 $\mu$ L), 1:7 (15 $\mu$ L), 1:5 (20 $\mu$ L), 1:4 (25 $\mu$ L); mouse anti-human CD42b monoclonal antibody conjugated to FITC: none (PBS), 1:20 (5 $\mu$ L), 1:10 (10 $\mu$ L), 1:7 (15 $\mu$ L), 1:5 (20 $\mu$ L), 1:4 (25 $\mu$ L); DiOC<sub>6</sub>: none (dimethyl sulfoxide (DMSO)), 10nM, 30nM, 100nM, 300nM, 1 $\mu$ M, 3 $\mu$ M, 10 $\mu$ M, 30 $\mu$ M; fixable viability dye conjugated to eFluor 520: none (DMSO), 1:1000 (1 $\mu$ L diluted 100x, then 10 $\mu$ L of this added to resuspended platelets), 1:100 (1 $\mu$ L), 1:50 (2 $\mu$ L), 1:33 (3 $\mu$ L), 1:25 (4 $\mu$ L), 1:20 (5 $\mu$ L), 1:12.5 (8 $\mu$ L). Incubation was performed for 30 minutes on ice, preventing exposure to light.

Samples were then washed with 1% BSA (400 $\mu$ L) and pelleted (1.2 g, 10 minutes, 4°C). The supernatant was aspirated, and samples were resuspended in 200 $\mu$ L PBS for flow cytometric analysis.

## **2) Barcode creation: assigning samples with unique signatures**

The purpose of barcoding was to assign unique dye signatures to each sample in a set, where they could each be independently identified if pooled together<sup>294,295</sup>. The primary antibody required in subsequent stages could then be added to the pooled sample instead of individual samples, meaning that less antibody was used. During optimisation, each stain was tested independently at various concentrations to obtain individual barcoding layers. Whether a layer was chosen as a barcode was determined by its emission spectrum, as observed in the BD Accuri C6 Software. A layer was deemed as a suitable barcode where spectral overlap with other layers did not occur.

Following permeabilisation and pelleting, the supernatant was aspirated, and the platelet pellet was resuspended in varying volumes of PBS, depending on the desired final concentration of barcoding stains (**Sample A1**: 92 $\mu$ L, **Sample B1**: 90 $\mu$ L, **Sample**

**C1:** 99 $\mu$ L, **Sample D1:** 92 $\mu$ L, **Sample A2:** 90 $\mu$ L, **Sample B2:** 88 $\mu$ L, **Sample C2:** 97 $\mu$ L, **Sample D2:** 90 $\mu$ L). Once barcode layers were chosen, they were combined. Individual barcodes could only be combined if the fluorescence emitted from their respective fluorophores were read on different flow cytometer channels (e.g., dye 1 could be read on FL1 and one dye 2 could be read on FL3, and the fluorophore-conjugated to the secondary antibody mentioned in subsequent could be read on FL4). The combination of barcodes was a multiplicative process, such that if four independent barcode layers were successfully assigned to dye 1, and two independent barcode layers were successfully assigned to dye 2, a total of  $4 \times 2 = 8$  unique signature barcodes could be achieved.

In each set of eight samples, the following barcodes were used. **Sample A1:** DMSO only (8 $\mu$ L), **Sample B1:** fixable viability dye conjugated to eFluor 520 (1:1000), **Sample C1:** fixable viability dye conjugated to eFluor 520 (1:100), **Sample D1:** fixable viability dye conjugated to eFluor 520 (1:12.5), **Sample A2:** DMSO (8 $\mu$ L) + mouse anti-human CD41a monoclonal antibody conjugated to PE-Cy7 (2 $\mu$ L, 0.050 $\mu$ g (1:50)), **Sample B2:** fixable viability dye conjugated to eFluor 520 (1:1000) + mouse anti-human CD41a monoclonal antibody conjugated to PE-Cy7 (2 $\mu$ L, 0.050 $\mu$ g (1:50)), **Sample C2:** fixable viability dye conjugated to eFluor 520 (1:100) + mouse anti-human CD41a monoclonal antibody conjugated to PE-Cy7 (2 $\mu$ L, 0.050 $\mu$ g (1:50)), **Sample D2:** fixable viability dye conjugated to eFluor 520 (1:12.5) + mouse anti-human CD41a monoclonal antibody conjugated to PE-Cy7 (2 $\mu$ L, 0.050 $\mu$ g (1:50)).

In summary, the vehicle set contained eight samples, barcoded as above, the test drug 1 set contained eight samples, barcoded as above, and the test drug 2 set contained eight samples, barcoded as above. This would generate three response curves. As previously mentioned, a maximum of 24 samples could be tested due to the sample accommodation limits of the centrifuge used for pelleting. Incubations were performed

for 30 minutes on ice, preventing exposure to light. Samples were then washed with 1% BSA (400 $\mu$ L) and pelleted (1.2 g, 10 minutes, 4°C).

### **3) Pooling barcoded samples**

Samples containing combined barcodes were pooled into one tube, for each set. This was performed by first resuspending the pellet in each tube with 1% BSA (100 $\mu$ L), and then transferring the contents of each tube to a single combination tube (e.g., eight individual samples resuspended in 100 $\mu$ L BSA each could be combined to a total volume of 800 $\mu$ L in the new tube). Platelets were then pelleted (1.2 g, 10 minutes, 4°C).

#### *Addition of primary antibody*

Following barcoding and pooling of barcoded platelets, the pellet was resuspended in ice-cold BSA (1%) before the addition of anti-phospho-VASP (Ser-157) rabbit monoclonal primary antibody (final concentration: 2 $\mu$ g/mL in 100 $\mu$ L) to each pooled sample. The antibody was mixed thoroughly by pipetting. Samples were incubated on ice for 30 minutes. Samples were then washed using BSA (300 $\mu$ L), and pelleted (1.2 g, 10 minutes, 4°C).

#### *Isotype controls*

Rabbit (DA1E) monoclonal antibody immunoglobulin G (IgG) isotype control was added to control tubes, at the same final concentration as the primary antibody in 100 $\mu$ L. Isotype control samples were not to be combined with the pooled sample containing the signature barcodes at any point during the protocols. Samples were incubated on ice for 30 minutes. Samples were then washed using BSA (300 $\mu$ L), and

pelleted (1.2 g, 10 minutes, 4°C). The isotype control was tested with the secondary antibody extensively in preliminary experiments.

#### *Addition of secondary antibody*

The pellet was resuspended in ice-cold BSA (1%) before the addition of anti-rabbit IgG (H+L), F(ab')<sub>2</sub> fragment, Alexa Fluor 647 conjugate (final concentration: 1 µg/mL in 100 µL). The antibody was mixed thoroughly by pipetting. The same concentration of secondary antibody was added to the isotype control tubes in 100 µL. Samples were incubated on ice for 30 minutes, preventing exposure to light. They were then washed using 300 µL ice-cold BSA (1%), and pelleted (1.2 g, 10 minutes, 4°C). The supernatant was aspirated and the pellet in each sample was resuspended in 1000 µL ice cold, filtered PBS, for flow cytometry readings on the BD Accuri C6 flow cytometer. For flow cytometry readings on the BD FACSCanto II, samples were first resuspended in 500 µL ice-cold, filtered HBS in Eppendorf tubes, and then transferred round bottom FACS polystyrene tubes. In these tubes, the samples were made up to 3.5 mL using ice-cold, filtered HBS.

#### *Flow cytometry*

Using the controller BD Accuri™ C6 Software, 20,000 events were set to be collected using the 'Collect' tab of the software. For the BD FACSCanto II, the BD FACSDiva software (version 9.0.1) was used. Events on FSC-H less than 20,000 were permanently eliminated for all samples in each software. Fluorescence (FL) emission was detected according to the wavelength of light emitted from the fluorophores in the samples (four colours: FL1 green (also referred to as the 'FITC' channel): 533/30nm; FL2 yellow:

585/40nm; FL3 red ('PE-Cy7') > 670nm; FL4 far-red ('APC'): 675/25nm). The MFI was recorded for each sample. Four barcode spectra (layers) should be detected on FL1, two barcode spectra should be detected on FL2, and one spectrum should be detected on FL4, indicative of pVASP levels (which is deconvoluted to find individual sample MFI values).

To test the robustness of this multiplexed protocol, samples were read on two flow cytometers: the BD Accuri C6 and the BD FACSCanto II, as previously mentioned. Single-colour compensation controls were tested on each instrument. Due to the variable gain/voltage on different machines, which affects the fluorescence intensity on each channel, all MFI values were normalised to % pVASP using the unstimulated and stimulated controls (equation below).

#### *Data analysis: barcode deconvolution*

Barcoded samples, which were read using the FL of the barcoding dye were deconvoluted using the same software to derive the MFI of Alexa Fluor 647 (read on FL4), correlating to pVASP levels in each sample. For deconvolution, the pooled sample FSC file was first exported from the initial data file and imported into FlowJo Software, version 10 (Becton, Dickinson and Company, Ashland, Oregon, USA) for deconvolution<sup>316</sup>. The Alexa Fluor 647 MFI value was deconvoluted for each sample by analysing them according to their barcodes. Colour compensation was performed to account for fluorescence overlap between the fluorescence channels. The spectra for the eight samples contained in the pooled sample could be observed independently from each other.

MFI values were noted and transferred to GraphPad Prism for data visualisation (see section '2.2.8. *General data analysis using GraphPad Prism*'), and converted to % pVASP using the following equation:

$$\% \text{ pVASP: } \frac{\text{MFI of test sample} - \text{MFI of unstimulated control}}{\text{MFI of stimulated control}} \times 100$$

### *2.2.7. Calcium assay*

#### *Loading platelets with Cal-520, AM dye*

Platelets were loaded with the Ca<sup>2+</sup>-sensitive fluorescent dye Cal-520, AM to monitor the effect of compounds on cytosolic Ca<sup>2+</sup> levels. PRP was isolated from whole blood, as previously described. After the addition of apyrase (0.02 U/mL) to non-diluted PRP, the platelets were rested in the water bath (30°C) for 20 minutes. Cal-520, AM dye was prepared in DMSO at a stock concentration of 5mM, and further diluted to 2mM using DMSO. Cal-520 (2mM) was added to the non-diluted PRP (1μL/mL) at a final concentration of 2μM and the platelets were incubated with dye for 10 minutes in the water bath. PRP was then supplemented with HBS-glucose (1:1), accompanied by the addition of apyrase (1μL/ml). The PRP was spun (600 g, 10 minutes, RT) to obtain a platelet pellet. The pellet was resuspended in HBS-glucose, and platelet count measured by flow cytometry. Platelets were diluted to 1 x 10<sup>8</sup> platelets/mL. Prior to experiments, CaCl<sub>2</sub> was added at a final concentration of 2mM.

#### *Platelets' incubation with compounds*

A black, flat-bottom, opaque 96-well plate (Thermo Fisher Scientific; catalogue number 10499572) was used for this assay. Test compounds were dispensed in the desired wells at a volume of 9μL. Washed platelets, which had been distributed into

another plate, were transferred to the desired wells of the black plate at a volume of 81  $\mu$ L. Compounds were incubated with platelets loaded with Cal-520 for 30 minutes at RT, avoiding exposure to light. Control wells included platelets pre-loaded with Cal-520 treated with Triton (0.1%), which would later be used for gain adjustment on the microplate reader.

#### *Microplate reader settings*

The FLUOStar Omega microplate reader was prepared by priming the pump(s) with the desired stock concentration of the agonist. Both pumps were primed with varying concentrations of agonist where concentration-response curves were desired. Where a single concentration of agonist was required, one pump was primed. The fluorescence intensity was set to be measured using the plate mode option. The excitation filter was set to 492nm, and the emission filter was set to 520nm in the BMG LabTech Omega plate controller software. The kinetic window was composed of 80 cycles, with three flashes per well and cycle. The shaking mode was set to double orbital (frequency: 700rpm) to occur for two seconds after the injection cycle. The pump speed was set to 430  $\mu$ L/second with the option to use smart dispensing selected. The injection was set to occur at cycle 30 (approximately 6 minutes after the reading began). Agonist was injected at a dispensing volume of 10  $\mu$ L or less, depending on the concentrations desired.

The plate was placed into the plate reader after 25 minutes of incubation to acclimatise to the machine temperature (25°C). The final assay volume (with agonist) was 100  $\mu$ L, and HBS was added where required to increase well volumes before agonist injection. The plate was shaken for 2 seconds before the first of 80 cycles were initiated. The gain adjustment was performed to a Triton (0.1%) well, where Cal-520-

loaded platelets were permeabilised to expose the contents. Fluorescence gain was adjusted on this sample because it had the highest expected signal.

### *Data analysis*

Data was first analysed in Microsoft Excel<sup>317</sup>. For each sample, a mean value was calculated for all fluorescence intensity values obtained before agonist injection ( $F_0$ ). Then, every fluorescence intensity value obtained from cycle 1 to cycle 80 ( $F$ ) were divided by  $F_0$  value obtained for the sample i.e., all values were normalised to that of the initial unstimulated vehicle control values. Peak values were determined from  $F/F_0$  values in GraphPad Prism. Baseline correction was performed as necessary.

#### *2.2.8. General data analysis with GraphPad Prism*

GraphPad Prism version 8.0.0 for Windows (GraphPad Software, San Diego, California, USA; graphpad.com) was employed throughout the project for data analysis. Data are presented as mean  $\pm$  standard error of the mean (SEM) of five independent biological repeats (5 independent blood donors), unless otherwise stated. Statistical analysis was performed accordingly using the (unpaired) t-test or the one-way analysis of variance (ANOVA). Where appropriate, the one-way ANOVA was followed-up by Dunnett's multiple comparisons (post-hoc) test. Where required, concentration-response curves were compared using the extra-sum-of-squares F test.

#### *2.2.9. Chemical preparations and sources*

Compounds were typically dissolved according to instructions on the manufacturer's data sheets, where available. The supplier, catalogue number, and stock preparation for each compound is shown in **Table 3**, **Table 4**, and **Table 5** (antibodies). Where

appropriate, compounds were vortexed (Clifton Cyclone Vortex Mixer) and/or sonicated (Camlab Transsonic T310 water bath) to be fully dissolved.

**Table 3: List of chemicals/reagents used.** Supplier, catalogue number, and stock preparations are specified (continued on page 97).

Chemical/reagent	Supplier	Catalogue number
2MeSADP trisodium salt	Bio-Techne (Tocris)	1624
Adenosine 3'-5'- cyclic monophosphate sodium salt monohydrate (cAMP)	Sigma Aldrich	A6885
Adenosine 5'-diphosphate, disodium salt hydrate	Fisher Scientific	AC164672500
Adenosine monophosphate (AMP)	MedChemExpress	HY-A0181
Altanserin hydrochloride	Bio-Techne (Tocris)	1809
Apyrase	Sigma Aldrich	A6535-100UN
AR-C66096 tetrasodium salt	Bio-Techne (Tocris)	3321
AR-C69931 tetrasodium salt	Bio-Techne (Tocris)	5720
AZD1283	Bio-Techne (Tocris)	6085
Bovine serum albumin, heat shock fraction, pH 7	Sigma Aldrich	A7906
Brinzolamide	Sigma Aldrich	SML0216
Cal-520	AAT Bioquest	21130
Citric acid monohydrate	Sigma Aldrich	C1909
D-glucose anhydrous	Fisher Scientific	G/0500/53
Dimethyl sulfoxide	Sigma Aldrich	276855
DiOC <sub>6</sub>	Sigma Aldrich	318426
Dulbecco's phosphate buffered saline	Sigma Aldrich	D8537
Eptifibatide	Bio-Techne (Tocris)	4725
Fixable viability dye eFluor 520	Thermo Fisher Scientific	65-0867-14
Forskolin	MedChemExpress	HY-15371
Gelatin, type B from bovine skin. Approx. 225 bloom	Sigma Aldrich	G-9382
HEPES free acid	VWR	0511
IBMX	Sigma Aldrich	15879
Ketanserin	MedChemExpress	HY-10562
Magnesium chloride hexahydrate	Sigma Aldrich	M2670
MRS 2179 tetrasodium salt	Bio-Techne (Tocris)	0900
N6-(4-hydroxybenzyl) adenosine (paratopolin riboside)	MedChemExpress	HY-18775

Paraformaldehyde, 4% in PBS	Alfa Aesar	J61899
PGE <sub>1</sub>	Santa Cruz Biotechnology	sc-201223
Potassium chloride	Sigma Aldrich	P9333
Rivaroxaban	Cayman Chemicals	16043
Roxindole hydrochloride	Bio-Techne (Tocris)	1559
SB228357	Bio-Techne (Tocris)	1375
Sodium chloride	Sigma Aldrich	57653
Sodium citrate dihydrate	Sigma Aldrich	W302600
Sodium phosphate monobasic	Sigma Aldrich	50751
TRAP-6 amide trifluoroacetate salt	VWR	H-2936.0005BA
Trazodone hydrochloride	MedChemExpress	HY-B0478
Triton X-100	Sigma Aldrich	X-100

**Table 4: List of screening compounds used.** The screening ID, supplier, catalogue number and stock preparation are specified (continued on page 99). All compounds were sonicated in a water bath and vortexed to dissolve.

Screening compound ID	Supplier	Catalogue number	Stock preparation
E1	Enamine	Z82206144	50mM in DMSO
E2	Enamine	Z82252275	50mM in DMSO
E3	Enamine	Z362646412	50mM in DMSO
E4	Enamine	Z1134155388	50mM in DMSO
E5	Enamine	Z1340686566	50mM in DMSO
E6	Enamine	Z972768400	50mM in DMSO
E7	Enamine	Z165233186	10mM in DMSO
E8	Enamine	Z31064985	50mM in DMSO
E9	Enamine	Z373312862	10mM in DMSO
E10	Enamine	Z226752442	10mM in DMSO
E11	Enamine	Z31996047	50mM in DMSO
E12	Enamine	Z24120595	10mM in DMSO
E13	Enamine	Z28011715	10mM in DMSO
E14	Enamine	Z56789157	10mM in DMSO
E15	Enamine	Z369968936	Did not dissolve
V1	Vitas Broadway	STK985924	50mM in DMSO
V2	Vitas Broadway	STK162937	50mM in DMSO
V3	Vitas Broadway	STK006837	100mM in DMSO
V4	Vitas Broadway	STK184218	10mM in DMSO
V5	Vitas Broadway	STK174744	100mM in DMSO
B1	Specs	AH-487/11778013	10mM in DMSO
B2	Specs	AE-848/12124340	100mM in DMSO
B3	Specs	AK-778/12434116	100mM in DMSO
B4	Specs	AN-465/40743314	50mM in DMSO
B5	Specs	AN-988/40680540	100mM in DMSO
B6	Specs	AG-205/33135033	10mM in DMSO
B7	Specs	AF-399/13907005	10mM in DMSO
B8	Specs	AP-685/41280738	50mM in DMSO
B9	Specs	AE-848/33210059	10mM in DMSO
B10	Specs	AK-778/11467046	100mM in DMSO
B11	Specs	AN-988/40679805	10mM in DMSO
B12	Specs	AP-970/43204668	100mM in DMSO
B13	Specs	AN-989/41900311	100mM in DMSO
B14	Specs	AE-848/36328005	100mM in DMSO
S1	MolPort	MolPort-007-573-601	10mM in DMSO
S2	MolPort	MolPort-007-573-855	10mM in DMSO
S3	MolPort	MolPort-003-814-738	10mM in DMSO
S4	MolPort	MolPort-003-815-910	10mM in DMSO
S5	MolPort	MolPort-000-798-805	10mM in DMSO

S6	MolPort	MolPort-002-327-249	10mM in DMSO
S7	MolPort	MolPort-002-322-100	10mM in DMSO
S8	MCULE	MCULE-8557495993	10mM in DMSO
S9	MCULE	MCULE-3801925789	10mM in DMSO

**Table 5: List of antibodies used.** The supplier and catalogue number are specified. The primary, isotype, and secondary antibodies for the pVASP assay are shown in blue font.

<b>Antibody</b>	<b>Supplier</b>	<b>Catalogue number</b>
Mouse anti-human CD41a monoclonal antibody conjugated to FITC	Thermo Fisher Scientific	11-0419-42
Mouse anti-human CD41a monoclonal antibody conjugated to APC	BioLegend	303709
Mouse anti-human CD45 monoclonal antibody conjugated to APC	Thermo Fisher Scientific	17-0459-42
Mouse anti-human CD14 monoclonal antibody conjugated to APC	Thermo Fisher Scientific	17-0419-42
Mouse anti-human CD15 monoclonal antibody conjugated to FITC	BD Biosciences	555401
Mouse anti-human CD235 monoclonal antibody conjugated to PE	Thermo Fisher Scientific	12-9987-82
Mouse anti-human CD41a monoclonal antibody conjugated to PE-Cy7	Thermo Fisher Scientific	25-0419-42
Mouse anti-human CD42a monoclonal antibody conjugated to FITC	BD Biosciences	558818
Mouse anti-human CD42b monoclonal antibody conjugated to FITC	BD Biosciences	555472
Phospho-VASP (Ser-157) (D1C8O) rabbit monoclonal primary antibody	Cell Signalling Technology	84519S
Rabbit (DA1E) monoclonal antibody IgG XP isotype control	Cell Signalling Technology	3900S
Anti-rabbit IgG (H+L), F(ab') <sub>2</sub> fragment, Alexa Fluor 647 conjugate	Cell Signalling Technology	4414S

**Chapter 3.**  
**Unveiling a novel mode of action**  
**for cangrelor**

### 3.1. Aim of the study and approach taken

The binding mode of the most recently approved P2Y<sub>12</sub> antagonist, cangrelor, is not fully known. The consensus in the literature is that cangrelor is a competitive antagonist<sup>318-321</sup>. However, *in vitro* data has suggested that it prevents the binding of the active metabolites of the covalent antagonists clopidogrel and prasugrel<sup>238</sup>. Docking has predicted that the active metabolite of prasugrel binds in a second pocket in the orthosteric site (where Cys-97<sup>3,25</sup> is found), which is separate to where the reversible, competitive antagonist AZD1283 binds<sup>17</sup>. Moreover, pharmacodynamic evidence has shown that competition exists between cangrelor and the active metabolite of clopidogrel<sup>282-284</sup>. This study aimed to further explore the mechanisms by which cangrelor inhibits platelet aggregation. First, a plate-based aggregation assay was established and validated. Next, the effect of cangrelor on platelet aggregation was compared to the effect of the related P2Y<sub>12</sub> antagonist, AR-C66096. Finally, a flow cytometry-based assay of VASP phosphorylation was established and used to explore the mode of action of cangrelor.

### 3.2. Establishing a plate-based platelet aggregation assay

To monitor the effect of P2Y<sub>12</sub> antagonists on platelet aggregation, a light absorbance assay was established in a 96-well plate format. The principles of light transmission aggregometry were established by Gustav Born who developed the Born aggregometer<sup>322</sup>. The Born aggregometer can be used to measure the transmission of light through samples. Light transmission through samples is higher with platelet aggregation. Conversely, light transmission through samples is lower where there is less platelet aggregation (e.g., where platelets have been incubated with a P2Y<sub>12</sub> antagonist prior to activation). Upon agonist (ADP) addition, platelets will undergo shape change as they activate, and increase in optical density, which results in a transient drop in light

transmission. As the primary wave of aggregation occurs, the optical density will decrease, and light transmission will increase. Granule secretion will then occur, and the platelets will undergo the secondary wave of aggregation until maximal aggregation is reached. Importantly, these principles are applied in clinical settings using the VerifyNow P2Y<sub>12</sub> aggregation assay to measure patient responsiveness to oral P2Y<sub>12</sub> antagonists<sup>323-325</sup>.

Although the Born aggregometer is a 'gold' standard for platelet function testing, a method which allowed greater throughput than conventional aggregometry was required for this work. 96-well plate-based aggregometry is based on the Born principles but is more efficient for measuring large numbers of samples. Instead of light transmission, absorbance of light in samples is measured by a plate reader. In this case, light absorbance decreases with platelet aggregation, and increases where there is less platelet aggregation.

For these experiments, PRP was isolated from whole blood by centrifugation. As shown in **Figure 20**, the FSC vs. SSC profile of platelets in plasma was obtained using flow cytometry. As previously described, the FSC is proportional to platelet size and is measured as the scatter of light along the laser path. The SSC is proportional to the internal complexity of the platelet and is measured as the scatter of light at a 90° angle to the laser path. This plot showed a dense region (black) of platelets. A shadow (grey) was present around the main platelet population, which showed platelets of varying internal complexity (alpha granule content) and size. This was expected, as proplatelet formation in the bone marrow results in a heterogenous population of platelets circulating in the blood. The platelet count in PRP was approximately  $3.5 \times 10^6$  platelets/mL in each experiment. The PRP was undiluted.

### 3.2.1. PRP purity analysis

Although centrifugation is commonly used to isolate platelets in plasma, removing red blood cells and leukocytes, it is possible that contamination by these cells could affect the assay. Therefore, the purity of the isolated PRP was first assessed using a range of fluorophore-conjugated antibodies (**Figure 21**). As shown in **Figure 21a**, mouse anti-human CD41a monoclonal antibody conjugated to FITC was used to detect platelets using their surface marker integrin  $\alpha_{IIb}\beta_3$ . Mouse anti-human CD45 monoclonal antibody conjugated to APC was used to detect contaminating leukocytes using their surface marker protein tyrosine phosphatase receptor type C (CD45). The plot showed that the PRP was highly pure (99.4% platelets), with minor contamination from leukocytes (0.2%). Leukocyte contamination was further investigated using mouse anti-human CD14 monoclonal antibody conjugated to APC (**Figure 21b**). With this antibody, 0.0% leukocytes were picked up, once again indicating high PRP purity. The PRP was then checked for contamination from red blood cells. As shown in **Figure 21c**, mouse anti-human CD235 monoclonal antibody conjugated to PE was used to detect red blood cells by their marker glycoprotein A (CD235). 0.3% of the sample was positively stained for red blood cells, which was a minor contamination. Most of the sample was pure, with the mouse anti-human CD41a monoclonal antibody conjugated to APC staining 92.8% platelets. **Figure 21d** also showed high sample purity (99.5% platelets), with mouse anti-human CD235 monoclonal antibody conjugated to PE picking up 0.5% red blood cells, and the mouse anti-human CD15 monoclonal antibody conjugated to FITC picking up 0.0% leukocytes.

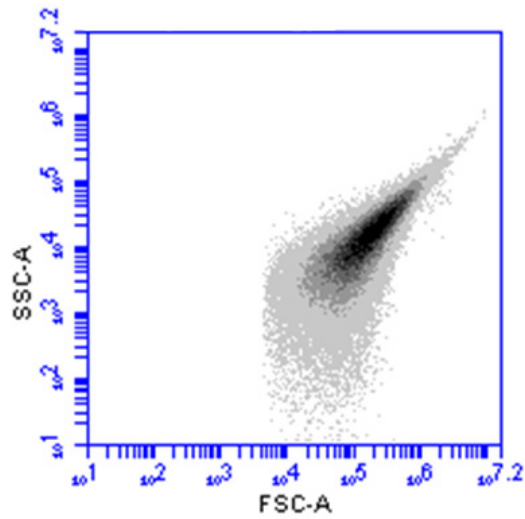


**Figure 20: Representative forward scatter-area vs. side scatter-area plot for platelets in plasma (platelet rich plasma).** A dense region (black) shows the main platelet population, with the shadow (grey) being representative of platelets of varying size and complexity. The values on the x and y scales are arbitrary. The platelet count was  $\sim 3.5 \times 10^6$  platelets/mL. The plot was obtained using the BD Accuri C6 software.

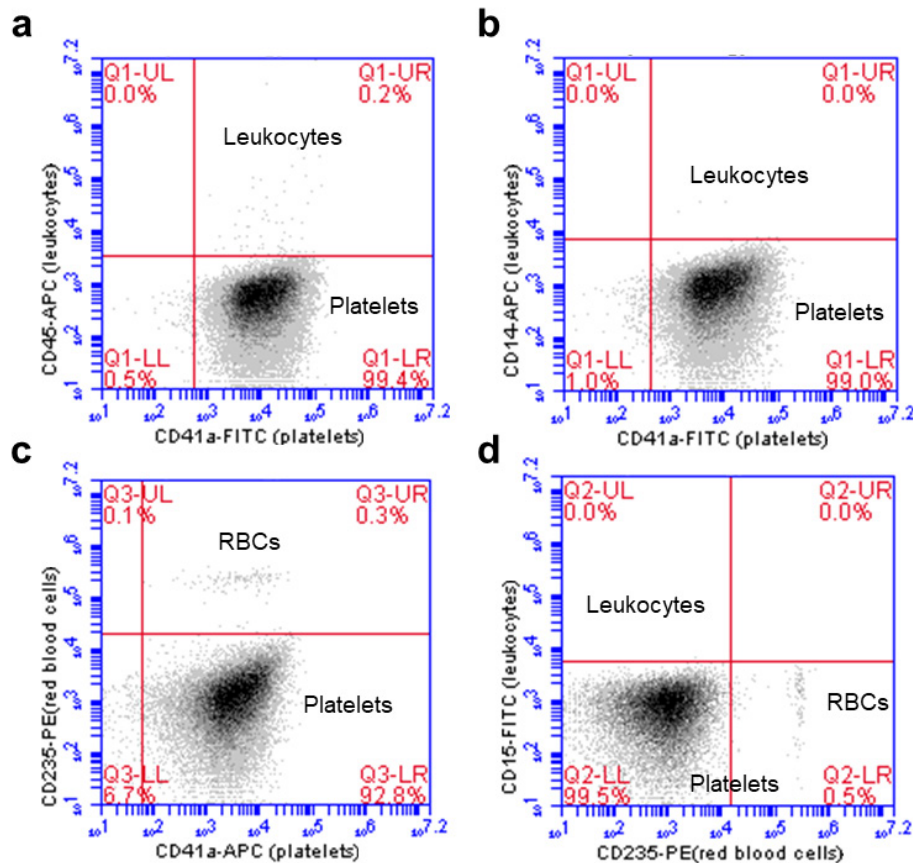


**Figure 21: PRP purity analysis.** **a)** Mouse anti-human CD41a monoclonal antibody conjugated to FITC and mouse anti-human CD45 monoclonal antibody conjugated to APC were used to detect platelets and leukocytes, respectively. The sample was highly pure (99.4% platelets as shown in quadrant 1-lower right (Q1-LR)), with minor contamination from leukocytes (0.2% leukocytes, as shown in quadrant 1-upper right (Q1-UR)). **b)** Mouse anti-human CD41a monoclonal antibody conjugated to FITC and mouse anti-human CD14 monoclonal antibody conjugated to APC were used to detect platelets and leukocytes, respectively. The sample was highly pure (99.0% platelets, as shown in quadrant 1-lower right (Q1-LR)), with no contamination from leukocytes (0.0% leukocytes, as shown in quadrant 1-upper right (Q1-UR)). **c)** Mouse anti-human CD41a monoclonal antibody conjugated to APC and mouse anti-human CD235 monoclonal antibody conjugated to PE were used to detect platelets and red blood cells, respectively. The sample was highly pure (92.8% platelets, as shown in quadrant 3-lower right (Q3-LR)), with 0.3% contamination from red blood cells (quadrant 3-upper right (Q3-UR)). **d)** Mouse anti-human CD235 monoclonal antibody conjugated to PE and mouse anti-human CD15 monoclonal antibody conjugated to FITC were used to detect red blood cells and leukocytes, respectively. The sample was highly pure (0.0% leukocytes, as shown in quadrant 2-upper left (Q2-UL)), and 0.5% red blood cells, as

shown in quadrant 2-lower right (Q2-LR)). The plots were obtained using the BD Accuri C6 software.

### 3.2.2. Aggregometry assay validations

The 96-well plate-based aggregometry assay was used to determine % aggregation in samples. PRP was stimulated with various concentrations of ADP. As expected, ADP triggered platelet aggregation in a concentration-dependent manner (**Figure 22a**).

2MeSADP also triggered aggregation in a concentration-dependent manner, and was more potent than ADP, also as expected (**Figure 22b**).

These measures of ‘aggregation’ were based on increased light transmission. To confirm that this was due to integrin-mediated platelet aggregation, the reversible integrin  $\alpha_{IIb}\beta_3$  antagonist eptifibatide was used. Eptifibatide inhibits the interaction between integrin  $\alpha_{IIb}\beta_3$  and fibrinogen, preventing aggregation. PRP was incubated with eptifibatide (10 $\mu$ M) for 30 minutes (RT) prior to platelet stimulation with varying concentrations of ADP or 2MeSADP.

As shown in **Figure 22a**, ADP + vehicle reached a maximum response ( $E_{max}$ ) of 83.8% (to 3 significant figures, 3 s.f.) mean aggregation. The  $E_{max}$  value was calculated by GraphPad Prism by finding a best-fit value for the top plateau of the curve.

Conversely, consistent with its mode of action, eptifibatide prevented aggregation in platelets at ADP concentrations of 1nM to 100 $\mu$ M. Some minor aggregation (below 20%) was present at ADP concentrations of 300 $\mu$ M to 10mM. In the presence of eptifibatide (10 $\mu$ M), ADP reached an  $E_{max}$  value of 16.89%. At the highest concentration of ADP tested (10mM), in the presence of vehicle a mean % aggregation value of  $75.5 \pm 3.18\%$  was obtained, and in the presence of eptifibatide, a mean % aggregation value of  $14.9 \pm 7.28\%$  was obtained. Similar results were achieved when the more potent platelet activator 2MeSADP was tested (**Figure 22b**). In the presence of vehicle, 2MeSADP reached an  $E_{max}$  value of 78.3%. Eptifibatide prevented

aggregation in platelets at 2MeSADP concentrations of 1nM to 100 $\mu$ M. In the presence of eptifibatide, an  $E_{max}$  value of 2.39% was obtained for 2MeSADP. At the highest concentration of 2MeSADP tested (100 $\mu$ M), in the presence of vehicle a mean % aggregation value of  $86.3 \pm 4.27\%$  was obtained, and in the presence of eptifibatide, a mean % aggregation value of  $-1.092 \pm 11.5\%$  was obtained. Note that, within the limits of the experiment, 2MeSADP could only be tested at concentrations up to 100 $\mu$ M. These data indicate that the changes in light transmission triggered by ADP or 2MeSADP are due to integrin-mediated platelet aggregation.

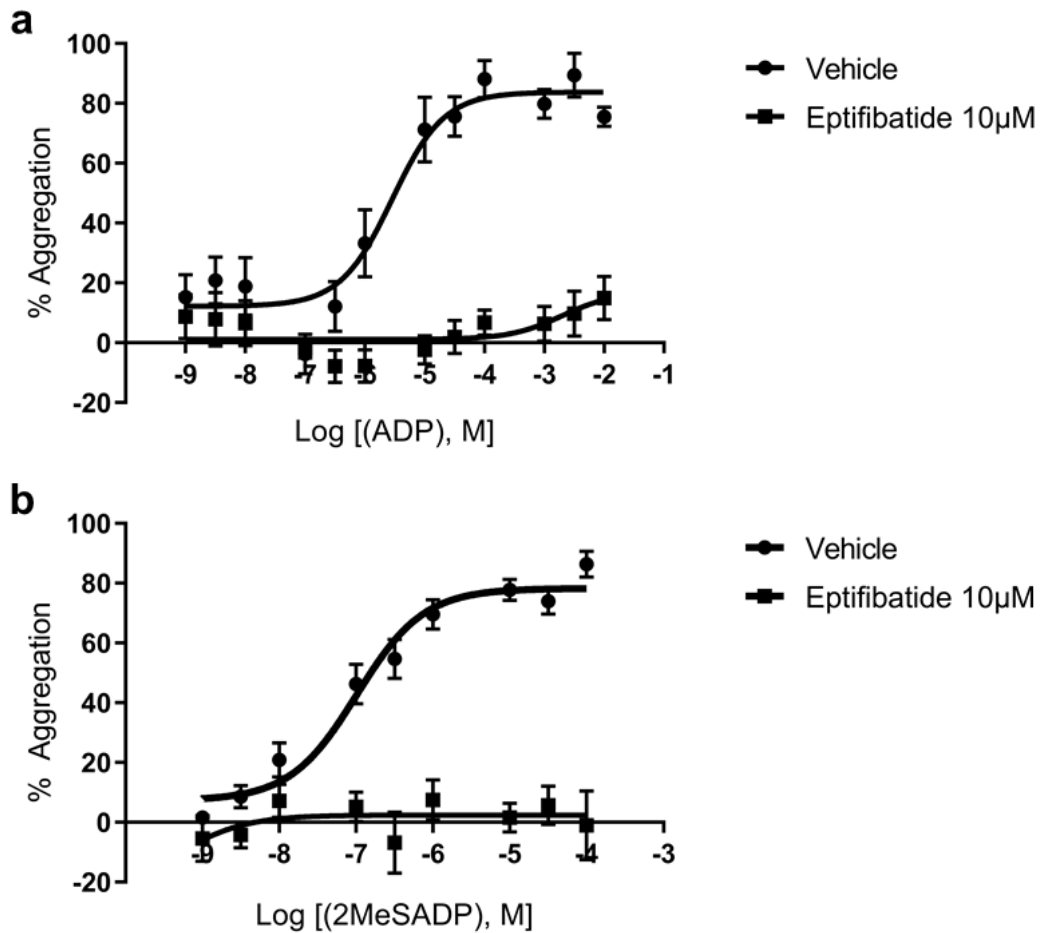


**Figure 22: Validation of the aggregometry assay using eptifibatide.** **a)** Platelets were treated with either vehicle or eptifibatide (10µM) for 30 minutes (RT), and then activated with varying concentrations of ADP (mean ± SEM; *n* = 5 independent blood donors). **b)** Platelets were treated with either vehicle or eptifibatide (10µM) for 30 minutes (RT), and then activated with varying concentrations of 2MeSADP (mean ± SEM; *n* = 6 independent blood donors). End-point absorbance readings were recorded, and the % aggregation was determined. Note the scale differences on the x-axis between the two agonists, as 2MeSADP could only be tested at concentrations up to 100µM.

Another expected feature of platelet aggregation is that it is inhibited by an increase in intracellular cAMP. Therefore, the adenylyl cyclase activator forskolin was tested. As shown in **Figure 23**, in the presence of vehicle, ADP reached an  $E_{max}$  value of 62.01%, and in the presence of forskolin (10 $\mu$ M), an  $E_{max}$  value of 16.5% was obtained for ADP. At the highest concentration of ADP used (100 $\mu$ M), in the presence of vehicle a mean % aggregation value of  $67.4 \pm 9.36\%$  was obtained. In the presence of forskolin, this was reduced to  $28.8 \pm 17.2\%$ . Activation of the platelets using ADP could not overcome the inhibitory effects of forskolin.

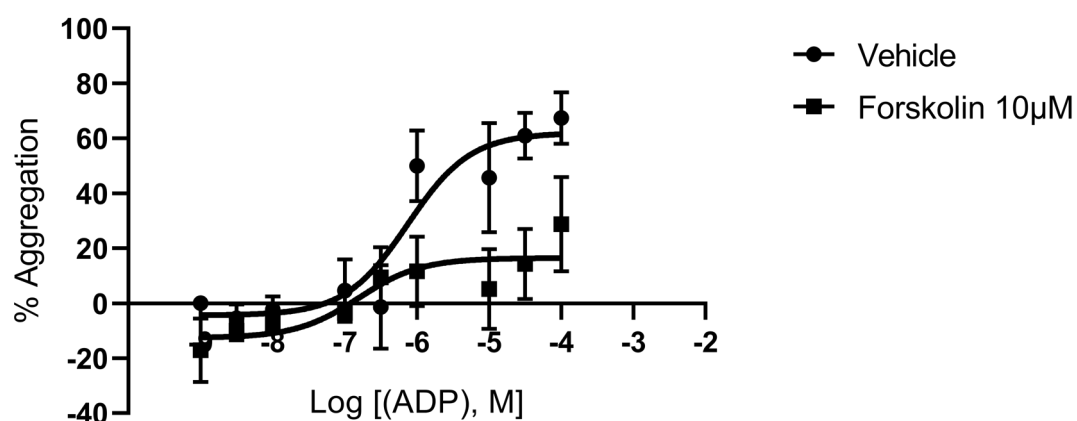


**Figure 23: Validation of the aggregometry assay using forskolin.** Platelets were treated with either vehicle or forskolin (10 $\mu$ M) for 30 minutes (RT), and then activated with varying concentrations of ADP (mean  $\pm$  SEM;  $n = 5$  independent blood donors). End-point absorbance readings were recorded, and the % aggregation was determined.

Another stimulator of adenylyl cyclase, PGE<sub>1</sub> (100nM), was also tested. Rather than directly activating adenylyl cyclase, PGE<sub>1</sub> acts through the G<sub>s</sub>-coupled IP receptor. As shown in **Figure 24**, ADP + vehicle reached an E<sub>max</sub> value of 70.02%. In presence of PGE<sub>1</sub>, this was reduced to 53.1%. At the highest concentration of ADP tested (100μM), in the presence of vehicle a mean % aggregation value of 69.0 ± 6.48% was obtained. In the presence of PGE<sub>1</sub>, this was reduced to 50.8 ± 6.15%. Together, these data show that, in this assay, platelet aggregation is inhibited by an increase in cAMP, as expected.

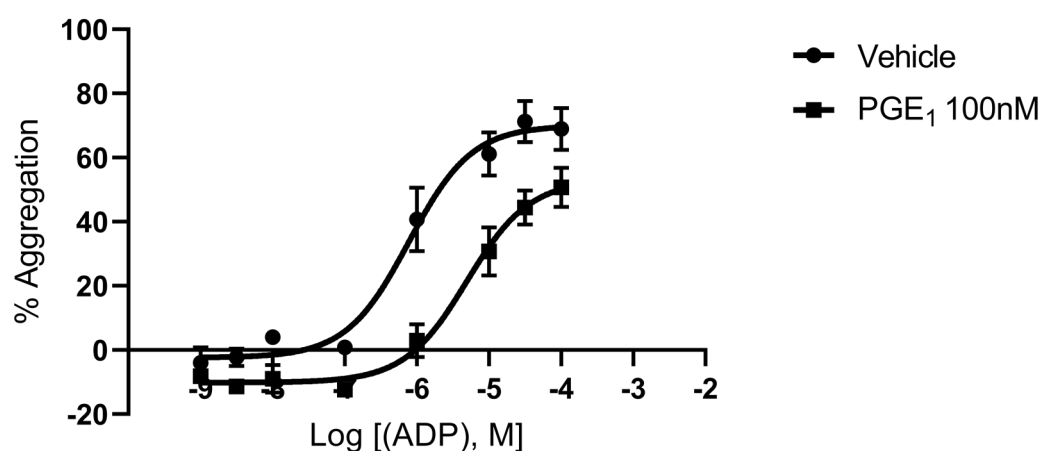


**Figure 24: Validation of the aggregometry assay using PGE<sub>1</sub>.** Platelets were treated with either vehicle or PGE<sub>1</sub> (100nM) for 30 minutes (RT), and then activated with varying concentrations of ADP (mean ± SEM; *n* = 3 independent blood donors). End-point absorbance readings were recorded, and the % aggregation was determined.

ADP and 2MeSADP both activate two purinergic receptors, P2Y<sub>1</sub> and P2Y<sub>12</sub>. The P2Y<sub>1</sub> inhibitor, MRS 2179 (10µM) was then tested. As shown in **Figure 25**, ADP + vehicle reached an E<sub>max</sub> value of 69.7%, and in the presence of MRS 2179 (10µM), an E<sub>max</sub> value of 79.8% was obtained for ADP. At the highest concentration of ADP used (100µM), in the presence of vehicle a mean % aggregation value of 71.5 ± 10.1% was obtained. In the presence of MRS 2179, a mean % aggregation value of 69.2 ± 6.23% was obtained. A rightward shift of the ADP concentration-response curve was produced in the presence of MRS 2179, with a higher log half maximal effective concentration (LogEC<sub>50</sub>) (-4.85) achieved compared to that of the ADP + vehicle curve (-6.070). These results were consistent with the mode of action of MRS 2179, which is a competitive antagonist at P2Y<sub>1</sub>. Schild analysis revealed a dissociation constant (K<sub>D</sub>) value of 6.44 x 10<sup>-7</sup> M (644nM) for MRS 2179.

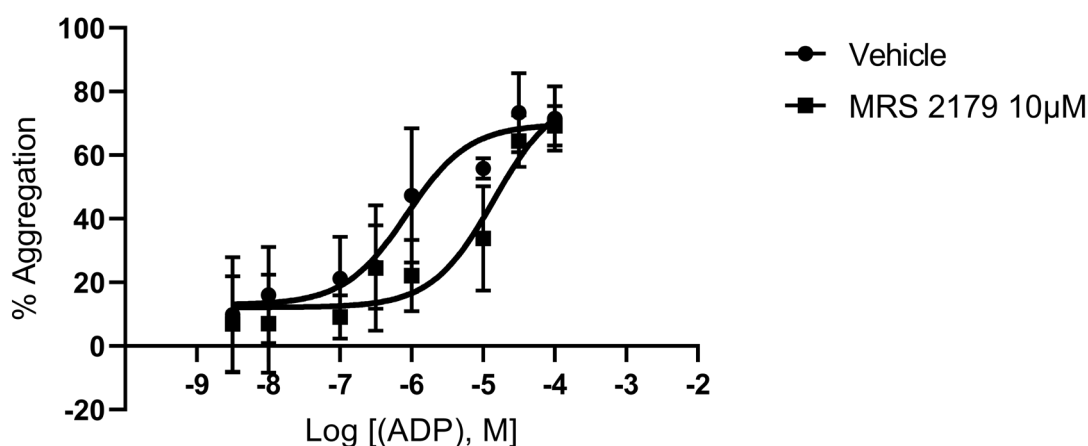


**Figure 25: Validation of the aggregometry assay using MRS 2179.** Platelets were treated with either vehicle or MRS 2179 (10µM) for 30 minutes (RT), and then activated with varying concentrations of ADP (mean ± SEM; *n* = 3 independent blood donors). End-point absorbance readings were recorded, and the % aggregation was determined.

In the next validation, the known weak inhibitor of platelet aggregation, adenosine monophosphate (AMP) was tested. AMP was initially found to be an inhibitor of ADP-induced platelet aggregation in the first experiments on an aggregometer by Gustav Born<sup>326-328</sup>. As shown in **Figure 26a**, AMP (10 $\mu$ M) was tested alongside the potent P2Y<sub>12</sub> antagonist AR-C66096 (10 $\mu$ M) as a positive control, and a ‘decoy’ compound, cAMP (10 $\mu$ M), which is structurally related to AMP but has no known effects on platelet aggregation when applied extracellularly. Following incubation (30 minutes, RT), platelets were activated with ADP (3 $\mu$ M).

The % inhibition was determined from % aggregation values using the following equation:  $v \times \chi = d \times 100$ , where  $v$  = maximal % aggregation obtained for vehicle,  $d$  = maximal % aggregation obtained for drug. Once  $\chi$  was obtained, subtracting it from 100% determined the % inhibition for the drug. As expected, AR-C66096 achieved the greatest inhibition of aggregation (95.06%), where its mean % aggregation was significantly different (\*\*\*\*  $p \leq 0.0001$ ) compared to vehicle. This was followed by AMP (30.6% inhibition), which also achieved a significantly different mean % aggregation value (\*\*  $p \leq 0.01$ ) compared to vehicle. The mean % aggregation value obtained in the presence of cAMP was not significantly different ( $p > 0.05$ ) compared to vehicle.

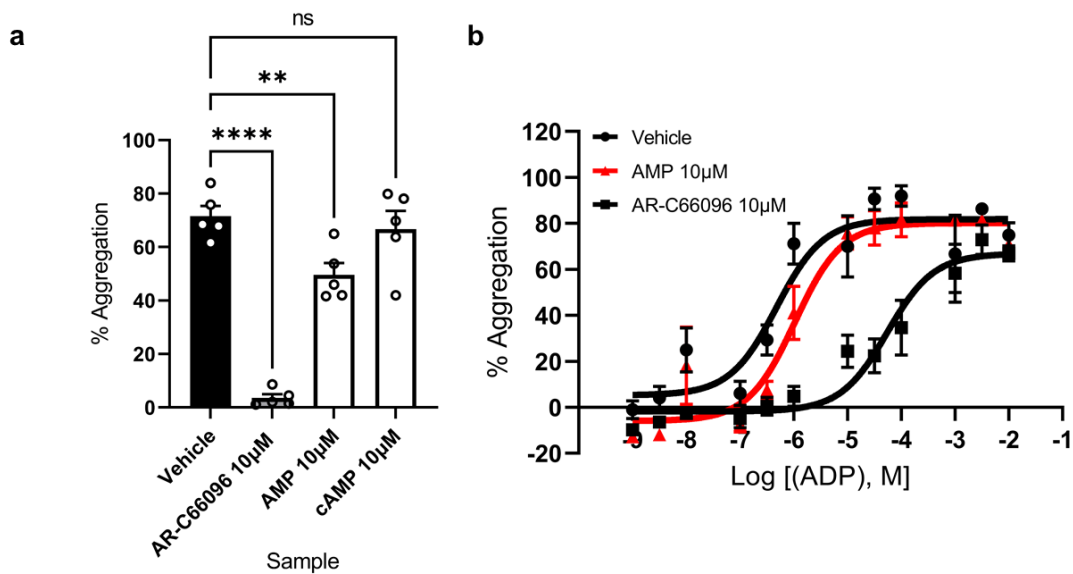


**Figure 26: Validation of the aggregometry assay using the weak inhibitor of platelet aggregation, AMP. a)** Platelets were incubated with vehicle, the positive control AR-C66096 (10µM), AMP (10µM), or cAMP (10µM). Agonist, ADP (3µM) was used for platelet activation. \*\*\*\*  $p \leq 0.0001$ , \*\*  $p \leq 0.01$ , ns: not significant, compared to vehicle (mean  $\pm$  SEM;  $n = 5$  independent blood donors). **b)** Platelets were incubated with vehicle, AMP (10µM), or AR-C66096 (10µM). ADP (varying concentrations) was used for platelet stimulation (mean  $\pm$  SEM;  $n = 6$  independent blood donors).

Platelets were then incubated with AMP (10 $\mu$ M) or AR-C66096 (10 $\mu$ M) and activated with twelve concentrations of ADP using blood from another set of donors (**Figure 26b**). The concentration-response curves obtained showed that AMP and AR-C66096 appeared to act in a competitive manner to ADP (ADP + vehicle  $E_{max}$ : 81.9%, ADP + AMP  $E_{max}$ : 80.2%, ADP + AR-C66096  $E_{max}$ : 66.9%). At the maximum concentration of ADP used (10mM), the drugs achieved comparable mean % aggregation to vehicle (74.9  $\pm$  5.42%), with AMP achieving 70.9  $\pm$  3.94% aggregation and AR-C66096 achieving 67.01  $\pm$  3.29% aggregation. The ADP + vehicle curve obtained a LogEC<sub>50</sub> of -6.32, whereas in the presence of AR-C66096, the concentration-response curve shifted to the right (LogEC<sub>50</sub>: -4.26). In the presence of AMP, the ADP concentration-curve shifted slightly to the right (LogEC<sub>50</sub>: -5.98), exhibiting the greatest inhibition of aggregation at 1 $\mu$ M. Schild analysis was performed, where AR-C66096 obtained a  $K_D$  of 8.83  $\times$  10<sup>-8</sup> M (88.3nM), and AMP obtained a  $K_D$  of 8.42  $\times$  10<sup>-6</sup> M (8.42 $\mu$ M).

An extra-sum-of-squares F test was performed, where the null hypothesis (one curve adequately fits the vehicle and AMP data sets) was rejected, thus the AMP curve was significantly different from vehicle control ( $p < 0.0001$ ). This comparison of fits indicated that AMP is a model of weak antagonism. These experiments do not indicate whether AMP is antagonising P2Y<sub>1</sub> or P2Y<sub>12</sub>, as either would inhibit platelet aggregation. Although 2-methylthio-AMP (2MeSAMP) has been shown to be an antagonist at P2Y<sub>12</sub>, there has not yet been any evidence of this for AMP<sup>329</sup>. However, the aim of these experiments was to simply use AMP as a tool to validate the aggregometry assay, given its known weak inhibitory effects on aggregation.

Together, the data validates that our assay is reporting platelet aggregation: ADP triggers aggregation in a P2Y<sub>1</sub>-, P2Y<sub>12</sub> and  $\alpha_{IIb}\beta_3$ -dependent manner that can be inhibited by agents that increase intracellular cAMP.

### 3.3. Cangrelor may act in a non-competitive manner to ADP

The work in this section was performed to further understand the mode of antagonism shown by cangrelor with the endogenous P2Y<sub>12</sub> agonist, ADP. The following experiments suggested that cangrelor may act in a non-competitive manner to ADP. As shown in **Figure 27a**, cangrelor (10 $\mu$ M) was tested with varying concentrations of ADP. The following E<sub>max</sub> values were obtained for ADP: (ADP + vehicle E<sub>max</sub>: 83.8% aggregation), (ADP + cangrelor E<sub>max</sub>: 40.9% aggregation). In the presence of vehicle, 10mM ADP achieved 75.5  $\pm$  3.18% mean aggregation, and in the presence of cangrelor (10 $\mu$ M), 10mM ADP achieved 24.4  $\pm$  4.90% mean aggregation. At this concentration of ADP, cangrelor (10 $\mu$ M) caused 67.8% inhibition of platelet aggregation. Thus, a very high concentration of ADP (10mM) could not overcome cangrelor's (10 $\mu$ M) inhibitory effects, which may indicate insurmountable antagonism.

Subsequently, lower concentrations of cangrelor were incubated with PRP (30 minutes, RT) from the blood of another set of donors (**Figure 27b**). Platelets were then activated with the highest concentration of ADP possible within the experimental limits (10mM). In comparison to vehicle, every concentration of cangrelor tested caused inhibition of platelet aggregation. There was a distinct pattern of increased inhibition as higher concentrations of cangrelor were used. ADP (10mM) could not overcome the inhibitory effects of cangrelor at any of these concentrations, despite being 10,000-200,000-fold greater than the concentration of cangrelor.

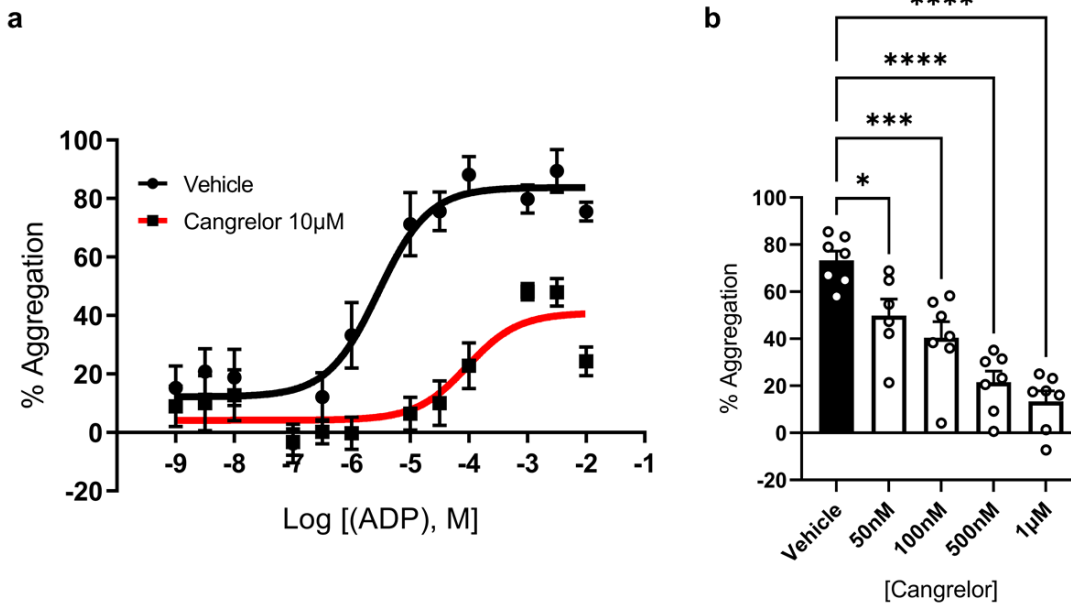


**Figure 27: Cangrelor may act in a non-competitive manner to ADP. a)** PRP was incubated with cangrelor (10 μM), and platelets were then activated with varying concentrations of ADP (mean ± SEM,  $n = 5$  independent blood donors). **b)** PRP was incubated with varying concentrations of cangrelor, and platelets were then activated with 10 μM ADP. Statistical analysis was performed using the one-way ANOVA and Dunnett's post-hoc test (50nM: \*  $p \leq 0.05$ , 100nM: \*\*\*  $p \leq 0.001$ , 500nM and 1 μM: \*\*\*\*  $p \leq 0.0001$ ); mean ± SEM,  $n = 7$  independent blood donors.

The cangrelor analogue, AR-C66096 (10 $\mu$ M), which had already been shown to display competitive antagonism with (up to 10mM) ADP in the validation experiments (**Figure 26b**), was tested again with another set of blood donors. AR-C66096 (10 $\mu$ M) was incubated with PRP (30 minutes, RT), and platelets were then stimulated with varying concentrations of ADP (**Figure 28a**). AR-C66096 acted in a competitive manner to ADP (ADP + vehicle  $E_{max}$ : 86.5%, ADP + AR-C66096  $E_{max}$ : 73.5%), with a rightward shift in the ADP + AR-C66096 concentration response curve. In the presence of AR-C66096, a LogEC<sub>50</sub> of -4.14 was obtained for ADP, compared to the ADP + vehicle curve LogEC<sub>50</sub> of -5.99. For AR-C66096, a K<sub>D</sub> value of 1.43 x 10<sup>-7</sup> M (143nM) was determined. At 3mM ADP, in the presence of vehicle a mean % aggregation value of 84.6  $\pm$  3.52 % was obtained, and in the presence of AR-C66096 a mean % aggregation value of 74.3  $\pm$  5.50% was obtained. ADP (3mM) could overcome AR-C66096's (10 $\mu$ M) inhibitory effects, further indicating surmountable antagonism.

Additionally, varying concentrations of AR-C66096 were incubated (30 minutes, RT) with PRP from another set of donors (**Figure 28b**). Platelets were then stimulated with 10mM ADP, as before. In comparison to vehicle, the inhibition caused by AR-C66096 was not statistically significant at any of the concentrations tested ( $p > 0.05$ ). This is not to say that AR-C66096 is not an effective antagonist, but that its inhibitory effects could be overcome using a very high concentration of agonist (10mM ADP), which is indicative of surmountable antagonism.

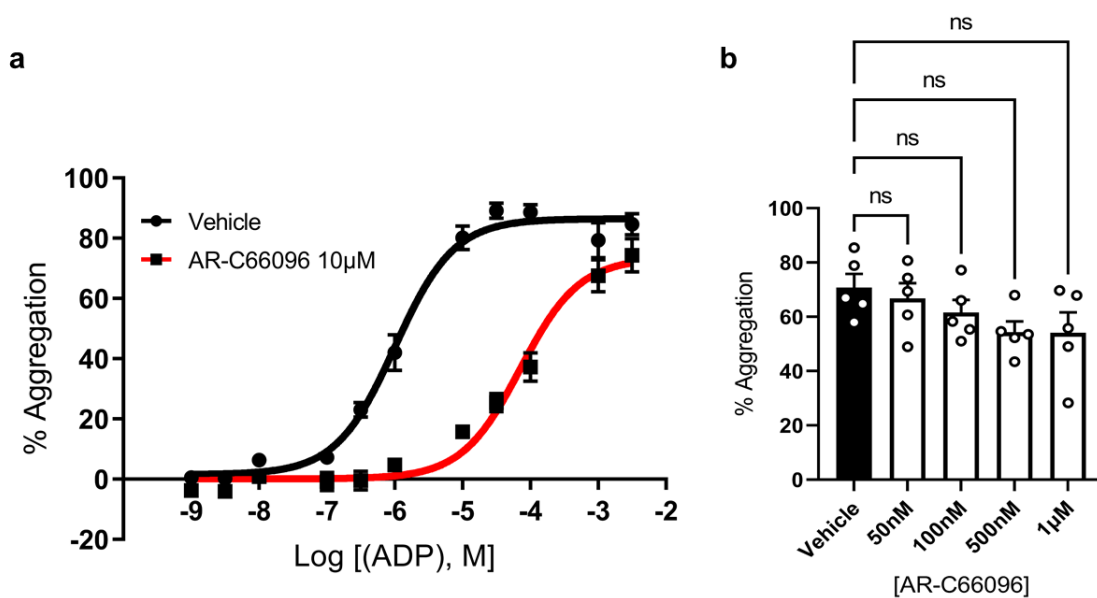


**Figure 28: AR-C66096 acts in a competitive manner to ADP.** **a)** PRP was incubated with AR-C66096 (10µM), and platelets were then activated with varying concentrations of ADP (mean ± SEM,  $n = 5$  independent blood donors). **b)** PRP was incubated with varying concentrations of AR-C66096, and platelets were then activated with 10mM ADP. Statistical analysis was performed using the one-way ANOVA and Dunnett's post-hoc test (ns: not significant;  $p > 0.05$ ); mean ± SEM,  $n = 5$  independent blood donors.

### 3.4. Cangrelor and AR-C66096 act in a competitive manner to 2MeSADP

PRP was then incubated with either cangrelor (10 $\mu$ M) or AR-C66096 (10 $\mu$ M), and platelets were activated with varying concentrations of the more potent P2Y<sub>12</sub> agonist, 2MeSADP. As shown in **Figure 29**, the 2MeSADP + vehicle concentration-response curve achieved a LogEC<sub>50</sub> of -6.99, and cangrelor produced a rightward shift of the curve, with a LogEC<sub>50</sub> of -4.93. In the presence of vehicle, 2MeSADP achieved an E<sub>max</sub> value of 78.3%, and in the presence of cangrelor, it achieved an E<sub>max</sub> value of 68.4%. Within the limits of the experiment, 2MeSADP could not be tested beyond 100 $\mu$ M. However, this would have been useful to gain a more accurate picture of the E<sub>max</sub> that could be achieved by 2MeSADP in the presence of cangrelor. Due to this limitation, Schild analysis was not performed on this set of data.

As shown in **Figure 30**, the 2MeSADP + vehicle concentration-response curve achieved a LogEC<sub>50</sub> of -7.33, and AR-C66096 produced a rightward shift of the curve, with a LogEC<sub>50</sub> of -5.83. In the presence of vehicle, 2MeSADP achieved an E<sub>max</sub> value of 78.5% aggregation, and in the presence of AR-C66096 achieved an E<sub>max</sub> value of 75.4% aggregation. At 100 $\mu$ M 2MeSADP, in the presence of vehicle a mean % aggregation value of 85.2  $\pm$  4.90 % was obtained, and in the presence of AR-C66096 a mean % aggregation value of 75.1  $\pm$  6.24% was obtained. Schild analysis revealed a K<sub>D</sub> value of 3.26 x 10<sup>-7</sup> M (326nM) for AR-C66096.

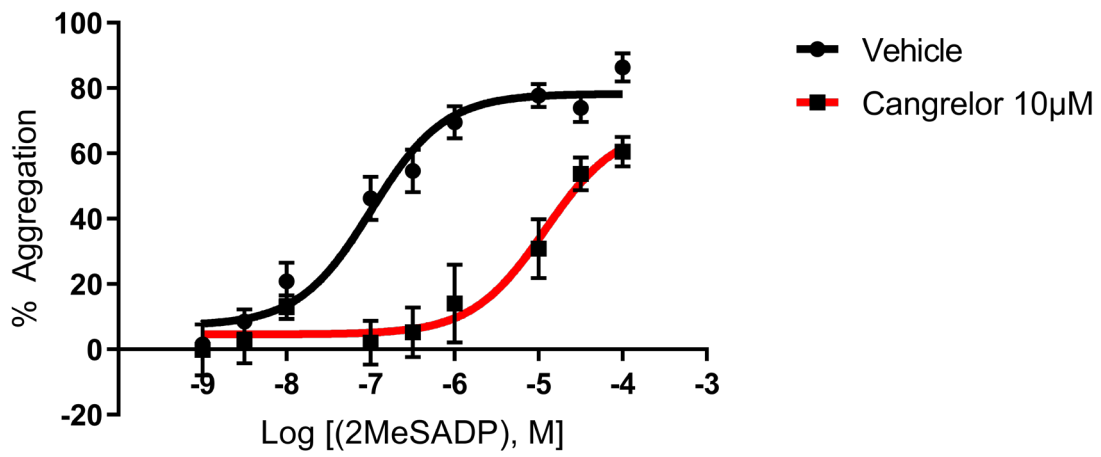


**Figure 29: Cangrelor acts in a competitive manner to 2MeSADP.** PRP was incubated with cangrelor (10µM) for 30 minutes (RT), and platelets were then activated with varying concentrations of the P2Y<sub>12</sub> agonist, 2MeSADP (mean ± SEM; *n* = 6 independent blood donors).

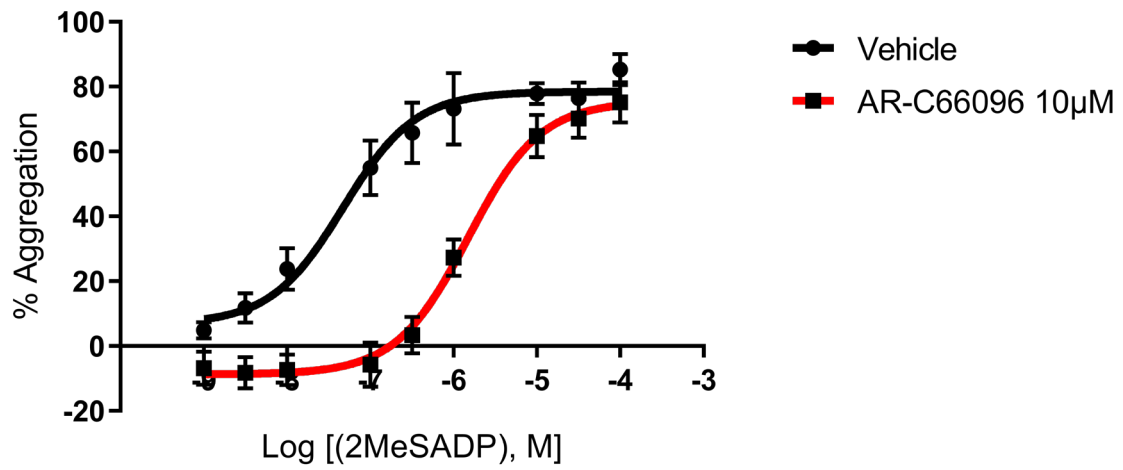


**Figure 30: AR-C66096 acts in a competitive manner to 2MeSADP.** PRP was incubated with AR-C66096 (10µM) for 30 minutes (RT), and platelets were then activated with varying concentrations of the P2Y<sub>12</sub> agonist, 2MeSADP (mean ± SEM; *n* = 6 independent blood donors).

### 3.5. Cangrelor (10nM) acts in a competitive manner to ADP

In previous experiments (**Figure 27**), high concentrations of ADP (up to 10mM) were unable to overcome the effects of cangrelor at nanomolar (50nM) concentrations. To find out if this could still be observed at an even lower concentration, PRP was incubated with 10nM of cangrelor or AR-C66096 and activated using varying concentrations of ADP. As shown in **Figure 31**, cangrelor and AR-C66096 acted in a competitive manner to ADP (ADP + vehicle  $E_{max}$ : 68.4%, ADP + cangrelor  $E_{max}$ : 68.0%, ADP + AR-C66096  $E_{max}$ : 65.3%). An extra-sum-of-squares F test was performed, where the null hypothesis (one curve adequately fits the vehicle and antagonist data sets) was rejected, thus the antagonist curves were significantly different from vehicle control ( $p \leq 0.05$ ). Furthermore, the following  $LogEC_{50}$ s were obtained: ADP + vehicle  $LogEC_{50}$ : -6.59, ADP + cangrelor  $LogEC_{50}$ : -6.16, ADP + AR-C66096  $LogEC_{50}$ : -6.16. Schild analysis revealed the  $K_D$  values to be  $5.75 \times 10^{-9}$  M (5.75nM) and  $5.83 \times 10^{-9}$  M (5.83nM) for cangrelor and AR-C66096, respectively.

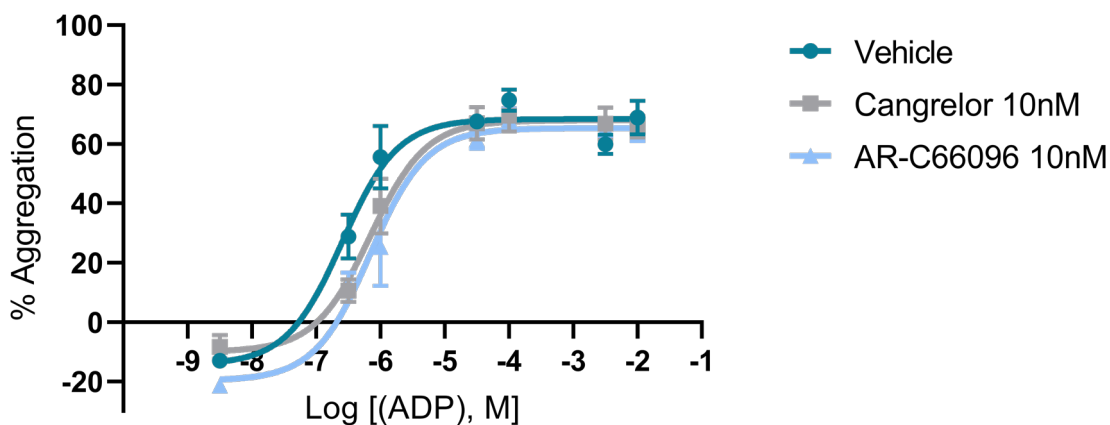


**Figure 31: Cangrelor (10nM) and AR-C66096 (10nM) act in a competitive manner to ADP.** PRP was incubated with vehicle, cangrelor (10nM) or AR-C66096 (10nM) for 30 minutes (RT), and platelets were then activated with varying concentrations of ADP (mean  $\pm$  SEM;  $n = 5$  independent blood donors).

### 3.6. Cangrelor's electrostatic profile reveals a missing field of negative potential compared to AR-C66096

In the search for answers as to why cangrelor may act in a non-competitive manner to ADP, whereas its analogue does not, their structures were analysed. Furthermore, their 3D structures were aligned in Forge (Cresset) software, which was used to perform electrostatic potential comparisons. As shown in **Figure 32a-b**, cangrelor has several differences in its chemical structure when compared to AR-C66096, namely its (methylthio)ethyl group and its trifluoropropyl group. These major group differences exist in the region of the adenosine moiety. It was here where AR-C66096 was found to possess a field of negative electrostatic potential, which was not present in cangrelor (**Figure 32c-d**). Conversely, as shown in **Figure 32e-f**, there did not appear to be any major differences in positive electrostatic potential between cangrelor and AR-C66096. The difference in negative electrostatic potential between cangrelor and AR-C66096 may be important in governing their possible different modes of antagonism with ADP. The significance of this difference in electrostatic potential is not yet known, but may be further understood as more information is gathered about the compounds' mode of action.

Molecular docking was also performed to predict the binding modes of the antagonists at P2Y<sub>12</sub>. The agonist-bound (nucleotide-bound) structure's usefulness is limited in this case because blind (unbiased) docking cannot be performed with this structure. This is because the 2MeSADP binding pocket is confined to a buried region, which is incompatible with blind docking. It is also small sub-cavity, with little room to be considered as 'search space' to dock ligands, therefore cangrelor's potential as a non-competitive binder cannot be explored. Furthermore, even though this structure is ideal for docking nucleotide-based ligands, there are questions as to how this closed 'lid' conformation (model for P2Y<sub>12</sub> agonism) is useful for exploring nucleotide-based

antagonist binding, where an open 'lid' would supposedly be expected<sup>16,17</sup>. Focused docking, where the coordinates for docking are specified, did not help to explore the *in vitro* results because all the ligands are simply docked in the same location.

The antagonist (non-nucleotide) bound structure is composed of two pockets which are clearly distinguished. Although this structure has a large extracellular pocket which is suitable for blind docking, it is not ideal for docking the nucleotide-based ligands. This is because the receptor is in a conformation that is stabilised by a non-nucleotide antagonist. However, it is still the most useful structure for distinguishing between the reversible antagonist binding pocket and the second pocket where the covalent antagonists are predicted to bind. When blindly docked against this structure, cangrelor obtained variable and inconsistent poses, including docking against a pocket in an intracellular region (which was also the case for 2MeSADP). This is not possible, as cangrelor is too polar to cross the cell membrane to reach this site. Therefore, due to their lack of usefulness, the molecular docking results are not shown here.

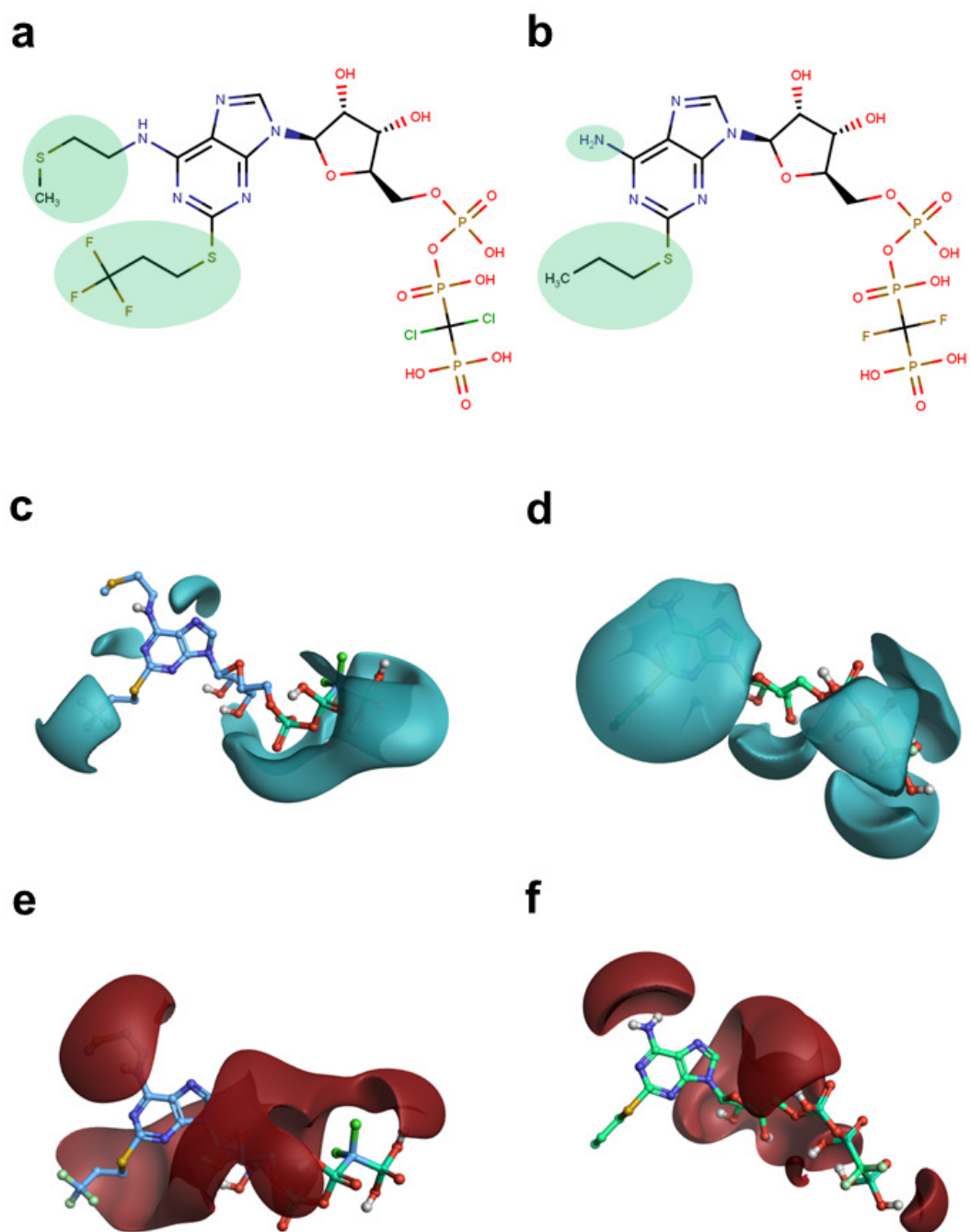


**Figure 32: The structures and electrostatic potential field comparisons of cangrelor and AR-C66096.** **a)** 2D structure of cangrelor, drawn in MarvinSketch (ChemAxon). **b)** 2D structure of AR-C66096, drawn in MarvinSketch (ChemAxon). Highlighted in green are major group differences between the two structures. **c)** 3D structure of cangrelor (energy-minimised in Open Babel using the MMFF94) with regions of negative electrostatic potential shown in cyan (analysis performed using Forge (Cresset) software). **d)** 3D structure of AR-C66096 with regions of negative electrostatic potential shown in cyan. **e)** 3D structure of cangrelor with regions of positive electrostatic potential shown in red. **f)** 3D structure of AR-C66096 with regions of positive electrostatic potential shown in red.

### 3.7. Establishing an assay of P2Y<sub>12</sub> activity

#### 3.7.1. The LANCE cAMP assay is not compatible with P2Y<sub>12</sub>

In the next stage, an assay was sought after which could assess the effect of ligands on P2Y<sub>12</sub> activity. The LANCE cAMP assay (Perkin Elmer) detects accumulation of the second messenger, cAMP, inhibition of which is a key component of the P2Y<sub>12</sub> pathway. As previously mentioned in the **Materials and methods**, the protocol had to be specially optimised for platelets.

Optimisation of cell number was a necessary starting point for the assay. During initial trials, platelets were tested in different numbers in a 384-well plate to determine the optimal number of platelets required (per well) for the assay. Forskolin was used to stimulate adenylyl cyclase and bring cAMP production to detectable levels, where the decrease in cAMP could then be assessed upon P2Y<sub>12</sub> activation. The stimulation of platelets with forskolin maximises cAMP production and gives the maximal range of cAMP production.

As shown in **Figure 33a**, the dynamic range of the assay was assessed using a cAMP standard curve. It was found that 9,000 platelets per well was the most optimal number for the forskolin concentration-response curve to cover the linear region of the cAMP standard curve and showed the largest signalling window. Due to normalisation to forskolin values, the lower end of the cAMP standard curve fell within a negative % response range. This indicated that the baseline response from the platelets is quite high, but still within the appropriate range of detection. In additional data analysis, the forskolin concentration-response curve was normalised to the cAMP standard curve to show the % cAMP response (**Figure 33b**). The aim of creating the forskolin concentration-response curve was to find the single optimal concentration of forskolin (EC<sub>80</sub>: 80% of the E<sub>max</sub>) that could be used to stimulate platelets in future experiments.

It was found from this data that the optimal forskolin concentration for 9,000 platelets per well was  $1 \times 10^{-5}$  M ( $10\mu\text{M}$ ).

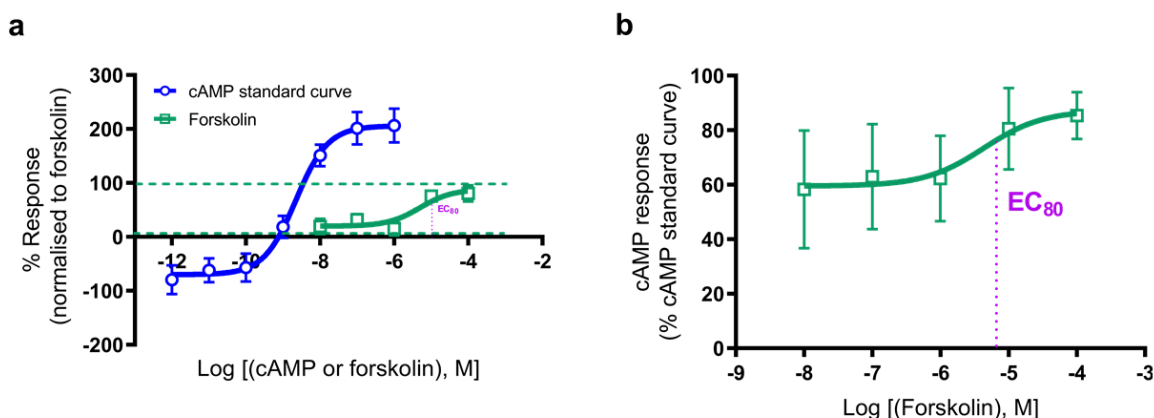


**Figure 33: Finding the optimal concentration ( $EC_{80}$ ) of forskolin to stimulate adenylyl cyclase in platelets. a)** The cAMP standard curve is shown in blue (no platelets), and the forskolin concentration-response curve (with platelets) is shown in green. The linear region of the cAMP standard curve is shown by green dashed lines, which was achieved using 9,000 platelets per well of the 384-well plate. The  $EC_{80}$  (labelled in purple) of forskolin for 9,000 platelets per well was  $1 \times 10^{-5}$  M ( $10\mu\text{M}$ ). As mentioned in the methods, IBMX was present in the stimulation buffer to achieve this response. Data is normalised to forskolin values. **b)** The cAMP response was found by interpolating the forskolin response to the standard curve (% cAMP standard curve). Data is shown as mean  $\pm$  SEM,  $n = 5$  independent blood donors.

Upon testing the  $P2Y_{12}$  agonists, ADP or 2MeSADP, inaccurate concentration-response curves were obtained (not shown), where the agonists seemingly caused an increase in cAMP production. The agonists should in fact cause a decrease in cAMP production, as  $P2Y_{12}$  is  $G_i$ -coupled. It was then found that the anti-cAMP antibody was binding to ADP and 2MeSADP, as if they were cAMP. This is because ADP and 2MeSADP have very similar structures to cAMP. It can be seen in **Figure 34** that when ADP and 2MeSADP were tested against the anti-cAMP antibody (with no platelets), they were picked up as cAMP at concentrations of  $1 \times 10^{-6}$  M ( $1\mu\text{M}$ ) to  $1 \times 10^{-4}$  M

(100 $\mu$ M), with ADP being picked up to a higher extent. The LANCE signal decreased at these concentrations, which usually occurs in the presence of excess cAMP.

However, neither was picked up as cAMP in the lower nanomolar range. An ADP concentration-response curve could adequately be constructed in this range using the kit; however, this small window of opportunity would be unlikely to provide useful information on test compounds. cAMP, ADP, and 2MeSADP, all possess a sugar backbone, and an adenine, and this similarity in structure was likely to cause the anti-cAMP antibody to cross-react with ADP and 2MeSADP. Importantly, although this cAMP kit is not fully compatible with P2Y<sub>12</sub>, the successfully optimised platelet protocol described here can still be used if testing cAMP levels from another receptor system in platelets (e.g., a G<sub>s</sub>-coupled pathway), where the agonist is not structurally similar to cAMP.

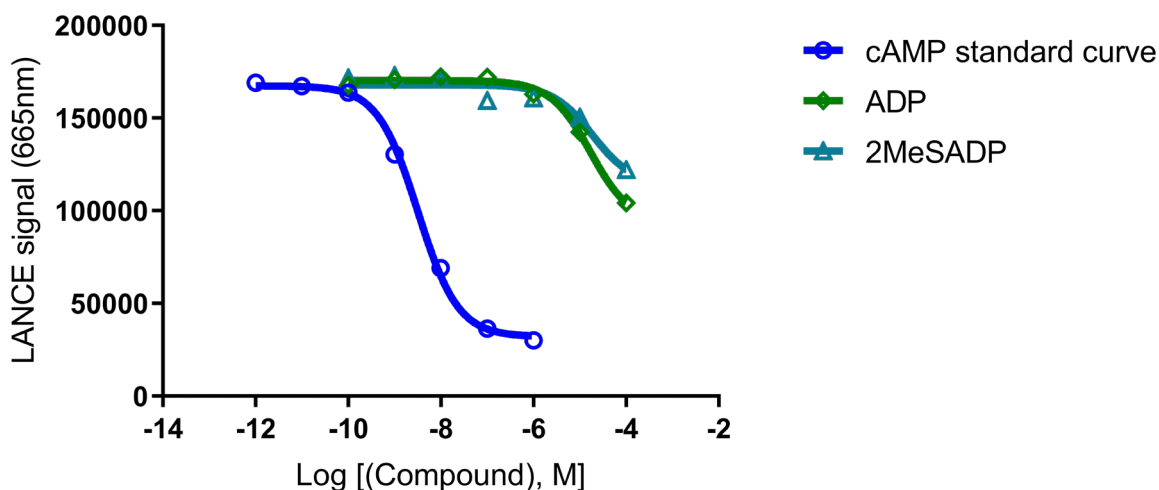


**Figure 34: P2Y<sub>12</sub> agonists, ADP and 2MeSADP, are picked up as cAMP by the anti-cAMP antibody.** The cAMP standard curve is shown in dark blue, the ADP concentration response curve is shown in green, and the 2MeSADP concentration-response curve is shown in teal. These experiments were conducted in the absence of platelets. The LANCE signal denotes Alexa Fluor 647 fluorescence measured at 665nm. The experiment was repeated 5 times.

### 3.7.2. Setting up a multiplexed VASP phosphorylation assay for platelets

Subsequently, to assess the effect of ligands on P2Y<sub>12</sub> activity, a multiplexed VASP phosphorylation (pVASP) assay was developed. pVASP is a read-out of cAMP signalling, and a highly specific biomarker of P2Y<sub>12</sub> activity<sup>330</sup>. Upon P2Y<sub>12</sub> activation, the G<sub>i</sub> signalling pathway results in an inhibition of adenylyl cyclase, a decrease in cAMP levels (which leads to a reduction in PKA activity), and PKA cannot phosphorylate VASP at serine 157. Thus, unphosphorylated VASP correlates with P2Y<sub>12</sub> agonism, and increased phosphorylated VASP correlates with P2Y<sub>12</sub> antagonism. PRP or washed platelets (1 x 10<sup>8</sup> platelets/mL) were used for this assay. As a platelet pellet was formed, the size and complexity of the washed platelets (**Figure 35**) were more homogenous than in the PRP preparation.

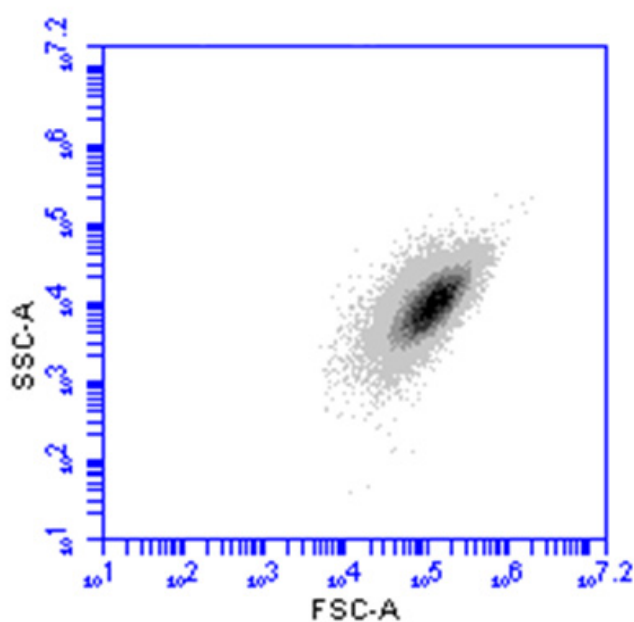


**Figure 35: Representative forward scatter-area (FSC-A) vs. side scatter-area (SSC-A) plot for washed platelets.** A dense region (black) shows the main platelet population, with the shadow (grey) being representative of platelets of varying size and complexity. The values on the x and y scales are arbitrary. The washed platelets were diluted to a concentration of 1 x 10<sup>8</sup> platelets/mL using HBS.

As shown in **Figure 36**, validation of the phospho-VASP (serine 157) rabbit monoclonal primary antibody and the anti-rabbit IgG (H+L), F(ab')<sub>2</sub> fragment, Alexa Fluor 647 conjugate secondary antibody were performed. Initially, PRP was incubated with PGE<sub>1</sub> at a concentration of 1 μM to stimulate adenylyl cyclase, bringing cAMP and, hence, pVASP above baseline to detectable levels.

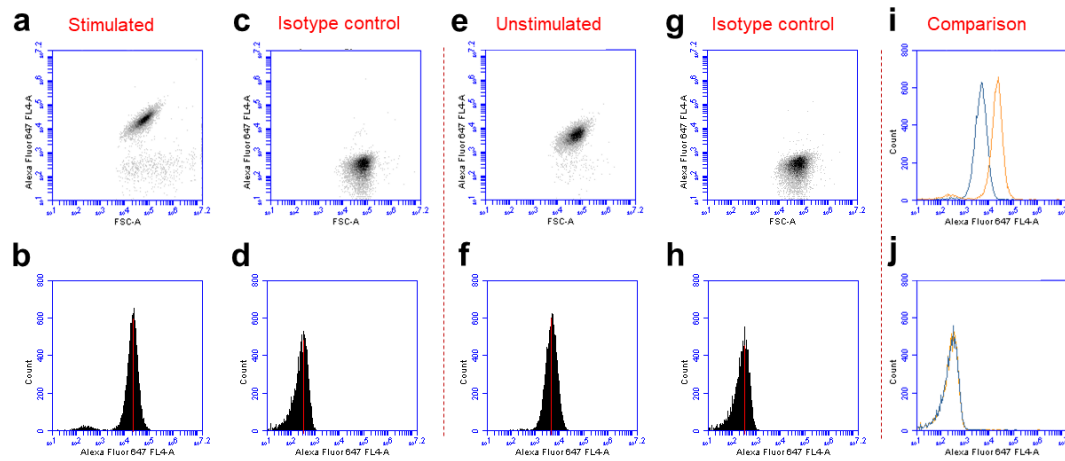


**Figure 36: Validation of phospho-VASP (serine 157) rabbit monoclonal primary antibody and anti-rabbit IgG (H+L), F(ab')<sub>2</sub> fragment, Alexa Fluor 647 conjugate.**

Alexa Fluor 647 fluorescence (measured on fluorescence channel 4, FL4) denotes pVASP signal. Throughout this figure, 10,000 events collected. **(a)** Shows forward scatter-area (FSC-A) vs. Alexa Fluor 647 fluorescence for the stimulated sample (obtained by incubating PRP with PGE<sub>1</sub> (1 μM) for 10 minutes (RT)). **(b)** Shows Alexa Fluor 647 fluorescence vs. count for the stimulated sample. **(c-d)** Isotype control (rabbit monoclonal antibody IgG XP isotype control) for the stimulated sample. **(e-f)** Alexa Fluor 647 fluorescence denoting pVASP signal obtained for the unstimulated sample (using PRP). **(g-h)** Isotype control for the unstimulated sample. **(i)** Comparison of spectra for unstimulated sample (blue) and stimulated sample (orange). **(j)** Comparison of spectra for isotype controls (unstimulated sample: blue, stimulated sample: orange).

Alexa 647 fluorescence was measured in platelets. **Figure 36a-b** showed that the platelet population stimulated with PGE<sub>1</sub> (1 μM) achieved a median fluorescence intensity (MFI) value of 23,400. In **Figure 36c-d**, the primary antibody was replaced

with a rabbit monoclonal antibody IgG isotype control. In this case, the stimulated platelets achieved a median fluorescence intensity (MFI) of 392. This showed that the staining observed in **Figure 36a-b** was, indeed, due to specific antibody binding to VASP's phosphorylated serine 157 and was not a non-specific background signal or artefact.

In contrast to platelets stimulated with PGE<sub>1</sub>, unstimulated platelets (**Figure 36e-f**) achieved an MFI value of 5,220. Thus, PGE<sub>1</sub> treatment caused an approximate 4.48x increase in fluorescence when comparing the MFI values for stimulated and unstimulated platelets. The spectra for stimulated and unstimulated platelets can be compared in **Figure 36i**. As previously, the unstimulated platelets were also tested with an isotype control antibody. An MFI value of 287 was obtained. Isotype controls for the stimulated and unstimulated platelets achieved similar MFI values when compared (**Figure 36j**).

In the next step, a barcoding technique was used to reduce primary antibody consumption. Barcoding involves assigning samples with unique dye signatures. This is so that multiple samples can be pooled into one tube and the original Alexa Fluor 647 MFI values of the individual samples can be deconvoluted according to the barcodes. Different dyes or conjugated antibodies were first tested to find the ideal stains for barcoding. Two dyes with intracellular targets were initially tested. DiOC<sub>6</sub> is a fluorescent, green, lipophilic dye that is used to stain a cell's intracellular membranes (excitation: 484nm, emission: 501nm). This dye was incubated with washed platelets (1 x 10<sup>8</sup> platelets/mL) for 30 minutes (RT) at various concentrations. As shown in **Figure 37a**, the fluorescence spectra for the following samples did not overlap: none, 100nM, 3µM, 30µM. Thus, the dye achieved four barcoding layers.

The next dye tested was the eBioscience fixable viability dye eFluor 520 (excitation: 488nm, emission: 522nm). This dye binds covalently to primary amines inside cells and may also bind to secondary amines. This dye was also incubated with washed platelets ( $1 \times 10^8$  platelets/mL) for 30 minutes (RT) at various concentrations. As shown in **Figure 37b**, the fluorescence spectra for the following samples did not overlap: none, 1:1000, 1:100, 1:12.5. This dye also achieved 4 barcoding layers.

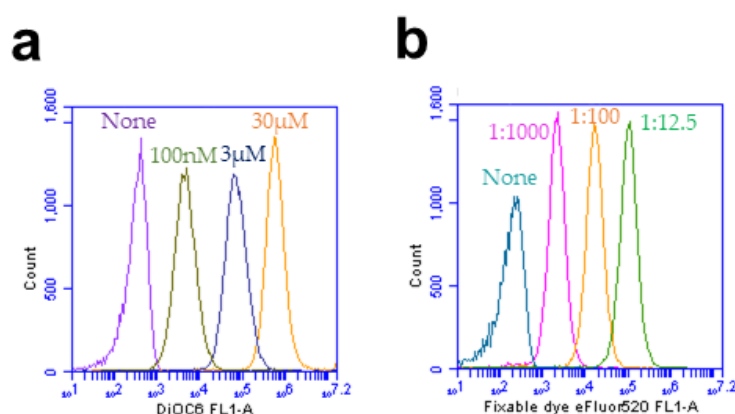


**Figure 37: Testing stains with intracellular targets for barcoding in washed platelets.** a) Barcoding layers achieved with non-covalent binding dye, DiOC<sub>6</sub>, in washed platelets (20,000 events collected). b) Barcoding layers achieved with covalent-binding fixable viability dye, eFluor 520, in washed platelets (20,000 events collected).

Various fluorophore-conjugated antibodies with extracellular targets were also tested with washed platelets ( $1 \times 10^8$  platelets/mL); 30-minute incubation (RT). These included mouse anti-human CD41a monoclonal antibody conjugated to PE-Cy7 (excitation: 488nm, emission: 775nm), mouse anti-human CD42a monoclonal antibody conjugated to FITC (excitation: 488nm, emission: 520nm), and mouse anti-human CD42b monoclonal antibody conjugated to FITC (excitation: 488nm, emission: 520nm). There are no reports in the literature of conjugated antibodies being used as barcoding stains, thus the approach here was novel.

As shown in **Figure 38a**, CD41a conjugated to PE-Cy7 achieved two barcoding layers, with spectra that did not overlap in the following samples: none, 1:50. No further layers were achieved when it was tested at higher concentrations (**Figure 38b**). CD42a conjugated to FITC and CD42b conjugated to FITC also achieved two barcoding layers each (none, 1:20) (**Figure 38c**, **Figure 38e**), and no further layers were achieved at higher concentrations (**Figure 38d**, **Figure 38f**).

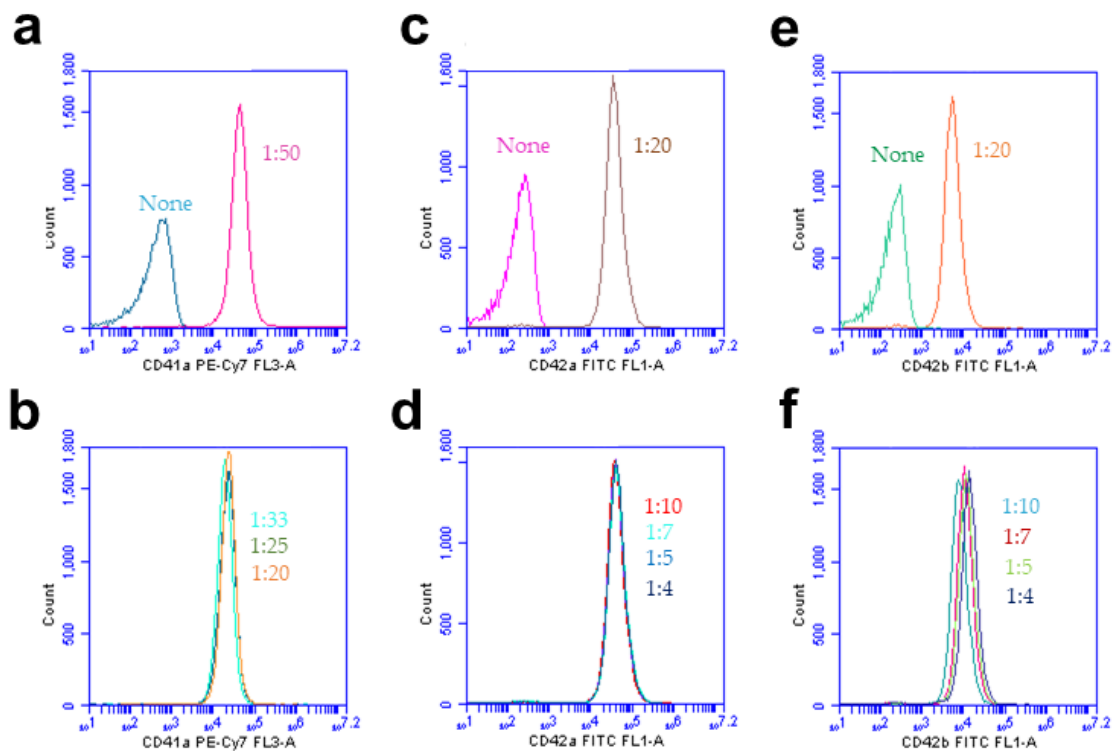


**Figure 38: Testing stains with extracellular targets for barcoding in washed platelets.** **a)** Barcoding layers achieved with mouse anti-human CD41a monoclonal antibody (clone: HIP8) conjugated to phycoerythrin-cyanine 7 (PE-Cy7) (20,000 events collected). **b)** Higher concentrations of (a) were tested to explore whether further layers could be achieved. **c)** Barcoding layers achieved with mouse anti-human CD42a monoclonal antibody conjugated to fluorescein isothiocyanate (FITC) (20,000 events collected). **d)** Higher concentrations of (c) were tested to explore whether further layers could be achieved. **e)** Barcoding layers achieved for mouse anti-human CD42b monoclonal antibody conjugated to FITC (20,000 events collected). **f)** Higher concentrations of (e) were tested to explore whether further layers could be achieved.

As summarised in **Figure 39**, dyes with intracellular targets achieved a maximum of four barcoding layers, and fluorophore-conjugated antibodies with extracellular targets achieved a maximum of two barcoding layers. For further guidance on barcoding, the **Decision box flow chart for barcoding** in the **Appendix** may be referred to.

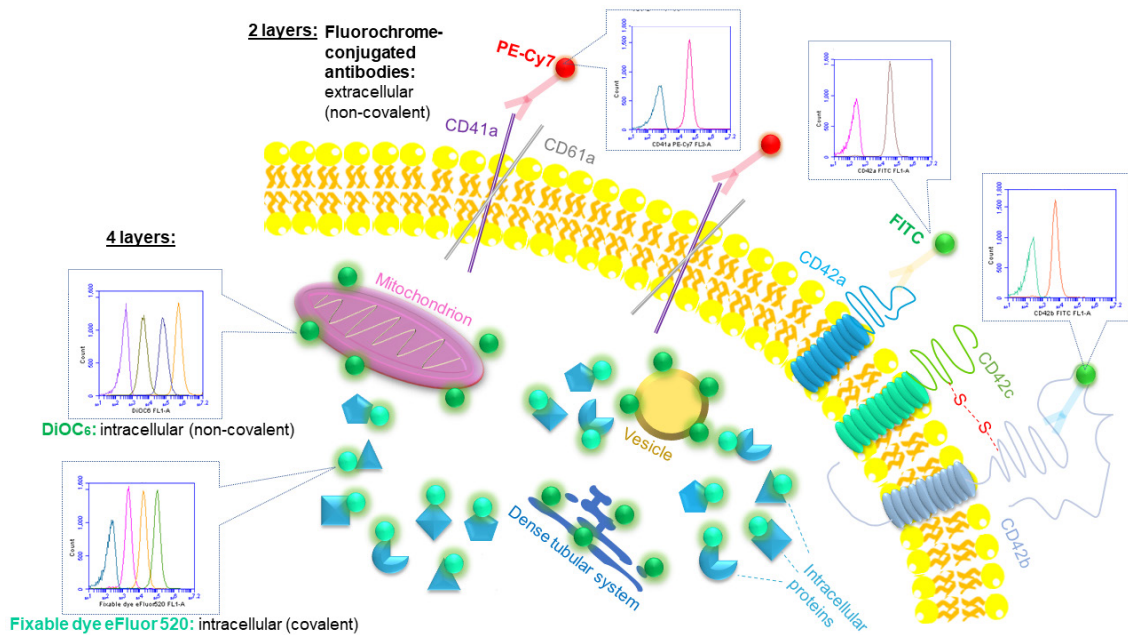


**Figure 39: A schematic diagram summarising the barcoding layers achieved for each stain, with the target location and binding type specified.** Fluorochrome-conjugated antibodies with extracellular targets achieved two layers with no overlap (binding through non-covalent interactions). Pure dyes (DiOC<sub>6</sub>: non-covalent binding; Fixable viability dye eFluor 520: covalent binding) with intracellular targets achieved four layers with no overlap. In general, dyes with intracellular targets achieved more layers. The results shown were obtained using washed platelets ( $1 \times 10^8$  platelets/mL).

Upon testing the barcodes with the full pVASP protocol, the DiOC<sub>6</sub> barcodes were lost and did not survive pooling in PRP or washed platelets (**Figure 40**). This is likely because DiOC<sub>6</sub> is a non-covalent binding dye, and the strength of binding cannot withstand the multiple wash and spin steps within the protocol.

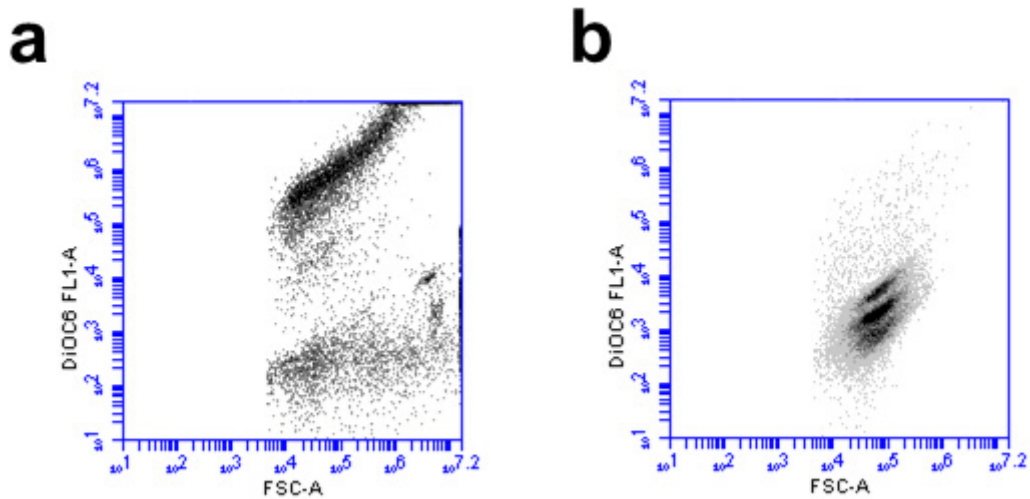


**Figure 40: Non-covalent binding dye, DiOC<sub>6</sub>, barcodes were lost and did not survive pooling in PRP or washed platelets.** The results obtained were ambiguous and the four expected barcodes were not observed. **a)** Plot shown for the experiment conducted using PRP. **b)** Plot shown for the experiment conducted using washed platelets. The plots were obtained using the BD Accuri C6 software.

Conversely, the four barcodes for the covalent-binding fixable viability dye, eFluor 520, were retained upon testing the barcodes with the full pVASP protocol (**Figure 41**). Likewise, the two barcodes for CD41a conjugated to PE-Cy7 were also retained (**Figure 42**). To test the robustness of the barcoding technique, samples were read using the BD Accuri C6 flow cytometer (**Figure 41a-c, Figure 42a-c**), and the BD FACSCanto II (**Figure 41d-e, Figure 42d-e**). The barcodes appeared as expected using either flow cytometer. The barcodes were also successfully achieved in PRP (not shown). These individual layers could be combined to assign each sample with a unique dye signature or ‘barcode’. Therefore,  $4 \times 2 = 8$  barcodes could be achieved by labelling samples with different concentration combinations of these two dyes. The barcodes could then be deconvoluted to determine the Alexa Fluor 647 fluorescence (representative of pVASP levels) in each sample.

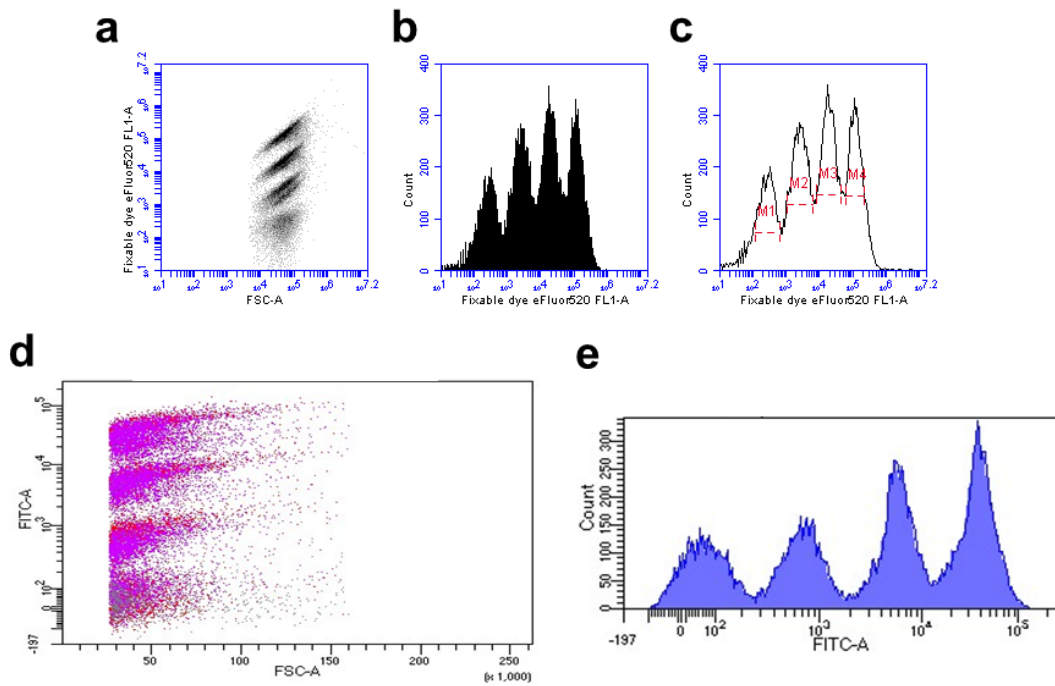


**Figure 41: Barcodes achieved for fixable viability dye eFluor 520.** a-c) Dot plots and spectra showing the four barcodes achieved for fixable viability dye eFluor 520; samples read using the BD Accuri C6 flow cytometer (20,000 events collected); FSC-A: forward scatter-area; FL1: samples were read using the FL1 fluorescence channel. d-e) Four barcodes achieved for fixable viability dye eFluor 520; samples read using the BD FACSCanto II (20,000 events collected); this experiment was performed using blood from a separate donor to that used in a-c. FSC-A: forward scatter-area; FITC-A: samples were read using the FITC fluorescence channel (equivalent of FL1).

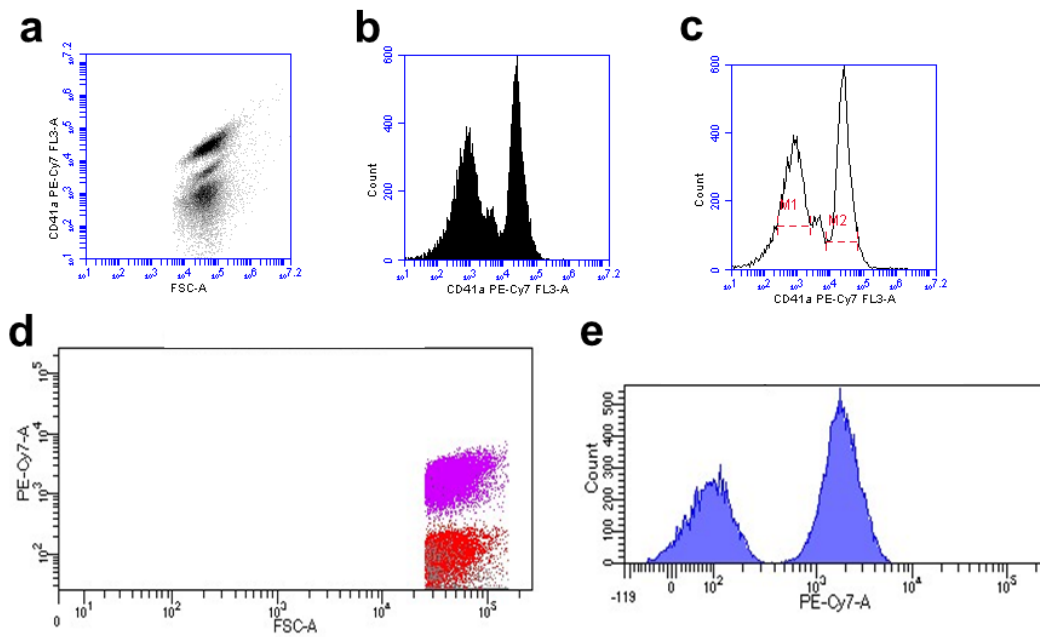


**Figure 42: Barcodes achieved for CD41a monoclonal antibody conjugated to PE-Cy7. a-c)** Dot plots and spectra showing the two barcodes achieved for CD41a conjugated to FITC; samples read using the BD Accuri C6 flow cytometer (20,000 events collected); FSC-A: forward scatter-area; FL3: samples were read using the FL3 fluorescence channel. **d-e)** Two barcodes achieved for CD41a conjugated to FITC; samples read using the BD FACSCanto II (20,000 events collected); this experiment was performed using blood from a separate donor to that used in a-c. FSC-A: forward scatter-area; PE-Cy7-A: samples were read using the PE-Cy7 fluorescence channel (equivalent of FL3).

After the barcodes were set up, a preliminary experiment was performed where various concentrations of PGE<sub>1</sub> were tested with a high concentration of ADP (30μM). As previously mentioned, PGE<sub>1</sub> stimulates adenylyl cyclase through its effects on the G<sub>s</sub>-coupled IP receptor, and the downstream effect is increased pVASP levels. ADP will counteract this effect and decrease pVASP levels through activation of P2Y<sub>12</sub>. The aim of this experiment was to find the single concentration of PGE<sub>1</sub> which gave the largest difference +/- ADP. This concentration of PGE<sub>1</sub> could then be used to stimulate platelets and bring pVASP to detectable levels in all future experiments. The compounds were incubated simultaneously in washed platelets for 10 minutes (RT). As shown in **Figure 43**, 100nM and 1μM PGE<sub>1</sub> were similarly affected by 30μM ADP (as in the % decrease compared to vehicle). A slightly larger window of effect was observed with 100nM PGE<sub>1</sub> (55.4% reduction).

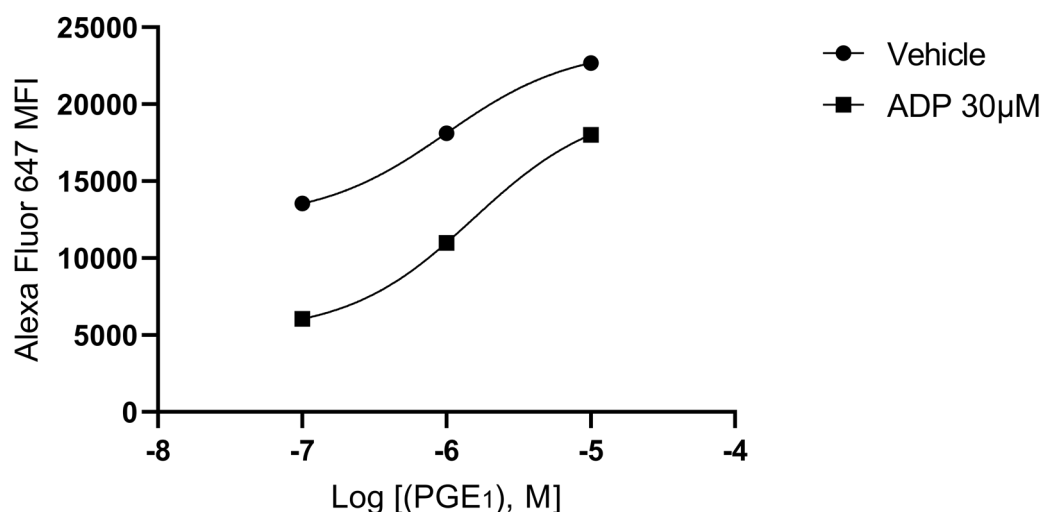


**Figure 43: Testing various concentrations of PGE<sub>1</sub> with 30μM ADP.** Washed platelets (1 x 10<sup>8</sup> platelets/mL) were incubated with various concentrations of PGE<sub>1</sub> in the absence or presence of 30μM ADP. Alexa Fluor 647 fluorescence (MFI: median fluorescence intensity) was measured.

The extent of inhibition of PGE<sub>1</sub>-induced pVASP depends on the concentration of ADP<sup>331</sup>. Platelets were incubated simultaneously with PGE<sub>1</sub> (100nM) and ADP (various concentrations) for 10 minutes (RT) to create a full concentration-response curve for ADP. The effects of varying concentrations of ADP on pVASP have not previously been shown in the literature. As observed in **Figure 44**, the IC<sub>50</sub> of ADP was found to be 1 x 10<sup>-7</sup> M (100nM). Although only one replicate is shown in **Figure 44**, multiple repeats of this result appear as the control (vehicle) data in subsequent figures.

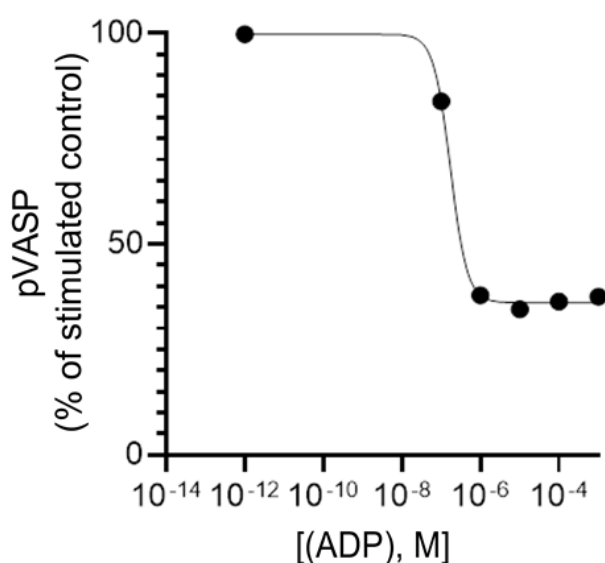


**Figure 44: Testing various concentrations of ADP with 100nM PGE<sub>1</sub>.** Washed platelets (1 x 10<sup>8</sup> platelets/mL) were incubated simultaneously with PGE<sub>1</sub> (100nM) and ADP (various concentrations) for 10 minutes (RT). Percentage of phosphorylated VASP (pVASP) was determined from Alexa Fluor 647 fluorescence values, as a % of the PGE<sub>1</sub>-stimulated control.

### 3.8. pVASP assay shows ADP is unable to overcome the effects of cangrelor (10 $\mu$ M) or AR-C66096 (10 $\mu$ M)

The successfully optimised pVASP assay was used to further explore the modes of action of cangrelor and AR-C66096 (10 $\mu$ M) with varying concentrations of ADP. Washed platelets were first incubated with vehicle, cangrelor (10 $\mu$ M), or AR-C66096 (10 $\mu$ M) for 30 minutes (RT). The platelets were then simultaneously incubated with PGE<sub>1</sub> (100nM) and ADP (varying concentrations) for 10 minutes (RT). Surprisingly, ADP was unable to overcome the effects of either drug (**Figure 45**), even when it was tested at a concentration of 1mM. Cangrelor and AR-C66096 caused pVASP levels to reach maximum (100%) levels. Although the results obtained here for cangrelor were consistent with the possible non-competitive effect observed for this drug in the aggregometry experiments, the results obtained for AR-C66096 were unexpected (see section 3.13. **Discussion**, for further elaboration).

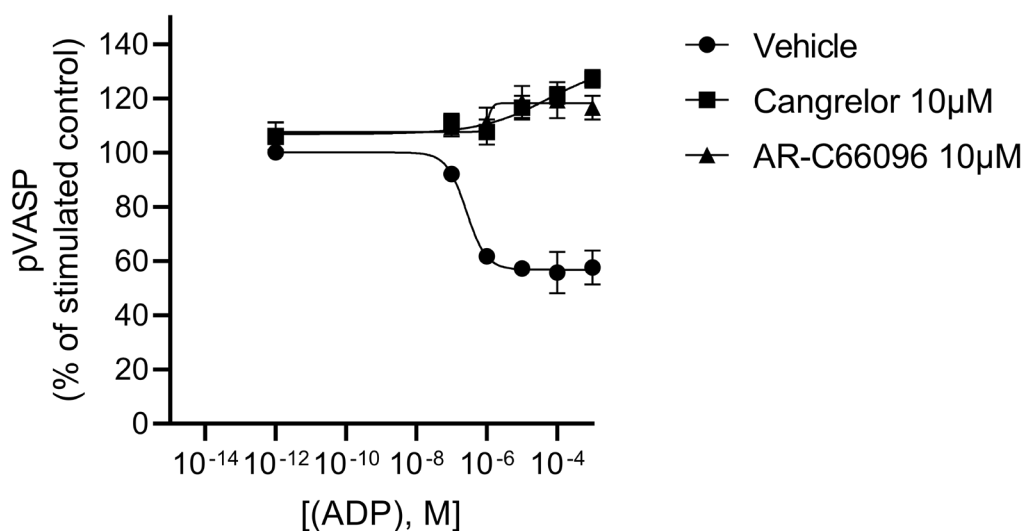


**Figure 45: pVASP assay shows ADP is unable to overcome the effects of cangrelor or AR-C66096 (10 $\mu$ M).** Washed platelets (1 x 10<sup>8</sup> platelets/mL) were incubated with vehicle, cangrelor (10 $\mu$ M), or AR-C66096 (10 $\mu$ M) for 30 minutes (RT), and then simultaneously incubated with PGE<sub>1</sub> (100nM) and varying concentrations of ADP (mean  $\pm$  SEM; *n* = 3 independent blood donors). Phosphorylated VASP (pVASP) levels are shown as a % of stimulated control.

### 3.9. pVASP assay shows ADP is unable to overcome the effects of cangrelor (100nM) but not AR-C66096 (100nM)

In the next set of experiments, cangrelor and AR-C66096 were investigated at lower and more biologically relevant concentrations. Washed platelets ( $1 \times 10^8$  platelets/mL) were incubated with a lower concentration (100nM) of cangrelor or AR-C66096 for 30 minutes (RT). Platelets were then simultaneously incubated with PGE<sub>1</sub> (100nM) and varying concentrations of ADP for 10 minutes (RT). As shown in **Figure 46**, a rightward shift was observed in the ADP + drug groups compared to vehicle, indicating antagonism, as expected. The ADP (up to 1mM) + cangrelor (100nM) E<sub>max</sub> did not reach that of ADP (up to 1mM) + vehicle, whereas AR-C66096 did. At the maximum concentration of ADP tested (1mM), the % pVASP values were as follows: ADP + vehicle ( $68.6 \pm 3.31$ ), ADP + cangrelor ( $90.9 \pm 2.23$ ), and ADP + AR-C66096 ( $59.8 \pm 5.29$ ).

A one-way ANOVA was performed for each data set at this point of 1mM ADP (each drug condition compared to vehicle) to explore if the mean values obtained were significantly different. The ANOVA showed there was a significant difference (\*\*  $p \leq 0.01$ ) amongst the means of the drug treatment groups in comparison to vehicle. A follow-up multiple comparisons test was performed (Dunnett's test), which indicated that the mean % pVASP value obtained for ADP + cangrelor (100nM) was significantly different (\*  $p \leq 0.05$ ) compared to ADP + vehicle. The mean % pVASP value obtained for ADP + AR-C66096 (100nM) was not significantly different compared to ADP + vehicle. These results further indicated that cangrelor may act in a non-competitive manner to ADP on P2Y<sub>12</sub>, and that AR-C66096 acts in a competitive manner to ADP.

Interestingly, in the cangrelor and AR-C66096 samples there was consistently an increase in pVASP (above the 100% threshold set by the stimulated control value) at some ADP concentrations before a decrease was seen. In particular, this effect was

observed at  $1 \times 10^{-5}$  M ( $10\mu\text{M}$ ) and  $1 \times 10^{-4}$  M ( $100\mu\text{M}$ ) ADP. This apparent enhancement of pVASP reflected an increase in cAMP under these conditions. The reasons underlying this observation are unknown.

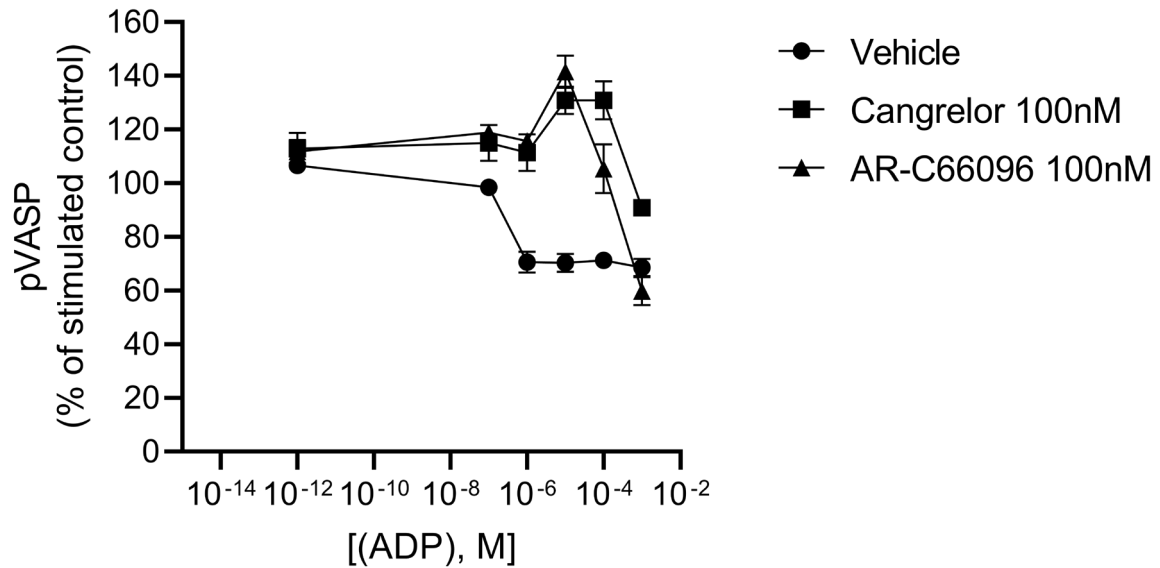


**Figure 46: pVASP assay shows ADP is unable to overcome the effects of cangrelor (100nM), but not AR-C66096 (100nM).** Washed platelets ( $1 \times 10^8$  platelets/mL) were incubated with either vehicle, cangrelor (100nM) or AR-C66096 (100nM) for 30 minutes (RT), and then incubated simultaneously with PGE<sub>1</sub> (100nM) and ADP (varying concentrations) for 10 minutes (RT). Data is shown as mean  $\pm$  SEM;  $n = 3$  independent blood donors). Phosphorylated VASP (pVASP) levels are shown as a % of stimulated control.

### 3.10. pVASP assay shows AR-C66096 (10nM) acts in a competitive manner to ADP

After the antagonists were tested at 100nM, their concentration was reduced further to 10nM to explore whether the possible non-competitive effect of cangrelor could still be seen. Washed platelets ( $1 \times 10^8$  platelets/mL) were incubated with 10nM of cangrelor or AR-C66096 for 30 minutes (RT). Platelets were then simultaneously incubated with PGE<sub>1</sub> (100nM) and varying concentrations of ADP for 10 minutes (RT). As shown in **Figure 47**, AR-C66096 (10nM) acted in a competitive manner to ADP, however it was unclear whether cangrelor (10nM) was acting in a competitive or non-competitive manner to ADP. The  $E_{max}$  values were as follows: ADP + vehicle (45.5% pVASP), ADP + cangrelor (53.0% pVASP), ADP + AR-C66096 (39.4% pVASP). At the maximum concentration of ADP tested (1mM), the % pVASP values were as follows: ADP + vehicle ( $43.1 \pm 3.83$ ), ADP + cangrelor ( $54.9 \pm 5.07$ ), and ADP + AR-C66096 ( $40.4 \pm 3.90$ ).

As the ADP + cangrelor  $E_{max}$  did not quite reach the % pVASP value obtained for ADP + vehicle, a one-way ANOVA was performed for each data set at this point of 1mM ADP (each drug compared to vehicle) to explore if the mean values obtained were significantly different. The ANOVA did not show a significant difference amongst the means of the drug treatment groups in comparison to vehicle, indicating competitive antagonism for cangrelor and AR-C66096. Subsequently, Schild analysis was performed, which showed that AR-C66096 had a  $K_D$  value of  $1.58 \times 10^{-9}$  (1.58nM), and cangrelor had a  $K_D$  value of  $2.18 \times 10^{-10}$  (0.218nM). However, the  $K_D$  value obtained for cangrelor should still be interpreted with some caution as the curve did not visually indicate competitive antagonism.

These results suggested that cangrelor binds with a greater affinity to P2Y<sub>12</sub> than AR-C66096, which is consistent with reports that cangrelor is more potent than its analogue<sup>152</sup>. Furthermore, the rightward shift in the concentration-response curve for

ADP + cangrelor ( $IC_{50}$ :  $3.97 \times 10^{-5}$  M) was greater than that of ADP + AR-C66096 ( $IC_{50}$ :  $6.19 \times 10^{-6}$  M), when both were compared to ADP + vehicle ( $IC_{50}$ :  $8.45 \times 10^{-7}$  M).

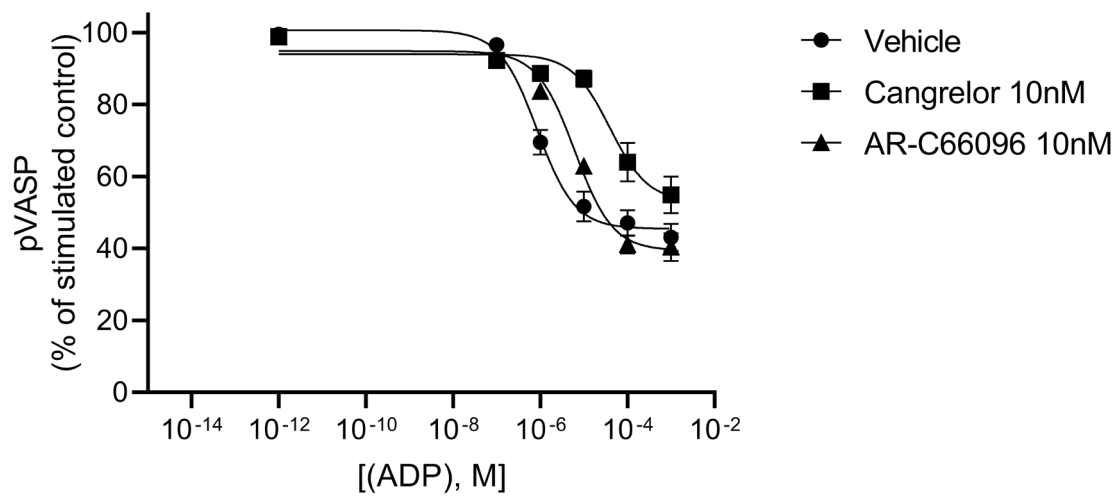


**Figure 47: pVASP assay shows AR-C66096 (10nM) acts in a competitive manner to ADP.** Washed platelets ( $1 \times 10^8$  platelets/mL) were incubated with either vehicle, cangrelor (10nM) or AR-C66096 (10nM) for 30 minutes (RT), and then incubated simultaneously with PGE<sub>1</sub> (100nM) and ADP (varying concentrations) for 10 minutes at RT (mean  $\pm$  SEM;  $n = 5$  independent blood donors). Phosphorylated VASP (pVASP) levels are shown as a % of stimulated control.

### 3.11. Cangrelor affects calcium signalling

As the aggregometry experiments were a readout of multiple signalling receptors, including P2Y<sub>1</sub> (G<sub>q</sub>-coupled), the effects of cangrelor and AR-C66096 were then tested in a calcium assay. As shown in **Figure 48**, activation of the P2Y<sub>1</sub> receptor results in increased cytosolic Ca<sup>2+</sup> (the full P2Y<sub>1</sub> signalling pathway can be viewed in the **Introduction, Figure 4**). Calcium levels can be measured using the calcium-sensitive dye, Cal-520. Washed platelets (1 x 10<sup>8</sup> platelets/mL) were loaded with Cal-520. Platelets were then incubated with varying concentrations of the antagonists (30 minutes, RT). The aim of the experiment was to create a calcium trace of Cal-520 fluorescence over time. Cal-520 fluorescence was measured at 520nm. Initially, a baseline was established, and then platelets were activated with ADP (10µM) at ~400 seconds. Readings were continuously recorded for a total of 1033 seconds (~17 minutes). The peak of the curve was noted.

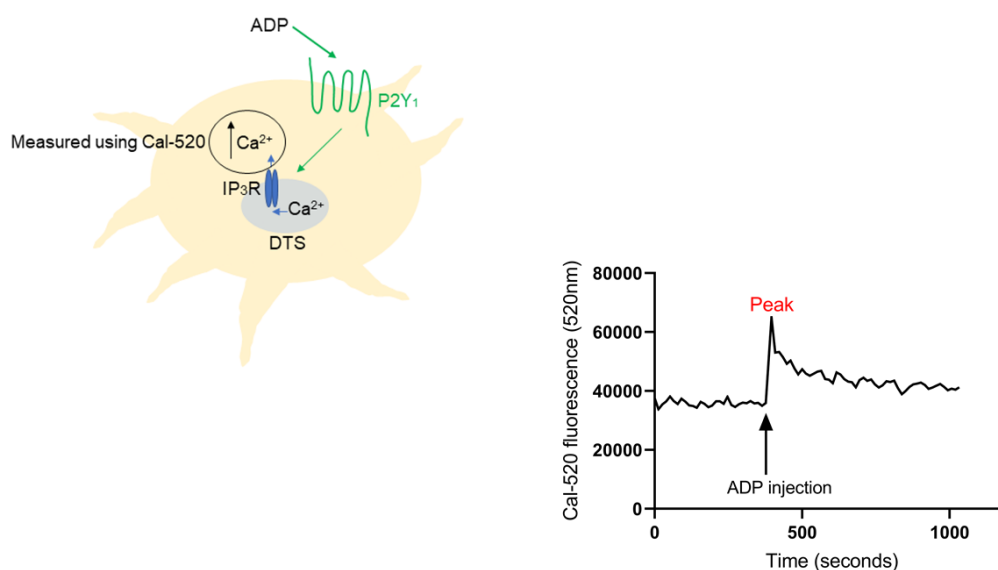


**Figure 48: Calcium levels can be measured using the calcium-sensitive dye, Cal-520.** Activation of the P2Y<sub>1</sub> receptor results in an efflux of Ca<sup>2+</sup> from the dense tubular system via the IP<sub>3</sub>Rs. Ca<sup>2+</sup> levels can be measured using Cal-520. A representative calcium trace (raw data) is shown, which was created by measuring Cal-520 fluorescence (520nm) over time (1033 seconds) in washed platelets. A baseline was established, and ADP was injected into the wells at 400 seconds by the plate reader injector. The peak of the curve was noted.

All Cal-520 fluorescence values (F) were normalised to that of the initial unstimulated vehicle control values ( $F_0$ ). As shown in **Figure 49**, nine concentrations of AR-C66096 and cangrelor were tested, with 10 $\mu$ M ADP. The LogIC<sub>50</sub> value of the AR-C66096 curve was -7.60, whilst the LogIC<sub>50</sub> of the cangrelor curve was -8.0. Within daily experiments, it was observed that AR-C66096-treated platelets consistently produced higher peak cytosolic calcium values upon agonist addition, compared to cangrelor-treated platelets. However, both drugs exhibited a concentration-dependent effect on cytosolic calcium levels, as shown by the decreased mean peak F/F<sub>0</sub> values with increasing concentrations of each drug. An extra-sum-of-squares F test was performed, where the null hypothesis (one curve adequately fits the cangrelor and AR-C66096 data sets) was rejected, thus the cangrelor curve was significantly different from that of AR-C66096 ( $p < 0.01$ ). In contrast, the AR-C66096 effect was weaker and more variable.

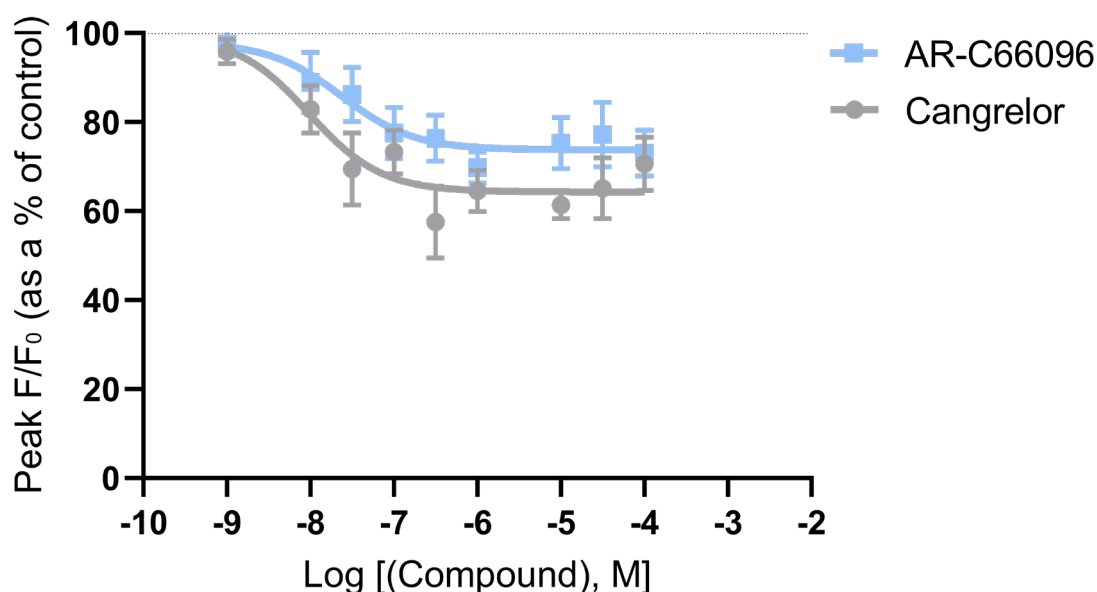


**Figure 49: Calcium assay shows cangrelor affects calcium signalling.** Washed platelets ( $1 \times 10^8$  platelets/mL) loaded with Cal-520 were incubated with varying concentrations of AR-C66096 or cangrelor. All Cal-520 fluorescence values (F) were normalised to that of the unstimulated vehicle control values ( $F_0$ ). The peak of the trace was determined (with baseline correction), and the results were further analysed using the extra-sum-squares F test. Mean  $\pm$  SEM;  $n = 6$  independent blood donors.

The results obtained in **Figure 49** for the antagonists are shown in further detail in **Figure 50** (10 $\mu$ M antagonist) and **Figure 51** (10nM antagonist), where groups were analysed using the one-way ANOVA.

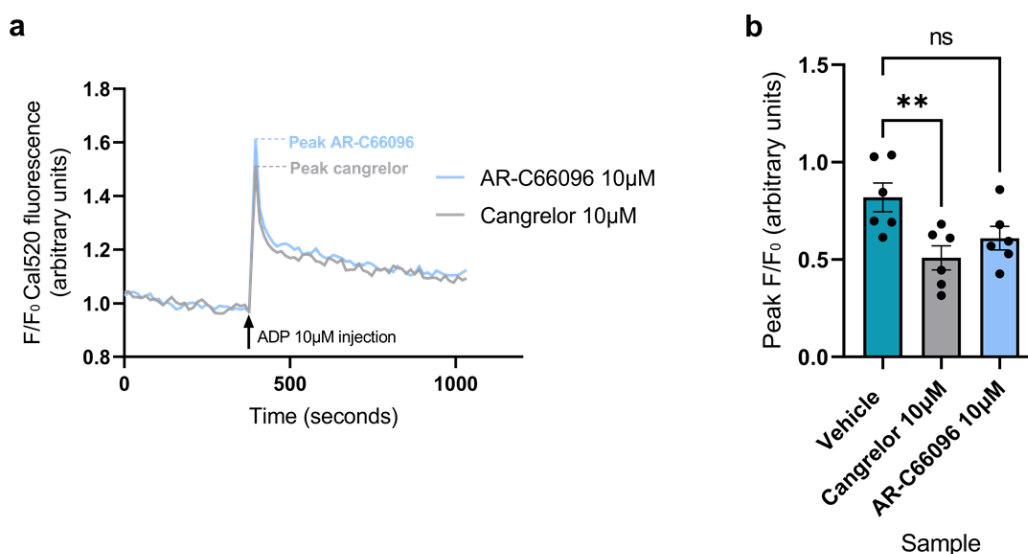


**Figure 50: Cangrelor (10 $\mu$ M) but not AR-C66096 (10 $\mu$ M) has a significantly different effect on Cal-520 fluorescence compared to vehicle. a)** F/F<sub>0</sub> Cal-520 fluorescence traces obtained for AR-C66096 (10 $\mu$ M) and cangrelor (10 $\mu$ M), with ADP 10 $\mu$ M injection into the wells at 400 seconds by the plate reader injector. All Cal-520 fluorescence values (F) were normalised to that of the initial unstimulated vehicle control values (F<sub>0</sub>). **b)** The peak of the trace was determined (with baseline correction), and the results were further analysed using a one-way ANOVA followed up by Dunnett’s multiple comparisons test (\*\*  $p \leq 0.01$ , ns: not significantly different from vehicle).

**Figure 50b** showed that cangrelor (10 $\mu$ M) achieved a significantly different (\*\*  $p \leq 0.01$ ) mean peak F/F<sub>0</sub> compared to vehicle, whereas AR-C66096 did not. However, visually the bars of the cangrelor and AR-C66096 treatment groups did not appear different to each other. This ‘non-significant’ statistical outcome for AR-C66096 may be related to the result of an individual donor in the AR-C66096 group (higher peak F/F<sub>0</sub> value than the rest of the donors). This result was kept in the data set and not omitted because of the subjectiveness of omitting individual donor values, and the lack

of criteria as to what exactly defines an ‘outlier’ within any of these experiments. Thus, power is important to consider here, and a higher sample size may change the statistical outcome. This result may be interpreted with caution. Moreover, **Figure 51b** showed that cangrelor (10nM) and AR-C66096 (10nM) did not achieve a significantly different mean peak  $F/F_0$  compared to vehicle. Taken together, these data indicated that cangrelor significantly decreases cytosolic calcium levels in the platelets. The results obtained for AR-C66096 were weaker and more variable, but **Figure 49** showed it did cause a decrease in cytosolic calcium levels. The key question that remains is whether this is significant or not.

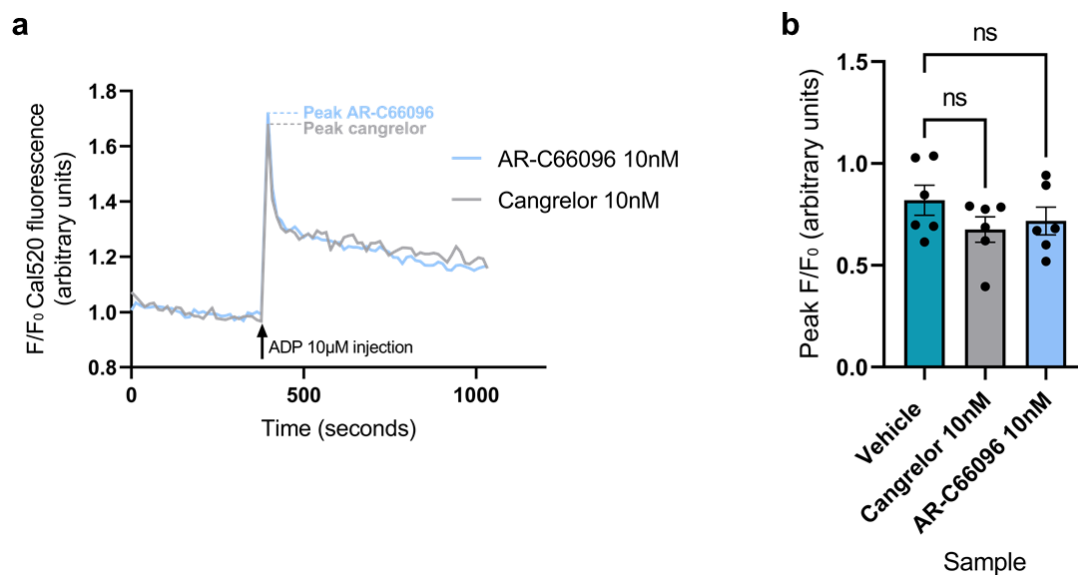


**Figure 51: Cangrelor (10nM) and AR-C66096 (10nM) do not have a significantly different effect on Cal-520 fluorescence compared to vehicle.** **a)**  $F/F_0$  Cal-520 fluorescence traces obtained for AR-C66096 (10nM) and cangrelor (10nM), with ADP 10 $\mu$ M injection into the wells at 400 seconds by the plate reader injector. All Cal-520 fluorescence values ( $F$ ) were normalised to that of the initial unstimulated vehicle control values ( $F_0$ ). **b)** The peak of the trace was determined (with baseline correction), and the results were further analysed using a one-way ANOVA followed up by Dunnett’s multiple comparisons test (ns: not significantly different from vehicle).

### 3.12. Cangrelor achieves a different time vs. % inhibition profile to vehicle in the aggregometry

In previous aggregometry experiments in this chapter, it was observed that cangrelor may be acting in a non-competitive manner to ADP. In those experiments, end-point measurements were recorded on the FLUOstar Omega plate reader after 5 minutes of continuous shaking. In this set of experiments, the effects of cangrelor and AR-C66096 on ADP-induced platelet aggregation were recorded in kinetic mode with 20-second shaking intervals for around 6 minutes (333 seconds). It was expected that inhibition would initially be seen but overcome over time.

The % platelet aggregation was analysed over time for platelets treated with vehicle, cangrelor (500nM) and AR-C66096 (500nM). In these experiments, PRP was incubated with vehicle, cangrelor, or AR-C66096 for 30 minutes (RT). Platelets were then activated by ADP (10mM), which was added by the plate reader injector. The run consisted of ten 37 seconds cycles, each of which was followed by 20 seconds of shaking (700rpm, double orbital). Absorbance values were recorded at the end of each cycle. Mean % aggregation values were determined, with consideration to the absorbance values of the control PRP and PPP controls at each time point. The total run time was 333 seconds. In contrast, the shaking in all previous aggregometry experiments occurred continuously throughout the 5 minutes (300 seconds) run, and end-point measurements were recorded (thus, the results cannot be directly compared).

As shown in **Figure 52**, % platelet aggregation continued to rise over time for platelets that had been treated with vehicle or AR-C66096. At the final time point (333 seconds), ADP + vehicle reached a maximum mean % aggregation value of  $48.3 \pm 5.049\%$ , and ADP + AR-C66096 reached a maximum mean % aggregation value of  $41.3 \pm 5.21\%$ . However, the % platelet aggregation trace for ADP + cangrelor-treated platelets remained stable at below 15% for the entire run. At the final time point, ADP +

cangrelor reached a mean % aggregation value of  $9.67 \pm 4.021\%$ . The sample reached its maximum % platelet aggregation value (11.2%) at the previous time point (296 seconds). These results were surprising because it was expected that cangrelor's inhibitory effect would be overcome over time. A one-way ANOVA followed up by Dunnett's multiple comparisons test showed that platelets incubated with cangrelor achieved a significantly different ( $*** p \leq 0.001$ ) % inhibition profile compared to platelets incubated with vehicle control, whereas platelets incubated with AR-C66096 had not ( $ns; p > 0.05$ ). This data suggested that a very high concentration of ADP (10mM) was unable to overcome the inhibitory effects of cangrelor, which may indicate insurmountable antagonism.

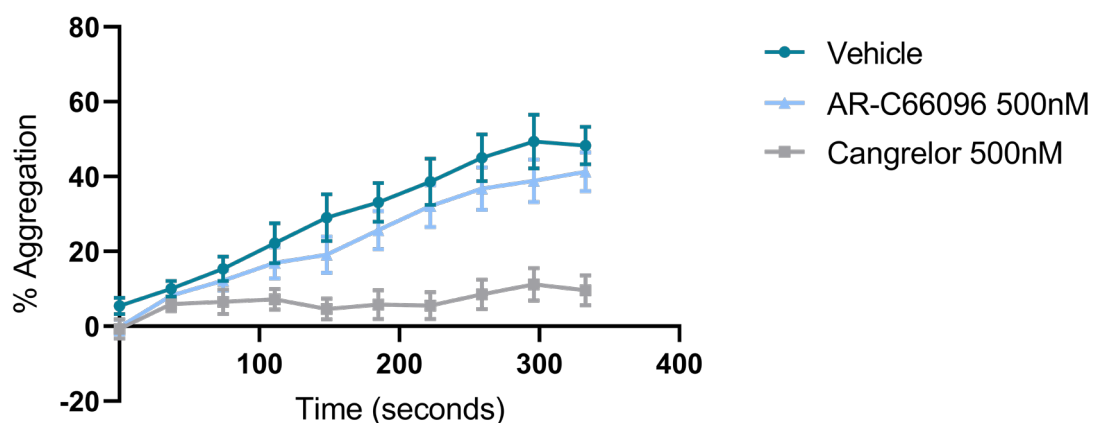


**Figure 52: Cangrelor achieves a different time vs. inhibition profile to vehicle in the aggregometry.** PRP was incubated with AR-C66096 (500nM) or cangrelor (500nM) for 30 minutes (RT). ADP (10mM) was added using the plate reader injector. Absorbance was measured over time (333 seconds), and the % aggregation was determined. The run consisted of ten cycles, each lasting 37 seconds, after which a reading was made. Shaking occurred for 20 seconds after each cycle. Data is presented as the mean  $\pm$  SEM;  $n = 5$  independent blood donors.

### 3.13. Discussion

In this chapter, 96-well aggregometry experiments showed that cangrelor may act in a non-competitive manner to the endogenous P2Y<sub>12</sub> agonist, ADP. ADP was unable to overcome the inhibitory effects of cangrelor (50nM-10μM), even at very high ADP concentrations (up to 10mM). Since cangrelor is stated to act in a competitive manner to ADP in the literature, concentration-curves indicating competitive antagonism with ADP were expected<sup>318,319,321,332</sup>. Interestingly, the possible non-competitive mode of antagonism was not observed with the cangrelor analogue, AR-C66096, which acted in a competitive manner to ADP.

Aggregation concentration-response curves for the agonists vs. cangrelor or AR-C66096 (tested in PRP) could not be found in the literature. Additionally, the original publication which presented cangrelor and its analogue did not include any binding studies<sup>152</sup>. Binding studies where the antagonists have been tested with ADP and 2MeSADP could not be found. However, there has recently been some suggestion in the literature using P2Y<sub>12</sub>-expressing cell lines that cangrelor may be an inverse agonist at P2Y<sub>12</sub>, and not a competitive antagonist<sup>333,334</sup>. Although a main question that arises from such studies is whether P2Y<sub>12</sub> is constitutively active or not *in vivo* (the platelet-based pVASP assay in this work did not indicate this). Moreover, recent MD simulations have shown that ADP and 2MeSADP may bind in separate pockets at P2Y<sub>12</sub><sup>335</sup>. Thus, there may be mechanistic differences between how the agonists activate P2Y<sub>12</sub>. Furthermore, the data presented in this chapter are reminiscent of previously published findings that ticagrelor may act in a non-competitive manner to ADP, but in a competitive manner to 2MeSADP<sup>7,192,201</sup>. There is controversy in the literature as to whether ticagrelor is competitive or non-competitive antagonist, or inverse agonist<sup>7,188,195,201</sup>.

Surprisingly, AR-C66096 and cangrelor were both shown to act in a competitive manner to 2MeSADP in the aggregometry. Cangrelor's possible non-competitive mode

of antagonism with ADP and competitive mode of antagonism with 2MeSADP suggested that the agonists may act in different pockets at a receptor, which could be the P2Y<sub>12</sub> receptor (see **General Discussion** for further elaboration). This would be in line with MD simulations in the literature. However, it could not be determined for certain which receptor (i.e., P2Y<sub>12</sub>) this was occurring at, as the aggregometry is a readout of the activity multiple proteins. Interestingly, mutagenesis data has shown that mutating residues in ‘pocket 2’ of P2Y<sub>12</sub>, as observed in the antagonist-bound structure, results in reduced binding affinity of [<sup>3</sup>H]2MeSADP<sup>17</sup>. Docking performed by the same group showed that 2MeSADP could bind in either pocket 1 or pocket 2 of P2Y<sub>12</sub>. Binding studies would be beneficial and may allow us to further understand these findings. However, it is important to consider that they may not be useful if this effect is only observed in platelets (where P2Y<sub>12</sub> is not overexpressed as in cell lines). Furthermore, such studies will not consider the portion of the drug that is bound to plasma proteins in the blood, as in PRP. It is also important to consider other dynamics within the blood environment, which cannot be replicated using a transfected cell line. This was an advantage of conducting these experiments using the blood of human donors.

An important counterargument to acknowledge regarding the above-mentioned aggregometry findings relates to the affinity of the agonists for the P2Y<sub>12</sub> receptor. ADP (PK<sub>i</sub>: 5.9) and 2MeSADP (PK<sub>i</sub>: 9.2) have varying affinities (**Table 1b**) for P2Y<sub>12</sub>, thus the possible ‘non-competitive’ phenomenon of (higher concentrations of) cangrelor observed with ADP may be due to the competing agonist’s lower affinity for the receptor. For this reason, increasing the concentration of ADP may still not overcome the inhibitory effects of cangrelor, given the agonist’s lower affinity for the receptor. Future studies should consider the varying affinities of the agonists as a possible limitation of this study, and one that may need to be further explored in future work.

Moreover, further evidence for cangrelor's possible different mode of antagonism to AR-C66096 was obtained by testing % platelet aggregation over time in platelets treated with the drugs and activated using 10mM ADP. It was expected that inhibition would initially be seen but overcome over time, which was not observed. ADP was unable to overcome the inhibitory effects of cangrelor (10 $\mu$ M) over the time of the run. Some limitations of this set of results were that they could not be directly compared to previous aggregometry figures in the chapter as the shaking mode was different. However, the results still highlighted that the antagonists may show different modes of antagonism with ADP.

Additionally, platelets incubated with cangrelor showed significantly different (decreased) cytosolic Ca<sup>2+</sup> levels compared to vehicle. Decreased cytosolic Ca<sup>2+</sup> levels are related to inhibition of the P2Y<sub>1</sub> pathway. There may be two reasons this effect was observed: 1) potential antagonism of P2Y<sub>1</sub> by cangrelor, 2) P2Y<sub>12</sub> antagonism by cangrelor resulting in P2Y<sub>12</sub>-P2Y<sub>1</sub> crosstalk<sup>336,337</sup>. Although, the latter appears more likely. A different pocket has also been predicted for 2MeSADP to ADP in P2Y<sub>1</sub><sup>338</sup>. However, these results from the calcium assay (**Figure 50**) should be interpreted with caution, as visually the bar charts did not appear to show a major difference in peak F/F<sub>0</sub> between cangrelor and AR-C66096. Thus, increased sample number and power may affect these results and produce a different statistical outcome. These results did not conclusively tell us whether AR-C66096 significantly modulates a calcium signalling pathway or not, and future studies may test this using P2Y<sub>1</sub>-expressing cell lines.

Interestingly, the pVASP assay showed that ADP with concentrations up to 1mM was unable to overcome the effects of either cangrelor (10 $\mu$ M) or AR-C66096 (10 $\mu$ M) on pVASP (**Figure 45**). These results are consistent with cangrelor's possible non-competitive mode of action with ADP in the aggregometry (**Figure 27**). However, they are not consistent with AR-C66096's competitive mode of action with ADP

**(Figure 28).** The implications of this are unknown. One possibility is that both cangrelor and AR-C66096 act non-competitively on P2Y<sub>12</sub>, but cangrelor acts additionally on a further target, leading to non-competitive inhibition of ADP-induced platelet aggregation. This suggests important differences between using pVASP and using aggregation to understand the mechanisms of action of P2Y<sub>12</sub> antagonists. Another possibility is that the drugs have higher plasma protein binding in the PRP experiments (aggregometry) vs. the washed platelet experiments (pVASP assay), thus a higher concentration of unbound drug is available to bind to P2Y<sub>12</sub> in the pVASP assay vs. the aggregometry. Additionally, ADP (up to 1mM) was unable to overcome the effects of cangrelor (100nM) on pVASP, but not that of AR-C66096 (100nM). This further suggested that cangrelor may act in a non-competitive manner to ADP at P2Y<sub>12</sub>.

The literature suggests that there is a strong correlation between the results from aggregometry and the pVASP assay<sup>339-341</sup>. However, some studies have suggested that results from the two assays cannot be directly compared<sup>342,343</sup>. This is because aggregometry is a phenotypic assay- a readout of P2Y<sub>12</sub>, P2Y<sub>1</sub> and integrin activity. However, pVASP is a molecular assay. Thus, different aspects of P2Y<sub>12</sub> inhibition are being assessed. Additionally, PGE<sub>1</sub>-induced stimulation of adenylyl cyclase is required in the pVASP assay to create a large enough window of inhibition for ADP. This may provide an overestimation or exaggeration of P2Y<sub>12</sub> inhibition, as the cAMP→pVASP pathway is being simultaneously stimulated through both P2Y<sub>12</sub> antagonism and adenylyl cyclase stimulation. Platelet treatment with PGE<sub>1</sub> is not required in the aggregometry experiments, thus it is probably not feasible to directly compare concentration-response curves obtained from the two assays presented here.

Whilst comparisons may be made between the K<sub>D</sub> values determined from aggregometry data vs. the pVASP assay, it is important to, again, acknowledge multiple varying factors exist within the assays. In the aggregometry, AR-C66096 (10nM)

obtained a  $K_D$  value of  $5.83 \times 10^{-9}$  M (5.83nM), and in the pVASP assay AR-C66096 (10nM) obtained a higher  $K_D$  value of  $1.58 \times 10^{-9}$  M (1.58nM). In the literature, AR-C66096 tested with ADP in aggregometry has been reported to have a  $pK_D$  value of 8.66 ( $K_D = 10^{-pK_D}$ ), thus a  $K_D$  value of  $2.19 \times 10^{-9}$  (2.19nM)<sup>344</sup>. However, those aggregometry experiments were performed using washed platelets (with added fibrinogen and  $PGI_2$ ), with an aggregometer and different shaking to that adopted in the 96-well aggregometry of this work. Additionally, in a molecular assay using P2Y<sub>12</sub>-expressing B10 cells from the rat brain and an adenylyl cyclase assay, AR-C66096 was found to act in a competitive manner to 2MeSADP<sup>345</sup>. It was reported to have a  $pK_D$  value of 7.60, thus a  $K_D$  value of  $2.51 \times 10^{-8}$  M (25nM). This value is slightly higher than what was obtained in the pVASP assay of this work, however this may be due to differences between experiments in platelets and cell lines.

Furthermore, in the aggregometry, cangrelor (10nM) obtained a  $K_D$  value of  $5.75 \times 10^{-9}$  M (5.75nM), and in the pVASP assay cangrelor (10nM) obtained a  $K_D$  value of  $2.18 \times 10^{-10}$  M (0.218nM), the latter of which should be interpreted with caution. Data from the pVASP assay suggested that cangrelor may have a higher affinity (for the P2Y<sub>12</sub> receptor) compared to AR-C66096. Thus, the possible varying affinities of the antagonists may also be considered as a potential limitation of the results observed. In the literature, varying  $pK_D$  values have been reported for cangrelor ( $pK_{DS}$ : 8.6-9.2;  $K_{DS}$ :  $2.51 \times 10^{-9}$  M to  $6.31 \times 10^{-10}$  M), using P2Y<sub>12</sub>-expressing cell-lines and cAMP assays<sup>208,346,347</sup>. In these studies, cangrelor was reported to act in a competitive manner to 2MeSADP. The  $K_D$  values appear to be similar to the  $K_D$  value obtained in the pVASP assay in this work, perhaps as pVASP is a readout of cAMP signalling, however the agonist used was ADP, thus the values cannot directly be compared.

Moreover, there is a lack of standardisation between groups for the aggregometry and pVASP assays, and limited data to compare the two methods. No

concentrations-response curves were found in the literature where varying concentrations of ADP were tested in the pVASP assay. Thus, this thesis presents the first concentration-response curves for ADP vs. the antagonists. The currently available pVASP kits are limited in contents and only a small number of samples can be tested. These kits are diagnostic and often used in a clinical environment to monitor P2Y<sub>12</sub> therapy. In practice, they are not ideal for testing large numbers of samples in a laboratory environment, where multiple concentrations-response curves are often required. Flow cytometric analysis of pVASP is a complex and laborious technique, conducted in specialised laboratories<sup>294,295,348-350</sup>. In this work, whilst barcoding did reduce antibody consumption, the pVASP assay was still expensive and highly time-consuming.

Additionally, aggregometry results in the literature are often in the form of single tracings from the Born aggregometer, which is considered a 'gold-standard' for assessing aggregation. Experiments are performed using human blood, or the blood of other mammals, such as mice. This may lead to slight differences in aggregation results. Additionally, experiments where the drug was administered *in vivo* followed by blood collection vs. blood collection followed by drug incubation may also cause differences in results. These points may also apply to other assays involving blood.

Born aggregometry and 96-well aggregometry work using the same principle (measurement of light transmission or absorbance through a sample). However, due to the large number of samples in this work, 96-well aggregometry was adopted for increased efficiency in constructing concentration-response curves. Other advantages included that platelet samples could be incubated with drug at the same time in the 96-well plate, and agonist could be added by the plate reader injectors at the same time. Furthermore, Born aggregometry requires more PRP per sample, and a limited number of reactions can be performed simultaneously<sup>351</sup>. The 96-well assay was validated using

known drugs, which was important to ensure its reliability. Importantly, studies such as this can allow further advancement of this technique, which is relatively new<sup>288-290,293</sup>.

Occasionally, some noise was picked up in the assay, which future studies may address to help to further optimise the assay. For example, in **Figure 22** (varying concentrations of ADP tested with 10 $\mu$ M eptifibatide), there was some minor platelet aggregation (below 20%) present from ADP concentrations of 1mM to 10mM. This was not expected as eptifibatide inhibits the integrin receptors, completely preventing aggregation. One possible explanation may be that ADP was being broken down by phosphatases (e.g., the phosphatase CD39 on white blood cells) in PRP to adenosine, causing undesired off-target effects on other receptors (e.g., adenosine receptors). However, the PRP had been checked for purity, and white blood cells were not present. Additionally, in an *in vivo* system, phosphatases are released by the vessel wall, which was not present in the *in vitro* model. The only way to determine for certain whether ADP was being broken down to adenosine would be to use mass spectrometry methods to detect adenosine. Such a method was outside the scope of this work, however future studies should consider and address what aspects may be causing noise in the assay.

Lastly, molecular docking was not useful in exploring the *in vitro* findings. It is likely that the conformation of P2Y<sub>12</sub> stabilised by cangrelor may be different to the nucleotide agonist-bound structure. This is because it is unlikely that cangrelor's binding would result in the receptor's 'lid' closing, which is a hallmark feature of P2Y<sub>12</sub> activation. Additionally, the antagonist-bound structure is stabilised by a non-nucleotide antagonist, which may be different to that stabilised by a nucleotide antagonist. MD simulations may be more useful in exploring cangrelor's predicted mode of binding. They may also help us to understand the significance of the missing field of negative electrostatic potential in cangrelor, compared to AR-C66096.

## **Chapter 4.**

# **Discovering compounds B6 and B11 as novel inhibitors of platelet aggregation**

#### 4.1. Aim of the study

The aim of this study was to find a novel non-nucleotide inhibitor of platelet aggregation through computational drug discovery. Currently, there is no reversible, non-nucleotide P2Y<sub>12</sub> antagonist on the market. Importantly, no novel P2Y<sub>12</sub> antagonists have yet been discovered using structure-based drug discovery. The recently solved P2Y<sub>12</sub> structure can now be used to pursue this, which will also facilitate the validation of the structure and the *in silico* method used.

#### 4.2. *In vitro* validations of the positive control, AZD1283

AZD1283 is a competitive, reversible P2Y<sub>12</sub> antagonist discovered by AstraZeneca<sup>205-207</sup>. It is the only antagonist whose structure has been solved in complex with P2Y<sub>12</sub><sup>17</sup>. The inhibitory effects of AZD1283 were validated in the plate-based aggregometry assay. PRP was incubated with AZD1283 (10µM) for 30 minutes (RT). Platelets were then activated with varying concentrations of ADP, followed by 5 minutes of shaking. As shown in **Figure 53**, a rightward shift of the ADP concentration-response curve was produced in the presence of AZD1283. AZD1283 exhibited competitive antagonism with ADP, as expected.

The LogEC<sub>50</sub> values were determined to be -5.87 and -4.80 for the ADP + vehicle curve and the ADP + AZD1283 curve, respectively. Schild analysis showed that AZD1283 had a K<sub>D</sub> value of 9.36 x 10<sup>-7</sup> M (936nM). The E<sub>max</sub> values obtained were 87.9% and 102% for ADP + vehicle and ADP + AZD1283, respectively. At the maximum concentration of ADP used (100µM), in the presence of vehicle a mean % aggregation value of 82.8 ± 6.35% was achieved, and in the presence of AZD1283 a mean % aggregation value of 84.3 ± 7.41% was achieved.

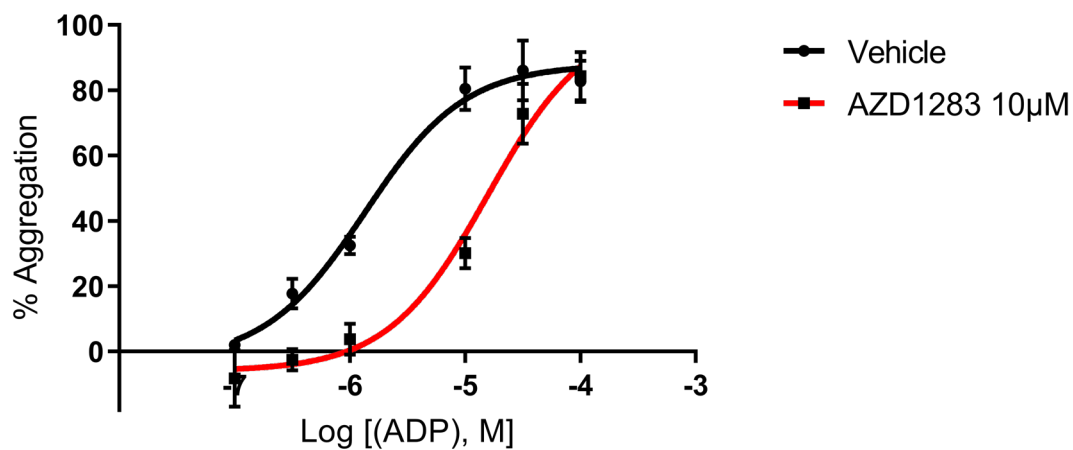


**Figure 53: Experimental validation of the positive control, AZD1283 (10µM), against platelet aggregation using varying concentrations of ADP.** PRP was incubated with AZD1283 10µM (30 minutes; RT) and platelets were activated with varying concentrations of ADP. Absorbance was measured, and the % aggregation was determined (mean ± SEM;  $n = 5$  independent blood donors).

In the next set of experiments, AZD1283 was tested with the synthetic, more potent P2Y<sub>12</sub> agonist, 2MeSADP. As shown in **Figure 54**, the ADP + vehicle curve achieved a LogEC<sub>50</sub> of -7.20, and the ADP + AZD1283 curve achieved a LogEC<sub>50</sub> of -6.56. The potency of 2MeSADP can be demonstrated by the decrease in LogEC<sub>50</sub> values compared to those obtained with ADP (**Figure 53**). Furthermore, the rightward shift produced by the AZD1283 concentration-response curve was lesser compared to **Figure 53**. The E<sub>max</sub> values obtained were 79.4% and 80.7% for 2MeSADP + vehicle and 2MeSADP + AZD1283, respectively. At the maximum concentration of 2MeSADP used (100μM), in the presence of vehicle a mean % aggregation value of 82.5 ± 3.20% was achieved, and in the presence of AZD1283 a mean % aggregation value of 78.0 ± 7.89% was achieved. Schild analysis showed that AZD1283 achieved a K<sub>D</sub> value of 2.94 x 10<sup>-6</sup> M (2.94μM).

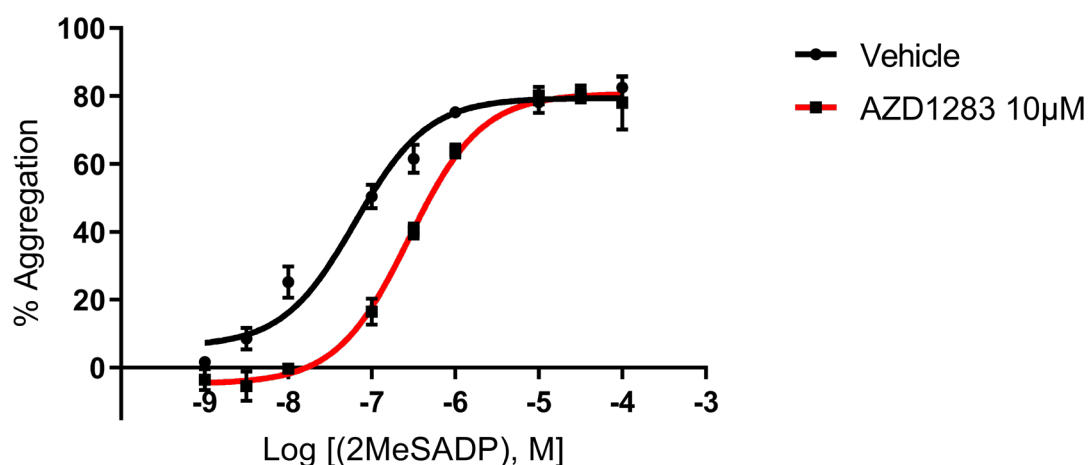


**Figure 54: Experimental validation of the positive control, AZD1283 (10μM), against platelet aggregation using varying concentrations of 2MeSADP.** PRP was incubated with AZD1283 10μM (30 minutes; RT) and platelets were activated with varying concentrations of 2MeSADP. Absorbance was measured, and the % aggregation was determined (mean ± SEM; n = 5 independent blood donors).

### 4.3. Initial trials: testing some FDA-approved drugs and special studies

In the search for a novel inhibitor of platelet aggregation, the aggregometry assay was initially trialled in multiple screens to assess its accuracy in reporting the inhibitory effects of the positive control (AZD1283). A selection of cherry-picked FDA-approved drugs (and two experimental drugs) which are not marketed as antiplatelet agents were tested alongside the positive control (**Figure 55a, Table 6**).

Additionally, two special studies were also performed using compounds with nucleotide scaffolds (**Figure 55b, Table 6**). Firstly, remdesivir, due to the recent attention to this drug in the COVID-19 pandemic. Secondly, the natural compound para-topolin riboside (also known as N<sup>6</sup>-(4-hydroxybenzyl)adenosine), which has been reported to inhibit collagen-induced platelet aggregation, but not tested on ADP-induced platelet aggregation<sup>352</sup>. Interestingly, the same paper proposed a potential interaction of the compound with P<sub>2</sub>Y<sub>12</sub> using computational docking studies only. Keyword searches were performed to check if any of the compounds were reported to inhibit ADP-induced platelet aggregation. Prior to testing, it was acknowledged that there was a report suggesting that the beta-blocker nebivolol may inhibit ADP-induced platelet aggregation through stimulation of NO production in platelets<sup>353</sup>.

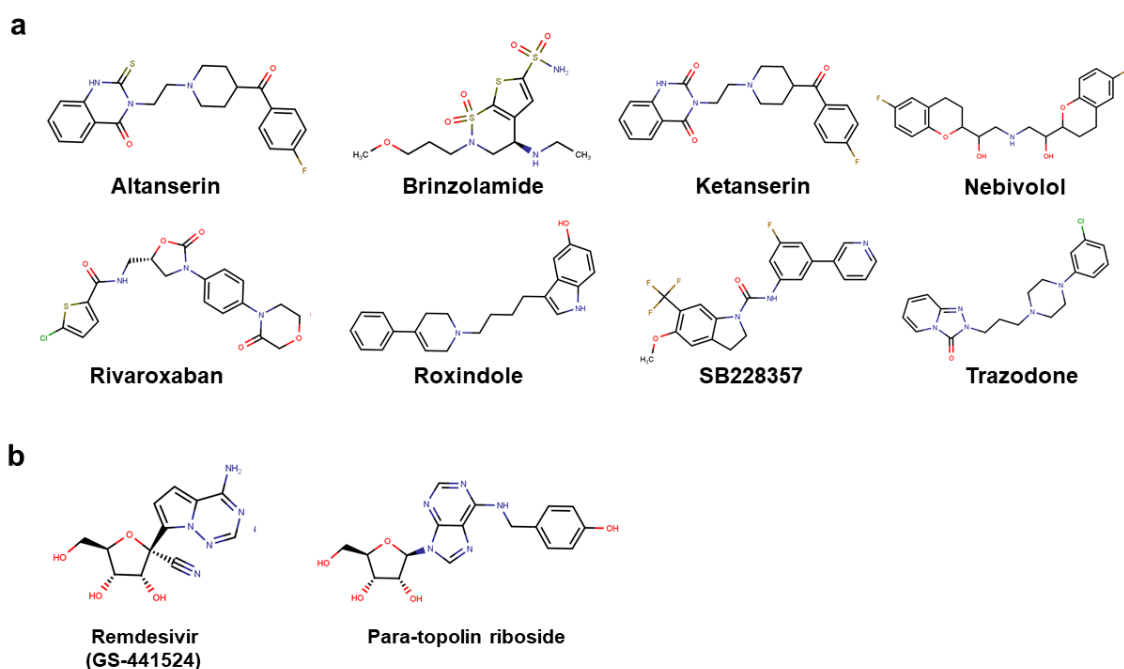


**Figure 55: Structures of some FDA-approved drugs (and two experimental drugs) and a natural compound used to trial the aggregometry assay. a) Screen 1: a selection of FDA-approved drugs, as well as the experimental drugs, roxindole and SB228357. Note that, whilst altanserin and ketanserin are administered in humans, their approval status with the FDA is unknown. b) Screen 2: remdesivir's active metabolite (GS-441524), and para-topolin riboside. The structures were drawn using MarvinSketch.**

**Table 6: Mechanisms of some FDA-approved drugs (and two experimental drugs) and a natural compound used to trial the aggregometry assay.**

<b>Drug</b>	<b>Mechanism</b>
<b>Altanserin</b>	5-HT <sub>2A</sub> receptor antagonist
<b>Brinzolamide</b>	Carbonic anhydrase inhibitor
<b>Ketanserin</b>	5-HT <sub>2A</sub> receptor antagonist
<b>Nebivolol</b>	Beta-3 adrenergic receptor agonist
<b>Rivaroxaban</b>	Factor Xa selective inhibitor
<b>Roxindole</b>	Dopamine receptor agonist
<b>SB228357</b>	5-HT <sub>2C/2B</sub> receptor antagonist
<b>Trazodone</b>	5-HT <sub>2A</sub> receptor antagonist
<b>Remdesivir</b>	Inhibits the RNA-dependent RNA polymerase (RdRp) of coronaviruses
<b>Para-topolin riboside</b>	Inhibitor of collagen-induced platelet aggregation

PRP was incubated with compounds for 30 minutes (RT), and platelets were activated with ADP (3 $\mu$ M). Statistical analysis was performed using the one-way ANOVA, followed up by Dunnett's multiple comparisons test. As shown in **Figure 56**, the positive control (AZD1283) achieved a significantly different mean % aggregation value compared to vehicle (\*\*\*\*  $p \leq 0.0001$ ), with 93.7% inhibition. As expected, the FDA-approved drugs (including nebivolol) did not produce significantly different mean % aggregation values compared to vehicle. This showed that the assay was reliable in distinguishing true inhibitors of platelet aggregation (AZD1283) from other drugs which served (phenotypically) as negative controls.

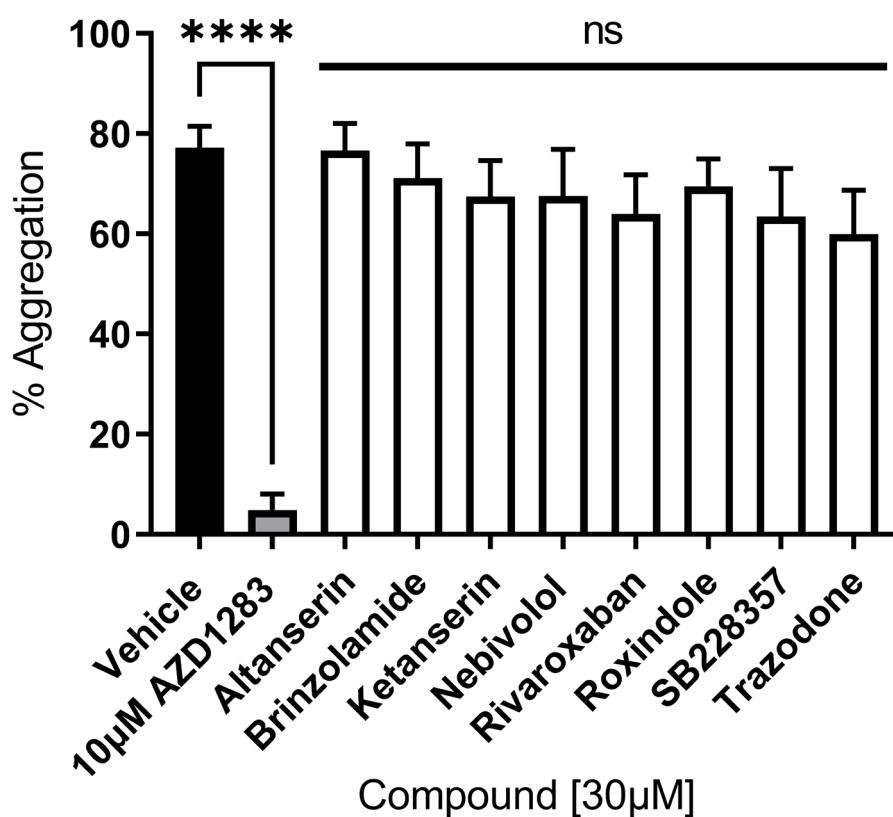


**Figure 56: Experimental evaluation of some FDA-approved drugs (and two experimental drug) used to trial the aggregometry assay.** PRP was incubated with compounds (30 $\mu$ M) and positive control (10 $\mu$ M) for 30 minutes (RT). Platelets were activated with ADP (3 $\mu$ M). Absorbance was measured, and the % aggregation was determined. Statistical analysis was performed using the one-way ANOVA, followed up by Dunnett's multiple comparisons test (\*\*\*\*  $p \leq 0.0001$ , ns:  $p > 0.05$ ). Mean  $\pm$  SEM;  $n = 6$  independent blood donors.

The next set of experiments were separate from the previous and entitled ‘special studies’. PRP was incubated with the nucleotide-based compound, GS-441524 (10 $\mu$ M) for 30 minutes (RT). Platelets were then activated with 3 $\mu$ M ADP. Statistical analysis was performed using the one-way ANOVA, followed up by Dunnett’s multiple comparisons test. As shown in **Figure 57**, the active metabolite of remdesivir did not achieve a significantly different mean % aggregation value from vehicle, whilst the positive control did (\*\*\*)  $p \leq 0.001$ ).

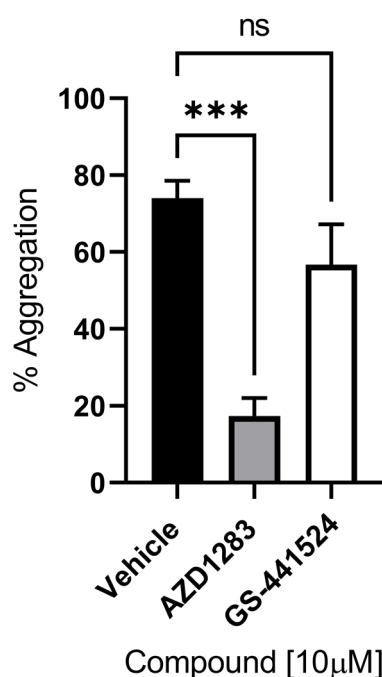


**Figure 57: Experimental evaluation of remdesivir’s active metabolite, GS-441524 (10 $\mu$ M), against platelet aggregation.** PRP was incubated with compounds (10 $\mu$ M) for 30 minutes (RT). Platelets were activated using 3 $\mu$ M ADP. Absorbance was measured and the % aggregation was determined. Statistical analysis was performed using the one-way ANOVA, followed up by Dunnett’s multiple comparisons test (\*\*\*)  $p \leq 0.001$ , ns:  $p > 0.05$ ). The data is presented as the mean  $\pm$  SEM;  $n = 5$  independent blood donors.

As shown in **Figure 58**, another nucleotide-based compound, para-topolin riboside, was tested at 10 $\mu$ M. Statistical analysis was performed using the one-way ANOVA, followed up by Dunnett's multiple comparisons test. The positive control had a significantly different mean % aggregation value compared to vehicle (\*\*\*\*  $p \leq 0.0001$ ). It produced 84.9% inhibition compared to vehicle. Para-topolin riboside was also found to have a significantly different (\*  $p \leq 0.05$ ) mean % aggregation value compared to vehicle. It produced 22.1% inhibition compared to vehicle. This was interesting because it supported computational work by others that para-topolin riboside may inhibit P2Y<sub>12</sub>.

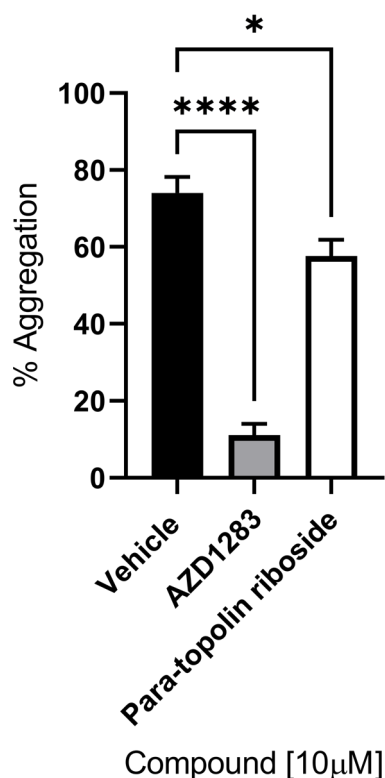


**Figure 58: Experimental evaluation of para-topolin riboside (10 $\mu$ M) against platelet aggregation.** PRP was incubated with compounds (10 $\mu$ M) for 30 minutes (RT). Platelets were activated using 3 $\mu$ M ADP. Absorbance was measured and the % aggregation was determined. Statistical analysis was performed using the one-way ANOVA, followed up by Dunnett's multiple comparisons test (\*\*\*\*  $p \leq 0.0001$ , \*  $p \leq 0.05$ ). The data is presented as the mean  $\pm$  SEM;  $n = 5$  independent blood donors.

Para-topolin riboside (10 $\mu$ M) was then tested with varying concentrations of ADP. As shown in **Figure 59**, para-topolin riboside caused a slight rightward shift of the ADP concentration-response curve compared to that of the vehicle (ADP + vehicle LogEC<sub>50</sub>: -6.39, ADP + para-topolin riboside LogEC<sub>50</sub>: -6.14, ADP + AZD1283 LogEC<sub>50</sub>: -5.03). The compounds were shown to act in a competitive manner to ADP (ADP + vehicle E<sub>max</sub>: 96.7%, ADP + para-topolin riboside E<sub>max</sub>: 94.05%, ADP + AZD1283 E<sub>max</sub>: 108.0%). At the maximum concentration of ADP used (100 $\mu$ M), vehicle achieved 97.9  $\pm$  0.630% aggregation, para-topolin riboside achieved 95.9  $\pm$  2.29% aggregation, and AZD1283 achieved 94.8  $\pm$  2.18% aggregation. Schild analysis showed that para-topolin riboside achieved a K<sub>D</sub> value of 1.28 x 10<sup>-5</sup> M (12.8 $\mu$ M), and AZD1283 achieved a K<sub>D</sub> value of 4.51 x 10<sup>-7</sup> M (451nM). An extra-sum-of-squares F test was performed, where the null hypothesis (one curve adequately fits the vehicle and para-topolin riboside data sets) was rejected, thus the para-topolin riboside curve was significantly different from vehicle control (p < 0.0001). This comparison of fits indicated that para-topolin riboside is a weak inhibitor of ADP-induced platelet aggregation.

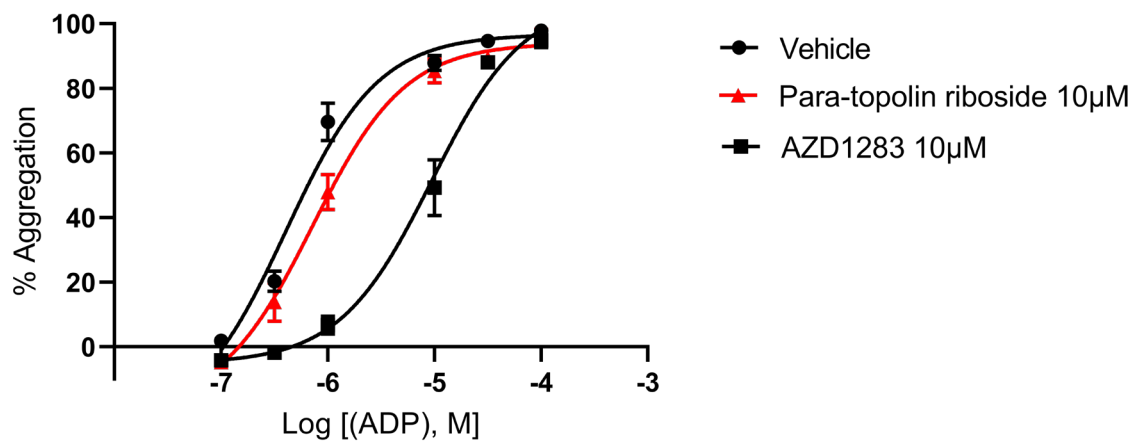


**Figure 59: Effect of para-topolin riboside (10µM) on platelet aggregation with varying concentrations of ADP.** PRP was incubated with compounds (10µM) for 30 minutes (RT). Platelets were activated with varying concentrations of ADP. Absorbance was measured and the % aggregation was determined (mean ± SEM; *n* = 5 independent blood donors).

#### 4.4. *In silico* validations of the positive control, AZD1283

Prior to using *in silico* tools to search for hits, validation of the docking protocol was performed using the structure of the positive control (**Figure 60**).

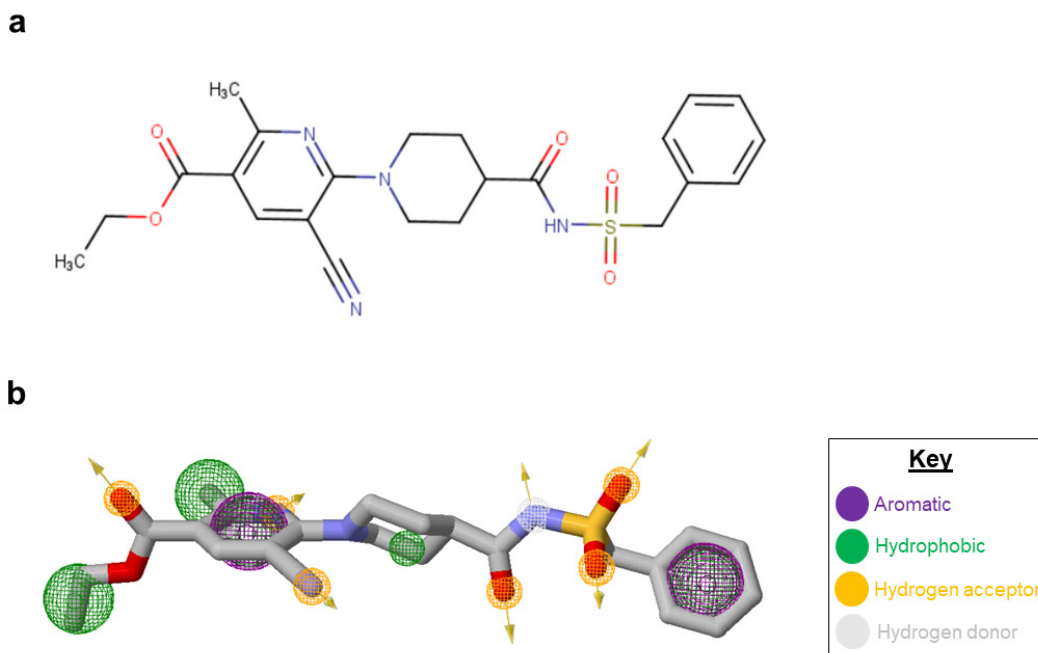


**Figure 60: Structure and key pharmacophore features of AZD1283. a)** 2D representation of AZD1283 (the structure was drawn using MarvinSketch); **b)** Key pharmacophore features of AZD1283 (the 3D structure was produced using ZINCPharmer <http://zincpharmer.csb.pitt.edu/>).

Blind (unbiased) docking of the ligand was performed against the structure of P2Y<sub>12</sub> (PDB ID: 4NTJ) in various programs. This validation docking required an energy-minimised form of the ligand, and a specially prepared version of the protein structure where water molecules were removed and hydrogen atoms (not typically resolved in crystal structures) added. As shown in **Figure 61**, the docked pose of the ligand was compared to the reference co-crystallised pose. The distance between poses was compared using the DockRMSD tool.

AutoDock Vina was the best performing program, with 0.895Å RMSD between the docked and co-crystallised pose (**Figure 61a**). The poses were highly reproducible

in five independent docking runs (mean predicted binding affinity ( $\Delta G$ )  $\pm$  SEM:  $-8.90 \pm 0.440$  kcal/mol). Generally, a more negative value correlates with ‘better’ predicted binding affinity. GlideXP followed closely behind, with an RMSD value of  $1.267\text{\AA}$  between the docked and co-crystallised pose (**Figure 61b**). The docked pose obtained a score of  $-12.7$  kcal/mol. AutoDock 4.0 and SwissDock performed less well, with RMSD scores of  $2.902\text{\AA}$  and  $20.902\text{\AA}$  between the docked and co-crystallised pose, respectively (**Figure 61c-d**).

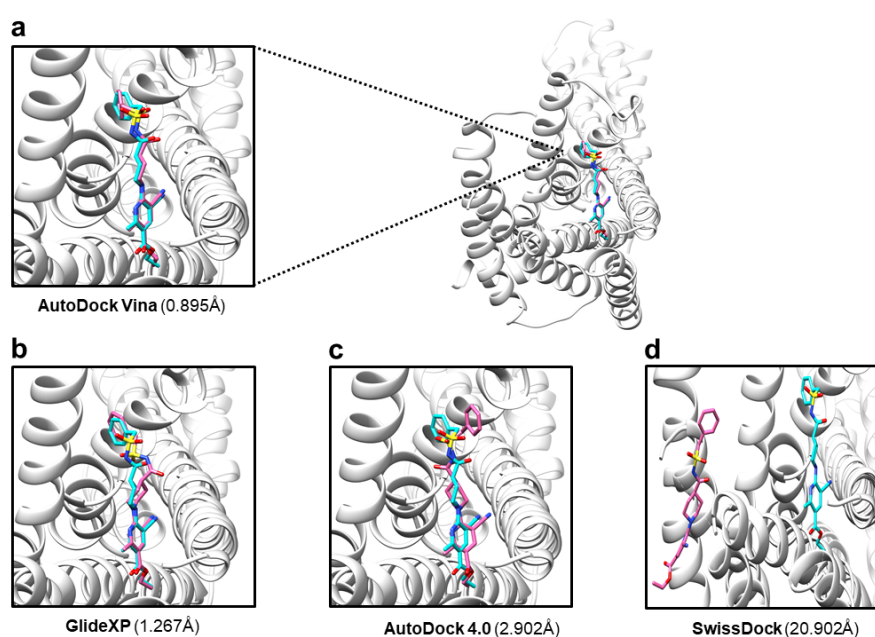


**Figure 61: Validation of blind docking of the positive control, AZD1283, against the human P2Y<sub>12</sub> structure.** **a)** The docked pose of the ligand (pink) vs. the co-crystallised pose of the ligand (cyan sticks) against the P2Y<sub>12</sub> structure (PDB ID: 4NTJ) in AutoDock Vina (blind docking). The protein is shown as white ribbons (cartoon representation). An exhaustiveness of 24 was used. **b)** The docked pose of the ligand (pink sticks) vs. the co-crystallised pose of the ligand (cyan sticks) against the P2Y<sub>12</sub> structure in GlideXP (blind docking). **c)** The docked pose of the ligand (pink sticks) vs. the co-crystallised pose of the ligand (cyan sticks) against the P2Y<sub>12</sub> structure in AutoDock 4.0 (blind docking). An exhaustiveness of 24 was used. **d)** The docked pose of the ligand (pink sticks) vs. the co-crystallised pose of the ligand (cyan sticks) against the P2Y<sub>12</sub> structure in SwissDock (blind docking). An exhaustiveness of 24 was used. The images were created using UCSF Chimera.

AZD1283 was then docked against P2Y<sub>12</sub> using the GOLD suite (CCDC, Cambridge). The binding site was defined as the centre of the AZD1283 binding pocket (pocket 1; coordinates: x: 16.584, y: 103.894, z: 51.041), and focused docking was performed. As shown in **Figure 62**, the docked pose was comparable to the co-crystallised pose and to the pose obtained in blind docking with AutoDock Vina (**Figure 61**). The pose was highly reproducible in each run. GOLD assigns a score (ChemPLP score as default) to each pose, which is a dimensionless value. For AZD1283, the ChemPLP score was calculated to be  $88.7 \pm 2.11$  for five independent docking runs. Importantly, there was a consensus between GOLD and AutoDock Vina as both could largely retrieve the co-crystallised pose of AZD1283. This showed that the two programs were reliable for subsequent docking experiments.

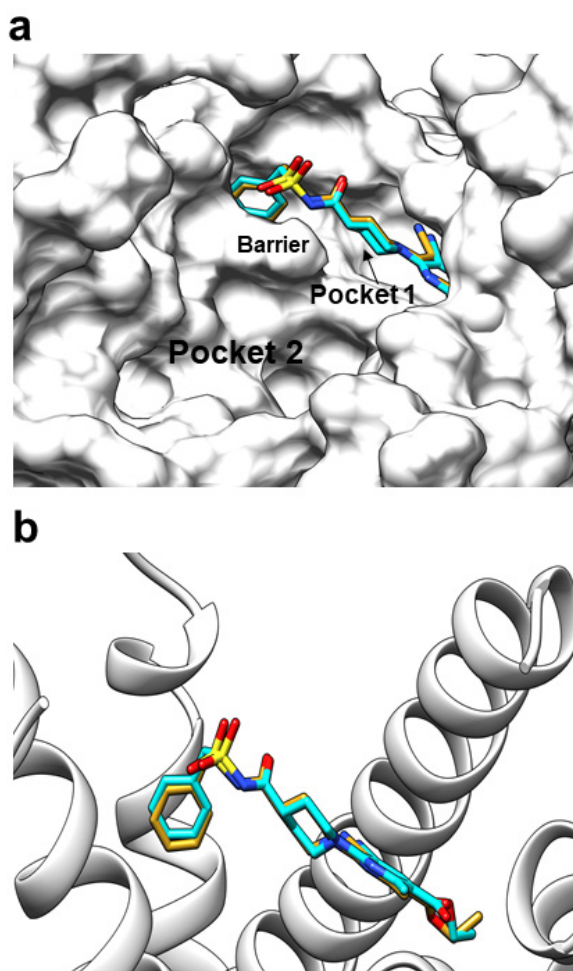


**Figure 62: Validation of focused docking of the positive control, AZD1283, against the human P2Y<sub>12</sub> structure.** **a)** Focused docking against P2Y<sub>12</sub> was performed in the GOLD suite, which produced a docked pose (gold sticks) comparable to the original (co-crystallised) pose of AZD1283 (cyan sticks). The binding site was defined as the centre mass of AZD1283. The barrier (Tyr-105<sup>3.33</sup> and Lys-280<sup>7.35</sup>) separating pocket 1 and pocket 2 is labelled. The protein is in white surface representation. **b)** Zoomed-in view of the docked pose (gold sticks) and co-crystallised pose (cyan sticks). The protein is shown as white ribbons (cartoon representation). The images were created using UCSF Chimera.

Moreover, protein-ligand interactions between the co-crystallised AZD1283 and its respective pocket on the human P2Y<sub>12</sub> structure (PDB ID: 4NTJ) were analysed using the 3D Protein-Ligand Interaction Profiler (PLIP)<sup>354</sup>. As shown in **Figure 63**, AZD1283's phenyl ring was predicted to form hydrophobic interactions with Phe-252<sup>6.51</sup> and Arg-256<sup>6.55</sup>, Tyr-259<sup>6.58</sup>, as well as Leu-276<sup>7.31</sup> and Lys-280<sup>7.35</sup>. The phenyl ring prevents the inward shift of these two helices; thus, these interactions may be crucial in preventing receptor activation. Furthermore, AZD1283 formed six hydrogen bonds with the receptor (Lys-280<sup>7.35</sup>, Arg-256<sup>6.55</sup> (two bonds), Gln-195<sup>5.44</sup>, Asn-191<sup>5.40</sup>, and Asn-159<sup>4.60</sup>). The cyano group, which is important for affinity to P2Y<sub>12</sub>, formed two hydrogen bonds with Gln-195<sup>5.44</sup><sup>205</sup>. The -CH<sub>3</sub> opposite the cyano group, formed a hydrophobic interaction with Val-102<sup>3.30</sup>. The pyridine moiety accommodating these two groups formed a hydrophobic interaction with Val-190<sup>5.39</sup>. This ring also formed  $\pi$ - $\pi$  stacking with Tyr-105<sup>3.33</sup>. PLIP picked up 12 out of the 14 interactions reported for AZD1283 in the original crystal structure paper<sup>17</sup>. The polar interaction between Tyr-109<sup>3.37</sup> and the cyano group was missing. Additionally, an interaction with Phe-106<sup>3.34</sup> was missing, which is suggested to form a part of the sub-cavity which accommodates AZD1283's ethyl ester group (interaction type not reported).

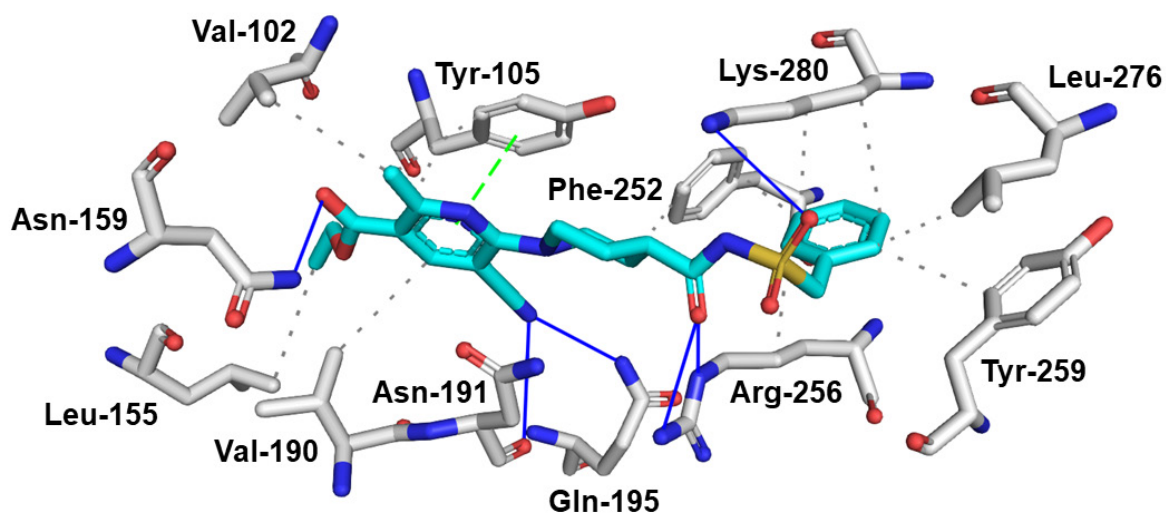


**Figure 63: Recognition of the co-crystallised AZD1283 within the orthosteric ligand binding pocket of the human P2Y<sub>12</sub> structure.** AZD1283 is shown in cyan. The protein is shown as silver sticks. Grey dashes represent hydrophobic interactions, blue lines represent hydrogen bonds, and green dashes represent  $\pi$ - $\pi$  stacking. The image was created using PyMOL.

#### 4.5. *In vitro* screens lead to the discovery of two novel inhibitors of platelet aggregation

Following *in vitro* and *in silico* validations of the positive control, the assay and software were deemed reliable to search for hits. Several criteria were established beforehand. The first criterion related to the outcome of *in silico* screens and required that only novel scaffolds would be considered for *in vitro* testing. Secondly, that compounds would have to meet a cut-off value of achieving at least 30% inhibition of ADP-induced platelet aggregation to warrant further exploration. When initially deciding the value to set as the threshold, the literature was explored. However, due to lack of data on such compound screens using 96-well plate aggregometry or Born aggregometry for guidance, a value had to be decided using in-house data. Thus, based on the weak antagonism explored earlier with AMP which achieved 30.6% inhibition of platelet aggregation (**Figure 26**), the threshold for inhibition was arbitrarily set at 30%.

Three chemical libraries containing diverse small-molecule scaffolds were first subject to ligand-based screens, a) for shape and structural similarity to AZD1283 in ROCS, and b) for electrostatic field similarity to AZD1283 in Forge. This was followed by a structure-based screen (docking) which allowed analysis of protein-ligand interactions. The libraries used for *in silico* screening were Enamine™ (200,000 molecules), Vitas Broadway™ (32,000 molecules), and Specs™ (208,670 molecules). The best hits were chosen based on scores ranked for (a) and (b), and subsequent manual inspection of protein-ligand interactions from docking. 33 compounds were purchased for *in vitro* validation.

As shown in **Figure 64**, 15 compounds from the Enamine™ library, which were identified as potential P2Y<sub>12</sub> ligands, were screened *in vitro*. Based on their solubility, the first set were screened at 50µM (**Figure 65**), and the second set were screened at 10µM (**Figure 66**). Compounds for all screens were dissolved in DMSO (with the final DMSO concentration not exceeding 0.1%). They were aliquoted and stored at -80°C.

Upon addition of HBS to create working solutions, compounds were sonicated and vortexed to ensure they were fully dissolved. PRP was incubated with compounds for 30 minutes (RT), and platelets were activated with 3 $\mu$ M ADP. This was followed by 5 minutes of shaking. End-point absorbance measurements were recorded. As shown in **Figures 65** the positive control (10 $\mu$ M) achieved 75.3% inhibition. However, the test compounds achieved little inhibition compared to vehicle. Thus, they did not meet the second criterion and were eliminated from the work.

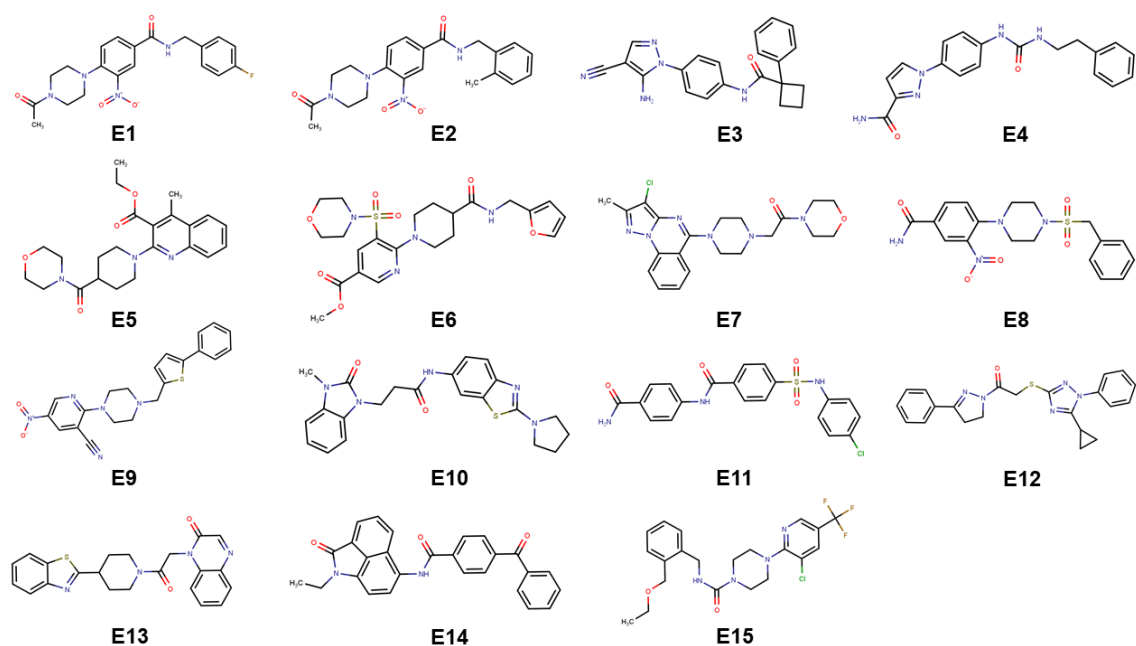


**Figure 64: 2D structures of 15 compounds purchased from Enamine for subsequent experimental testing.** The structures were drawn using MarvinSketch.

As shown in **Figure 66**, the second set of compounds from Enamine were also not effective. Whilst the positive control achieved 72.7% inhibition, the test compounds achieved little inhibition compared to vehicle. These compounds also did not meet the second criterion and were eliminated from the work. It was not possible to pin-point specific reasons as to why this set of 15 compounds were not effective, due to their highly diverse scaffolds.

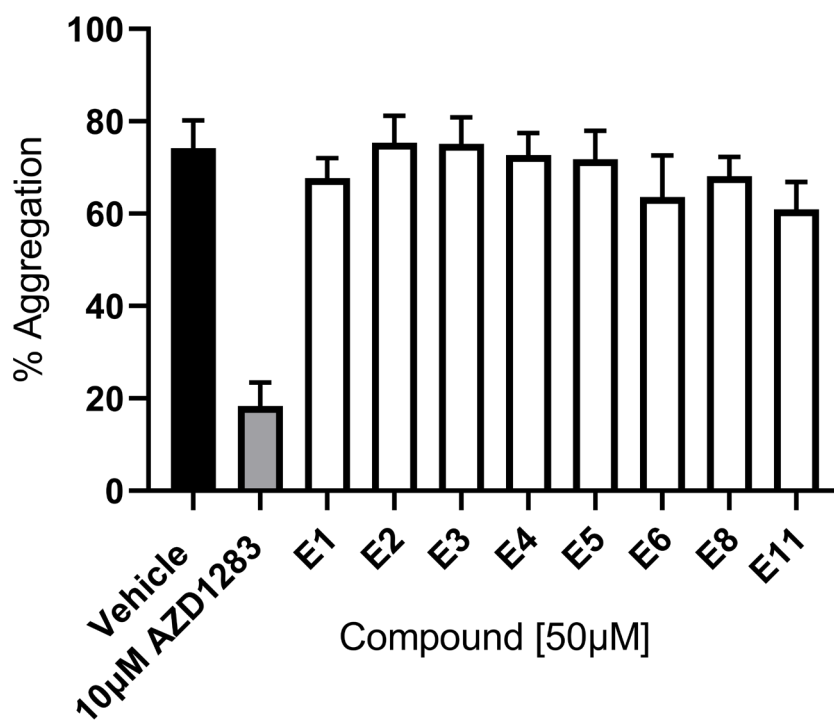


**Figure 65: Experimental evaluation of the purchased Enamine molecules (50 $\mu$ M) against platelet aggregation.** PRP was incubated with positive control (10 $\mu$ M) or test compounds (50 $\mu$ M) for 30 minutes (RT), and platelets were activated using 3 $\mu$ M ADP. This was followed by 5 minutes of shaking. Absorbance was measured and the % aggregation was determined (mean  $\pm$  SEM;  $n = 5$  independent blood donors).

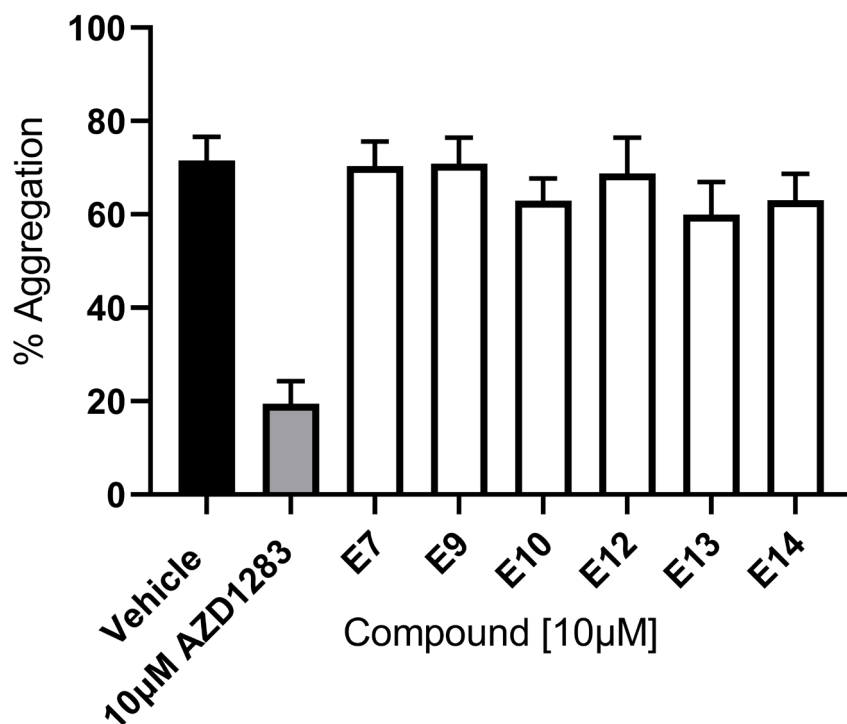


**Figure 66: Experimental evaluation of the purchased Enamine molecules (10µM) against platelet aggregation.** PRP was incubated with positive control (10µM) or test compounds (10µM) for 30 minutes (RT), and platelets were activated using 3µM ADP. This was followed by 5 minutes of shaking. Absorbance was measured and the % aggregation was determined (mean ± SEM;  $n = 5$  independent blood donors).

The next set of compounds were from the Vitas Broadway library (5 compounds - **Figure 67**). PRP was incubated with compounds for 30 minutes (RT), and platelets were then activated using 3 $\mu$ M ADP. The concentrations of the test compounds are stated in **Figure 68**.

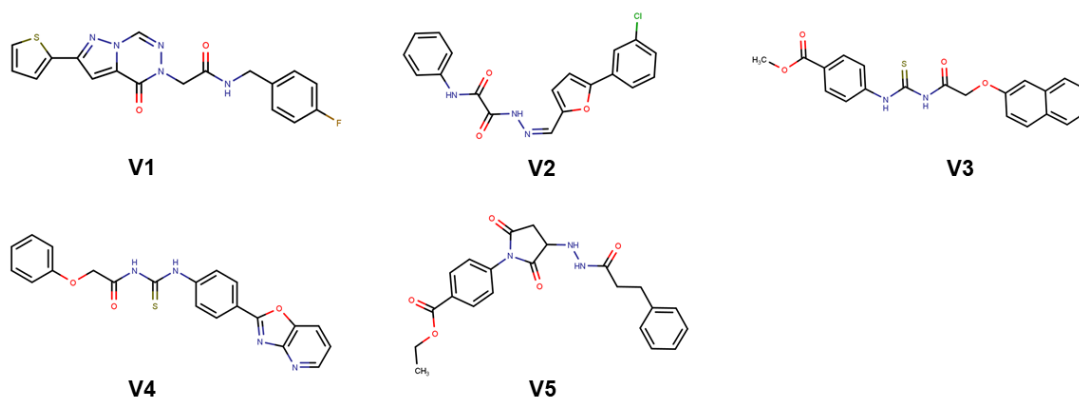


**Figure 67: 2D structures of five compounds purchased from Vitas for subsequent experimental evaluation.** The structures were drawn using MarvinSketch.

As shown in **Figures 68** the positive control (10 $\mu$ M) achieved 83.4% inhibition. However, four of the test compounds achieved little inhibition compared to vehicle. Thus, these compounds did not meet the second criterion and were eliminated from the work. Compound V3 showed some inhibition (23.1%). However, this value did not meet the inhibition threshold of 30% (criterion 2). Thus, the compound was not considered further.

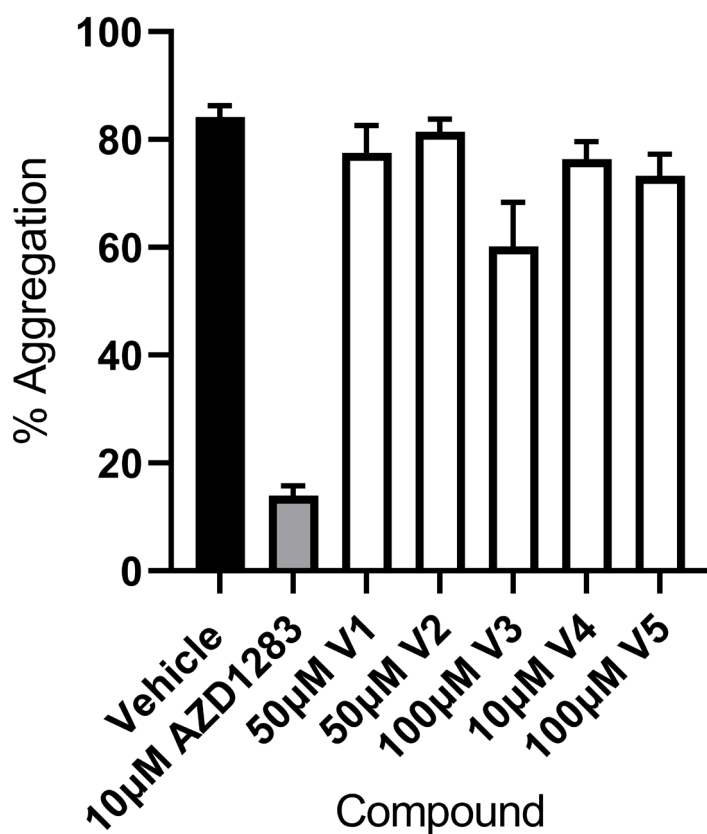


**Figure 68: Experimental evaluation of the purchased Vitas molecules against platelet aggregation.** PRP was incubated with positive control (10µM) or test compounds (stated concentration) for 30 minutes (RT), and platelets were activated using 3µM ADP. This was followed by 5 minutes of shaking. Absorbance was measured and the % aggregation was determined (mean  $\pm$  SEM;  $n = 5$  independent blood donors).

Subsequently, 14 compounds (**Figure 69**) chosen from the Specs library were tested. PRP was incubated with compounds for 30 minutes (RT), and platelets were activated using 3 $\mu$ M ADP. In the first screen, seven compounds were tested at 100 $\mu$ M (according to their solubility). As shown in **Figure 70**, the positive control (10 $\mu$ M) achieved 81.8% inhibition. However, the compounds achieved little inhibition compared to vehicle. Thus, these seven compounds did not meet the second criterion and were eliminated from the work.

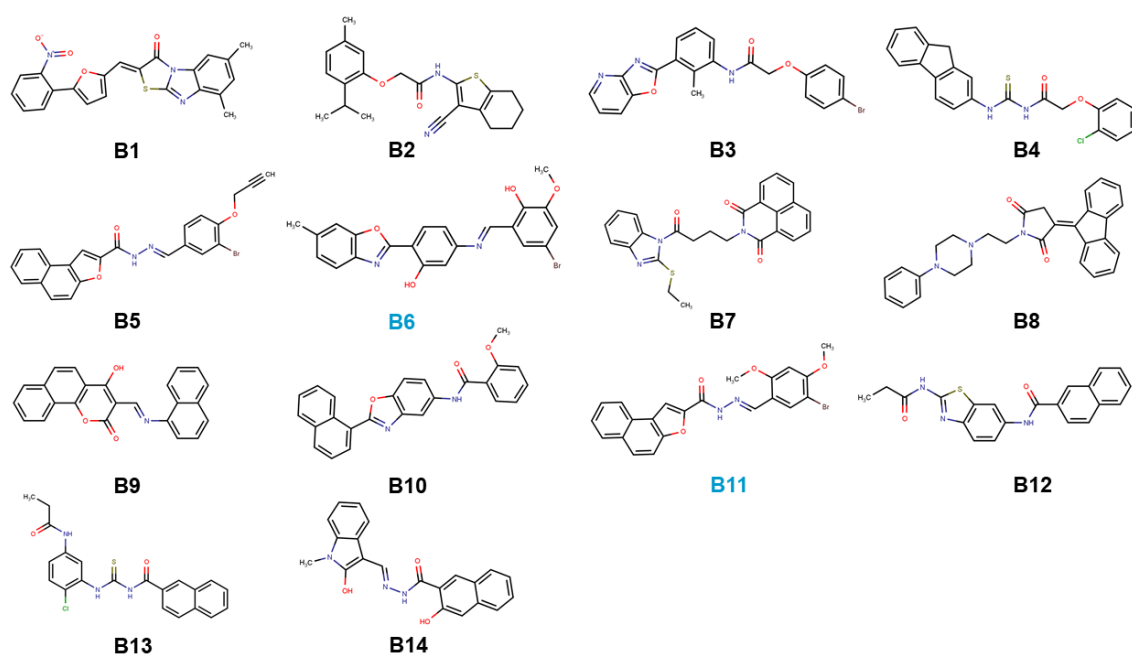


**Figure 69: 2D structures of 14 compounds purchased from Specs for subsequent experimental evaluation.** The structures were drawn using MarvinSketch.

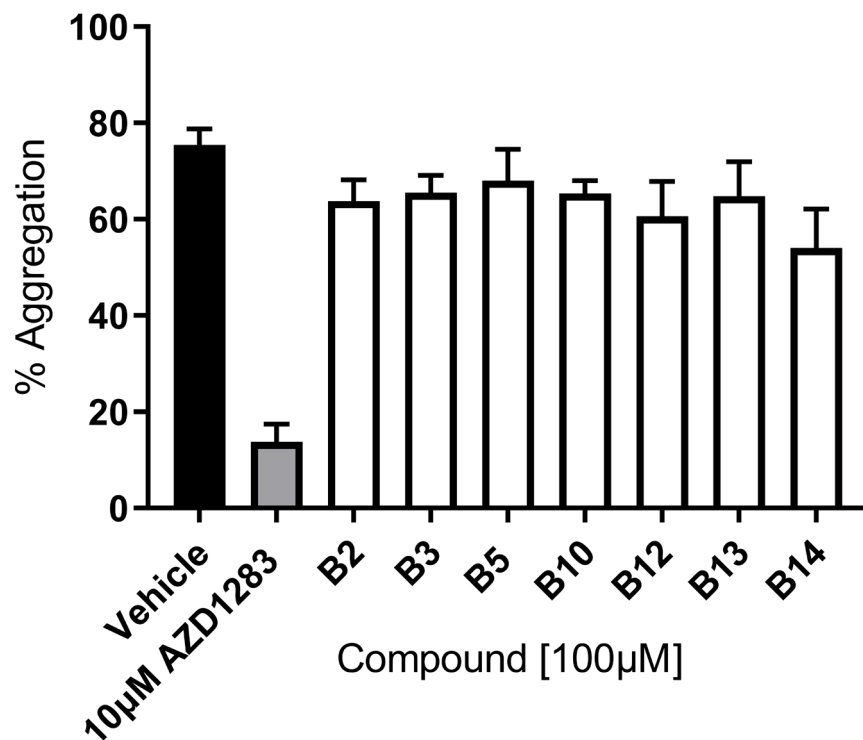


**Figure 70: Experimental evaluation of the purchased Specs molecules (100µM) against platelet aggregation.** PRP was incubated with positive control (10µM) or test compounds (100µM) for 30 minutes (RT), and platelets were activated using 3µM ADP. This was followed by 5 minutes of shaking. Absorbance was measured and the % aggregation was determined (mean ± SEM;  $n = 6$  independent blood donors).

In the second screen, five compounds were tested at 10 $\mu$ M, and two were tested at 50 $\mu$ M (according to their solubility). As shown in **Figure 71**, the positive control (10 $\mu$ M) achieved 76.6% inhibition compared to vehicle. Two compounds met the established criteria. Compared to vehicle, compound B6 (10 $\mu$ M) achieved 30.0% inhibition, and compound B11 (10 $\mu$ M) achieved 36.2% inhibition.

Like AZD1283, both compounds possess a phenyl ring. Between the compounds, two common groups are attached to the phenyl ring: a bromine and a methoxy group (**Figure 69**). Furthermore, near the phenyl ring is a nitrogen group, which is also a feature found in AZD1283. B6 contains a second phenyl ring in the mid-region of its scaffold, like the AZD1283 scaffold. However, this intermediary group is not present in the intermediary region of the B11 scaffold. In the final portion of their scaffolds, both compounds contain fused rings. B6 possesses a benzoxazole portion and B11 possessed a naphtho-furan portion.

B11 is closely related to B5, which caused very little inhibition (9.82% inhibition at 100 $\mu$ M) compared to vehicle (**Figure 70**). B5 has a group loss at the phenyl ring (the methoxy group) and a group addition (a methylidyne group). These group changes appear to not be well-tolerated at this region. Additionally, B3 had the same basic scaffold as B6, but with several group changes throughout its structure. It caused little inhibition (13.2%) at 100 $\mu$ M (**Figure 70**).

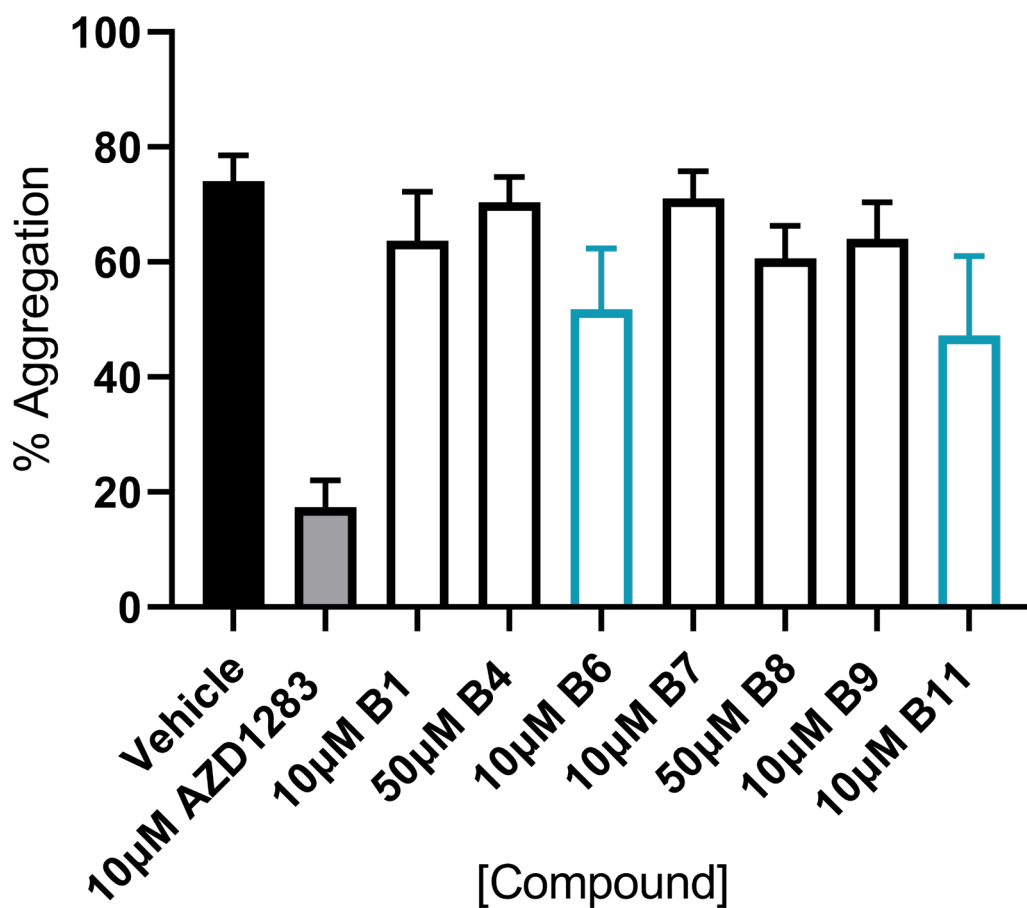


**Figure 71: Experimental evaluation of the purchased Specs molecules (10µM or 50µM) against platelet aggregation.** PRP was incubated with positive control (10µM) or the test compounds (concentration stated) for 30 minutes (RT), and platelets were activated using 3µM ADP. This was followed by 5 minutes of shaking. Absorbance was measured and the % aggregation was determined (mean ± SEM; *n* = 5 independent blood donors).

Subsequently, compound B6 (10 $\mu$ M) and compound B11 (10 $\mu$ M) were tested with varying concentrations of ADP. PRP was incubated with compound for 30 minutes (RT) and platelets were activated. As shown in **Figure 72**, the positive control produced a rightward shift of the ADP concentration-response curve (LogEC<sub>50</sub>: -5.34) compared to the vehicle (LogEC<sub>50</sub>: -6.60). Compound B6 also produced a rightward shift of the concentration-response curve (LogEC<sub>50</sub>: -6.04) compared to the vehicle. An extra-sum-of-squares F test was performed, where the null hypothesis (one curve adequately fits the vehicle and B6 data sets) was rejected, thus the B6 curve was significantly different from vehicle control ( $p < 0.0001$ ).

The E<sub>max</sub> value obtained for ADP in the presence of B6 indicated that B6 was a competitive antagonist (ADP + vehicle E<sub>max</sub>: 90.5%, ADP + B6 E<sub>max</sub>: 91.2%, ADP + AZD1283 E<sub>max</sub>: 96.3%). At the highest concentration of ADP tested (100 $\mu$ M), the following mean % aggregation values were achieved: ADP + vehicle: 91.6  $\pm$  6.29%, ADP + B6: 90.8  $\pm$  6.53%, and ADP + AZD1283: 91.3  $\pm$  6.63%. Schild analysis determined that AZD1283 achieved a K<sub>D</sub> value of 5.76 x 10<sup>-7</sup> M (576nM), and B6 achieved a K<sub>D</sub> value of 3.76 x 10<sup>-6</sup> M (3.76 $\mu$ M). In these experiments, B6 exhibited classical competitive antagonism.

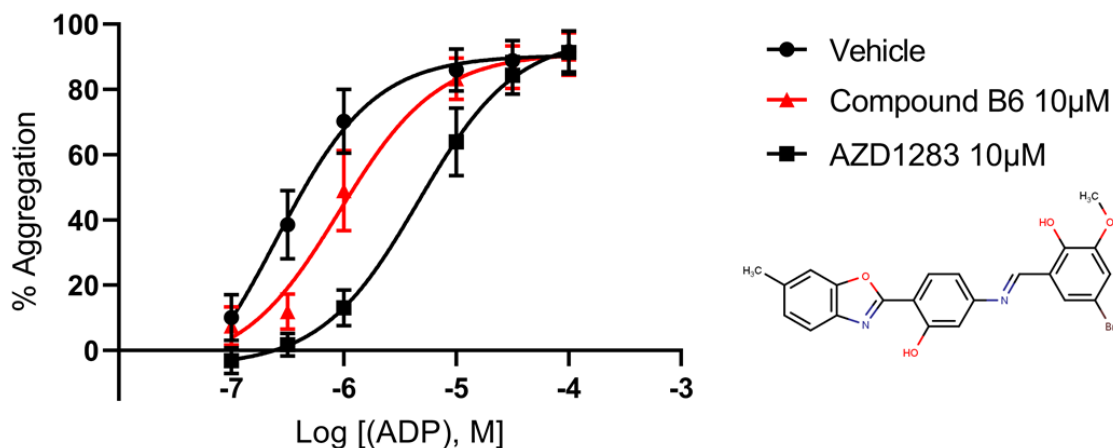


**Figure 72: Effect of compound B6 (10 μM) on platelet aggregation using varying concentrations of ADP.** PRP was incubated with compounds (10 μM) for 30 minutes (RT) and platelets were then activated with varying concentrations of ADP. Shaking occurred for 5 minutes. Absorbance was measured and the % aggregation was determined (mean ± SEM; *n* = 5 independent blood donors). The structure of compound B6 (drawn using MarvinSketch) is shown.

Compound B11 was then tested. As shown in **Figure 73**, the positive control produced a rightward shift of the ADP concentration-response curve (LogEC<sub>50</sub>: -5.25) compared to the vehicle (LogEC<sub>50</sub>: -6.50). Compound B11 also produced a rightward shift of the ADP concentration-response curve (LogEC<sub>50</sub>: -6.00) compared to the vehicle. An extra-sum-of-squares F test was performed, where the null hypothesis (one curve adequately fits the vehicle and B11 data sets) was rejected, thus the B11 curve was significantly different from vehicle control ( $p < 0.0001$ ).

The E<sub>max</sub> value obtained for ADP in the presence of compound B11 indicated that B11 was a competitive antagonist (ADP + vehicle E<sub>max</sub>: 94.8%, ADP + B11 E<sub>max</sub>: 95.1%, ADP + AZD1283 E<sub>max</sub>: 97.1%). At the highest concentration of ADP tested (100μM), the following mean % aggregation values were achieved: ADP + vehicle: 96.1 ± 3.28 % aggregation, ADP + B11: 92.1 ± 3.23 % aggregation, and ADP + AZD1283: 94.1 ± 3.44 %. Schild analysis determined that AZD1283 achieved a K<sub>D</sub> value of 5.94 x 10<sup>-7</sup> M (594nM), and B11 achieved a K<sub>D</sub> value of 4.53 x 10<sup>-6</sup> M (4.53μM). Like B6, compound B11 also exhibited classical competitive antagonism.

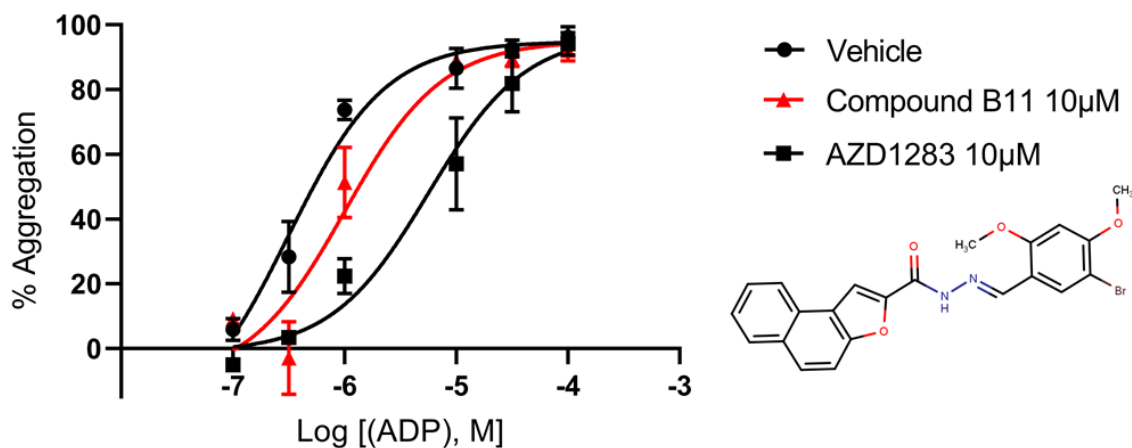


**Figure 73: Effect of compound B11 (10 µM) on platelet aggregation using varying concentrations of ADP.** PRP was incubated with compounds (10 µM) for 30 minutes (RT) and platelets were then activated with varying concentrations of ADP. Shaking occurred for 5 minutes. Absorbance was measured and the % aggregation was determined (mean ± SEM;  $n = 5$  independent blood donors). The structure of compound B11 (drawn using MarvinSketch) is shown.

The following results detail the *in silico* data that were generated for compounds B6 and B11 prior to *in vitro* experiments. Ligand-based screens were initially performed using the screening libraries previously described. To briefly reiterate the *in silico* methods, the bioactive conformation of AZD1283 was first retrieved from PDB and subsequently energy-minimised using the MMFF94 implemented in Open Babel (version 2.4.0). The structure of AZD1283 was then imported into ROCS as a query ligand. A conformer library was generated for each screening library using OMEGA, version 3.0.1.2.

ROCS aligned the query ligand to the multiple conformers of each screening compound. It compared the shape (denoting 3D shape) and colour (denoting chemical similarity) for each alignment to the query ligand. The program returned a Tanimoto Combo score for each alignment (minimum obtainable score: 0, maximum obtainable score: 2). This is a combination of the Shape Tanimoto and Color Tanimoto scores, both of which are individually scored out of a maximum obtainable score of 1. The top hits proceeded to further filtering in Forge, version 10.4.2, where molecular field-based alignment was performed, and compounds were ranked by electrostatic field similarity to AZD1283.

Subsequently, the best hits proceeded to docking against the antagonist-bound structure of the P2Y<sub>12</sub> receptor (PDB ID: 4NTJ). Blind docking was performed in AutoDock Vina and GlideXP. Focused docking was performed in the GOLD suite. Protein-ligand interactions obtained from docking were manually inspected in PLIP and compared to the interactions of the co-crystallised ligand with the receptor. Thus, all compounds were ranked according to the total number of interactions in common with AZD1283 (**Figure 63**; 12 interactions).

As shown in **Figure 74**, compound B6 achieved a Shape Tanimoto score of 0.621, and a Color Tanimoto score of 0.192. The aim of this approach was to find novel scaffolds which could retain significant similarities in shape and colour (thus, pharmacophore) to AZD1283, so that they would phenocopy the query molecule. Compound B6 achieved a Tanimoto Combo score of 0.813. Compound B11 achieved a Shape Tanimoto score of 0.516 and a Color Tanimoto score of 0.102. Its Tanimoto Combo score was lower than that of B6, at 0.618.

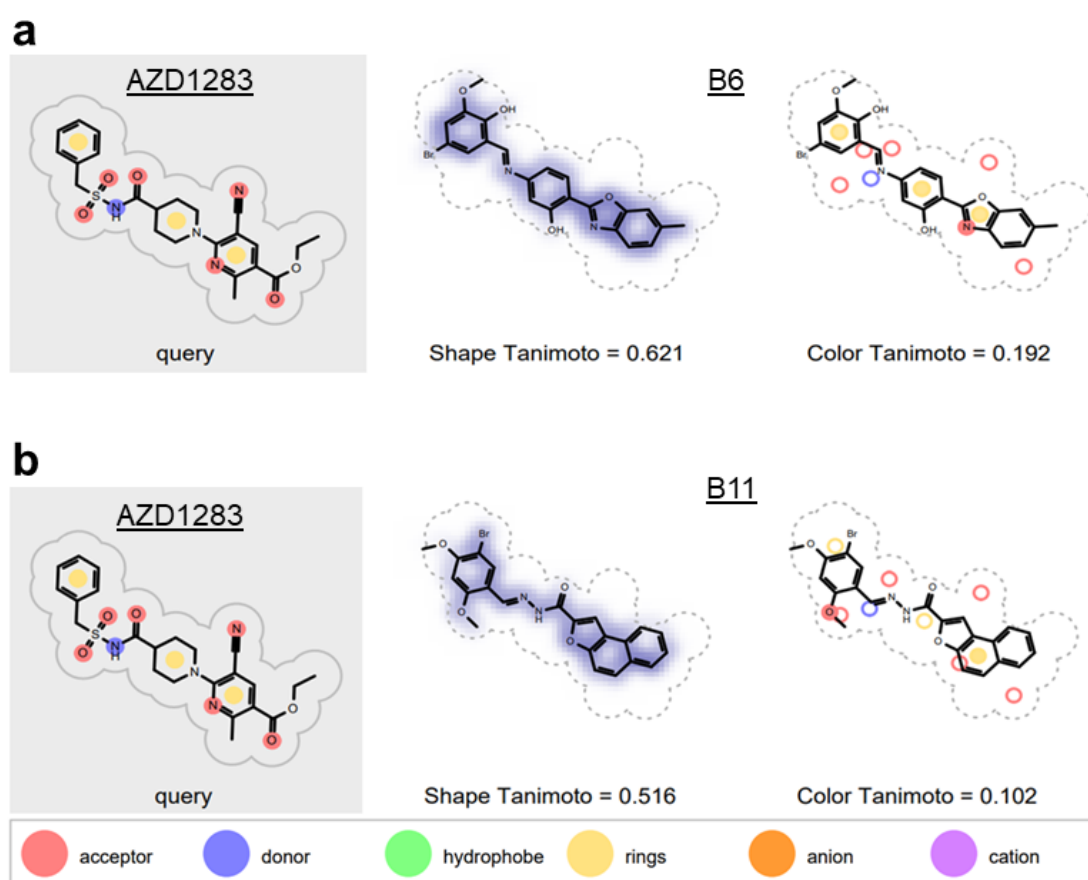


**Figure 74: Similarity indices for compounds B6 and B11 with respect to AZD1283.** 3D structures of compounds in the Specs library were aligned to that of the query ligand, AZD1283, in ROCS. Results are shown for compounds B6 (**a**) and B11 (**b**). A Shape Tanimoto and Color Tanimoto score (each out of 1) were generated for each compound, as well as a Tanimoto Combo score (mentioned in-text) out of 2. Shape similarity to AZD1283 is shown in dark blue. Key shows functional groups considered for evaluating chemical similarity. The images were created using the ROCS Report.

As shown in **Figure 75**, molecular field-based alignment in Forge revealed AZD1283's distinct regions of negative electrostatic potential (**Figure 75a**, **Figure 75d**). Forge scored the compounds out of a maximum of 1 for field similarity to AZD1283. B6 and B11 obtained field scores of 0.612 (**Figure 75b**) and 0.636 (**Figure 75c**), respectively. In agreement with ROCS, Forge aligned the phenyl ring of B6 against the phenyl ring of AZD1283, as expected. Conversely, Forge aligned the naphtho-furan portion of B11 against the phenyl ring of AZD1283, which was not in accordance with the results obtained for this compound in ROCS.

However, this may be expected as ROCS and Forge were not assessing the same criteria. This finding introduced some ambiguity as to the correct position in which B11 should be compared to AZD1283. Nevertheless, it was aimed that this would be further explored in the subsequent docking experiments, where B6 and B11's predicted mode of binding would be considered relative to the protein pocket where AZD1283 binds.

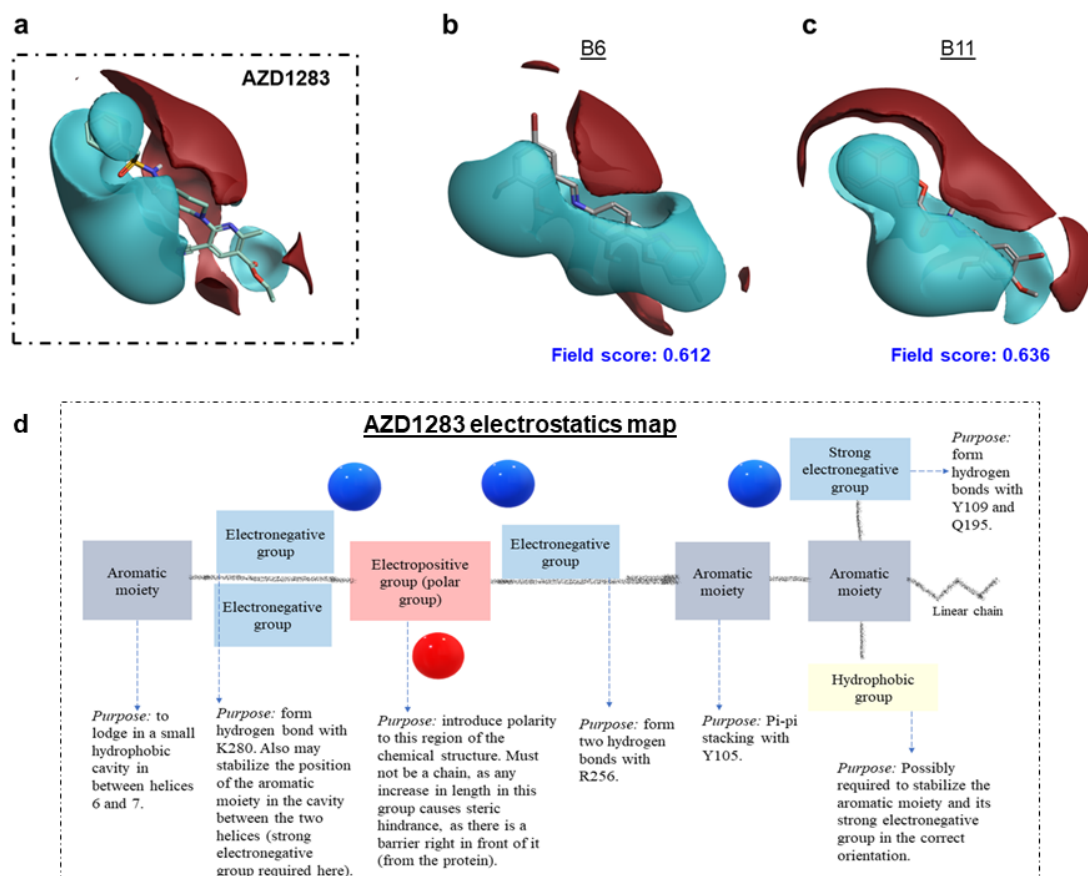


**Figure 75: Molecular field-based alignment of compounds B6 and B11 with respect to AZD1283.** Regions of positive electrostatic potential are shown in red. Regions of negative electrostatic potential are shown in cyan. Field scores are shown in blue font.

**a)** The reference ligand, AZD1283 (green sticks), to which molecules were aligned to in Forge. **b)** Compound B6 is shown as grey sticks. **c)** Compound B11 is shown as grey sticks. **d)** AZD1283 electrostatic map showing three distinct regions of negative electrostatic potential, and one distinct region of positive electrostatic potential. The purpose of each group relative to the protein is stated. Amino acid residues mentioned: K280 (Lys-280<sup>7,35</sup>), R256: (Arg-256<sup>6,55</sup>), Y105: (Tyr-105<sup>3,33</sup>), Y109: (Tyr-109<sup>3,37</sup>), Q195: (Gln-195<sup>5,44</sup>). Images (a)-(c) were created using Forge and image (d) was created using Microsoft PowerPoint.

Blind docking against the entire protein as search space was performed in GlideXP and AutoDock Vina. As shown in **Figure 76a-b**, GlideXP predicted that compound B6 binds in the same pocket as the co-crystallised ligand, AZD1283. B6 achieved a GlideXP score of -9.18 kcal/mol. As previously mentioned in the positive control validation section, AZD1283 was predicted to have a slightly better (more negative) predicted binding affinity of -12.7 kcal/mol in GlideXP. B6's mode of binding was predicted such that its phenyl ring overlaid that of AZD1283, in the sub-cavity between helices 6 and 7.

As shown in **Figure 76c-d**, AutoDock Vina also predicted that compound B6 binds in the same pocket as the co-crystallised ligand, AZD1283. Five independent docking runs were also performed, where the pose and score of B6 ( $-10.7 \pm 0.100$  kcal/mol) were highly reproducible. As previously mentioned in the positive control validation section, AZD1283 obtained a score of  $-8.90 \pm 0.440$  kcal/mol in AutoDock Vina. Thus, AutoDock Vina predicted a slightly better (more negative) predicted binding affinity for compound B6. As it has already been established *in vitro* that AZD1283 is more potent than B6, this score should be taken with caution.

Importantly, both programs reached a consensus on the pose of B6 against P2Y<sub>12</sub>, which was in the same pocket as the co-crystallised ligand. Focused docking was also performed using the GOLD suite. The predicted mode of binding for B6 (**Figure 77**) was similar to that obtained in GlideXP and AutoDock Vina with regards to the spatial positioning of chemical groups relative to the pocket and AZD1283. B6 obtained a ChemPLP score of  $89.8 \pm 0.66$  (mean  $\pm$  SEM; five independent docking runs), whereas AZD1283 obtained a ChemPLP score of  $88.7 \pm 2.11$ . Poses and scores were highly reproducible.

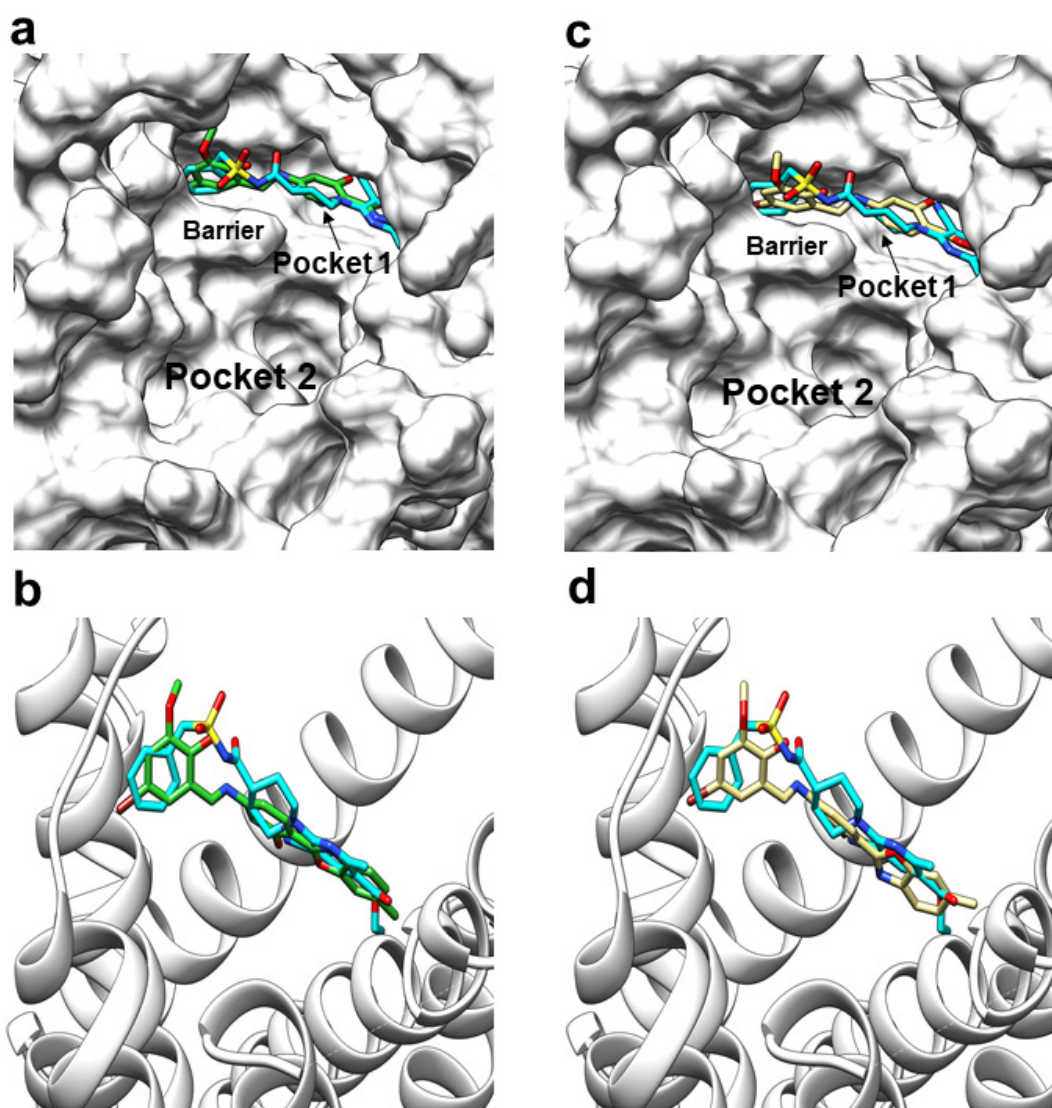


**Figure 76: Possible binding modes of compound B6 against the human P2Y<sub>12</sub> structure predicted through blind docking.** **a)** Blind docking against P2Y<sub>12</sub> in GlideXP showing compound B6 (green sticks) docked in the same pocket as the co-crystallised ligand, AZD1283 (cyan sticks). The protein is shown as a white surface representation (PDB ID: 4NTJ). Pocket 1, pocket 2, and the barrier between them is labelled (Tyr-105<sup>3,33</sup> and Lys-280<sup>7,35</sup>). **b)** Zoomed-in image of docking in GlideXP, where the protein is shown as white ribbons (cartoon representation), compound B6 is shown as green sticks, and AZD1283 is shown as cyan sticks. **c)** Blind docking in AutoDock Vina showing compound B6 (yellow sticks) docked in the same pocket as the co-crystallised ligand, AZD1283 (cyan sticks). The protein is shown as a white surface representation. Pocket 1, pocket 2, and the barrier between them is labelled. **d)** Zoomed-in image of docking in AutoDock Vina, where the protein is shown as white ribbons (cartoon representation), compound B6 is shown as yellow sticks, and AZD1283 is shown as cyan sticks. The images were created using UCSF Chimera.

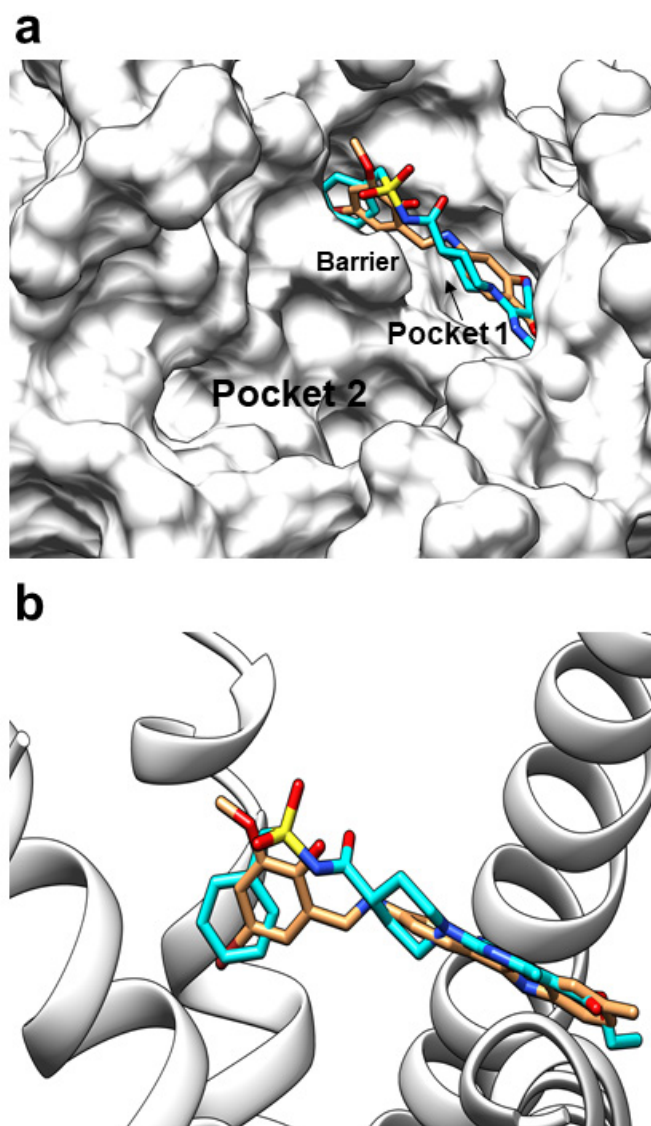


**Figure 77: Possible binding mode of compound B6 against the human P2Y<sub>12</sub> structure predicted through focused docking. a)** The pose obtained for compound B6 (orange sticks) through focused docking against P2Y<sub>12</sub> in the GOLD suite. The pose of the co-crystallised ligand, AZD1283 (cyan sticks), is also shown. The protein is shown as a white surface representation. Pocket 1, pocket 2, and the barrier between them is labelled (Tyr-105<sup>3.33</sup> and Lys-280<sup>7.35</sup>). **b)** Zoomed-in image of the docked poses from GOLD, where the protein is shown as white ribbons (cartoon representation), compound B6 is shown as orange sticks, and AZD1283 is shown as cyan sticks. The images were created using UCSF Chimera.

To explore protein-ligand interactions, the B6 docked pose from **Figure 76c-d** (blind docking in AutoDock Vina) was analysed in PLIP. As shown in **Figure 78**, B6 had 10 interactions in common with AZD1283 (**Figure 63**). The B6 phenyl ring formed hydrophobic interactions with Phe-252<sup>6.51</sup>, Arg-256<sup>6.55</sup>, and Lys-280<sup>7.35</sup>. However, B6 was missing a hydrophobic interaction with Tyr-259<sup>6.58</sup> in comparison to AZD1283. Furthermore, B6 formed one hydrogen bond with Arg-256<sup>6.55</sup>, whereas AZD1283 formed two interactions with this residue. Conversely, B6 formed two  $\pi$ - $\pi$  stacking interactions with Tyr-105<sup>3.33</sup>, whereas AZD1283 formed one  $\pi$ - $\pi$  stacking interaction with this residue. The hydrogen bond that AZD1283 formed with Asn-159<sup>4.60</sup> was replaced with a hydrophobic interaction in B6.

B6 was also missing a hydrophobic interaction with Leu-155<sup>4.56</sup>, which the ethyl ester group of AZD1283 interacts with. It has been reported that replacement of this ethyl ester group with an *i*-propyl or methyl group results in a loss of potency<sup>18,205</sup>. B6 has a methyl group attached to its benzoxazole portion, however this did not align directly with the position of the ethyl ester group in AZD1283 (**Figure 74**). B6 also formed a hydrophobic interaction with Tyr-109<sup>3.37</sup>. It has previously been suggested that the cyano group of AZD1283 may form a hydrophobic interaction with Tyr-109<sup>3.37</sup> based on protein-ligand interaction analysis in another software (the name of which was not stated in the paper, but may belong to the Schrödinger suite)<sup>17</sup>.

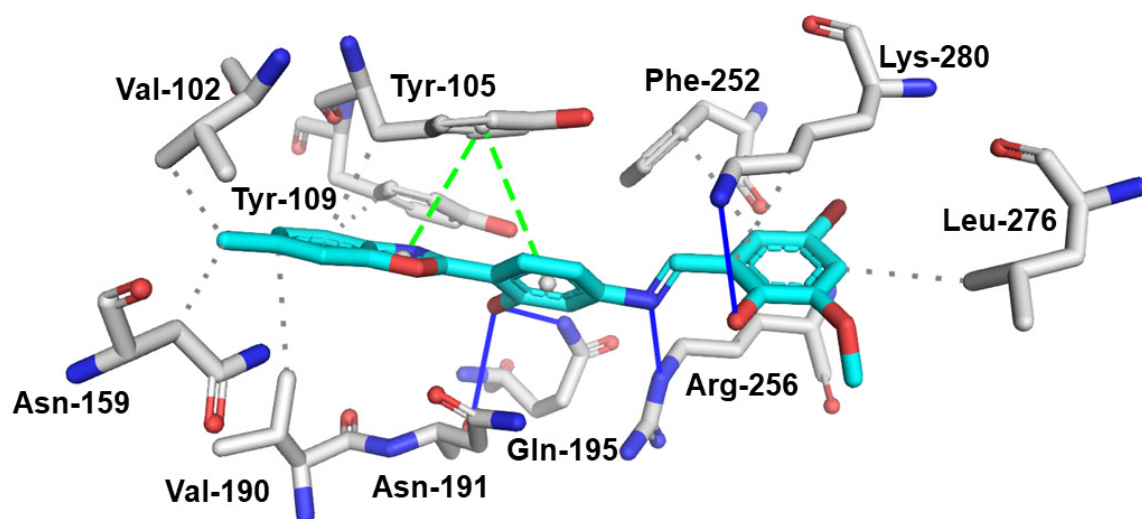


**Figure 78: Recognition of compound B6 within the orthosteric ligand binding pocket of the human P2Y<sub>12</sub> structure.** The blind docking pose of B6 from **Figure 76c-d** was analysed using PLIP. Compound B6 is shown in cyan. The protein is shown as silver sticks. Grey dashes represent hydrophobic interactions, blue lines represent hydrogen bonds, and green dashes represent  $\pi$ - $\pi$  stacking. The hydrogen bond with Arg-256<sup>6.55</sup> is out of view. The image was created using PyMOL.

As shown in **Figure 79a-b**, GlideXP predicted that compound B11 binds in the same pocket as the co-crystallised ligand, AZD1283. B11 achieved a GlideXP score of -9.15 kcal/mol (AZD1283 score: -12.7 kcal/mol). B11's mode of binding was predicted such that its naphtho-furan portion overlaid with AZD1283's phenyl ring, in the sub-cavity between helices 6 and 7 of P2Y<sub>12</sub>. As shown in **Figure 79c-d**, AutoDock Vina also predicted that compound B11 binds in the same pocket as the co-crystallised ligand, AZD1283. Five independent docking runs were also performed, where the pose and score of B11 ( $-11.4 \pm 0.0200$  kcal/mol) were highly reproducible (AZD1283 score:  $-8.90 \pm 0.440$  kcal/mol).

Focused docking was also performed using the GOLD suite. The predicted mode of binding for B11 (**Figure 80**) was different to that obtained in GlideXP and AutoDock Vina with regards to the spatial positioning of chemical groups relative to the pocket and AZD1283. GOLD predicted that B11's phenyl ring (and not its naphtho-furan portion) overlaid AZD1283's phenyl ring. B11 obtained a ChemPLP score of  $81.3 \pm 0.500$  (mean  $\pm$  SEM; five independent docking runs), compared to AZD1283's ChemPLP score of  $88.7 \pm 2.11$ . Poses and scores in GOLD were highly reproducible. There did not appear to be a consensus between the blind docking and focused docking software as to the predicted binding mode of B11. This was also reminiscent of the lack of consensus between ROCS and Forge as to how B11 aligns against AZD1283.

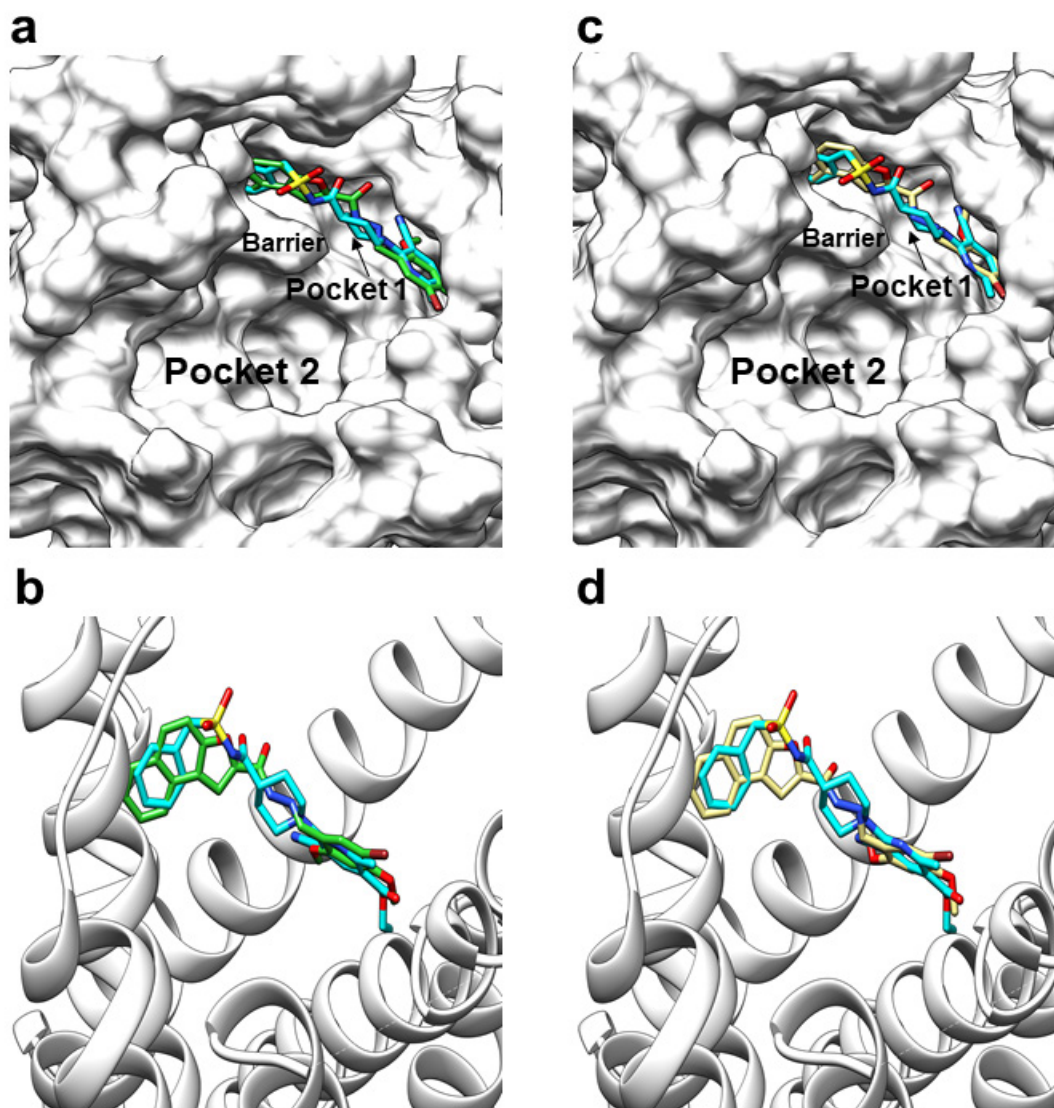


**Figure 79: Possible binding modes of compound B11 against the human P2Y<sub>12</sub> structure predicted through blind docking.** **a)** Blind docking against P2Y<sub>12</sub> in GlideXP showing compound B11 (green sticks) docked in the same pocket as the co-crystallised ligand, AZD1283 (cyan sticks). The protein is shown as a white surface representation (PDB ID: 4NTJ). Pocket 1, pocket 2, and the barrier between them is labelled (Tyr-105<sup>3,33</sup> and Lys-280<sup>7,35</sup>). **b)** Zoomed-in image of docking in GlideXP, where the protein is shown as white ribbons (cartoon representation), compound B11 is shown as green sticks, and AZD1283 is shown as cyan sticks. **c)** Blind docking in AutoDock Vina showed that compound B11 (yellow sticks) docked in the same pocket as the co-crystallised ligand, AZD1283 (cyan sticks). The protein is shown as a white surface representation. Pocket 1, pocket 2, and the barrier between them is labelled. **d)** Zoomed-in image of docking in AutoDock Vina, where the protein is shown as white ribbons (cartoon representation), compound B11 is shown as yellow sticks, and AZD1283 is shown as cyan sticks. The images were created using UCSF Chimera.

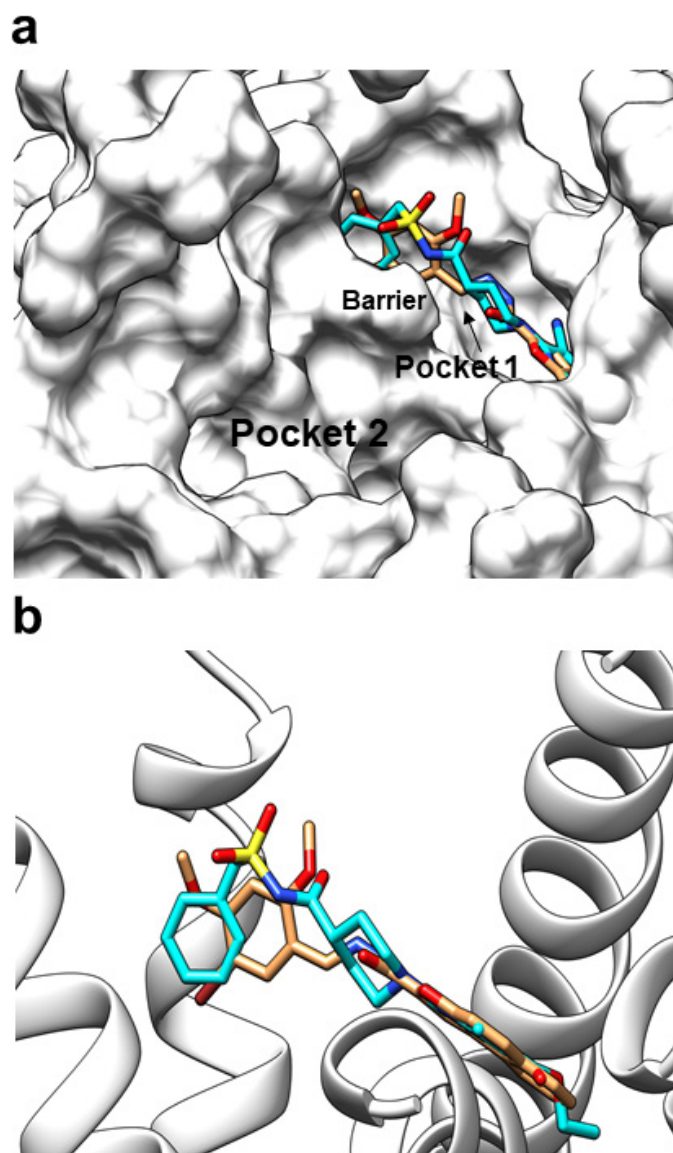


**Figure 80: Possible binding mode of compound B11 against the human P2Y<sub>12</sub> structure predicted through focused docking. a)** The pose obtained for compound B11 (orange sticks) through focused docking against the P2Y<sub>12</sub> structure in the GOLD suite. The pose of the co-crystallised ligand, AZD1283 (cyan sticks), is also shown. The protein is shown as a white surface representation. Pocket 1, pocket 2, and the barrier between them is labelled (Tyr-105<sup>3.33</sup> and Lys-280<sup>7.35</sup>). **b)** Zoomed-in image of docking in GOLD, where the protein is shown as white ribbons (cartoon representation), compound B11 is shown as orange sticks, and AZD1283 is shown as cyan sticks. The images were created using UCSF Chimera.

To explore protein-ligand interactions, the B11 docked pose from **Figure 79c-d** (blind docking in AutoDock Vina) was analysed in PLIP. As shown in **Figure 81**, B11 had nine interactions in common with AZD1283 (**Figure 63**). The B11 naphtho-furan portion was predicted to form hydrophobic interactions with Phe-252<sup>6.51</sup>, Ala-255<sup>6.54</sup>, Arg-256<sup>6.55</sup>, Tyr-259<sup>6.58</sup>, Leu-276<sup>7.31</sup>, Val-279<sup>7.34</sup>, and Lys-280<sup>7.35</sup>. The interactions with Ala-255<sup>6.54</sup> and Val-279<sup>7.34</sup> were not present for AZD1283. However, interaction with these residues may be important for B11's effects, as they belong to the hydrophobic pocket between helix 6 and 7 that is crucial for receptor antagonism<sup>18</sup>.

Moreover, the naphtho-furan portion of B11 was predicted to form a hydrophobic interaction and salt bridge with Lys-280<sup>7.35</sup>, instead of a hydrogen bond as formed by the sulfonylurea group of AZD1283. Furthermore, B11 formed two hydrogen bonds with Asn-191<sup>5.40</sup> instead of the one hydrogen bond AZD1283's cyano group formed with the residue. B11 was also missing  $\pi$ - $\pi$  stacking with Tyr-105<sup>3.33</sup>, and instead formed hydrophobic interactions with this residue. Lastly, B11 was missing interactions with Val-102<sup>3.30</sup>, Gln-195<sup>5.44</sup>, and Leu-155<sup>4.56</sup>. As explained previously, B6 was also missing an interaction with Leu-155<sup>4.56</sup>. AZD1283's ethyl ester group forms a hydrophobic interaction with this residue.

With consideration to the *in silico* results obtained for B6 and B11, it was decided that B6 would be explored further using an analogue-based approach. This is because B6 obtained consistent results in various programs, and its potential mode of binding was clearer depicted than that of B11. B11 obtained ambiguous results in ligand-based screens (as to its relative alignment to AZD1283) and the docking programs had not reached a consensus on its docking pose against the protein. In addition, a slightly higher *in vitro* affinity was found for B6.

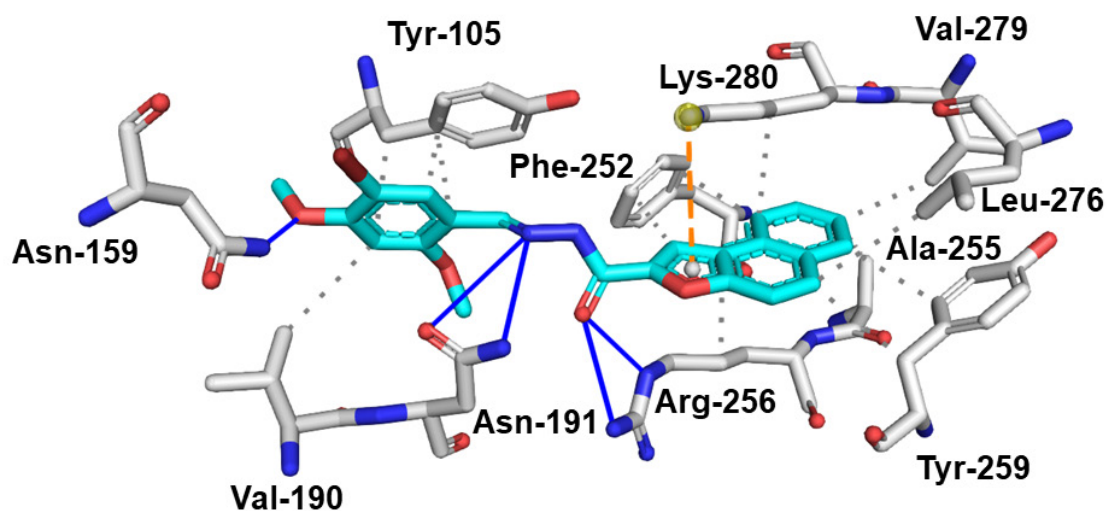


**Figure 81: Recognition of compound B11 within the orthosteric ligand binding pocket of the human P2Y<sub>12</sub> structure.** The blind docking pose of B11 from **Figure 79c-d** was analysed using PLIP. Compound B11 is shown in cyan. The protein is shown as silver sticks. Grey dashes represent hydrophobic interactions, blue lines represent hydrogen bonds, and green dashes represent  $\pi$ - $\pi$  stacking. The orange dashed lines represent a salt bridge. The image was created using PyMOL.

## 4.6. Discussion

In this chapter, ligand and structure-based *in silico* tools were used to discover two novel inhibitors of ADP-induced platelet aggregation. Some vendor libraries containing thousands of structurally diverse chemical scaffolds were virtually searched for compounds with comparable similarity indices to AZD1283. The most promising hits were then analysed for electrostatic similarity to AZD1283. Structure-based computational methods were then employed, where the best performing compounds from the ligand-based virtual screening were subjected to molecular docking against the AZD1283-stabilised conformation of P2Y<sub>12</sub>.

Hitherto, methodology similar to that described here has not been reported by anyone to identify novel modulators of the P2Y<sub>12</sub> receptor and inhibitors of platelet aggregation. In previous work, the crystal structure has mainly been used to show possible predicted binding modes for existing P2Y<sub>12</sub> ligands, or to explore possible binding modes for ligands found through iterative medicinal chemistry approaches<sup>355,356</sup>. However, the crystal structures of other class A GPCRs have been used in molecular to docking to successfully find novel ligands<sup>137,357-359</sup>. Furthermore, ligand-based screening approaches using the 3D structure of a known ligand have also been highly successful in finding novel modulators for proteins<sup>253,256</sup>. Ligand-centric software, such as ROCS, have shown a powerful ability in finding novel scaffolds and chemistries within a shape class<sup>360</sup>.

Several challenges exist in the search for novel P2Y<sub>12</sub> antagonists. High affinity in binding assays does not necessarily translate to high inhibition in a phenotypic assay like aggregometry<sup>151</sup>. For example, the free concentrations of ligand in PRP may be lower because of binding to plasma proteins. To take this into account, aggregometry was chosen as the major ‘go-to’ assay for this work. Furthermore, few changes are tolerated to the structures of the known P2Y<sub>12</sub> ligands, making analogue-based and

scaffold hopping work challenging. Dissemination of new scaffolds may allow us to further understand the key features required for novel inhibitors of platelet aggregation, as well as expand the GPCR chemical space.

Compounds B6 and B11 are novel scaffolds. The phenyl ring in compound B6 was predicted to lodge in between helices 6 and 7, which is consistent with the major proposed mechanism of antagonism for AZD1283. The phenyl ring possesses a bromine group, which gives the compound a characteristic orange-brown colour. Halogen bonds have previously been demonstrated to stabilise ligand binding in, for example, the 5-HT<sub>6</sub> receptor<sup>361,362</sup>. However, the bromine group in B6 was not found to directly interact with a residue. Although, this is likely because scoring functions in most docking programs (including Vina) do not account for halogen bonding<sup>363,364</sup>. Furthermore, it may play a role in determining the spatial positioning of the phenyl ring relative to the sub-cavity. B6 also contains a benzoxazole portion, which was predicted to interact with several key residues. Interestingly, although B6 has a non-nucleotide scaffold, its benzoxazole portion may mimic the adenine-like moieties found in ticagrelor and cangrelor<sup>150,152</sup>. However, the binding modes of these antagonists at P2Y<sub>12</sub> is not fully known. Additionally, benzoxazole derivatives have been found to be ligands at other class A GPCRs, including P2Y<sub>14</sub> and the adenosine A<sub>2A</sub> receptor<sup>365,366</sup>.

Compound B11 achieved inconsistent poses in docking, thus it is unclear whether its phenyl ring or naphtho-furan portion is more likely to bind in the cavity between helices 6 and 7. Notably, compound B5 has a structurally similar scaffold to B11, however caused little inhibition of aggregation. This compound has a significant modification at the phenyl ring - the substitution of a methyl group with a methylidyne group. SAR studies around the AZD1283 phenyl ring has suggested that few changes are tolerated at this region<sup>205</sup>. Vina and Glide predicted the naphtho-furan portion to bind in between helices 6 and 7, whereas GOLD predicted the phenyl ring to bind in

this region. This is likely because, although the programs adopt empirical scoring functions, the docking criteria that is assessed in each algorithm is different. This is useful to explore whether binding pose and score can be reproduced in programs with slightly different docking algorithms.

The details of these algorithms are outside the scope of this work but will be explained here briefly. The default scoring function in GOLD, namely the ChemPLP score, is designed to assess hydrogen bonds and shape complementarity within the binding cavity<sup>312,367,368</sup>. Vina and Glide assess more interaction terms<sup>305,306,369-371</sup>. Glide assesses hydrogen bonding, electrostatic interactions, and hydrophobic interactions. Vina assesses hydrogen bonding and hydrophobic interactions. Furthermore, Vina and Glide estimate the free of energy of binding, thus their output scores cannot be directly compared to GOLD's ChemPLP score. Importantly, compound B6 achieved similar poses in all the docking software used. Docking programs reaching a consensus on a particular pose for a compound may often mean that the compound is more likely to be promising to consider further<sup>368,372</sup>.

In AutoDock Vina, B6 and B11 achieved better mean predicted binding affinities than AZD1283. However, it is often the case that predicted binding affinities from docking do not always correlate with *in vitro* results. Docking is a complementary tool to explore the pose a ligand may adopt against a protein pocket and its potential interactions, and scores are merely to guide assessment and rank many hits. Predicted binding affinities obtained from docking seldom reflect true affinity, and this is a major limitation of docking<sup>373</sup>. High numbers of false positive hits are common in docking, which are compounds with good docking scores but little or no bioactivity. Thus, it is crucial that protein-ligand interactions are analysed in detail in comparison to the reference ligand during post-docking processing to eliminate false-positives<sup>372</sup>. Good docking scores generally indicate that the ligand has favourable contacts with the

binding pocket and is complementary in shape. However, these scores do not accurately predict whether the ligand is a strong or weak binder, or whether the ligand is an agonist or antagonist, and neither are they designed to. Although it may be more likely that the use of an antagonist-stabilised conformation of the protein in docking may lead to hits which are antagonists, this is merely an assumption.

Additionally, some X-ray crystal structures have crystal packing artefacts which are not biologically relevant<sup>374-378</sup>. The extent of crystal packing artefacts in the P2Y<sub>12</sub> crystal structures is unknown. Furthermore, as wild-type P2Y<sub>12</sub> is poorly stable, the crystal structure contains a b<sub>562</sub>RIL (BRIL) protein inserted at ICL 3 to increase stability, as well as a mutation at Asp-294<sup>7,49</sup> to increase protein yield. Although, it was reported that neither of these changes significantly affect ligand binding<sup>16,17</sup>.

Importantly, the P2Y<sub>12</sub> ligands bind via induced-fit, and the binding pocket displays extraordinary levels of plasticity, with dramatic conformational changes occurring - an effect that cannot be replicated in docking<sup>16,17,276</sup>. This is because docking programs, such as Vina and Glide, keep the protein 'rigid'<sup>379</sup>. This is a limitation of docking, as GPCRs are in constant motion and belong to a highly dynamic world. They adopt an everchanging array of conformational states. For example, when a GPCR is switching between conformational states, the transmembrane helices can move more than 10Å<sup>96</sup>. However, this limitation was partially overcome by using the antagonist-stabilised conformation of the receptor, and not the agonist-stabilised conformation. It has been suggested that accuracy of rigid docking is greater when using a bound state of the protein than an unbound (*apo*) state<sup>380</sup>. Additionally, GOLD considers the protein side chains as partially flexible, although GOLD is not generally considered more or less accurate in predicting poses than Vina and Glide. All the docking programs used here considered the ligand as flexible. This is advantageous because the algorithms sample multiple conformers of the ligand at the binding pocket to assess

complementarity and favourable contacts. Furthermore, protein contacts with the plasma membrane are not typically considered in docking software, including the ones used in this work.

Nevertheless, docking is still a powerful approach. Multiple bioactive ligands have been found through using structure-based tools, such as Vina<sup>262,263,381,382</sup>. *In silico* validations in this work showed that Vina was the best performing program to accurately reproduce the pose of the co-crystallised ligand. This result was consistent across multiple docking runs, which were performed due to the stochastic nature of the program. This consistency demonstrated the algorithm's accuracy in predicting power.

Vina is one of the popular AutoDock tools developed by the Scripps Institute. It uses a hybrid scoring function (empirical and knowledge-based)<sup>370</sup>. Whilst popularity does not necessarily translate to accuracy, a correlation has been observed between scores obtained from Vina and pIC<sub>50</sub> values obtained *in vitro*<sup>264</sup>. Although docking scores should not be over-interpreted, this demonstrates the success of the hybrid scoring function in predicting ligand binding affinities. It is based on experimental ligand binding affinity data which was fitted to a training set of protein-ligand complexes (empirical-based) and statistical analyses of ligand-bound crystal structures (knowledge-based)<sup>383-388</sup>.

Numerous studies have suggested that Vina is more accurate at predicting ligand pose than AutoDock 4.2<sup>264,370,389-393</sup>. However, there is more controversy as to which program is more accurate in scoring ligand poses<sup>391</sup>. It is likely that the programs' performance in pose and score varies across proteins, pockets shapes, and ligands. Thus, generalisations as to which program is more accurate are probably not useful, and validations are required prior to docking with each protein.

Analysis of protein-ligand interactions in 3D using PLIP showed that compound B6 was predicted to have more interactions in common with the reference ligand than

B11<sup>354</sup>. In the original crystal structure paper, it was unclear which software was used to generate the interaction map for AZD1283<sup>17</sup>. Compared to the interaction maps presented in that paper, PLIP predicted the same interactions, except that it did not pick up Phe-106<sup>3.34</sup> and Tyr-109<sup>3.37</sup>.

However, this does not necessarily mean that PLIP is less accurate than the software used in the paper. Currently, there is a lack of guidelines to assess the quality and performance of different interaction drawing algorithms<sup>394</sup>. Thus, no programs are currently regarded as more or less accurate. The same ligand may have variations in the predicted residue interactions in different papers, based on the software used by the authors. It is rare that interaction maps generated in different software are the same, either in the detail/number of residue interactions identified or the output format. 2D interaction profilers like PoseView, LigPlot+, MOE tools, and Maestro are also commonly used. In this work, the 3D interaction profiler PLIP was used to conserve 3D information and to prevent the reduction of dimensions as in 2D plots.



## **Chapter 5.**

**Analogue search: using the B6 scaffold to  
discover novel antiplatelet agent S8**

## 5.1. Aim of the study

In the previous chapter, B6 was shown to be a novel inhibitor of ADP-induced platelet aggregation. In this study, the B6 scaffold was to be used to guide analogue-based drug discovery. To explore SAR around the B6 scaffold, analogues with minor group modifications were sought after.

## 5.2. B6 analogue search leads to the discovery of novel antiplatelet agent S8

In the search for B6 analogues, the MolPort SMILES/SMARTS search tool was used (<https://www.molport.com/shop/find-chemicals-by-smiles>). A similarity threshold of 0.8 (Tanimoto metrics) was used to search for structurally similar chemical structures. As shown in **Figure 82**, nine analogues (S compounds) were chosen for testing based on visual inspection. The scaffold group modifications are highlighted in yellow.

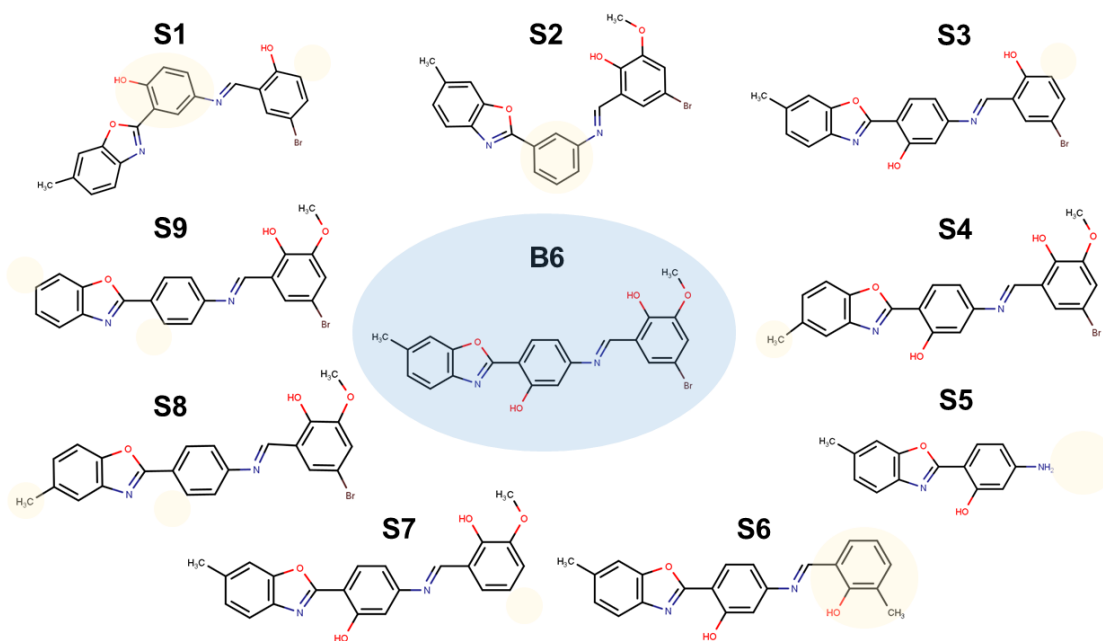


**Figure 82: 2D structures of the B6 analogues (S compounds) purchased from MolPort for subsequent experimental evaluation.** Nine B6 analogues were chosen for testing using the MolPort SMILES/SMARTS search tool. B6 is highlighted in blue, and differences in the analogues are highlighted in yellow. The structures were drawn using MarvinSketch.

An *in vitro* screen was then performed using the plate-based aggregometry assay. Compounds for the screen were dissolved in DMSO. They were aliquoted and stored at -80°C. Upon addition of HBS to create working solutions, compounds were sonicated and vortexed to ensure they were fully dissolved.

Blood from six independent human donors was tested in these experiments. PRP was incubated with compounds (10µM) for 30 minutes (RT). The final DMSO concentrations did not exceed 0.1%. Platelets were then activated using 1µM ADP added using the plate reader injector, followed by 5 minutes of continuous shaking. This concentration of ADP was used because when concentration-response curves were created for compounds B6 and B11 (**Figures 72 and 73**), the compounds exhibited the greatest extent of inhibition at this concentration of ADP. End-point absorbance measurements were recorded and the % aggregation was determined. As shown in **Figure 83**, ADP + vehicle achieved a mean % aggregation value of  $76.0 \pm 3.17\%$ . Statistical analysis using the one-way ANOVA (followed up by Dunnett's multiple comparisons test) revealed that ADP + AZD1283 and ADP + compound S8 achieved significantly different (\*\*  $p \leq 0.01$ ) mean % aggregation values compared to ADP + vehicle. AZD1283 achieved 90.1% inhibition, and S8 achieved 90.8% inhibition.

The following changes in the B6 scaffold resulted in the loss of inhibitory activity: the absence of the -OH group on the intermediary aromatic ring but no change in position of the -CH<sub>3</sub> group on the benzoxazole portion (compound S2), only a change in position of the -CH<sub>3</sub> group on the benzoxazole portion (compound S4), the absence of the phenyl ring (compound S5), the absence of the -OH group on the intermediary aromatic ring + the absence of the -CH<sub>3</sub> group on the benzoxazole portion (compound S9).

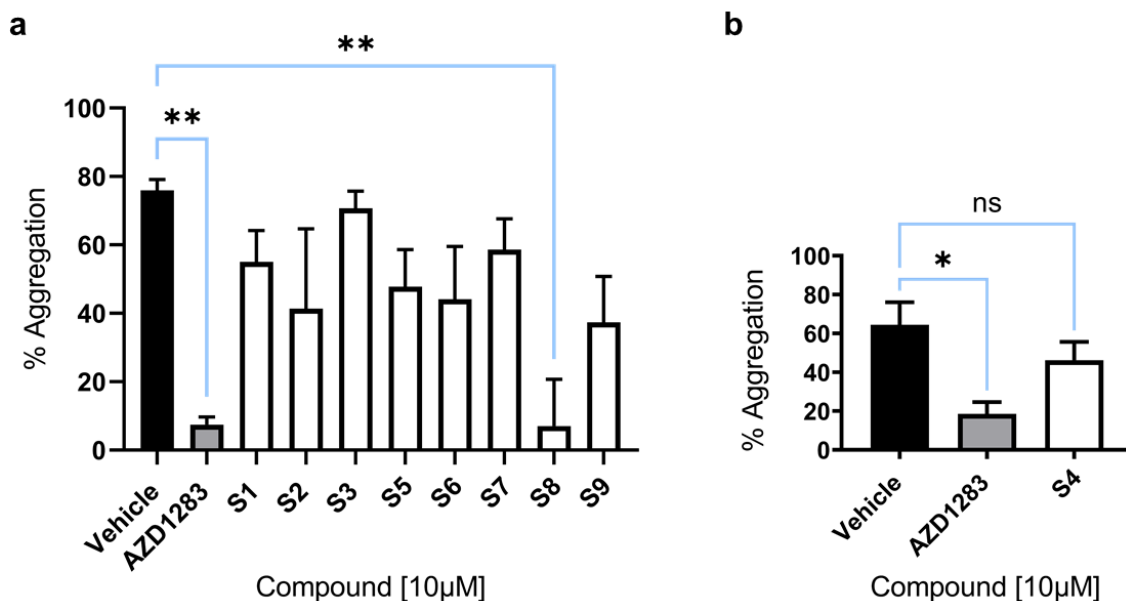


**Figure 83: Experimental evaluation of the purchased S compounds (10 $\mu$ M) against platelet aggregation. a)** PRP was incubated with compound (10 $\mu$ M) for 30 minutes (RT), and platelets were then activated with 1 $\mu$ M ADP using the plate reader injector. Shaking occurred continuously for 5 minutes. End-point absorbance measurements were recorded and the % aggregation was determined. The one-way ANOVA was followed up by Dunnett's multiple comparisons test, \*  $p \leq 0.05$ , \*\*  $p \leq 0.01$  (mean  $\pm$  SEM;  $n = 6$  independent blood donors). Whilst this is not labelled, all the S compounds (except S8) achieved a 'ns:  $p > 0.05$ , not significant' result. **b)** The experiment was performed as above for compound S4 (mean  $\pm$  SEM;  $n = 3$  independent blood donors) separately, as it arrived later. Statistical analysis was performed as above, ns:  $p > 0.05$  (not significant), \*  $p \leq 0.05$ .

Subsequently, blood from four other donors was used to further prove the inhibitory effect of compounds S8 and B6 on platelet aggregation. The reason this was performed again was so that both S8 and B6 could be tested with 1 $\mu$ M ADP (B6 had originally been tested with 3 $\mu$ M ADP in the *in vitro* screens). An ADP concentration of 1 $\mu$ M was used because B6 (and B11) had shown the most inhibition at this concentration of agonist. As shown in **Figure 84**, ADP + vehicle achieved a mean % aggregation value of  $67.3 \pm 8.47\%$ . The compounds achieved the following % inhibition values: AZD1283 (81.1%), S8 (91.1%), and B6 (64.5%). The one-way ANOVA was performed where samples' mean % aggregation values were compared to that of the positive control, AZD1283. Dunnett's multiple comparisons test showed that vehicle achieved a significantly different mean % aggregation value ( $* p \leq 0.05$ ) compared to AZD1283, while compounds S8 and B6 had not. This suggested that S8 and B6 had a comparable inhibitory effect on aggregation to AZD1283.

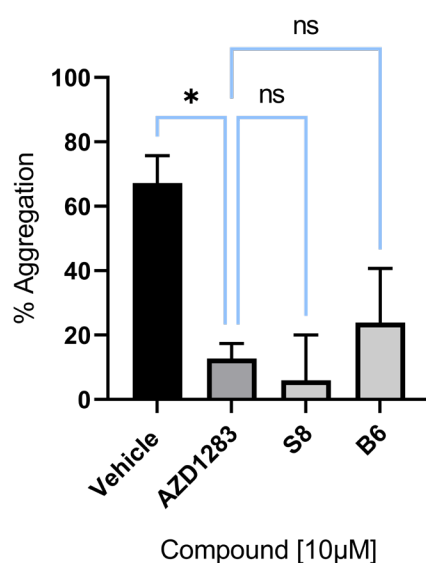


**Figure 84: Further experimental evaluation of compounds B6 and S8 (10 $\mu$ M) against platelet aggregation.** PRP was incubated with compounds for 30 minutes (RT) and platelets were activated using 1 $\mu$ M ADP (mean  $\pm$  SEM;  $n = 4$  independent blood donors). Mean % aggregation values for the samples were compared to that of the positive control, AZD1283. The one-way ANOVA was performed, followed up by Dunnett's multiple comparisons test,  $* p \leq 0.05$  (mean statistically different from that of AZD1283), ns:  $p > 0.05$  (mean not significantly different from that of AZD1283).

In the next stage, the properties of compounds B6 and S8 were analysed using the SwissADME server (<http://www.swissadme.ch/>). As shown in **Table 7**, compound B6 (453.29g/mol) and compound S8 (437.29g/mol) have similar molecular weights to AZD1283 (470.54g/mol). However, their iLOGP values are higher than that of AZD1283, showing increased lipophilicity<sup>395,396</sup>. This was reflected by the fact that the compounds required sonication and vortexing to adequately dissolve (both when making up the initial stock in DMSO, and when making up working solutions in HBS). Additionally, AZD1283 has seven hydrogen bond acceptors, whilst compounds B6 and S8 have six and five hydrogen bond acceptors, respectively. AZD1283 has one hydrogen bond donor, whilst compounds B6 and S8 have two and one hydrogen bond donors, respectively. AZD1283 has a higher number of rotatable bonds (nine) than compound B6 (four) and compound S8 (four). The total polar surface area (TPSA) was found to be higher in AZD1283 (137.84Å<sup>2</sup>) than compound B6 (88.08Å<sup>2</sup>) and compound S8 (67.85Å<sup>2</sup>). All three compounds met Lipinski's rule of five for drug likeness<sup>397-399</sup>.

None of the compounds were found to contain any pan-assay interference compounds (PAINS) alerts. However, compounds B6 and S8 both exhibited one Brenk alert - an imine group. Brenk alerts are undesirable chemical groups that may impede the drug discovery process (either due to toxicity, contributing to poor pharmacokinetics, being chemically reactive, or metabolically unstable)<sup>400</sup>.

**Table 7: Predicted physicochemical properties of AZD1283, B6, and S8.** Analysed using the SwissADME tool (<http://www.swissadme.ch/>).

	AZD1283	Compound B6	Compound S8
<b>Molecular weight (g/mol)</b>	470.54	453.29	437.29
<b>iLOGP</b>	2.23	4.23	4.35
<b>No. H bond acceptors</b>	7	6	5
<b>No. H bond donors</b>	1	2	1
<b>Number of rotatable bonds</b>	9	4	4
<b>Total polar surface area</b>	137.84Å <sup>2</sup>	88.08Å <sup>2</sup>	67.85Å <sup>2</sup>
<b>Meets Lipinski's rules?</b>	✓	✓	✓
<b>PAINS alerts</b>	0	0	0
<b>Brenk alerts</b>	0	1 alert - imine	1 alert - imine

In the next stage, compound S8 was further explored using *in silico* software. As shown in **Figure 85**, AutoDock Vina (blind docking) predicted that compound S8 binds in the same pocket as the co-crystallised ligand, AZD1283. Five independent docking runs were performed, where the pose and score of S8 ( $-10.6 \pm 0.0200$  kcal/mol; mean  $\pm$  SEM) were highly reproducible. As mentioned in the previous chapter, AZD1283 obtained a score of  $-8.90 \pm 0.440$  kcal/mol and B6 obtained a score of  $-10.7 \pm 0.100$  kcal/mol in AutoDock Vina. Compared to B6's docking pose (**Figure 76c-d**), the phenyl ring of S8 adopted a different orientation within the sub-cavity between helices 6 and 7. This can be seen in the different spatial positioning of the bromine group relative to the pocket.

Focused docking was also performed using the GOLD suite. The predicted mode of binding for S8 (**Figure 86**) was the same as that obtained in AutoDock Vina with regards to the spatial positioning of chemical groups relative to the pocket and AZD1283. S8 obtained a ChemPLP score of  $86.5 \pm 0.230$  (mean  $\pm$  SEM; five independent docking runs). As mentioned in the previous chapter, AZD1283 obtained a ChemPLP score of  $88.7 \pm 2.11$ . Poses and scores were highly reproducible.

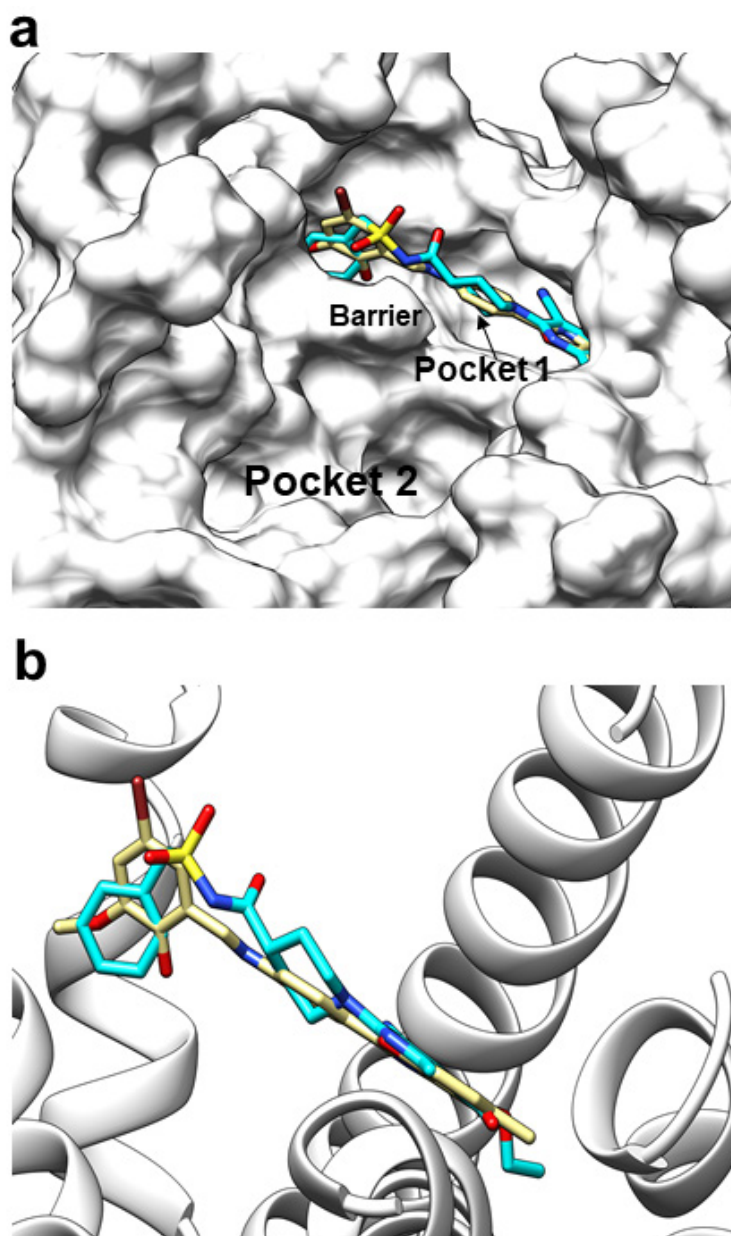


**Figure 85: Possible binding modes of compound S8 against the human P2Y<sub>12</sub> structure predicted through blind docking. a)** Blind docking against P2Y<sub>12</sub> in AutoDock Vina showing compound S8 (yellow sticks) docked in the same pocket as the co-crystallised ligand, AZD1283 (cyan sticks). The protein is shown as a white surface representation. Pocket 1, pocket 2, and the barrier between them is labelled (Tyr-105<sup>3,33</sup> and Lys-280<sup>7,35</sup>). **b)** Zoomed-in image of docking in AutoDock Vina, where the protein is shown as white ribbons (cartoon representation), compound S8 is shown as yellow sticks, and AZD1283 is shown as cyan sticks. The image created using UCSF Chimera.

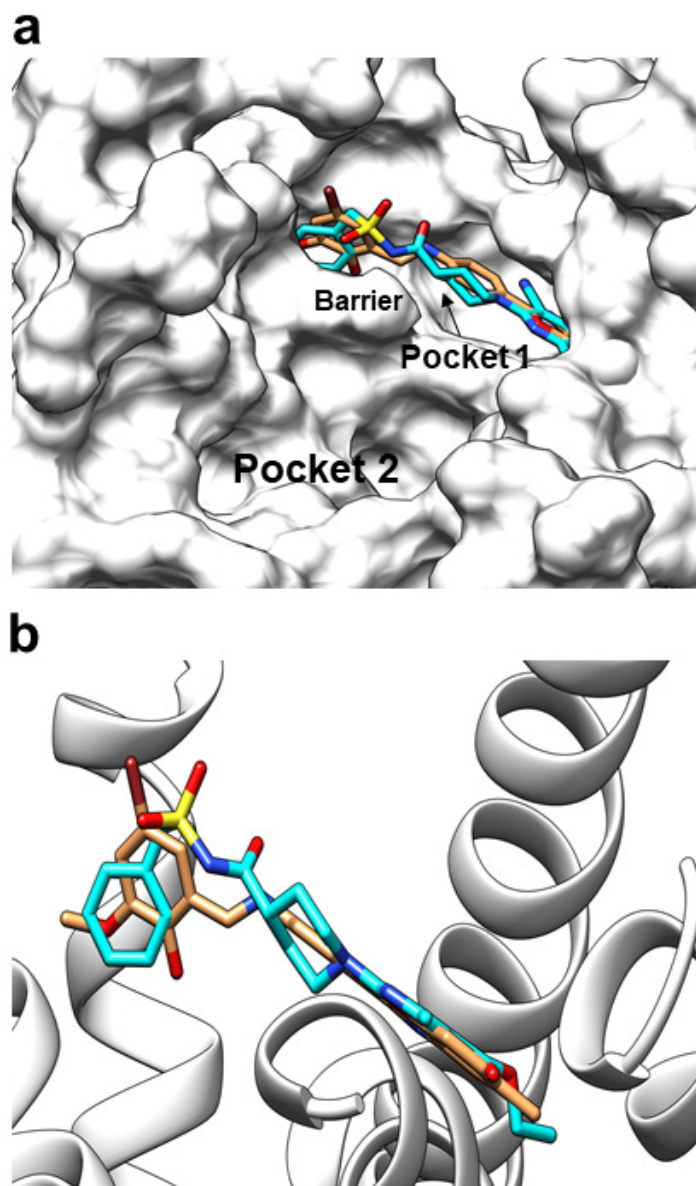


**Figure 86: Possible binding mode of compound S8 against the human P2Y<sub>12</sub> structure predicted through focused docking. a)** The pose obtained for compound S8 (orange sticks) through focused docking against the P2Y<sub>12</sub> structure in the GOLD suite. The pose of the co-crystallised ligand, AZD1283 (cyan sticks), is also shown. The protein is shown as a white surface representation. Pocket 1, pocket 2, and the barrier between them is labelled (Tyr-105<sup>3,33</sup> and Lys-280<sup>7,35</sup>). **b)** Zoomed-in image of docking in GOLD, where the protein is shown as white ribbons (cartoon representation), compound S8 is shown as orange sticks, and AZD1283 is shown as cyan sticks. The image was created using UCSF Chimera.

To explore protein-ligand interactions, the S8 docked pose from **Figure 85** (blind docking in AutoDock Vina) was analysed in PLIP. As shown in **Figure 87a**, S8 had seven interactions in common with AZD1283 (**Figure 63**). The S8 phenyl ring that docked in between helices 6 and 7 was predicted to form hydrophobic interactions with Arg-256<sup>6.55</sup>, Tyr-259<sup>6.58</sup>, and Leu-276<sup>7.31</sup>. In contrast to AZD1283 and compound B6 (**Figure 78**), S8 was missing an interaction with Lys-280<sup>7.35</sup> due to the change in orientation of its phenyl ring within this sub-cavity. However, S8 formed a hydrophobic interaction with Tyr-259<sup>6.58</sup> (also present with AZD1283), which B6 was missing. Additionally, the absence of the -OH group on the intermediary aromatic ring of S8 (compared to B6) resulted in a loss of hydrogen bonds with Asn-191<sup>5.40</sup> and Gln-195<sup>5.44</sup>. Furthermore, the change in position of the -CH<sub>3</sub> group (at the benzoxazole portion) in S8 resulted in a loss of interaction with Asn-159<sup>4.60</sup>. However, S8 also formed a hydrogen bond with Arg-256<sup>6.55</sup>, hydrophobic interactions with Phe-252<sup>6.51</sup>, Val-102<sup>3.30</sup>, Val-190<sup>5.39</sup>, and  $\pi$ - $\pi$  stacking with Tyr-105<sup>3.33</sup>, as in B6 and AZD1283. Compound S8 and B6 were both missing a hydrophobic interaction with Leu-155<sup>4.56</sup>, compared to AZD1283.

Further analysis of the S8 scaffold was performed in ROCS (**Figure 87b**). Alignment of S8 to AZD1283 determined a lower Shape Tanimoto score (0.567) than B6 (**Figure 74**), but a higher Color Tanimoto (0.210). This may be because both AZD1283 and S8 do not have any groups attached to the mid-scaffold phenyl ring. Furthermore, the spatial positioning of the -CH<sub>3</sub> group at the benzoxazole portion of S8 aligns with the ethyl ester group of AZD1283, which is not the case with B6. However, regardless of these advantages in the S8 scaffold, B6 still had a higher number of predicted interactions in common with the positive control. B6 also had a higher Tanimoto Combo score of 0.813, whereas S8 obtained a score of 0.777. Although, *in*

*in vitro*, S8 achieved more inhibition of ADP-induced platelet aggregation than B6 (Figures 83-84).

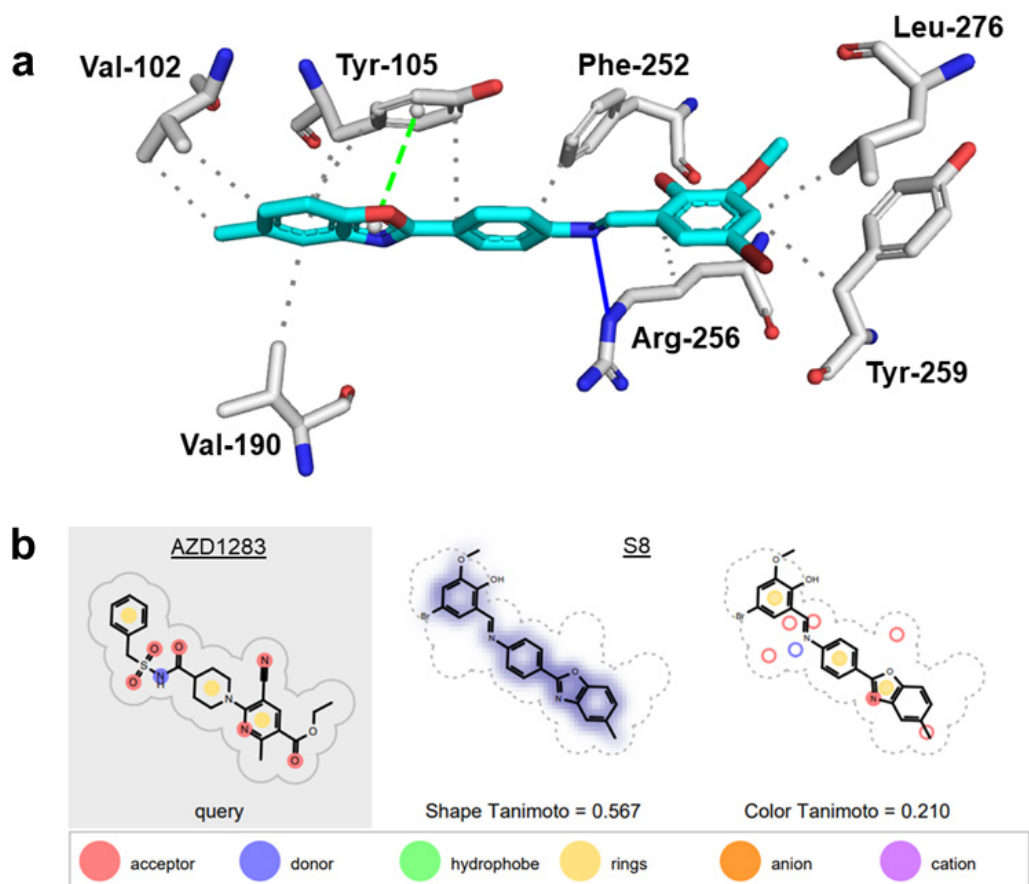


**Figure 87: Recognition of compound S8 within the orthosteric ligand binding pocket of the human P2Y<sub>12</sub> structure and similarity indices with respect to AZD1283.** **a)** The blind docking pose of compound S8 from **Figure 85** was analysed for predicted protein-ligand interactions using PLIP. Compound S8 is shown in cyan. The protein is shown as silver sticks. Grey dashes represent hydrophobic interactions, blue lines represent hydrogen bonds, and green dashes represent  $\pi$ - $\pi$  stacking. The image was created using PyMOL. **b)** The 2D structure of S8 was aligned to that of the query ligand, AZD1283, in ROCS. A Shape Tanimoto and Color Tanimoto score was generated (each out of 1), as well as a Tanimoto Combo score (mentioned in-text) out of 2. Shape similarity to AZD1283 is shown in purple. Key shows functional groups considered for evaluating chemical similarity. The images were created using the ROCS Report.

### 5.3. Compounds B6 and S8 did not affect pVASP levels significantly

In the final stage of experiments, compounds B6 and S8 were tested to assess their effects on several molecular pathways. The molecular pathways that were probed are summarised in **Figure 88**. Firstly, B6 and S8 were tested for their effects on P2Y<sub>12</sub> using the multiplexed pVASP assay, as described in **Chapter 2** and **Chapter 3**.

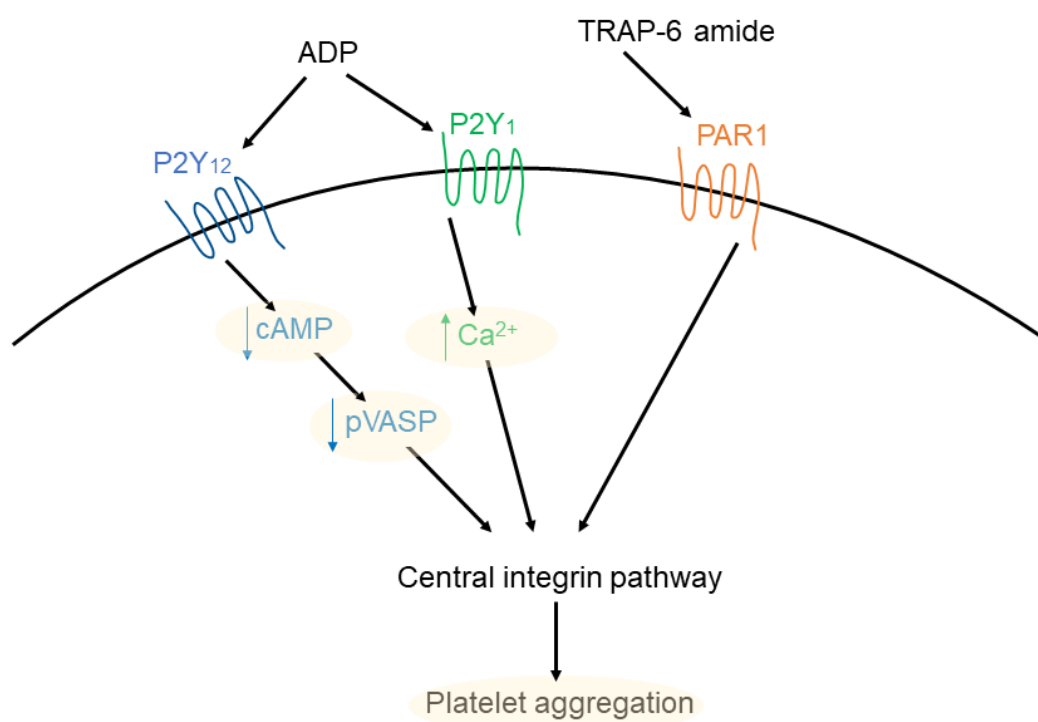


**Figure 88: A schematic diagram showing various molecular pathways that were probed using AZD1283, B6, and S8.** Effects on the P2Y<sub>12</sub> pathway (activated by ADP) was tested using the biomarker pVASP, which is a read-out of upstream cAMP signalling. Effects on the P2Y<sub>1</sub> pathway were tested using a calcium assay to assess cytosolic Ca<sup>2+</sup> levels (although it should be noted that changes in cytosolic Ca<sup>2+</sup> levels are not limited to P2Y<sub>1</sub> activity). Effects on the central integrin pathway were tested by activating PAR1 using TRAP-6 amide. If in the case that the compounds did not inhibit ADP-induced platelet aggregation through P2Y<sub>12</sub>, but through downstream effects on the central integrin pathway, this would be picked up through testing TRAP-6 amide-induced platelet aggregation. More information is provided in-text.

Preliminary experiments were first conducted using the pVASP assay (**Figure 89**). Washed platelets ( $1 \times 10^8$  platelets/mL) were incubated with compounds ( $10\mu\text{M}$ ) for 30 minutes (RT). Platelets were then simultaneously incubated with ADP ( $1\mu\text{M}$ ) and PGE<sub>1</sub> ( $100\text{nM}$ ) for 10 minutes (RT). As previously mentioned, PGE<sub>1</sub> was required for stimulation of adenylyl cyclase, to bring pVASP levels to detectable levels. Every experiment included an unstimulated control (no PGE<sub>1</sub> or ADP) in recognition of basal adenylyl cyclase activity and pVASP levels. The stimulated control contained  $100\text{nM}$  PGE<sub>1</sub>, and no ADP.

It was found during initial experiments that treatment of platelets with AZD1283 increases pVASP levels (this was not observed with cangrelor or AR-C66096). It is unknown whether AZD1283, for example, affects adenylyl cyclase activity. However, to account for this observation, the drug was included in the control samples. To maintain consistency, B6 and S8 were also included in their respective control samples. Each experiment resulted in three pooled samples (e.g., AZD1283, B6, S8). The pooled samples were barcoded such that they could include up to 8 sub-samples therein. Alexa Fluor 647 MFI values (correlating with pVASP levels) were measured using flow cytometric analysis. As shown in **Figure 89a**, an unpaired t-test showed that platelets incubated with AZD1283 ( $10\mu\text{M}$ ) had a significantly different (\*\*  $p \leq 0.01$ ) mean Alexa Fluor 647 MFI value ( $8560 \pm 202$ ) compared to its vehicle control ( $4860 \pm 290$ ). AZD1283 had a higher MFI value than vehicle, denoting increased pVASP levels. This is consistent with P2Y<sub>12</sub> antagonism. However, B6 (**Figure 89b**) did not have a significantly different mean Alexa Fluor 647 MFI value ( $5020 \pm 274$ ) compared to its vehicle control ( $4890 \pm 186$ ). S8 (**Figure 89c**) also did not have a significantly different mean Alexa Fluor 647 MFI value ( $5200 \pm 441$ ) compared to its vehicle control ( $5010 \pm 445$ ).

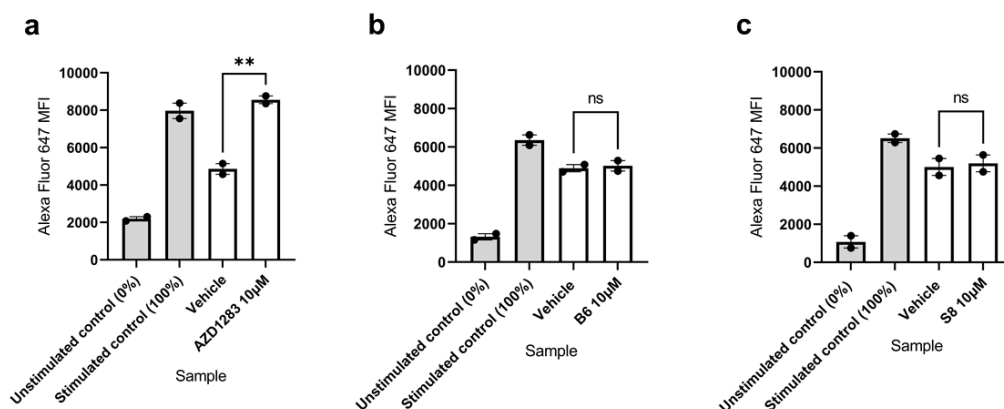


**Figure 89: Assessing the effect of AZD1283, B6, and S8 on platelet pVASP levels.**

For these experiments, washed platelets ( $1 \times 10^8$  platelets/mL) were incubated with compound (10µM) for 30 minutes (RT). Platelets were then simultaneously incubated with ADP (1µM) and PGE<sub>1</sub> (100nM) for 10 minutes (RT). PGE<sub>1</sub> was used to bring pVASP levels to detectable levels. The unstimulated control did not contain any PGE<sub>1</sub> (or ADP) and was representative of basal adenylyl cyclase activity/pVASP levels. The stimulated sample contained 100nM PGE<sub>1</sub> (no ADP). Alexa Fluor 647 MFI values were measured using flow cytometric analysis. Higher MFI values corresponded with increased pVASP levels. **a)** Bar chart shows Alexa Fluor 647 MFI values obtained by incubating platelets with AZD1283. Statistical analysis was performed using the unpaired t-test (\*\*  $p \leq 0.01$ ). MFI values: unstimulated control ( $2193 \pm 112$ ), stimulated control ( $7970 \pm 414$ ), vehicle ( $4860 \pm 290$ ), AZD1283 ( $8560 \pm 202$ ). **b)** Bar chart shows Alexa Fluor 647 MFI values obtained by incubating platelets with compound B6. Statistical analysis was performed using the unpaired t-test (ns:  $p > 0.05$ , not significant). MFI values: unstimulated control ( $1320 \pm 162$ ), stimulated control ( $6360 \pm 271$ ), vehicle ( $4890 \pm 186$ ), B6 ( $5020 \pm 274$ ). **c)** Bar chart shows Alexa Fluor 647 MFI values obtained by incubating platelets with compound S8. Statistical analysis was performed using the unpaired t-test (ns:  $p > 0.05$ , not significant). MFI values: unstimulated control ( $1080 \pm 320$ ), stimulated control ( $6510 \pm 227$ ), vehicle ( $5010 \pm 445$ ), S8 ( $5200 \pm 441$ ). Data for the above experiments is shown as mean  $\pm$  SEM;  $n = 2$  independent blood donors.

As the original B6/S8 aggregometry experiments were conducted using PRP and not washed platelets, the pVASP assay was then performed using PRP. Since S8 exhibited more inhibition of platelet aggregation than B6, it was selected for subsequent testing in the pVASP assay. For these experiments, PRP was incubated with S8 (10 $\mu$ M) for 30 minutes (RT). Platelets were then simultaneously incubated with ADP (varying concentrations) and PGE<sub>1</sub> (100nM) for 10 minutes (RT). As shown in **Figure 90**, the ADP + vehicle concentration-response curve reached an E<sub>max</sub> value of 33.7% pVASP, the ADP + AZD1283 concentration-response curve reached an E<sub>max</sub> value of 25.4% pVASP, and the ADP + S8 concentration-response curve reached an E<sub>max</sub> value of 24.5% pVASP. AZD1283 caused a rightward shift of the concentration response curve (ADP IC<sub>50</sub>: 2.78 x 10<sup>-5</sup> M) compared to vehicle (ADP IC<sub>50</sub>: 7.46 x 10<sup>-7</sup> M) and displayed competitive antagonism. Schild analysis revealed a K<sub>D</sub> value of 2.75 x 10<sup>-7</sup> M (275nM) for AZD1283. S8 did not cause a rightward shift of the concentration-response curve (ADP IC<sub>50</sub>: 1.55 x 10<sup>-6</sup> M).

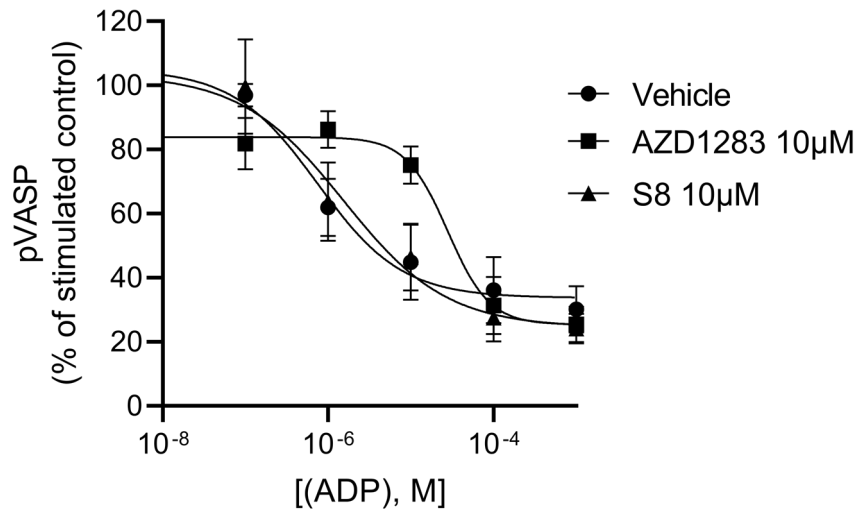


**Figure 90: Assessing the effect of AZD1283 and compound S8 on pVASP levels using varying concentrations of ADP.** PRP was incubated with vehicle, AZD1283 (10µM), or S8 (10µM) for 30 minutes (RT), and then incubated simultaneously with PGE<sub>1</sub> (100nM) and ADP (varying concentrations) for 10 minutes (RT). Phosphorylated VASP (pVASP) levels are shown as a % of stimulated control. Data is representative of mean ± SEM; *n* = 3 independent blood donors.

#### 5.4. Compound B6 significantly enhances cytosolic Ca<sup>2+</sup> levels

As previously mentioned, the aggregometry experiments were a readout of multiple signalling receptors, including P2Y<sub>1</sub> (G<sub>q</sub>-coupled). Thus, the effects of compounds S8 and B6 were then tested in a calcium assay. Washed platelets (1 x 10<sup>8</sup> platelets/mL) were loaded with the calcium-sensitive dye, Cal-520. Platelets were then incubated with compounds (10µM) for 30 minutes (RT). The aim of the experiment was to create a calcium trace of Cal-520 fluorescence over time. Cal-520 fluorescence was measured at 520nm. Initially, a baseline was established, and then platelets were activated with ADP (1µM) at ~400 seconds. ADP was added using the plate reader injector. Readings were continuously recorded for a total of 1033 seconds (~17 minutes). The peak of the curve was noted. As previously mentioned, all Cal-520 fluorescence values (F) were normalised to that of the unstimulated vehicle control values (F<sub>0</sub>). The one-way ANOVA was then used to compare the mean peak F/F<sub>0</sub> of the drugs to that of the vehicle.

As shown in **Figure 91a**, AZD1283-treated platelets achieved a mean peak F/F<sub>0</sub> value of 65.0 ± 6.09%, which reflected a decrease in cytosolic Ca<sup>2+</sup> levels compared to vehicle-treated platelets. Surprisingly, S8-treated platelets achieved a mean peak F/F<sub>0</sub> value of 115 ± 4.88%, which reflected higher cytosolic Ca<sup>2+</sup> levels were achieved than the vehicle. Similarly, B6-treated platelets achieved a mean peak F/F<sub>0</sub> value of 124 ± 1.85%. Statistical analysis using the one-way ANOVA followed up by Dunnett's multiple comparisons test showed that AZD1283-treated platelets achieved a significantly different (\*\*\*) mean peak F/F<sub>0</sub> value compared to the vehicle-treated platelets. However, the analysis showed that the mean peak F/F<sub>0</sub> value obtained for the S8-treated platelets was not significantly different (ns: p > 0.05) to that of the vehicle-treated platelets. Lastly, the mean peak F/F<sub>0</sub> value obtained for the B6-treated platelets was significantly different (\*\* p ≤ 0.01) to that of the vehicle-treated platelets.

The data in **Figures 91a-b** suggest that it is possible that B6 has undesired off-target effects on a receptor that is coupled to a calcium signalling pathway. This may be agonistic activity at P2Y<sub>1</sub>, however, as changes in cytosolic Ca<sup>2+</sup> levels are not limited to the P2Y<sub>1</sub> pathway, any suggestion of which target B6 may be having this off-target effect on would be purely speculative (allosteric modulation may also be possible). These results ruled out that B6 and S8 could be P2Y<sub>1</sub> antagonists, as a decrease in cytosolic Ca<sup>2+</sup> was not observed. Additionally, this data was further evidence that B6 and S8 are not likely to be P2Y<sub>12</sub> antagonists, because the decrease in cytosolic Ca<sup>2+</sup> levels indicative of P2Y<sub>12</sub>-P2Y<sub>1</sub> cross talk was not observed as with AZD1283.

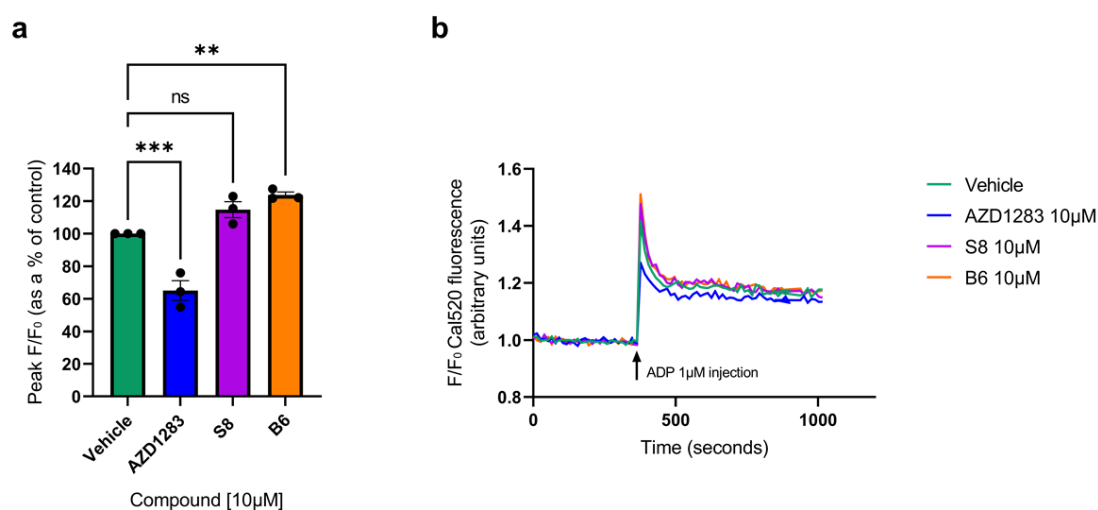


**Figure 91: Experimental evaluation of AZD1283, S8, and B6 in a platelet calcium assay.** Washed platelets ( $1 \times 10^8$  platelets/mL) loaded with Cal-520 were incubated with compound (10μM). Platelets were activated using ADP (1μM), which was added into the wells using the plate reader injector. Cal-520 fluorescence was measured (at 520nm) over time (1033 seconds). All Cal-520 fluorescence values (F) were normalised to that of the initial unstimulated vehicle control (F<sub>0</sub>) values. **a**) Bar chart showing peak F/F<sub>0</sub> values determined (with baseline correction) for platelets pre-incubated with compounds. Statistical analysis was performed using the one-way ANOVA followed up by Dunnett's multiple comparisons to compare the peak F/F<sub>0</sub> of the drugs to that of the vehicle. \*\*  $p \leq 0.01$ , \*\*\*  $p \leq 0.001$ , ns: not significant ( $p > 0.05$ ). **b**) F/F<sub>0</sub> Cal-520 fluorescence traces from which the peak F/F<sub>0</sub> was determined. ADP was injected at 400 seconds into the wells by the plate reader injector. Mean  $\pm$  SEM;  $n = 3$  independent blood donors.

## 5.5. Compounds B6 and S8 do not significantly affect TRAP-6 amide-induced platelet aggregation

So far, experiments mentioned in this thesis have involved the use of ADP to activate platelets. In the following set of experiments, the effect of the compounds was tested on another platelet aggregation pathway using the PAR1 agonist, TRAP-6 amide (**Figure 88, Figure 92**). This was to rule out that the compounds were inhibiting the central integrin pathway (and platelet aggregation) through a mechanism downstream of P2Y<sub>12</sub>. PRP was incubated with compounds (10µM) for 30 minutes (RT). Platelets were activated using TRAP-6 amide (5µM), followed by shaking for 5 minutes to induce aggregation. End-point absorbance measurements were recorded, and the % aggregation was determined.

As shown in **Figure 92**, ADP + vehicle achieved a mean aggregation value of  $79.7 \pm 5.22\%$ . Furthermore, ADP + AZD1283, achieved a mean aggregation value of  $61.8 \pm 15.4\%$ . In the presence of the test compounds S8 or B6, ADP achieved mean aggregation values of  $67.2 \pm 12.60\%$  and  $67.1 \pm 14.9\%$ , respectively. Statistical analysis using the one-way ANOVA (followed up by Dunnett's multiple comparisons test) showed that neither AZD1283, S8, or B6 achieved significantly different means from vehicle ( $p > 0.05$ ). These results showed that, whilst these compounds do cause inhibition of ADP-induced platelet aggregation, they do not cause significantly different mean % aggregation values (compared to vehicle) in response to another platelet activator. Thus, it was unlikely that these compounds were acting to inhibit the central integrin pathway through a mechanism downstream of P2Y<sub>12</sub>. The results also suggested that the compounds do not act through PAR1. Importantly, these data provided evidence that the inhibition of ADP-induced platelet aggregation achieved by B6 or S8 was not merely an artefact.

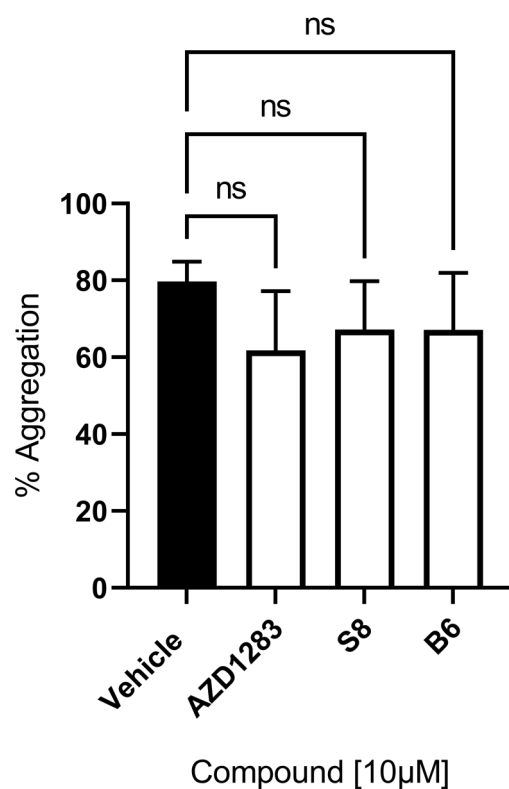


**Figure 92: Assessing the effect of AZD1283, S8, and B6 on TRAP-6 amide-induced platelet aggregation.** PRP was incubated with compound (10µM) for 30 minutes (RT). Platelets were activated using TRAP-6 amide (5µM). Shaking occurred continuously for 5 minutes to induce aggregation. End-point absorbance measurements were recorded, and the % aggregation was determined. Statistical analysis was performed using the one-way ANOVA followed up by Dunnett's multiple comparisons test (ns:  $p > 0.05$  (mean  $\pm$  SEM;  $n = 3$  independent blood donors)).

## 5.6. Scaffold novelty

To evaluate scaffold novelty, keyword searches were performed in PubMed ([www.pubmed.ncbi.nlm.nih.gov](http://www.pubmed.ncbi.nlm.nih.gov)), Google Scholar ([www.scholar.google.com](http://www.scholar.google.com)), Scopus ([www.scopus.com](http://www.scopus.com)), and Web of Science ([www.scholar.google.com](http://www.scholar.google.com)) for inhibitors of ADP-induced platelet aggregation and P2Y<sub>12</sub> antagonists. The scaffolds of compounds B6, B11, and S8 were not found to be mentioned in any previous papers. Additionally, the scaffolds were not found on the IUPHAR/BPS Guide to PHARMACOLOGY ([www.guidetopharmacology.org](http://www.guidetopharmacology.org)) or the ChEMBL (<https://www.ebi.ac.uk/chembl/>) P2Y<sub>12</sub> profiles. Lastly, the compounds' PubChem ([www.pubchem.ncbi.nlm.nih.gov](http://www.pubchem.ncbi.nlm.nih.gov)) Bioassay profiles were checked, and none of the scaffolds were previously tested on ADP-induced platelet aggregation or P2Y<sub>12</sub>.

## 5.7. Discussion

In this chapter, a novel inhibitor of ADP-induced platelet aggregation (compound S8) was discovered. This compound was found from SAR exploration around the B6 scaffold. From the scaffold point of view, compounds B6 and S8 are both 2-aryl benzoxazole derivatives. Both achieved consistent inhibition of platelet aggregation using blood of different human donors. Statistical analysis showed that the extent of inhibition was comparable (not significantly different) to that of AZD1283 - a known antiplatelet compound used as a positive control. Compared to compound B6, compound S8 lacks the -OH group on its intermediary aromatic ring (**Figure 82**). Additionally, the position of the -CH<sub>3</sub> group on the benzoxazole portion is changed. These chemical modifications might have allowed compound S8 (10µM) to achieve greater inhibition of platelet aggregation than B6 (10µM), as shown in **Figure 84**.

Experimental evaluation of other selected analogues of compound B6 showed that several changes to the B6 scaffold were not well-tolerated. It may be interpreted from the SAR analysis that certain features of the scaffold are necessary for inhibition of platelet aggregation. The **General Discussion (Figure 94)** may be referred to for the features of this scaffold. As the target of the compounds remains unknown (discussed later), the amino acid residues that each group interacts with cannot be commented on.

An observation was made that S8 generally showed slightly more inhibition of platelet aggregation in blood from male than female donors. There may be numerous reasons why we may see small differences between drug effects in males and females. For example, there may be higher plasma protein binding of the compound in females. Studies have suggested that plasma protein profiles vary between the males and females<sup>401</sup>. Interestingly, a study suggested that because females have higher platelet count, this is associated with increased platelet reactivity<sup>402</sup>. Thus, that study concluded that females may benefit from a larger dose of the antiplatelet drug (clopidogrel) than

males. An effort was made to use blood from both genders in all experiments in this thesis. Although this observation was made through analysis of day-to-day % aggregation values, objective evidence (statistical analysis) is not presented in this work to substantiate that S8 causes more inhibition in males than females. Higher sample sizes (blood donors) would be required to undertake such a study.

Analogue-based approaches have previously been shown to be an effective tool in the search for novel chemical structures with comparable biological activity to the original scaffold<sup>403-406</sup>. Multiple scaffolds are commonly desired in drug discovery ventures, as attrition rates are high due to poor *in vivo* stability and/or poor pharmacokinetic profiles<sup>407</sup>. Multiple scaffolds are also useful in delineating the protein-ligand interactions around a particular biological target<sup>408</sup>. Previously, SAR analysis has successfully been used to find novel inhibitors of platelet aggregation<sup>409-413</sup>. However, that approach was more empirical or involving experimental testing of different chemical building blocks to improve on a particular starting point scaffold (medicinal chemistry initiative). The SAR analysis adopted in this work is different. Analogues of B6 were chosen manually through visual inspection of existing (i.e., readily purchasable) analogues in a vendor chemical library without any medicinal chemistry-driven analogue generation, which is often the common route adopted by industries and academic chemists.

*In silico* analysis suggested that the primary target of compounds B6 and S8 is the P2Y<sub>12</sub> receptor. Molecular docking predicted that both are likely to bind in the same cavity (the orthosteric site) as the co-crystallised ligand, AZD1283. In the previous chapter, compound B6 was found to have a good interaction profile with the receptor (high number of desired protein-ligand interactions in common with AZD1283). S8 had a slightly lower number of interactions in common with AZD1283 than the B6 compound, even though it showed better inhibition of platelet aggregation. S8 also had

an additional interaction (Tyr-259<sup>6,58</sup>), which is in the sub-cavity between helices 6 and 7, a region important for antagonism of the receptor.

Contrary to the *in silico* data, *in vitro* work showed that neither B6, nor S8, significantly affected pVASP levels. Increase in the latter is indicative of P2Y<sub>12</sub> antagonism. However, the scope of this work was limited to platelets. Thus, it is unknown whether the same observations may be made by testing these compounds on a P2Y<sub>12</sub>-expressing cell line and assessing cAMP or pVASP levels<sup>7</sup>. For comparison to the literature, a paper reported that AZD1283 obtained a pK<sub>D</sub> value of 8.17 (K<sub>D</sub>: 6.76 x 10<sup>-9</sup> M (6.76nM)) with 2MeSADP, upon assessing cAMP levels in Chinese hamster ovary (CHO) cells expressing the P2Y<sub>12</sub> receptor<sup>16</sup>. In the pVASP assay of this work (using platelets), AZD1283 obtained a K<sub>D</sub> value of 2.75 x 10<sup>-7</sup> M (275nM) with ADP.

Moreover, the data from the calcium assay showed that neither B6, nor S8, significantly decrease Ca<sup>2+</sup> levels in platelets, as observed with AZD1283. The latter is likely due to P2Y<sub>12</sub>-P2Y<sub>1</sub> cross talk<sup>336,337,414</sup>. The results of the pVASP assay and the outcome of the calcium assay collectively suggested that P2Y<sub>12</sub> is unlikely to be the target of compounds B6 and S8. In hindsight, the protein-ligand interactions predicted for S8 (which showed that it had fewer interactions in common with AZD1283 than B6) may not be useful if it cannot be proven *in vitro* that P2Y<sub>12</sub> is the compounds' primary target. This may, at least partially, explain why S8 lacks several important interactions with the receptor despite it showing better inhibition of platelet aggregation compared to B6. The contradictory results between the aggregometry (inhibition of aggregation) and the calcium assay (increase in cytosolic calcium) for B6 were interesting because they suggested that B6 may act on multiple protein sites to modulate opposing pathways. One way this could be possible is if the increased cytosolic calcium is too weak of an effect to overcome the strong inhibitory effect exerted elsewhere.

Moreover, the discordance between the *in silico* and *in vitro* data highlights the limitations and challenges of using computational tools to find novel modulators for some biological targets opposed to some other targets. B6 was initially discovered due to promising results in, 1) ligand-based screening (similarity indices to AZD1283), 2) molecular docking against P2Y<sub>12</sub>, 3) detailed analysis of protein-ligand interactions. It passed all filters (or ‘check-points’) to be validated *in vitro*, where it produced further promising results in inhibiting ADP-induced aggregation. Thus, it was surprising that the compound and its analogue did not affect pVASP levels.

Nevertheless, the approach still resulted in three novel inhibitors of platelet aggregation (B6, B11, and S8), even if somewhat serendipitous in nature. Thus, the second aim of the project in finding a novel inhibitor of platelet aggregation was met, although the expected target was not proven. It is worth noting that serendipity has played an important part in science and drug discovery, where even the most acclaimed discoveries have had a serendipitous element to them<sup>252,415,416</sup>. The first P2Y<sub>12</sub> antagonist, ticlopidine, was also discovered accidentally when searching for novel anti-inflammatory drugs<sup>162</sup>. Analogue-based work led to clopidogrel, which went on to become one of the best-selling drugs of all time. Although known to be highly effective inhibitors of platelet aggregation, their protein target remained unknown for years after discovery. Their story of discovery raises questions as to whether they could be discovered today through rational drug design.

Another study, where a similar approach was taken with regards to *in silico* tools in the search for a novel anti-human immunodeficiency virus (anti-HIV) agent resulted in a false positive *in vitro*<sup>417</sup>. The work involved a screen of 70,000 molecules involving ligand similarity filter, followed by docking. However, the authors then proceeded to take the scaffold of the false positive and use a ‘ligand-growing’ tool, the Biochemical and Organic Model Builder, to dynamically sample different chemical groups on the

scaffold<sup>417,418</sup>. This was performed with knowledge of the protein binding pocket. That approach then resulted in a true active ligand. Importantly, the work showed that lessons can be gained from each screening protocol, and that extension of the protocol to include additional tools may increase the chances of finding true binders. That study also suggests that no *in silico* protocol should be overlooked simply because it did not initially result in a true binder. Additional steps may be required within the protocol. *In silico* drug discovery tools have only begun to advance over the past two decades, thus all attempted approaches may lay the foundation for improved protocols within such programs. It is possible that with *in silico* ligand growing tools (and medicinal chemistry approaches) there may still be hope that the scaffolds presented in this work could be used to inform the design of future P2Y<sub>12</sub> inhibitors. To complement this, one approach could be to consider structural plasticity of the antagonist-bound P2Y<sub>12</sub> structure and sample conformations of the receptor through MD simulations. This could then be followed by ensemble docking (docking ligands against multiple superimposed conformations of the receptor).

The mechanism by which B6 and S8 inhibit platelet aggregation remains unknown. Interestingly, they did not inhibit TRAP-6 amide induced platelet aggregation, showing that it is likely their mode of antagonism is selective to a protein/pathway that is activated by ADP. Importantly, it showed that the compounds' inhibition of ADP-induced aggregation is not an artefact, such as toxicity to platelets, or an effect on the platelet aggregation assay. Due to the large number of proteins present on the surface of platelets, it is challenging to speculate which protein these compounds target. Benzoxazole derivatives were previously shown to have antiplatelet activity. For example, in one case it was shown that the compounds were glycoprotein IIb/IIIa inhibitors, and in another it was shown that the compounds inhibited AA-induced platelet aggregation<sup>419-421</sup>.

Moreover, the compounds were highly lipophilic. Their higher iLOGP values (than AZD1283), and lower total surface polarity also indicates they may be able to cross the cell membrane and target an intracellular protein. This could indirectly result in the inhibition of an extracellular protein's pathway<sup>422</sup>. It is worth noting that B6 and S8 required sonication to dissolve adequately prior to each assay. They were sonicated until it could visually be confirmed that the solution was clear from undissolved particles of compound.

In the search for the target of compounds B6 and S8, several avenues may be taken. Firstly, *in silico* tools which predict the protein target of input ligands may be used. Secondly, similar scaffolds to B6 and S8 may also be searched for (e.g., in PubChem) to find any with known biological targets<sup>423</sup>. Thirdly, a chemical proteomics approach for target deconvolution may be useful, which will require functionalisation of these compounds and chemical crosslinking with cellular targets<sup>424,425</sup>. Cellular thermal shift assays coupled with proteomics may also be performed or coupling the compounds to beads and attempting affinity purification<sup>426-428</sup>. Lastly, artificial intelligence techniques may be used to seek out proteins with similar shape and electrostatic profiles to the P2Y<sub>12</sub> sub-cavity where compounds B6 and S8 were predicted to bind. It would involve building an electrostatic/shape model of the binding pocket. This technique (DeeplyTough) uses deep learning to rule out dissimilar pockets and identify pockets with similar descriptors to that of the input protein pocket<sup>429</sup>. The technique is newly developed and was first reported in 2020. However, in pursuing such a technique, experience in artificial intelligence/deep learning would be required.

**Chapter 6.**  
**General discussion**

## 6.1. Summary of results

This thesis increased our understanding of cangrelor's mode of action, and several 2-aryl benzoxazole derivatives are described as competitive and reversibly acting inhibitors of ADP-induced platelet aggregation. A multiplexed flow cytometric pVASP assay was also optimised to create full concentration-pVASP response curves assessing P2Y<sub>12</sub> activity and antagonism. The combination of dye and fluorophore-conjugated antibody opens a new avenue for barcoding.

### 6.1.1. Cangrelor may act in a non-competitive manner to ADP

Plate-based aggregometry experiments in **Chapter 3** showed that nanomolar concentrations of cangrelor may act in a non-competitive manner to ADP (millimolar concentrations), and in a competitive manner to 2MeSADP<sup>430</sup>. Its analogue, AR-C66096 acted in a competitive manner with both agonists. Molecular assessment of pVASP in platelets showed that the ADP (up to 1mM) + cangrelor (100nM) concentration-response curve  $E_{max}$  did not reach the ADP (up to 1mM) + vehicle curve  $E_{max}$ . Furthermore, cangrelor (500nM) had a significantly different time vs. inhibition profile compared to vehicle in the aggregometry (with 10mM ADP), whereas AR-C66096 (500nM) did not. Cangrelor also significantly decreased cytosolic Ca<sup>2+</sup> levels, whereas the AR-C66096 effect was weaker and more variable.

These results had multiple implications. Using platelets, this thesis proposes that cangrelor may be a non-competitive antagonist (**Figure 93**). In support of this data, previous studies have suggested: 1) cangrelor prevents the active metabolites of clopidogrel and prasugrel binding *in vitro* (suggestion of a negative pharmacodynamic interaction), 2) ticagrelor binding is not compromised by cangrelor<sup>238,286,287</sup>. Due to the first observation, and that cangrelor co-administration decreases P2Y<sub>12</sub> blockade by the thienopyridines, clinical guidelines have stated that thienopyridine therapy should be

stopped before cangrelor administration. Recently, another group has also suggested that ADP and 2MeSADP may act in different pockets at P2Y<sub>12</sub><sup>335</sup>.

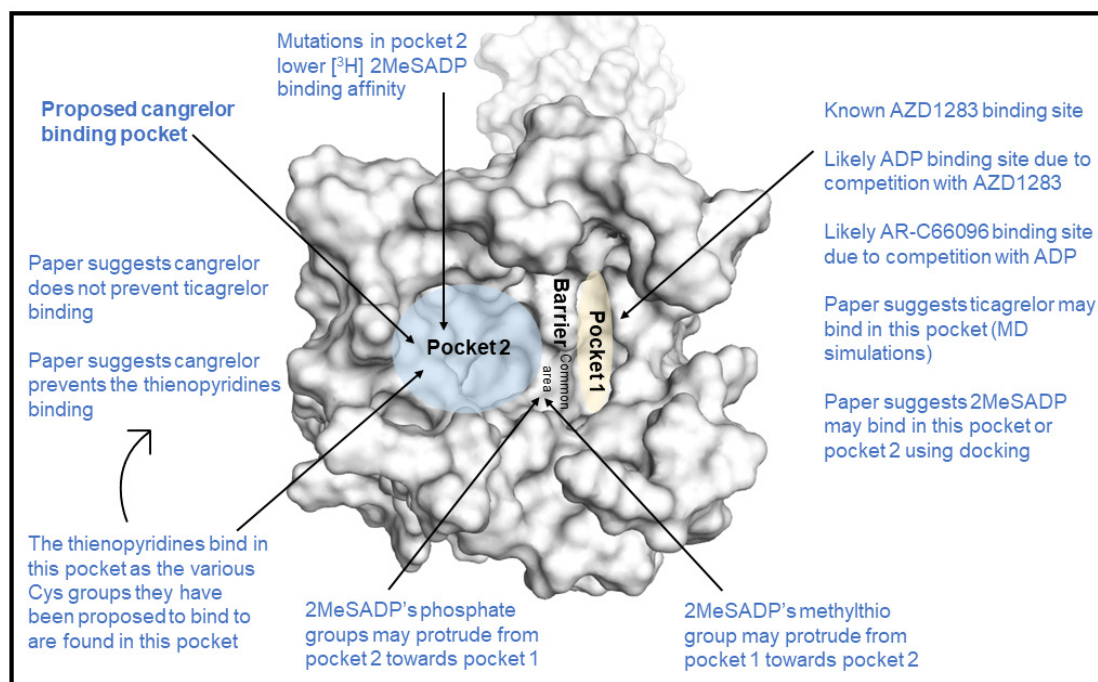


**Figure 93: Proposed cangrelor binding pocket.** Pocket 1 (yellow) is the known binding site of the co-crystallised ligand, AZD1283<sup>17</sup>. This is also the likely binding pocket for ADP, and AR-C66096, as demonstrated in the aggregometry data. MD simulations (by others) have suggested ticagrelor binds in this pocket<sup>18</sup>. 2MeSADP has been suggested to bind in either pocket 1 or pocket 2 (docking by others)<sup>17</sup>. Pocket 2 is in blue. Mutagenesis studies have shown that mutating residues in pocket 2 decreases the binding affinity of [<sup>3</sup>H]2MeSADP<sup>17</sup>. Regarding binding in pocket 1, docking has predicted 2MeSADP's methylthio group protrudes towards pocket 2 into the 'common area' between the pockets. Regarding binding in pocket 2, docking has predicted 2MeSADP's phosphate groups protrude towards pocket 1 into the 'common area'. The thienopyridines likely bind in pocket 2 as the various cysteines they have been proposed to bind to (mainly Cys-97<sup>3,25</sup> or Cys-175<sup>45,50</sup>) are in this pocket. Cangrelor has been suggested to prevent the thienopyridine active metabolites from binding *in vitro*<sup>238,282,284</sup>. It does not prevent ticagrelor binding<sup>286,287</sup>. Cangrelor is proposed to bind in pocket 2 in this thesis due to its possible non-competitive mode of antagonism with ADP. The protein structure is shown as a white surface. The structure was obtained from the PDB (PDB ID: 4NTJ), and the figure was created in PyMOL and Microsoft PowerPoint.

Taken together, a model is possible where ADP, AZD1283, ticagrelor, and AR-C66096 bind in pocket 1, and 2MeSADP, cangrelor, and the thienopyridines bind in pocket 2. As previously mentioned, cangrelor has been shown to prevent the active metabolites of clopidogrel and prasugrel from binding *in vitro*<sup>238,282</sup>. However, it does not prevent ticagrelor binding<sup>284,286,287</sup>. Additionally, even though 2MeSADP is a synthetic agonist, it has served here as a valuable tool to tell us more about the pharmacology of the receptor. Molecular docking by others has suggested that 2MeSADP may bind in pocket 1 or 2<sup>17</sup>. It is not clearly defined in the literature exactly where pocket 1 ends and where pocket 2 begins. However, the model in **Figure 93** shows the pockets are separated by a barrier, and that (what is referred to in this thesis as) a ‘common area’ exists which belongs to neither pocket<sup>17</sup>. The paper where docking of 2MeSADP was performed showed that if docked in pocket 1, its methylthio group protrudes into the ‘common area’ towards pocket 2 (Extended Data Figure 6 in the paper). If docked in pocket 2, its phosphate groups can protrude into the ‘common area’ towards pocket 1. Either of these scenarios may make competitive activity with AZD1283 (pocket 1) and cangrelor (pocket 2) possible.

MD simulations by others have suggested that ticagrelor binds in pocket 1<sup>18</sup>. Docking has also suggested the active metabolite of prasugrel binds in pocket 2<sup>17</sup>. However, this docking was not performed covalently (due to limitations in docking to simulate the formation of covalent bonds) for the thienopyridines. Notably, all the four cysteines that have been proposed in various papers to bind to the thienopyridines are in/around pocket 2 in the antagonist-bound structure, and not near pocket 1. This is relevant because if cangrelor can prevent the binding of the thienopyridine active metabolites then this may be due to its binding in pocket 2, where these cysteines are. Additionally, mutation of residues in pocket 2 have decreased binding affinity of the

radioligand [<sup>3</sup>H]2MeSADP<sup>16,17</sup>. This is in line with the aggregometry data here that showed cangrelor acting in a competitive manner to 2MeSADP.

Moreover, it may be argued that the results here may suggest that cangrelor could be an inverse agonist i.e., acting in the same site as ADP. However, there are several reasons why the findings presented here are unlikely to point to inverse agonism. Firstly, P2Y<sub>12</sub> in the platelets of healthy patients does not display high/basal constitutive activity, although it has been observed in those with diabetes mellitus (DM)<sup>431</sup>, which will be discussed in further detail later. Secondly, even if P2Y<sub>12</sub> did naturally display high constitutive activity, this still does not explain the unusual feature of possible different modes of antagonism with the different agonists. That is, why one agonist (2MeSADP) appears to more readily reverse cangrelor's antagonism compared to another agonist (ADP). Although, it may be possible that the effects of an inverse agonist would be overcome more readily by a more potent full agonist (like 2MeSADP), than a weaker full agonist (like ADP). It is likely that the findings presented here are only observed in platelets, where P2Y<sub>12</sub> exists in its natural environment and expressed at numbers found *in vivo*. Different observations may be expected in a cell-based system where P2Y<sub>12</sub> is over-expressed. There are questions as to how relevant inverse agonism would be to a biological setting where the receptor has not been reported to be over-expressed. Thirdly, inverse agonism would not explain why cangrelor prevents the active metabolites of the thienopyridines from binding *in vitro*<sup>238,282,284</sup>.

Cangrelor's possible non-competitive antagonism with ADP suggests that reversibly acting, non-thienopyridine scaffolds can also bind in pocket 2, and the pocket is not limited to accommodating the irreversibly binding thienopyridines. This could pave the way for new P2Y<sub>12</sub> inhibitors which target this pocket. Additionally, from a clinical perspective, a non-competitive, reversible antagonist that can be intravenously

administered may be useful in an emergency/surgical setting to reduce aggregation in a patient undergoing a thrombotic event. Cangrelor has a fast onset and offset of action, and platelet function is restored within an hour of stopping cangrelor infusion<sup>432-434</sup>. Importantly, these findings bring into question broad statements in the literature that ADP, cangrelor, and the thienopyridines target the same pocket in P2Y<sub>12</sub>. There should be more acknowledgement in the field that the orthosteric site of this receptor is composed of two sub-pockets. Furthermore, this work proposes a pharmacological explanation which supports clinical guidelines that thienopyridine therapy should be stopped before cangrelor administration. As the last generation of approved antiplatelet drug, it is important to continue to further understand the clinical implications of these findings for cangrelor. This is because P2Y<sub>12</sub> is not currently known to have any non-competitively acting antagonists. Finding out the key features for non-competitive antagonism of the receptor is useful, as a non-competitive antagonist may be more superior over a neutral antagonist in preventing thrombotic events.

More evidence is required as to how cangrelor may bind in pocket 2. For example, it is not known which residues it may interact with. Exploring this was limited as docking tools did not produce a consistent, reproducible pose for cangrelor against the antagonist-bound crystal structure of P2Y<sub>12</sub>. This is likely because this structure is stabilised by a non-nucleotide ligand (AZD1283), and cangrelor is a nucleotide-based ligand. One *in silico* study showed that neither the agonist-bound structure, nor the antagonist-bound structure is ideal for predicting ticagrelor's binding mode, and that a hybrid model of both structures was preferred. This may also be the case for cangrelor.

However, as an 'open-lid' is required for P2Y<sub>12</sub> antagonism, we can assume that the only available antagonist-bound structure is better for exploring how cangrelor may bind compared to the 'closed-lid'/agonist-bound structure. The proposed mode of antagonism for the co-crystallised ligand, AZD1283, is that it prevents inward shift of

helices 6 and 7 keeping the receptor ‘lid’ open<sup>17</sup>. It would be useful to explore how cangrelor prevents ‘lid’ closure, and through what mechanism this may be achieved in pocket 2. How the orthosteric site’s sub-cavities may change shape upon cangrelor binding is unknown. However, the cysteine residues which bind the thienopyridines (the pocket where 2MeSADP and cangrelor are predicted to bind in this work) are not near the ADP, AZD1283, AR-C66096 binding pocket in the antagonist-bound structure. Thus, a two-pocket orthosteric site is still likely upon cangrelor binding.

During this work, a new fluorescent barcoding protocol was developed which allowed multiplexed analysis of pVASP levels in human platelets. Barcoding and deconvolution are relatively new, and few protocols have been developed<sup>294,296</sup>. Previously, analysis of pVASP relies on traditional flow cytometry methods (one sample run at a time, with increased antibody consumption) or immunoblotting<sup>7</sup>. With the latter, it is also challenging to create one or multiple concentration-response curves across a broad range of agonist concentrations. A combination of dye and fluorophore-conjugated antibody was used, which opens a new avenue for barcoding platelets and lays the framework for future protocols. New barcoding protocols can benefit labs which rely on flow cytometric methods, reducing antibody consumption and time taken to read large numbers of samples.

### **6.1.2. 2-aryl benzoxazole derivatives as novel inhibitors of platelet aggregation**

The aim to find novel, reversibly acting inhibitors of platelet aggregation was driven by the unmet clinical need for new classes of antiplatelet drugs with improved bleeding profiles. Additionally, current antiplatelet drugs also have other problems such as interindividual variability and it is difficult to fine-tune the effects of covalent antagonists. Side effects, such as dyspnoea, may lower patient compliance putting them at risk of developing secondary thrombotic events. New scaffolds will inform drug

discovery ventures, and as many scaffolds as possible are required, especially because attrition rates in drug discovery are high due to toxicity, low solubility, and poor pharmacokinetic profiles. This can be demonstrated with the experimental P2Y<sub>12</sub> antagonist, AZD1283. It was the result of an extensive medicinal chemistry campaign by AstraZeneca and failed clinical trials due to metabolite instability.

The crystal structures of P2Y<sub>12</sub> were recently solved (2014), but no publications were found showing them being used in structure-based screening to find novel modulators<sup>16-18</sup>. *In silico* work here contributed to our understanding of the binding mode of the co-crystallised antagonist, AZD1283, in pocket 1, as well as its essential pharmacophore points. Over 440,000 molecules were searched for to find ligands with similarity indices to AZD1283. The best hits were then docked against the P2Y<sub>12</sub> crystal structure, and 33 compounds were purchased for *in vitro* validation. Two competitively acting, novel scaffolds with consistent inhibition of ADP-induced platelet aggregation were discovered: compound B6 and compound B11. SAR around the B6 scaffold led to the discovery of another inhibitor: compound S8. Few changes were tolerated around the B6 scaffold. Whilst the other S compounds did cause some inhibition, S8 was the most effective. This work presents a scaffold (**Figure 94**) that can be used to aid drug design in the search for novel inhibitors of platelet aggregation.

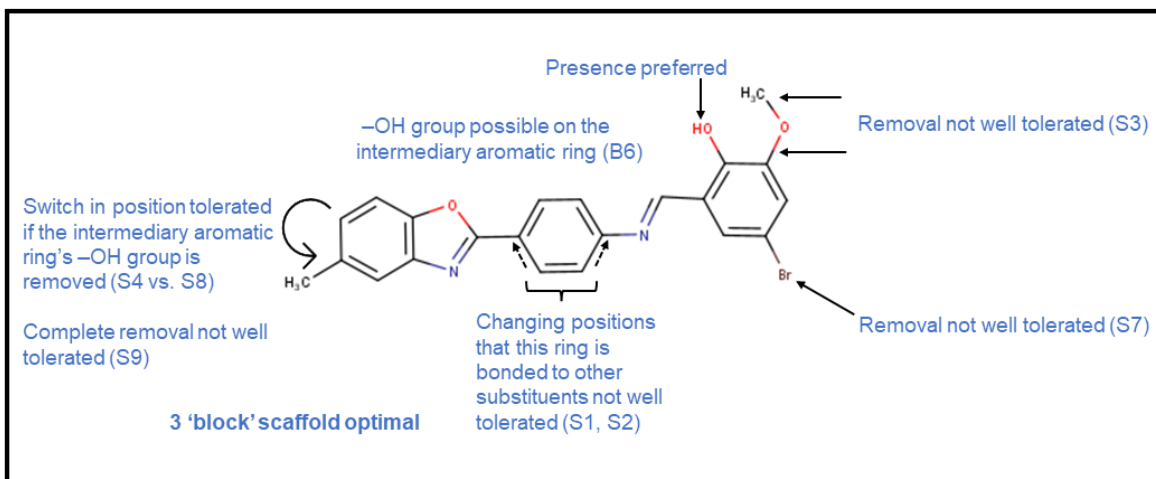


**Figure 94: SAR analysis around the 2-aryl benzoxazole scaffold based on the experimental evaluation of nine analogues of compound B6.**

However, compound B6 and S8 could not be proven to target P2Y<sub>12</sub> upon analysis of pVASP levels. Their biological target remains unknown. *In silico* work provided insight into what the target pocket of the compounds may look like, measuring approximately 14Å in length. The compounds have four rotatable bonds, limiting their flexibility within the pocket. *In vitro* data (effects on TRAP-6-amide induced platelet aggregation) suggested that the compounds' inhibition is limited to a pathway that is modulated by ADP, although future work could confirm this by examining a wider range of platelet activators. Analysis of the compounds' physicochemical properties, such as TPSA and iLOGP values suggested the compounds may be able to pass the plasma membrane to act on an intracellular target. Their lipophilic nature also makes allosteric regulation of membrane proteins through interaction with membrane phospholipids possible<sup>435-439</sup>.

## 6.2. Limitations and future directions

### 6.2.1. Limitations of the *in vitro* methods

#### 6.2.1.1. Phenotypic assay: 96-well aggregometry

Blood was collected from healthy, drug-free volunteers. Platelet count was performed using a flow cytometer to check the platelet count was normal. However, several factors that increase platelet reactivity were not accounted for. These were: smoking status, age, body mass index (BMI), and genetic factors.

In this work, 96-well aggregometry was performed instead of LTA because a broad number of agonist concentrations and a higher number of samples could be tested simultaneously. Concentration-response curves could be constructed more efficiently, and platelets in different wells were activated with agonist at the same time, which is not the case in LTA. Additionally, a higher number of replicates could be tested in the plate, which was particularly important for the PRP and PPP controls. Furthermore, as 96-well aggregometry is a relatively new method of determining % aggregation in samples, work such as this is required to allow the method to advance. Whilst there are papers in the literature on how the assay has been optimised, there is a lack of studies where the performance of the assay has been assessed using test compounds, especially screening compounds. However, as the method is new, various validation experiments were performed here before it was used to answer key questions.

96-well aggregometry has several limitations. Notable differences in response are obtained between 96-well aggregometry and LTA. This is due to the different mechanical forces present within the environment of the two assays<sup>290</sup>. In LTA, a stir bar is used (1000-1200 rpm), whereas in this work the shaking mode of the plate reader was used (double orbital, 700rpm). There is a lack of standardisation between labs for both LTA and 96-well aggregometry. Furthermore, results between different plate

readers cannot be compared if using different shaking modes and frequencies.

Additionally, shaking using a plate reader and shaking using an external vortex mixer may produce different results<sup>291</sup>. Interestingly, it has been suggested that the effects of P2Y<sub>12</sub> antagonism are more pronounced in 96-well aggregometry than LTA<sup>290</sup>. This was demonstrated by a group using AR-C66096, where they showed that in 96-well aggregometry the compound showed strong inhibition to all concentrations of collagen tested, whereas in LTA, it only showed inhibition to the lowest concentration of collagen tested<sup>290</sup>. A major difference between how the method was conducted in that work versus this work, was that the shaking was performed using an external thermoshaker (1200rpm). Other work has also suggested that clopidogrel showed more inhibition of collagen-induced platelet aggregation in 96-well aggregometry, than LTA<sup>440,441</sup>.

A marked difference observed between 96-well aggregometry and LTA (or, indeed, 96-well aggregometry performed using different shaking modes and frequencies), is that agonists show an apparent change in potency. Additionally, antagonists appear to show different levels of effectiveness when shaking frequency or mode is changed and whether a stir bar is present or not. For example, agonist potency appeared to decrease in LTA (less aggregation) when the stir bar speed was reduced from 1200rpm to 300rpm or lower<sup>290</sup>. This is because different flow dynamics affect how platelet aggregates are formed. Platelets are more likely to encounter each other at higher speeds, but aggregates with weaker platelet-platelet interactions are also more likely to be broken up due to higher forces. Since shaking frequency and stirring speed appear to affect agonist potency, it is likely that different forces influence how different agonists play their role in activating platelets. The volume of PRP used also affected this. More work is required into exploring the most optimal shaking conditions and flow dynamics which best mimic the *in vivo* environment.

Moreover, 96-well aggregometry in this work was performed at room temperature, whereas LTA is usually performed at 37°C. There were several reasons this choice was made. It has been suggested that experiments involving PRP can be performed in at either room temperature or 37°C. In clinical settings, PRP can be stored at RT for 3-4 hours before administering to the patient<sup>442,443</sup>. During this time, there will not be a loss in platelet function and platelets remain stable. Additionally, it has been suggested that heating platelets may affect their metabolic function, which was not desired<sup>443,444</sup>. When the blood was collected for this work, it was spun for 25 minutes at room temperature to isolate PRP, which was used for the experiment immediately. The PRP was then kept at the same temperature until the end of the experiment.

Although it is acknowledged that LTA is performed at 37°C (PRP is heated in the cuvette) to mimic the *in vivo* environment, this is not as simple with a 96-well plate. For example, when using the plate reader's heating function, some outer wells will heat up faster than others owing to the 'edge effect'<sup>445</sup>. This would mean that, at any given time, it is possible that the platelets in different wells (of the same concentration-response curve or screen) are not kept at the same temperature. It is difficult to know if, and when, this is happening, or to account for it. Additionally, within the enclosed space in the plate reader, condensation of the plate may begin to occur as the PRP temperature is increased due to the presence of water in the plasma. This typically occurs at a greater extent in the central wells. Even small levels of condensation may make a large difference to results.

Furthermore, it has been suggested that temperature changes have no effect on the action of some agonists, like ADP, TRAP-6 amide, thrombin, and collagen, but may influence AA or 5-HT-induced platelet aggregation<sup>446-448</sup>. In another study, temperature did not affect AA-induced platelet aggregation<sup>289</sup>. Some work has suggested that keeping PRP at room temperature may activate platelets prior to agonist addition<sup>449</sup>.

However, this was not found to be a problem in the experiments in this thesis, as shown by consistently reproducible concentration-response curves both in validation experiments and experiments used to answer key questions, and effectiveness of positive controls. If significant activation had occurred prior to agonist addition, we would expect desensitisation of the P2Y<sub>12</sub> receptor, and low levels of aggregation upon agonist addition.

Additionally, even though keeping platelets at 37°C would more closely mimic the *in vivo* environment, it is important to acknowledge that once PRP is isolated from whole blood, the model system has already far deviated from physiological conditions. *In vivo*, platelets function in whole blood and not citrated PRP, where calcium concentrations are different from physiological settings<sup>450</sup>. PRP is highly concentrated, containing more platelets than whole blood, and other blood cells present in the natural system have been lost<sup>451</sup>. For example, interactions may exist between erythrocytes (or leukocytes) and platelets during aggregation events *in vivo*<sup>450</sup>. These may include mechanical interactions or release of chemicals which may influence platelet activity. Thus, major differences are expected to exist between the physiological environment and the *in vitro* system, and all differences are impossible to control for.

Another limitation of the assay is that, occasionally, the bottom-end of concentration-response curves would go below 0% to negative values. This occurred when the test sample absorbance reached a higher value than the PRP control absorbance. Preferably, this should not occur, as the PRP absorbance value is considered 100% absorbance in the formula used to determine % aggregation (found in the **Materials and methods** section). Six replicate PRP control wells were used to find a mean control value. Although no agonist is added to the control wells, the platelets still undergo a shape change during the 5 minutes of shaking, which may explain this phenomenon.

Moreover, several factors in the well environment can affect absorbance readings in all samples. These include formation of bubbles, platelets adhering to the side of wells, impurities in the sample which reflect light, and scratches at the bottom of the plate (and plate type/bottom thickness). Wells were blocked with 0.75% gelatin to ensure that platelets did not stick to the plastic. High binding plates were not used. Additionally, the results are highly dependent on the plate reader injectors accurately dispensing the desired volume of agonist. It is important that there are no bubbles in the lines connecting the pump to the injector, as this will cause erroneous readings. End-point readings were performed, thus another factor that may affect results is the location of the aggregates within the well when the run ends. They were often stuck to the bottom of the plate, at the centre. For this reason, bottom readings were performed. Additionally, the excitation filter was set to 595nm because wavelengths of 575-650nm have been found optimal for minimal light absorption of particles in plasma<sup>288</sup>.

Lastly, in LTA, as agonist is added the platelet shape change and subsequent primary and secondary waves of aggregation can be observed as a tracing. The peak and AUC of the tracing is recorded. In 96-well aggregometry, as the 5 minutes of shaking occurs, these events cannot be observed as end-point measurements are taken. Each method has its own advantages and disadvantages, and they are not interchangeable. In this thesis, 96-well aggregometry was focused on because more work in the area is required to give the method a chance to advance and be used more universally in platelet function testing.

#### **6.2.1.2. Molecular assays**

In this work, the LANCE cAMP immunoassay by Perkin Elmer was optimised for platelets. In initial plans, it was decided that this kit could be used to assess P2Y<sub>12</sub> activity by measuring TR-FRET in platelets, and later in the work, a cell line. However,

the use of this assay was dramatically limited when it was found that the anti-cAMP antibody was picking up the test agonists ADP and 2MeSADP, as if they were cAMP. There were concerns that spending more time optimising another cAMP assay for either platelets or cells would lead to similar problems.

Thus, the decision was made to focus on optimising a flow cytometric pVASP assay. A barcoding technique was further optimised assigning samples a unique combination of dye and fluorophore-conjugated antibody so that 8 samples could be read at one time. The barcodes had good resolving power when samples were read on two different flow cytometers, in either PRP or washed platelets. These barcodes were then deconvoluted to find the MFI value of interest (determining pVASP levels). Deconvolution is a manual process and requires highly advanced knowledge of gating strategies. Erroneous MFI values can be obtained if the gating is not performed accurately. A limitation of the protocol is that it cannot be used as it is with a cell-line because the anti-CD41a antibody conjugated to PE-Cy7 is specific to a marker present on platelets.

Optimising barcoding protocols is challenging because the barcoding dyes/fluorophores should, preferably, be excited by a distinct flow cytometer laser (argon laser with fluorescence channels 1 and 2) to the Alexa Fluor 647 (He-Ne laser with fluorescence channel 4) which determines pVASP levels. This is to be certain spectral overlap is prevented. Every dye will also require its own optimisation stages to find the most effective concentrations for barcoding. Not every barcoding protocol may be used for every flow cytometer, however the protocol presented here worked well with two flow cytometers. Reproducibility of the multiplexing technique is important, especially where precious human samples are involved.

## 6.2.2. Limitations of the *in silico* methods

The main limitation in this thesis is the lack of reconciliation between the *in silico* results and the *in vitro* pVASP assay results for the proposed novel inhibitors. Thus, the main question that needs to be addressed is: why have these compounds passed multiple filters (or ‘check-points’) in the virtual screening if, in fact, they are not P2Y<sub>12</sub> modulators? It is probably likely that the *in silico* protocol is flawed in some way, which is making it prone to picking up false positives. It is challenging to know where exactly in the process the flaw lies, especially since the protocol was validated using the co-crystallised ligand and docking poses were analysed in different programs for consensus.

However, this problem is not unique to this work. False positives are a major issue in docking studies<sup>373,452</sup>. It is probably unlikely that the issue lies in the initial stages of the protocol (ligand-based screening) as the aim there was to simply pick up scaffolds with similarity indices to AZD1283. These screens looked at a very large chemical space. Realistically, most of the compounds in this space were unlikely to be P2Y<sub>12</sub> modulators, even if structurally like AZD1283. Thus, the problem is likely to lie in the subsequent stages where the structure of P2Y<sub>12</sub> was involved.

Some limitations of structure-based work have already been discussed in previous chapters. This is mainly to do with the common observation in docking that many compounds achieve high scores. However, to combat this, the protocol adopted here looked at both scores and protein-ligand interactions. It was difficult to know which interactions were most important, as we do not know about them experimentally. Interestingly, the interactions picked up in PLIP for AZD1283 almost matched those proposed by the authors in the original crystal structure paper<sup>17</sup>. Compounds for prospective *in vitro* studies were analysed carefully and ranked according to these interactions. Still, one of the possible reasons for high numbers of false positives in

docking is that the receptor is rigid or static. The crystal structure is a ‘snapshot’ of the protein in time. Protein plasticity, or the rearrangements the pocket undergoes upon ligand binding, is not considered in the scoring function<sup>373,452,453</sup>. This is particularly important, as GPCRs are highly dynamic and in constant motion. MD simulations after docking may have helped to prove or refute the docking poses. This is because these simulations consider receptor plasticity and the fluidity of the surrounding plasma membrane. MD simulations sometimes reveal unstable docking poses. However, if that path had been followed, compounds B6 and B11 may not have been purchased in the B series.

A critical challenge in *in silico* studies is determining the most effective screening protocol or strategy (for the protein of interest). Here, a common workflow in computational drug discovery was used: 1) ligand-based screening including electrostatic analysis, 2) docking, 3) analysis of protein-ligand interactions. In hindsight, ensemble docking may have also been useful to consider the protein in multiple conformations. This is where several crystal structures of the protein are superimposed for structure-based work. However, the usefulness of considering the closed ‘lid’ structures of the nucleotide-based agonist 2MeSADP and the partial agonist 2MeSATP is questionable. It would not be expected that a prospective antagonist would close the ‘lid’. That approach may also have increased the chance for picking up more false positives with each protein conformation. Agonists may also be more likely to be picked up instead of antagonists. Additionally, the structure of the receptor in its *apo* state is not a crystal structure but generated using MD simulations. There are questions as to whether this structure would be useful in docking since side chains will be in a different position and ‘filling’ the vacant AZD1283 binding site. In docking, it is preferred that a high-resolution crystal structure (stabilised by a known ligand) is used, as in this work<sup>418</sup>.

Additionally, since initial ligand-based work was focused on finding a non-nucleotide scaffold based on AZD1283, it made sense to then use the AZD1283-stabilised structure for subsequent docking. This protocol may be useful in other work, but it was not optimal with the P2Y<sub>12</sub> structure. However, now that this is known, other studies can invest time in alternative *in silico* approaches. It is important to continue to focus on finding the optimal *in silico* protocol for finding novel modulators of P2Y<sub>12</sub>. This is because if an approach is successful, it can help to validate the P2Y<sub>12</sub> crystal structure, as well as leading to the discovery of novel modulators.

### **6.2.3. Limitations of the findings**

#### **6.2.3.1. Cangrelor may act in a non-competitive manner to ADP**

Cangrelor's possible non-competitive mode of antagonism with ADP, and competitive mode of antagonism with 2MeSADP, suggested that ADP and 2MeSADP may act in different pockets at the P2Y<sub>12</sub> orthosteric site. However, the main limitation to this finding is that AZD1283 and AR-C66096 acted in a competitive manner with both ADP and 2MeSADP in the aggregometry assay. This was in line with evidence in the literature that AZD1283 acts in a competitive manner to ADP. Since we already know the binding mode of the co-crystallised ligand, AZD1283, its competitive mode of antagonism with the two agonists suggests that they may bind in the same sub-pocket. If ADP and 2MeSADP act in the same pocket as AZD1283 and AR-C66096 do, this still does not explain why or how cangrelor may exhibit different modes of antagonism with the two agonists. However, as explained previously in this Chapter, docking by others has shown that 2MeSADP may bind in either pocket 1 or pocket 2. In either case, it is possible for it to act in a competitive manner to AZD1283 (pocket 1) and cangrelor (pocket 2).

There are also two possible counter arguments to the ‘non-competitive antagonism’ theory for cangrelor. Firstly, that cangrelor is an inverse agonist, and its effects are more readily overcome with 2MeSADP than ADP. However, the problem with this argument is that inverse agonism would still be overcome if sufficient ADP is added (and very high - millimolar - concentrations of ADP were used in these experiments). Additionally, P2Y<sub>12</sub> in platelets from healthy individuals has not been reported to display constitutive activity. In such a scenario, platelets in healthy individuals would be in a constant state of hyperactivation - which would increase thrombotic risk. The receptor may display constitutive activity because of mutation(s) or overexpression<sup>454</sup>. In DM patients, who have been reported to have hyperactivated platelets, the P2Y<sub>12</sub> receptor does display constitutive activity<sup>431,454,455</sup>. This is because P2Y<sub>12</sub> is expressed 4-fold higher in platelets from DM patients than healthy controls<sup>431</sup>. Cangrelor and the potent P2Y<sub>12</sub> inverse agonist, AR-C78511 were shown to have similar antiplatelet effects on platelets from healthy individuals<sup>431</sup>. However, AR-C78511 displayed greater antiplatelet effects than cangrelor in platelets from DM patients.

Similarly, thrombosis models in Goto-Kakizaki rats (which develop DM in early life) were used to demonstrate that AR-C78511 displayed greater antithrombotic effects than cangrelor. AR-C78511 was further shown to be an inverse agonist in transgenic mice generated to express constitutively active (chimeric) P2Y<sub>12</sub><sup>454</sup>. It was also demonstrated with the transgenic mice line that constitutively active P2Y<sub>12</sub> increases platelet reactivity and thrombotic events. Importantly, in the literature, P2Y<sub>12</sub> is often studied in cell lines where it is overexpressed. In such a system, constitutive activity would be expected, and antagonists may display inverse agonism. For this reason, the results obtained from testing compounds in platelets (from healthy individuals) and P2Y<sub>12</sub>-expressing cell-lines cannot directly be compared.

The second counter argument is that cangrelor may act on both P2Y<sub>12</sub> and P2Y<sub>1</sub>. The aggregometry assay is a readout of P2Y<sub>12</sub>, P2Y<sub>1</sub>, and integrin activity (as well as other proteins involved in aggregation), and not just P2Y<sub>12</sub>. However, in line with the aggregometry data, cangrelor would also need to be acting in a non-competitive manner to ADP and in a competitive manner to 2MeSADP at P2Y<sub>1</sub>. For example, in the aggregometry validations where platelets were pre-incubated with the P2Y<sub>1</sub> antagonist, MRS 2179, it exhibited competitive antagonism with ADP. Thus, if cangrelor was acting competitively with ADP at P2Y<sub>1</sub>, we would expect the concentration-response curve E<sub>max</sub> value to indicate this, similarly to that of MRS 2179. Although, it is possible ADP may not be potent enough to overcome the powerful effect of a dual antagonist.

The crystal structure of P2Y<sub>1</sub> in complex with the nucleotide-based antagonist, MRS 2500 is deposited in the PDB. Unlike the antagonist-stabilised two-pocket conformation of P2Y<sub>12</sub>, the P2Y<sub>1</sub> orthosteric site is composed of one small pocket accommodating MRS 2500<sup>456</sup>. The size of this pocket does not allow enough room for cangrelor to display non-competitive antagonism with ADP. It may be possible if cangrelor stabilises a completely different conformation of the receptor, where there is more space in the orthosteric site (like the two-pocket orthosteric site stabilised by AZD1283 in P2Y<sub>12</sub>). Although there is no P2Y<sub>12</sub> structure co-crystallised with cangrelor, the antagonist-bound structure (open 'lid') is likely more useful than the agonist-bound (closed 'lid') structure. This is because we would not expect cangrelor to stabilise a closed 'lid' conformation of the receptor, which is a hallmark feature of P2Y<sub>12</sub> activation.

Moreover, platelets that were pre-incubated with cangrelor had significantly lower cytosolic Ca<sup>2+</sup> after activation with ADP, than platelets that were pre-incubated with AR-C66096. It cannot be determined whether this was due to P2Y<sub>12</sub>-P2Y<sub>1</sub> cross talk (due to cangrelor's antagonism of P2Y<sub>12</sub>), or the effects of cangrelor's direct action

on P2Y<sub>1</sub>. It was also unexpected that AR-C66096 did not significantly decrease cytosolic Ca<sup>2+</sup> levels, whilst cangrelor and AZD1283 do. As previously mentioned, this may just be because the AR-C66096 effect was weaker and more variable. It may be useful to further explore the effects of these compounds in a P2Y<sub>1</sub>-expressing cell-line using a calcium assay or perform ligand binding studies at P2Y<sub>1</sub>. However, even if cangrelor can be proven to act on P2Y<sub>1</sub>, this still does not rule out its possible non-competitive mode of antagonism at P2Y<sub>12</sub>. Additionally, whilst AZD1283 was shown in this work to significantly decrease cytosolic Ca<sup>2+</sup> levels, there is no evidence that AZD1283 acts on P2Y<sub>1</sub>. Thus, the decrease in Ca<sup>2+</sup> levels may be a feature of some P2Y<sub>12</sub> antagonists (because of P2Y<sub>12</sub>-P2Y<sub>1</sub> crosstalk). Whilst P2Y<sub>1</sub> antagonism cannot be ruled out, it is also important to note that there are other protein pathways coupled to calcium signalling in platelets, and not just P2Y<sub>1</sub>.

Additionally, in the pVASP assay, ADP (up to 1mM) + cangrelor (100nM) E<sub>max</sub> did not reach that of ADP (1mM) + vehicle, whereas AR-C66096 did. This was further evidence in support of cangrelor's possible non-competitive mode of antagonism at P2Y<sub>12</sub>, as VASP is a component of the P2Y<sub>12</sub> signalling pathway. However, it is also acknowledged that VASP is not only limited to the P2Y<sub>12</sub> pathway, but that any protein acting through cAMP signalling will affect VASP. In general, several counter arguments have been presented here. One point that is certain is that cangrelor and its analogue, AR-C66096 may have different modes of antagonism with the two agonists. Cangrelor also had a different time vs. inhibition profile to vehicle in the aggregometry (with ADP), whereas AR-C66096 did not (**Figure 52**).

#### 6.2.3.2. 2-aryl benzoxazole derivatives as novel inhibitors of platelet aggregation

These compounds had several limitations. Firstly, they were poorly soluble (in DMSO). This was reflected by their lower TPSA values and higher iLOGP, compared to the

positive control AZD1283. When aliquots of the compounds were made up in HBS, it took several rounds of vortexing and sonication to ensure they were fully dissolved. The most optimal method of dissolving was as follows: 1) addition of HBS to the aliquot, 2) approximately 60-70 minutes in a sonicator, 3) vortexing, 4) 10 additional minutes of sonication, 5) vortexing. Compound S8 was 'sticky', thus when HBS is added to the tube, it should not directly be vortexed. This will lead to the compound sticking to the sides of the tube. Future studies of these compounds should also consider the size of the sonicator, as this makes a difference to the temperature in the water over the hour or so of sonication. It may be possible that the increase in temperature aids in dissolving the compounds. Poor solubility is a commonly encountered issue with screening compounds, as they have usually not previously been tested for solubility.

Secondly, these compounds violated two rules of leadlikeness (**Table 7**). This was because the compounds' molecular weight and iLOGP values exceeded set limits for leadlikeness<sup>457</sup>. An iLOGP value of less than 4 is also preferred in drug discovery because the compound will have more optimal physicochemical and ADME properties in developing orally administered drugs<sup>398,458-460</sup>. Additionally, they contained an imine group, which is a Brenk alert. As previously described, Brenk alerts are groups which may be toxic, chemically reactive, or (metabolically) unstable. A third limitation of these compounds is that their purity may not be as high as the positive control, AZD1283 ( $\geq 98\%$ ). The manufacturer stated that their purity is guaranteed to be 90% or above, but that the exact value of purity is unknown. How the purity varies between vials of the same compound is also unknown. Moreover, at the molecular level compound B6 also significantly enhanced cytosolic  $\text{Ca}^{2+}$  levels, which was an undesired off-target effect. Lastly, the inhibitory effect of compounds B6 and S8 in the aggregometry was more variable between blood donors than the positive control, which

was reflected by larger SEM bars. This is probably expected, as the AZD1283 scaffold has gone through years of medicinal chemistry optimisation by AstraZeneca.

## 6.2.4. Future work

### 6.2.4.1. For groups interested in the mode of action of cangrelor or structural biology

The structure of P2Y<sub>12</sub> co-crystallised to cangrelor would provide a definite answer to cangrelor's mode of binding. The nucleotide-based compounds 2MeSADP and 2MeSATP have already been co-crystallised with P2Y<sub>12</sub>, suggesting that a cangrelor-P2Y<sub>12</sub> complex is possible in X-ray crystallography. There are no papers suggesting this has been attempted yet. P2Y<sub>12</sub> is conformationally dynamic (like most GPCRs), and it is unknown whether it is stable enough to lend itself to crystallisation in the presence. If this is the case, then future work may focus on coming up with some means to reduce inherent conformational stability of the protein in complex with cangrelor to make X-ray crystallography possible. Perhaps more possible, a technique such as cryogenic electron microscopy (cryo-EM), where crystallisation is not required, may also be useful to elucidate the cangrelor-P2Y<sub>12</sub> complex. A further advantage of cryo-EM is that it could be performed in phospholipid nanodiscs, so that the effect of plasma membrane phospholipids on receptor structure can be determined<sup>461,462</sup>.

Since the release of the AZD1283, 2MeSADP, and 2MeSATP-bound structures, no other structures of P2Y<sub>12</sub> in complex with a ligand have been released. However, considering the findings here that cangrelor may act in a non-competitive manner to ADP and in a competitive manner to 2MeSADP, it may appeal to structural biologists to now solve the crystal structure of P2Y<sub>12</sub> in complex with cangrelor. Although we know how a non-nucleotide-based antagonist (AZD1283) stabilises P2Y<sub>12</sub>, we do not know how a nucleotide-based antagonist stabilises the protein, and what the orthosteric site

will look like. Regarding the latter, it would be helpful to know what pocket 1 and pocket 2 look like upon cangrelor binding. It is likely that cangrelor stabilises an open-lid model, like AZD1283. Such a structure may also lead us to a novel mechanism by which P2Y<sub>12</sub> can be reversibly inhibited through effects in pocket 2.

P2Y<sub>12</sub> in complex with the endogenous ligand, ADP, would also be useful to see if ADP and 2MeSADP bind in the same pocket. In this thesis, there was more focus on how cangrelor acts with ADP, because the endogenous ligand is more physiologically relevant even though it has not been co-crystallised with the receptor. However, future studies may perform more experiments with 2MeSADP, which serves as a valuable tool to further explore the two-pocket theory at the P2Y<sub>12</sub> orthosteric site. Additionally, using (high concentrations e.g., 10mM) of either agonist, studies may be conducted into how cangrelor or AR-C66096 affect platelet morphology. For example, platelet spreading can be assayed using surfaces coated with fibrinogen or collagen, stained, and observed using a fluorescence microscope<sup>463</sup>. Electron microscopy may be used to observe shape changes and aggregation in the presence of cangrelor or AR-C66096 with the two agonists, which can lead to useful qualitative data. However, this may take more time to optimise than the spreading assay. To complement these studies, flow cytometric analysis of platelet integrin activation may also be performed.

More broadly, future work may also focus on how antagonist binding in pocket 1 vs. binding in pocket 2 may affect bleeding risk. This would be useful with clinically available P2Y<sub>12</sub> inhibitors that have bleeding information available from patients. For example, ticagrelor may bind in a similar manner to the experimental drug AZD1283 (in pocket 1). Surprisingly, it has a higher bleeding risk than the irreversibly binding compounds, clopidogrel and prasugrel, which binds in pocket 2. They completely prevent P2Y<sub>12</sub> activity for the remainder of the platelet's life. It is unknown whether this difference in bleeding risk between ticagrelor and clopidogrel may be related to the

ligands binding in different pockets. However, some studies suggested there is no difference in bleeding risk between cangrelor, ticagrelor, and prasugrel<sup>464,465</sup>.

Nevertheless, as more information on bleeding risk is made available for compounds proposed/proven to bind in pocket 1 vs. compounds proposed/proven to binding in pocket 2, it may help to build up a picture of whether targeting different pockets in the orthosteric site affects bleeding risk. This could be useful because a future class of P2Y<sub>12</sub> antagonists could be developed to target pocket 2, if it can be proven there is a decreased bleeding risk compared to pocket 1.

Lastly, from a clinical perspective, groups may be interested in exploring whether cangrelor's possible non-competitive mode of antagonism with ADP may be useful for it to be used in an emergency setting in a patient undergoing thrombotic events (to inhibit further aggregation). This is also considering the drug is reversible, has a fast onset/offset of action, and can be intravenously administered. Such studies may be precluded by *in vitro* analysis of whether cangrelor can dissolve pre-formed thrombi/decrease thrombi size compared to the competitively acting reversible inhibitors<sup>466</sup>. In such an instance, there is potential for cangrelor to be useful in inhibiting further aggregation, whilst also dissolving pre-formed thrombi.

#### **6.2.4.2. For groups interested in novel inhibitors of platelet aggregation**

Future work should focus on finding the biological target of compounds B6 and S8. Initially, to further support the conclusion reached with platelets in the pVASP assay, a P2Y<sub>12</sub>-expressing cell line and a bioluminescence resonance energy transfer (BRET)-based cAMP assay, may be useful<sup>335</sup>. Some potential ideas as to other targets have been described in the previous chapter's discussion. A 'trial and error' approach may also have to be taken to probe different pathways and find clues that point towards the potential target. Additionally, the scaffolds may be improved upon using medicinal

chemistry. The solubility of the compounds should preferably be improved. Thus, the structures should be modified such that their iLOGP values are lower and their TPSA values higher. This is because drugs with higher lipophilicity can have more off-target effects, greater plasma protein binding, and less desirable pharmacokinetic properties. Regarding off-target effects, it would be useful to find out how B6 is enhancing cytosolic  $\text{Ca}^{2+}$  levels, and how future scaffolds may be designed to prevent this. Modifying the scaffold may be challenging to do, as little change was tolerated around the B6 scaffold. It is also unknown how these changes (to lipophilicity) may influence the effectiveness of the compounds, for example if they need to cross the plasma membrane to reach an intracellular target. Furthermore, their imine group is undesirable, and other groups may be tested in this region of the scaffold using a SAR approach. However, some marketed drugs have an imine group, and this group can play an important role in the action of the drug<sup>467</sup>. Additionally, it may be useful to further explore the observation that S8 scaffold (but not B6) appeared to cause more inhibition in males than females. Such work would require larger sample numbers of male and female blood donor groups to perform more powerful statistical analysis.

In this thesis, one aim was to find chemical building blocks which could inhibit aggregation. This involved showing that the SAR/analogue based approach was successful when using it to find S8 from the B6 scaffold. As in other screens performed by pharmaceutical companies, a concentration of  $10\mu\text{M}$  was commonly used. Additionally, it is common in pharmacology to initially screen compounds at higher concentrations before moving to lower concentrations upon finding a hit. In future work, these compounds may be tested at lower concentrations to further test their inhibitory effects, including finding their  $\text{pIC}_{50}$  values using 96-well aggregometry. Such concentrations may also be more relevant physiologically. It would also be interesting to test the compounds in LTA and obtain tracings, which may be

complementary to current results<sup>468</sup>. Although the peak and AUC values from these tracings may be used to construct concentration vs. response curves, these results cannot directly be compared to the results obtained in 96-well aggregometry. The reasons for this have previously been discussed. To that end, analogues of compound B11 (which was originally found alongside B6 and has a different scaffold) may also be tested in aggregometry.

Moreover, time-course studies may also be performed to see if incubation time makes a difference to the level of inhibition produced by the compounds. This may be important in allostery (e.g., binding to intracellular site on a GPCR) or if the compounds act on an intracellular target<sup>469,470</sup>. In both cases, they will need more time to cross the plasma membrane than if they target an extracellular site on a protein. Such studies may serve useful in finding clues to discover the target in question. If a particular protein is proposed as the target, knockout studies may then be useful.

Lastly, the compounds may be tested using *in vitro* or *in vivo* models of thrombosis to explore whether they prevent (or decrease) occlusion compared to known inhibitors of aggregation, such as AZD1283<sup>206,431,454,471</sup>. It may also be useful to observe how the compounds affect bleeding in an animal model by determining the rat tail bleeding time<sup>454,472,473</sup>.



## References

- 1 World Health Organisation. *The top 10 causes of death.* ,  
<<https://www.who.int/news-room/fact-sheets/detail/the-top-10-causes-of-death>>  
(2020) (accessed January 31st, 2022).
- 2 Jackson, S. P. Arterial thrombosis—insidious, unpredictable and deadly. *Nature Medicine* **17**, 1423-1436, doi:10.1038/nm.2515 (2011).
- 3 Roth, G. A. *et al.* Global Burden of Cardiovascular Diseases and Risk Factors, 1990–2019: Update From the GBD 2019 Study. *Journal of the American College of Cardiology* **76**, 2982-3021, doi:<https://doi.org/10.1016/j.jacc.2020.11.010> (2020).
- 4 Nowbar, A. N., Gitto, M., Howard, J. P., Francis, D. P. & Al-Lamee, R. Mortality From Ischemic Heart Disease. *Circulation: Cardiovascular Quality and Outcomes* **12**, e005375, doi:10.1161/CIRCOUTCOMES.118.005375 (2019).
- 5 Alexopoulos, D., Varlamos, C., Mpahara, A. & Lianos, I. P2Y<sub>12</sub> inhibitors for the treatment of acute coronary syndrome patients undergoing percutaneous coronary intervention: current understanding and outcomes. *Expert Review of Cardiovascular Therapy* **17**, 717-727, doi:10.1080/14779072.2019.1675513 (2019).
- 6 Capranzano, P. & Capodanno, D. Switching between P2Y<sub>12</sub> inhibitors: Rationale, methods, and expected consequences. *Vascul Pharmacol* **116**, 4-7, doi:10.1016/j.vph.2019.03.001 (2019).
- 7 Aungraheeta, R. *et al.* Inverse agonism at the P2Y<sub>12</sub> receptor and ENT1 transporter blockade contribute to platelet inhibition by ticagrelor. *Blood* **128**, 2717-2728, doi:10.1182/blood-2016-03-707844 (2016).
- 8 Siller-Matula, J. M. & Jilma, B. Ticagrelor: from discovery to Phase III clinical trial. *Future Cardiology* **6**, 753-764, doi:10.2217/fca.10.89 (2010).
- 9 Parodi, G. & Storey, R. F. Dyspnoea management in acute coronary syndrome patients treated with ticagrelor. *Eur Heart J Acute Cardiovasc Care* **4**, 555-560, doi:10.1177/2048872614554108 (2015).
- 10 Wittfeldt, A. *et al.* Ticagrelor enhances adenosine-induced coronary vasodilatory responses in humans. *J Am Coll Cardiol* **61**, 723-727, doi:10.1016/j.jacc.2012.11.032 (2013).
- 11 Armstrong, D. *et al.* Characterization of the Adenosine Pharmacology of Ticagrelor Reveals Therapeutically Relevant Inhibition of Equilibrative Nucleoside Transporter 1. *Journal of Cardiovascular Pharmacology and Therapeutics* **19**, 209-219, doi:10.1177/1074248413511693 (2014).
- 12 Wadowski, P. P. *et al.* Ticagrelor Inhibits Toll-Like and Protease-Activated Receptor Mediated Platelet Activation in Acute Coronary Syndromes. *Cardiovasc Drugs Ther* **34**, 53-63, doi:10.1007/s10557-019-06932-7 (2020).
- 13 Cattaneo, M., Schulz, R. & Nylander, S. Adenosine-Mediated Effects of Ticagrelor: Evidence and Potential Clinical Relevance. *Journal of the American College of Cardiology* **63**, 2503-2509, doi:<https://doi.org/10.1016/j.jacc.2014.03.031> (2014).
- 14 Serebruany, V. L., Sibbing, D. & DiNicolantonio, J. J. Dyspnea and reversibility of antiplatelet agents: ticagrelor, elinogrel, cangrelor, and beyond. *Cardiology* **127**, 20-24, doi:10.1159/000354876 (2014).
- 15 Caldeira, D., Pinto, F. J. & Ferreira, J. J. Dyspnea and Reversibility Profile of P2Y<sub>12</sub> Antagonists: Systematic Review of New Antiplatelet Drugs. *American*

- Journal of Cardiovascular Drugs* **14**, 303-311, doi:10.1007/s40256-014-0071-6 (2014).
- 16 Zhang, J. *et al.* Agonist-bound structure of the human P2Y<sub>12</sub> receptor. *Nature* **509**, 119-122, doi:10.1038/nature13288 (2014).
- 17 Zhang, K. *et al.* Structure of the human P2Y<sub>12</sub> receptor in complex with an antithrombotic drug. *Nature* **509**, 115-118, doi:10.1038/nature13083 (2014).
- 18 Paoletta, S. *et al.* Modeling ligand recognition at the P2Y<sub>12</sub> receptor in light of X-ray structural information. *J Comput Aided Mol Des* **29**, 737-756, doi:10.1007/s10822-015-9858-z (2015).
- 19 Saab, S., Bernstein, D., Hassanein, T., Kugelmas, M. & Kwo, P. Treatment Options for Thrombocytopenia in Patients With Chronic Liver Disease Undergoing a Scheduled Procedure. *J Clin Gastroenterol* **54**, 503-511, doi:10.1097/mcg.0000000000001338 (2020).
- 20 Machlus, K. R., Thon, J. N. & Italiano, J. E., Jr. Interpreting the developmental dance of the megakaryocyte: a review of the cellular and molecular processes mediating platelet formation. *Br J Haematol* **165**, 227-236, doi:10.1111/bjh.12758 (2014).
- 21 Machlus, K. R. & Italiano, J. E., Jr. The incredible journey: From megakaryocyte development to platelet formation. *J Cell Biol* **201**, 785-796, doi:10.1083/jcb.201304054 (2013).
- 22 Nassa, G. *et al.* Splicing of platelet resident pre-mRNAs upon activation by physiological stimuli results in functionally relevant proteome modifications. *Scientific Reports* **8**, 498, doi:10.1038/s41598-017-18985-5 (2018).
- 23 Schwertz, H., Rowley, J. W., Tolley, N. D., Campbell, R. A. & Weyrich, A. S. Assessing protein synthesis by platelets. *Methods Mol Biol* **788**, 141-153, doi:10.1007/978-1-61779-307-3\_11 (2012).
- 24 Weyrich, A. S., Schwertz, H., Kraiss, L. W. & Zimmerman, G. A. Protein synthesis by platelets: historical and new perspectives. *J Thromb Haemost* **7**, 241-246, doi:10.1111/j.1538-7836.2008.03211.x (2009).
- 25 Denis, M. M. *et al.* Escaping the nuclear confines: signal-dependent pre-mRNA splicing in anucleate platelets. *Cell* **122**, 379-391, doi:10.1016/j.cell.2005.06.015 (2005).
- 26 Schwertz, H. *et al.* Signal-dependent splicing of tissue factor pre-mRNA modulates the thrombogenicity of human platelets. *J Exp Med* **203**, 2433-2440, doi:10.1084/jem.20061302 (2006).
- 27 Landry, P. *et al.* Existence of a microRNA pathway in anucleate platelets. *Nature Structural & Molecular Biology* **16**, 961-966, doi:10.1038/nsmb.1651 (2009).
- 28 Zimmerman, G. A. & Weyrich, A. S. Signal-dependent protein synthesis by activated platelets: new pathways to altered phenotype and function. *Arterioscler Thromb Vasc Biol* **28**, s17-24, doi:10.1161/atvbaha.107.160218 (2008).
- 29 Selvadurai, M. V. & Hamilton, J. R. Structure and function of the open canalicular system – the platelet’s specialized internal membrane network. *Platelets* **29**, 319-325, doi:10.1080/09537104.2018.1431388 (2018).
- 30 Ebbeling, L., Robertson, C., McNicol, A. & Gerrard, J. M. Rapid Ultrastructural Changes in the Dense Tubular System Following Platelet Activation. *Blood* **80**, 718-723, doi:<https://doi.org/10.1182/blood.V80.3.718.718> (1992).
- 31 van Nispen tot Pannerden, H. *et al.* The platelet interior revisited: electron tomography reveals tubular  $\alpha$ -granule subtypes. *Blood* **116**, 1147-1156, doi:10.1182/blood-2010-02-268680 (2010).

- 32 Broos, K., De Meyer, S. F., Feys, H. B., Vanhoorelbeke, K. & Deckmyn, H. Blood platelet biochemistry. *Thrombosis Research* **129**, 245-249, doi:<https://doi.org/10.1016/j.thromres.2011.11.002> (2012).
- 33 Gerrard, J. M., White, J. G., Rao, G. H. & Townsend, D. Localization of platelet prostaglandin production in the platelet dense tubular system. *Am J Pathol* **83**, 283-298 (1976).
- 34 Zaninetti, C., Sachs, L. & Palankar, R. Role of Platelet Cytoskeleton in Platelet Biomechanics: Current and Emerging Methodologies and Their Potential Relevance for the Investigation of Inherited Platelet Disorders. *Hamostaseologie* **40**, 337-347, doi:10.1055/a-1175-6783 (2020).
- 35 Cerecedo, D. Platelet cytoskeleton and its hemostatic role. *Blood Coagul Fibrinolysis* **24**, 798-808, doi:10.1097/MBC.0b013e328364c379 (2013).
- 36 Thomas, S. G. in *Platelets (Fourth Edition)* (ed Alan D. Michelson) 47-77 (Academic Press, 2019).
- 37 Schwer, H. D. *et al.* A lineage-restricted and divergent beta-tubulin isoform is essential for the biogenesis, structure and function of blood platelets. *Curr Biol* **11**, 579-586, doi:10.1016/s0960-9822(01)00153-1 (2001).
- 38 Bearer, E. L., Prakash, J. M. & Li, Z. Actin dynamics in platelets. *Int Rev Cytol* **217**, 137-182, doi:10.1016/s0074-7696(02)17014-8 (2002).
- 39 Fox, J. E., Reynolds, C. C., Morrow, J. S. & Phillips, D. R. Spectrin is associated with membrane-bound actin filaments in platelets and is hydrolyzed by the Ca<sup>2+</sup>-dependent protease during platelet activation. *Blood* **69**, 537-545 (1987).
- 40 Patel-Hett, S. *et al.* The spectrin-based membrane skeleton stabilizes mouse megakaryocyte membrane systems and is essential for proplatelet and platelet formation. *Blood* **118**, 1641-1652, doi:10.1182/blood-2011-01-330688 (2011).
- 41 Rosa, J.-P., Raslova, H. & Bryckaert, M. Filamin A: key actor in platelet biology. *Blood* **134**, 1279-1288, doi:10.1182/blood.2019000014 (2019).
- 42 Heijnen, H. & van der Sluijs, P. Platelet secretory behaviour: as diverse as the granules ... or not? *Journal of Thrombosis and Haemostasis* **13**, 2141-2151, doi:<https://doi.org/10.1111/jth.13147> (2015).
- 43 Whiteheart, S. W. Platelet granules: surprise packages. *Blood* **118**, 1190-1191, doi:10.1182/blood-2011-06-359836 (2011).
- 44 Kim, D. A., Ashworth, K. J., Di Paola, J. & Ku, D. N. Platelet  $\alpha$ -granules are required for occlusive high-shear-rate thrombosis. *Blood Advances* **4**, 3258-3267, doi:10.1182/bloodadvances.2020002117 (2020).
- 45 Heijnen, H. & Korporaal, S. Platelet Morphology and Ultrastructure. 21-37, doi:10.1007/978-3-319-47462-5\_3 (2017).
- 46 Whiteheart, S. W. Fueling Platelets. *Arteriosclerosis, Thrombosis, and Vascular Biology* **37**, 1592-1594, doi:10.1161/ATVBAHA.117.309841 (2017).
- 47 Periyah, M. H., Halim, A. S. & Mat Saad, A. Z. Mechanism Action of Platelets and Crucial Blood Coagulation Pathways in Hemostasis. *Int J Hematol Oncol Stem Cell Res* **11**, 319-327 (2017).
- 48 Mortensen, M. B. & Nordestgaard, B. G. Elevated LDL cholesterol and increased risk of myocardial infarction and atherosclerotic cardiovascular disease in individuals aged 70-100 years: a contemporary primary prevention cohort. *The Lancet* **396**, 1644-1652, doi:10.1016/S0140-6736(20)32233-9 (2020).
- 49 Fruchart, J.-C., Nierman, M. C., Stroes, E. S. G., Kastelein, J. J. P. & Duriez, P. New Risk Factors for Atherosclerosis and Patient Risk Assessment. *Circulation* **109**, III-15-III-19, doi:10.1161/01.CIR.0000131513.33892.5b (2004).

- 50 Bevan, G. H., Al-Kindi, S. G., Brook, R. D., Münzel, T. & Rajagopalan, S. Ambient Air Pollution and Atherosclerosis. *Arteriosclerosis, Thrombosis, and Vascular Biology* **41**, 628-637, doi:10.1161/ATVBAHA.120.315219 (2021).
- 51 Borén, J. *et al.* Low-density lipoproteins cause atherosclerotic cardiovascular disease: pathophysiological, genetic, and therapeutic insights: a consensus statement from the European Atherosclerosis Society Consensus Panel. *European Heart Journal* **41**, 2313-2330, doi:10.1093/eurheartj/ehz962 (2020).
- 52 Bentzon, J. F., Otsuka, F., Virmani, R. & Falk, E. Mechanisms of Plaque Formation and Rupture. *Circulation Research* **114**, 1852-1866, doi:10.1161/CIRCRESAHA.114.302721 (2014).
- 53 Shioi, A. & Ikari, Y. Plaque Calcification During Atherosclerosis Progression and Regression. *J Atheroscler Thromb* **25**, 294-303, doi:10.5551/jat.RV17020 (2018).
- 54 Akers, E. J., Nicholls, S. J. & Bartolo, B. A. D. Plaque Calcification. *Arteriosclerosis, Thrombosis, and Vascular Biology* **39**, 1902-1910, doi:10.1161/ATVBAHA.119.311574 (2019).
- 55 Shi, X. *et al.* Calcification in Atherosclerotic Plaque Vulnerability: Friend or Foe? *Frontiers in Physiology* **11**, doi:10.3389/fphys.2020.00056 (2020).
- 56 Insull, W., Jr. The Pathology of Atherosclerosis: Plaque Development and Plaque Responses to Medical Treatment. *The American Journal of Medicine* **122**, S3-S14, doi:10.1016/j.amjmed.2008.10.013 (2009).
- 57 Owens, A. P., 3rd & Mackman, N. Role of tissue factor in atherothrombosis. *Curr Atheroscler Rep* **14**, 394-401, doi:10.1007/s11883-012-0269-5 (2012).
- 58 Toschi, V. *et al.* Tissue factor modulates the thrombogenicity of human atherosclerotic plaques. *Circulation* **95**, 594-599, doi:10.1161/01.cir.95.3.594 (1997).
- 59 Steffel, J., Lüscher, T. F. & Tanner, F. C. Tissue Factor in Cardiovascular Diseases. *Circulation* **113**, 722-731, doi:10.1161/CIRCULATIONAHA.105.567297 (2006).
- 60 Rekhter, M. D. Collagen synthesis in atherosclerosis: too much and not enough. *Cardiovascular Research* **41**, 376-384, doi:10.1016/s0008-6363(98)00321-6 (1999).
- 61 Chernysh, I. N. *et al.* The distinctive structure and composition of arterial and venous thrombi and pulmonary emboli. *Scientific Reports* **10**, 5112, doi:10.1038/s41598-020-59526-x (2020).
- 62 Stalker, T. J. *et al.* Hierarchical organization in the hemostatic response and its relationship to the platelet-signaling network. *Blood* **121**, 1875-1885, doi:10.1182/blood-2012-09-457739 (2013).
- 63 Sakariassen, K. S., Orning, L. & Turitto, V. T. The impact of blood shear rate on arterial thrombus formation. *Future Sci OA* **1**, FSO30-FSO30, doi:10.4155/fso.15.28 (2015).
- 64 Aarts, P. A. *et al.* Blood platelets are concentrated near the wall and red blood cells, in the center in flowing blood. *Arteriosclerosis* **8**, 819-824, doi:10.1161/01.atv.8.6.819 (1988).
- 65 Turitto, V. T. Blood viscosity, mass transport, and thrombogenesis. *Prog Hemost Thromb* **6**, 139-177 (1982).
- 66 Wang, G. R., Zhu, Y., Halushka, P. V., Lincoln, T. M. & Mendelsohn, M. E. Mechanism of platelet inhibition by nitric oxide: in vivo phosphorylation of thromboxane receptor by cyclic GMP-dependent protein kinase. *Proceedings of the National Academy of Sciences of the United States of America* **95**, 4888-4893, doi:10.1073/pnas.95.9.4888 (1998).

- 67 José, R., María Luisa, L., Leyre, N.-N. & Vicente, V. Platelet receptors and signaling in the dynamics of thrombus formation. *Haematologica* **94**, 700-711, doi:10.3324/haematol.2008.003178 (2009).
- 68 Ruggeri, Z. M. & Mendolicchio, G. L. Adhesion Mechanisms in Platelet Function. *Circulation Research* **100**, 1673-1685, doi:10.1161/01.RES.0000267878.97021.ab (2007).
- 69 Peyvandi, F., Garagiola, I. & Baronciani, L. Role of von Willebrand factor in the haemostasis. *Blood Transfus* **9 Suppl 2**, s3-8, doi:10.2450/2011.002s (2011).
- 70 Nieswandt, B. & Watson, S. P. Platelet-collagen interaction: is GPVI the central receptor? *Blood* **102**, 449-461, doi:10.1182/blood-2002-12-3882 (2003).
- 71 Pugh, N. *et al.* Differential integrin activity mediated by platelet collagen receptor engagement under flow conditions. *Thromb Haemost* **117**, 1588-1600, doi:10.1160/th16-12-0906 (2017).
- 72 Rayes, J., Watson, S. P. & Nieswandt, B. Functional significance of the platelet immune receptors GPVI and CLEC-2. *The Journal of Clinical Investigation* **129**, 12-23, doi:10.1172/JCI122955 (2019).
- 73 Stegner, D., Haining, E. J. & Nieswandt, B. Targeting Glycoprotein VI and the Immunoreceptor Tyrosine-Based Activation Motif Signaling Pathway. *Arteriosclerosis, Thrombosis, and Vascular Biology* **34**, 1615-1620, doi:10.1161/ATVBAHA.114.303408 (2014).
- 74 Menter, D. G. *et al.* Platelets and cancer: a casual or causal relationship: revisited. *Cancer and Metastasis Reviews* **33**, 231-269, doi:10.1007/s10555-014-9498-0 (2014).
- 75 Liu, Y. *et al.* Phospholipase C $\gamma$ 2 Signaling Cascade Contribute to the Antiplatelet Effect of Notoginsenoside Fc. *Frontiers in Pharmacology* **09**, 1293, doi:10.3389/fphar.2018.01293 (2018).
- 76 Pietraforte, D. *et al.* Redox Control of Platelet Functions in Physiology and Pathophysiology. *Antioxidants & redox signaling* **21**, doi:10.1089/ars.2013.5532 (2014).
- 77 Ekambaram, P., Lambiv, W., Cazzolli, R., Ashton, A. W. & Honn, K. V. The thromboxane synthase and receptor signaling pathway in cancer: an emerging paradigm in cancer progression and metastasis. *Cancer Metastasis Rev* **30**, 397-408, doi:10.1007/s10555-011-9297-9 (2011).
- 78 Fitzgerald, D. J. & Fitzgerald, G. A. Historical lessons in translational medicine: cyclooxygenase inhibition and P2Y<sub>12</sub> antagonism. *Circulation research* **112**, 174-194, doi:10.1161/CIRCRESAHA.111.300271 (2013).
- 79 Hirata, T., Ushikubi, F., Kakizuka, A., Okuma, M. & Narumiya, S. Two thromboxane A<sub>2</sub> receptor isoforms in human platelets. Opposite coupling to adenylyl cyclase with different sensitivity to Arg60 to Leu mutation. *J Clin Invest* **97**, 949-956, doi:10.1172/jci118518 (1996).
- 80 COUGHLIN, S. R. Protease-activated receptors in hemostasis, thrombosis and vascular biology. *Journal of Thrombosis and Haemostasis* **3**, 1800-1814, doi:<https://doi.org/10.1111/j.1538-7836.2005.01377.x> (2005).
- 81 Fabre, J.-E. & Gurney, M. E. Limitations of current therapies to prevent thrombosis: a need for novel strategies. *Molecular BioSystems* **6**, 305-315, doi:10.1039/B914375K (2010).
- 82 Duerschmied, D., Bode, C. & Diehl, P. Clinical potential of vorapaxar in cardiovascular risk reduction in patients with atherosclerosis. *Therapeutics and Clinical Risk Management* **11**, 1133, doi:10.2147/TCRM.S55469 (2015).
- 83 Di Minno, M. N. D. *et al.* Overcoming limitations of current antiplatelet drugs: A concerted effort for more profitable strategies of intervention. *Annals of medicine* **43**, 531-544, doi:10.3109/07853890.2011.582137 (2011).

- 84 Shankar, H., Garcia, A., Prabhakar, J., Kim, S. & Kunapuli, S. P. P2Y<sub>12</sub> receptor-mediated potentiation of thrombin-induced thromboxane A<sub>2</sub> generation in platelets occurs through regulation of Erk1/2 activation. *Journal of Thrombosis and Haemostasis* **4**, 638-647, doi:<https://doi.org/10.1111/j.1538-7836.2006.01789.x> (2006).
- 85 Lee, D., Fong, K. P., King, M. R., Brass, L. F. & Hammer, D. A. Differential dynamics of platelet contact and spreading. *Biophysical journal* **102**, 472-482, doi:10.1016/j.bpj.2011.10.056 (2012).
- 86 Lecut, C. *et al.* Principal Role of Glycoprotein VI in  $\alpha 2\beta 1$  and  $\alpha_{IIb}\beta_3$  Activation During Collagen-Induced Thrombus Formation. *Arteriosclerosis, Thrombosis, and Vascular Biology* **24**, 1727-1733, doi:10.1161/01.ATV.0000137974.85068.93 (2004).
- 87 Shattil, S. J., Kashiwagi, H. & Pampori, N. Integrin Signaling: The Platelet Paradigm. *Blood* **91**, 2645-2657, doi:10.1182/blood.V91.8.2645.2645\_2645\_2657 (1998).
- 88 Huang, J. *et al.* Platelet integrin  $\alpha_{IIb}\beta_3$ : signal transduction, regulation, and its therapeutic targeting. *Journal of Hematology & Oncology* **12**, 26, doi:10.1186/s13045-019-0709-6 (2019).
- 89 Wonerow, P., Pearce, A. C., Vaux, D. J. & Watson, S. P. A Critical Role for Phospholipase C $\gamma 2$  in  $\alpha_{IIb}\beta_3$ -mediated Platelet Spreading. *Journal of Biological Chemistry* **278**, 37520-37529, doi:10.1074/jbc.M305077200 (2003).
- 90 Born, G. V. Adenosine diphosphate as a mediator of platelet aggregation in vivo: an editorial view. *Circulation* **72**, 741-746, doi:10.1161/01.CIR.72.4.741 (1985).
- 91 Mebius, M. M. *et al.* Interference with the Host Haemostatic System by Schistosomes. *PLOS Pathogens* **9**, e1003781, doi:10.1371/journal.ppat.1003781 (2013).
- 92 Kaczmarek, E. *et al.* Identification and characterization of CD39/vascular ATP diphosphohydrolase. *J Biol Chem* **271**, 33116-33122, doi:10.1074/jbc.271.51.33116 (1996).
- 93 Sévigny, J. *et al.* Differential catalytic properties and vascular topography of murine nucleoside triphosphate diphosphohydrolase 1 (NTPDase1) and NTPDase2 have implications for thromboregulation. *Blood* **99**, 2801-2809, doi:10.1182/blood.v99.8.2801 (2002).
- 94 Fontana, P. *et al.* Adenosine diphosphate-induced platelet aggregation is associated with P2Y<sub>12</sub> gene sequence variations in healthy subjects. *Circulation* **108**, 989-995, doi:10.1161/01.Cir.0000085073.69189.88 (2003).
- 95 Baqi, Y. & Müller, C. E. Antithrombotic P2Y<sub>12</sub> receptor antagonists: recent developments in drug discovery. *Drug Discovery Today* **24**, 325-333, doi:<https://doi.org/10.1016/j.drudis.2018.09.021> (2019).
- 96 Latorraca, N. R., Venkatakrisnan, A. J. & Dror, R. O. GPCR Dynamics: Structures in Motion. *Chemical Reviews* **117**, 139-155, doi:10.1021/acs.chemrev.6b00177 (2017).
- 97 Gąsecka, A. *et al.* Role of P2Y Receptors in Platelet Extracellular Vesicle Release. *Int J Mol Sci* **21**, doi:10.3390/ijms21176065 (2020).
- 98 Cattaneo, M. & Gachet, C. ADP Receptors and Clinical Bleeding Disorders. *Arteriosclerosis, Thrombosis, and Vascular Biology* **19**, 2281-2285, doi:10.1161/01.ATV.19.10.2281 (1999).
- 99 Harper, M. T. & Poole, A. W. Diverse functions of protein kinase C isoforms in platelet activation and thrombus formation. *Journal of Thrombosis and Haemostasis* **8**, 454-462, doi:<https://doi.org/10.1111/j.1538-7836.2009.03722.x> (2010).

- 100 Mizuno, N. & Itoh, H. Functions and regulatory mechanisms of G<sub>q</sub>-signaling  
pathways. *Neurosignals* **17**, 42-54, doi:10.1159/000186689 (2009).
- 101 Barbara, L. *et al.* Severe bleeding and absent ADP-induced platelet aggregation  
associated with inherited combined CalDAG-GEFI and P2Y<sub>12</sub> deficiencies.  
*Haematologica* **105**, e361-e364, doi:10.3324/haematol.2019.232850 (2020).
- 102 Offermanns, S. Activation of Platelet Function Through G Protein-Coupled  
Receptors. *Circulation Research* **99**, 1293-1304,  
doi:10.1161/01.RES.0000251742.71301.16 (2006).
- 103 Bromberger, T., Zhu, L., Klapproth, S., Qin, J. & Moser, M. Rap1 and  
membrane lipids cooperatively recruit talin to trigger integrin activation. *Journal  
of Cell Science* **132**, doi:10.1242/jcs.235531 (2019).
- 104 Chinthalapudi, K., Rangarajan, E. S. & Izzard, T. The interaction of talin with the  
cell membrane is essential for integrin activation and focal adhesion formation.  
*Proceedings of the National Academy of Sciences* **115**, 10339,  
doi:10.1073/pnas.1806275115 (2018).
- 105 Yang, J. *et al.* Structure of an integrin  $\alpha_{IIb}\beta_3$  transmembrane-cytoplasmic  
heterocomplex provides insight into integrin activation. *Proceedings of the  
National Academy of Sciences* **106**, 17729-17734, doi:10.1073/pnas.0909589106  
(2009).
- 106 Lin, F.-Y., Zhu, J., Eng, E. T., Hudson, N. E. & Springer, T. A.  $\beta$ -Subunit  
Binding Is Sufficient for Ligands to Open the Integrin  $\alpha_{IIb}\beta_3$  Headpiece. *Journal  
of Biological Chemistry* **291**, 4537-4546, doi:10.1074/jbc.M115.705624 (2016).
- 107 Jackson, S. P. The growing complexity of platelet aggregation. *Blood* **109**, 5087-  
5095, doi:10.1182/blood-2006-12-027698 (2007).
- 108 Kattula, S., Byrnes, J. R. & Wolberg, A. S. Fibrinogen and Fibrin in Hemostasis  
and Thrombosis. *Arteriosclerosis, Thrombosis, and Vascular Biology* **37**, e13-  
e21, doi:10.1161/ATVBAHA.117.308564 (2017).
- 109 Rui, V., Richard, J. F., Alessandro, C. & Marguerite, N.-A. Fibrin(ogen) in  
human disease: both friend and foe. *Haematologica* **105**, 284-296,  
doi:10.3324/haematol.2019.236901 (2020).
- 110 Kollman, J. M., Pandi, L., Sawaya, M. R., Riley, M. & Doolittle, R. F. Crystal  
Structure of Human Fibrinogen. *Biochemistry* **48**, 3877-3886,  
doi:10.1021/bi802205g (2009).
- 111 Hantgan, R. R., Stahle, M. C. & Lord, S. T. Dynamic Regulation of Fibrinogen:  
Integrin  $\alpha_{IIb}\beta_3$  Binding. *Biochemistry* **49**, 9217-9225, doi:10.1021/bi1009858  
(2010).
- 112 Podolnikova, N. P. *et al.* The interaction of integrin  $\alpha_{IIb}\beta_3$  with fibrin occurs  
through multiple binding sites in the  $\alpha_{IIb}$   $\beta$ -propeller domain. *The Journal of  
biological chemistry* **289**, 2371-2383, doi:10.1074/jbc.M113.518126 (2014).
- 113 Kloczewiak, M., Timmons, S., Lukas, T. J. & Hawiger, J. Platelet receptor  
recognition site on human fibrinogen. Synthesis and structure-function  
relationship of peptides corresponding to the carboxy-terminal segment of the  
gamma chain. *Biochemistry* **23**, 1767-1774, doi:10.1021/bi00303a028 (1984).
- 114 Kloczewiak, M., Timmons, S., Bednarek, M. A., Sakon, M. & Hawiger, J.  
Platelet receptor recognition domain on the gamma chain of human fibrinogen  
and its synthetic peptide analogues. *Biochemistry* **28**, 2915-2919,  
doi:10.1021/bi00433a025 (1989).
- 115 Alexopoulos, D. P2Y<sub>12</sub> Receptor Inhibitors in Acute Coronary Syndromes: From  
the Research Laboratory to the Clinic and Vice Versa. *Cardiology* **127**, 211-219,  
doi:10.1159/000357399 (2014).

- 116 Nergiz-Unal, R. *et al.* Stabilizing Role of Platelet P2Y<sub>12</sub> Receptors in Shear-  
Dependent Thrombus Formation on Ruptured Plaques. *PLOS ONE* **5**, e10130,  
doi:10.1371/journal.pone.0010130 (2010).
- 117 André, P. *et al.* P2Y<sub>12</sub> regulates platelet adhesion/activation, thrombus growth,  
and thrombus stability in injured arteries. *The Journal of Clinical Investigation*  
**112**, 398-406, doi:10.1172/JCI117864 (2003).
- 118 Gachet, C., Léon, C. & Hechler, B. The platelet P2 receptors in arterial  
thrombosis. *Blood Cells Mol Dis* **36**, 223-227, doi:10.1016/j.bcmd.2005.12.024  
(2006).
- 119 Evans, D. J. W. *et al.* Platelet P2Y<sub>12</sub> Receptor Influences the Vessel Wall  
Response to Arterial Injury and Thrombosis. *Circulation* **119**, 116-122,  
doi:10.1161/CIRCULATIONAHA.107.762690 (2009).
- 120 Stefanini, L. *et al.* RASA3 is a critical inhibitor of RAP1-dependent platelet  
activation. *J Clin Invest* **125**, 1419-1432, doi:10.1172/jci77993 (2015).
- 121 Scavone, M., Femia, E. A. & Cattaneo, M. P2Y<sub>12</sub> receptor gene mutations  
associated with bleeding. *Platelets* **28**, 421-423,  
doi:10.1080/09537104.2017.1316484 (2017).
- 122 Ivanov, I. I., Apta, B. H. R., Bonna, A. M. & Harper, M. T. Platelet P-selectin  
triggers rapid surface exposure of tissue factor in monocytes. *Scientific Reports*  
**9**, 13397, doi:10.1038/s41598-019-49635-7 (2019).
- 123 Merten, M. & Thiagarajan, P. P-Selectin Expression on Platelets Determines  
Size and Stability of Platelet Aggregates. *Circulation* **102**, 1931-1936,  
doi:10.1161/01.CIR.102.16.1931 (2000).
- 124 Larsen, E. *et al.* PADGEM protein: a receptor that mediates the interaction of  
activated platelets with neutrophils and monocytes. *Cell* **59**, 305-312,  
doi:10.1016/0092-8674(89)90292-4 (1989).
- 125 Mumford, A. D. *et al.* A review of platelet secretion assays for the diagnosis of  
inherited platelet secretion disorders. *Thromb Haemost* **114**, 14-25 (2015).
- 126 Théorêt, J. F., Yacoub, D., Hachem, A., Gillis, M. A. & Merhi, Y. P-selectin  
ligation induces platelet activation and enhances microaggregate and thrombus  
formation. *Thromb Res* **128**, 243-250, doi:10.1016/j.thromres.2011.04.018  
(2011).
- 127 Frenette, P. S. *et al.* P-Selectin glycoprotein ligand 1 (PSGL-1) is expressed on  
platelets and can mediate platelet-endothelial interactions in vivo. *The Journal of  
experimental medicine* **191**, 1413-1422, doi:10.1084/jem.191.8.1413 (2000).
- 128 Ballerini, P., Dovizio, M., Bruno, A., Tacconelli, S. & Patrignani, P. P2Y<sub>12</sub>  
Receptors in Tumorigenesis and Metastasis. *Frontiers in Pharmacology* **9**,  
doi:10.3389/fphar.2018.00066 (2018).
- 129 Ito, Y. *et al.* Vasodilator-stimulated phosphoprotein (VASP) is not a major  
mediator of platelet aggregation, thrombogenesis, haemostasis, and antiplatelet  
effect of prasugrel in rats. *Sci Rep* **8**, 9955, doi:10.1038/s41598-018-28181-8  
(2018).
- 130 Gachet, C. Identification, characterization, and inhibition of the platelet ADP  
receptors. *Int J Hematol* **74**, 375-381, doi:10.1007/bf02982079 (2001).
- 131 Zhang, F. L. *et al.* ADP Is the Cognate Ligand for the Orphan G Protein-coupled  
Receptor SP1999 \*. *Journal of Biological Chemistry* **276**, 8608-8615,  
doi:10.1074/jbc.M009718200 (2001).
- 132 Foster, C. J. *et al.* Molecular identification and characterization of the platelet  
ADP receptor targeted by thienopyridine antithrombotic drugs. *J Clin Invest*  
**107**, 1591-1598, doi:10.1172/jci12242 (2001).

- 133 Hockley, J. R. F. *et al.* P2Y Receptors Sensitize Mouse and Human Colonic Nociceptors. *The Journal of Neuroscience* **36**, 2364, doi:10.1523/JNEUROSCI.3369-15.2016 (2016).
- 134 Herbert, J. M. & Savi, P. P2Y<sub>12</sub>, a new platelet ADP receptor, target of clopidogrel. *Semin Vasc Med* **3**, 113-122, doi:10.1055/s-2003-40669 (2003).
- 135 Shiraga, M. *et al.* Impaired platelet function in a patient with P2Y<sub>12</sub> deficiency caused by a mutation in the translation initiation codon. *J Thromb Haemost* **3**, 2315-2323, doi:10.1111/j.1538-7836.2005.01554.x (2005).
- 136 Katritch, V., Cherezov, V. & Stevens, R. C. Structure-function of the G protein-coupled receptor superfamily. *Annu Rev Pharmacol Toxicol* **53**, 531-556, doi:10.1146/annurev-pharmtox-032112-135923 (2013).
- 137 Yang, D. *et al.* G protein-coupled receptors: structure- and function-based drug discovery. *Signal Transduction and Targeted Therapy* **6**, 7, doi:10.1038/s41392-020-00435-w (2021).
- 138 Sriram, K. & Insel, P. A. G Protein-Coupled Receptors as Targets for Approved Drugs: How Many Targets and How Many Drugs? *Molecular pharmacology* **93**, 251-258, doi:10.1124/mol.117.1111062 (2018).
- 139 Liu, F., Tantry, U. S. & Gurbel, P. A. P2Y<sub>12</sub> receptor inhibitors for secondary prevention of ischemic stroke. *Expert Opin Pharmacother* **16**, 1149-1165, doi:10.1517/14656566.2015.1035256 (2015).
- 140 Kupka, D. & Sibbing, D. P2Y(12) receptor inhibitors: an evolution in drug design to prevent arterial thrombosis. *Expert Opin Drug Metab Toxicol* **14**, 303-315, doi:10.1080/17425255.2018.1428557 (2018).
- 141 Cattaneo, M. New P2Y<sub>12</sub> Inhibitors. *Circulation* **121**, 171-179, doi:10.1161/CIRCULATIONAHA.109.853069 (2010).
- 142 Koski, R. & Kennedy, B. Comparative Review of Oral P2Y(12) Inhibitors. *P t* **43**, 352-357 (2018).
- 143 Holmes, M. V., Perel, P., Shah, T., Hingorani, A. D. & Casas, J. P. CYP2C19 genotype, clopidogrel metabolism, platelet function, and cardiovascular events: a systematic review and meta-analysis. *Jama* **306**, 2704-2714, doi:10.1001/jama.2011.1880 (2011).
- 144 Michelson, A. D. & Bhatt, D. L. How I use laboratory monitoring of antiplatelet therapy. *Blood* **130**, 713-721, doi:10.1182/blood-2017-03-742338 (2017).
- 145 Nylander, S. & Schulz, R. Effects of P2Y<sub>12</sub> receptor antagonists beyond platelet inhibition--comparison of ticagrelor with thienopyridines. *Br J Pharmacol* **173**, 1163-1178, doi:10.1111/bph.13429 (2016).
- 146 Belchikov, Y. G., Koenig, S. J. & Dipasquale, E. M. Potential role of endogenous adenosine in ticagrelor-induced dyspnea. *Pharmacotherapy* **33**, 882-887, doi:10.1002/phar.1293 (2013).
- 147 Serebruany, V. L., Stebbing, J. & Atar, D. Dyspnoea after antiplatelet agents: the AZD6140 controversy. *Int J Clin Pract* **61**, 529-533, doi:10.1111/j.1742-1241.2007.01294.x (2007).
- 148 Becker, R. C. *et al.* Bleeding complications with the P2Y<sub>12</sub> receptor antagonists clopidogrel and ticagrelor in the PLATElet inhibition and patient Outcomes (PLATO) trial. *Eur Heart J* **32**, 2933-2944, doi:10.1093/eurheartj/ehr422 (2011).
- 149 Fei, Y., Lam, C. K. & Cheung, B. M. Y. Efficacy and safety of newer P2Y<sub>12</sub> inhibitors for acute coronary syndrome: a network meta-analysis. *Scientific Reports* **10**, 16794, doi:10.1038/s41598-020-73871-x (2020).
- 150 Springthorpe, B. *et al.* From ATP to AZD6140: The discovery of an orally active reversible P2Y<sub>12</sub> receptor antagonist for the prevention of thrombosis.

- Bioorganic & Medicinal Chemistry Letters* **17**, 6013-6018, doi:<https://doi.org/10.1016/j.bmcl.2007.07.057> (2007).
- 151 Zetterberg, F. & Svensson, P. State of affairs: Design and structure-activity relationships of reversible P2Y<sub>12</sub> receptor antagonists. *Bioorg Med Chem Lett* **26**, 2739-2754, doi:10.1016/j.bmcl.2016.04.030 (2016).
- 152 Ingall, A. H. *et al.* Antagonists of the platelet P2T receptor: a novel approach to antithrombotic therapy. *J Med Chem* **42**, 213-220, doi:10.1021/jm981072s (1999).
- 153 Husted, S. & Boersma, E. Case Study: Ticagrelor in PLATO and Prasugrel in TRITON-TIMI 38 and TRILOGY-ACS Trials in Patients With Acute Coronary Syndromes. *Am J Ther* **23**, e1876-e1889, doi:10.1097/mjt.0000000000000237 (2016).
- 154 Navarese, E. P. *et al.* Comparative Efficacy and Safety of Oral P2Y<sub>12</sub> Inhibitors in Acute Coronary Syndrome. *Circulation* **142**, 150-160, doi:10.1161/CIRCULATIONAHA.120.046786 (2020).
- 155 Antman, E. M. *et al.* Early and late benefits of prasugrel in patients with acute coronary syndromes undergoing percutaneous coronary intervention: a TRITON-TIMI 38 (TRial to Assess Improvement in Therapeutic Outcomes by Optimizing Platelet Inhibition with Prasugrel-Thrombolysis In Myocardial Infarction) analysis. *J Am Coll Cardiol* **51**, 2028-2033, doi:10.1016/j.jacc.2008.04.002 (2008).
- 156 Yusuf, S. *et al.* Effects of clopidogrel in addition to aspirin in patients with acute coronary syndromes without ST-segment elevation. *N Engl J Med* **345**, 494-502, doi:10.1056/NEJMoa010746 (2001).
- 157 Husted, S. *et al.* Pharmacodynamics, pharmacokinetics, and safety of the oral reversible P2Y<sub>12</sub> antagonist AZD6140 with aspirin in patients with atherosclerosis: a double-blind comparison to clopidogrel with aspirin. *Eur Heart J* **27**, 1038-1047, doi:10.1093/eurheartj/ehi754 (2006).
- 158 Tan, G.-M., Lam, Y.-Y. & Yan, B. P. Novel Platelet ADP P2Y<sub>12</sub> Inhibitors in the Treatment of Acute Coronary Syndrome. *Cardiovascular Therapeutics* **30**, e167-e173, doi:<https://doi.org/10.1111/j.1755-5922.2011.00262.x> (2012).
- 159 A randomised, blinded, trial of clopidogrel versus aspirin in patients at risk of ischaemic events (CAPRIE). *The Lancet* **348**, 1329-1339, doi:10.1016/S0140-6736(96)09457-3 (1996).
- 160 Gibson, C. M. *et al.* Usefulness of clopidogrel in abolishing the increased risk of reinfarction associated with higher platelet counts in patients with ST-elevation myocardial infarction (results from CLARITY-TIMI 28). *Am J Cardiol* **98**, 761-763, doi:10.1016/j.amjcard.2006.03.062 (2006).
- 161 Anderson, J. L. *et al.* ACC/AHA 2007 guidelines for the management of patients with unstable angina/non-ST-elevation myocardial infarction: a report of the American College of Cardiology/American Heart Association Task Force on Practice Guidelines (Writing Committee to Revise the 2002 Guidelines for the Management of Patients With Unstable Angina/Non-ST-Elevation Myocardial Infarction) developed in collaboration with the American College of Emergency Physicians, the Society for Cardiovascular Angiography and Interventions, and the Society of Thoracic Surgeons endorsed by the American Association of Cardiovascular and Pulmonary Rehabilitation and the Society for Academic Emergency Medicine. *Journal of the American College of Cardiology* **50**, e1-e157 (2007).
- 162 Maffrand, J.-P. The story of clopidogrel and its predecessor, ticlopidine: Could these major antiplatelet and antithrombotic drugs be discovered and developed

- today? *Comptes Rendus Chimie* **15**, 737-743,  
doi:<https://doi.org/10.1016/j.crci.2012.05.006> (2012).
- 163 Féliste, R. *et al.* Broad spectrum anti-platelet activity of ticlopidine and PCR  
4099 involves the suppression of the effects of released ADP. *Thrombosis  
Research* **48**, 403-415, doi:[https://doi.org/10.1016/0049-3848\(87\)90398-7](https://doi.org/10.1016/0049-3848(87)90398-7)  
(1987).
- 164 Quinn, M. J. & Fitzgerald, D. J. Ticlopidine and Clopidogrel. *Circulation* **100**,  
1667-1672, doi:10.1161/01.CIR.100.15.1667 (1999).
- 165 Mehta, S. R. *et al.* Effects of pretreatment with clopidogrel and aspirin followed  
by long-term therapy in patients undergoing percutaneous coronary intervention:  
the PCI-CURE study. *The Lancet* **358**, 527-533, doi:10.1016/S0140-  
6736(01)05701-4 (2001).
- 166 Ko, D. T. *et al.* Clinical Outcomes of Plavix and Generic Clopidogrel for  
Patients Hospitalized With an Acute Coronary Syndrome. *Circulation:  
Cardiovascular Quality and Outcomes* **11**, e004194,  
doi:10.1161/CIRCOUTCOMES.117.004194 (2018).
- 167 Doll, J., Zeitler, E. & Becker, R. Generic Clopidogrel: Time to Substitute?  
*JAMA* **310**, 145-146, doi:10.1001/jama.2013.7155 (2013).
- 168 Berghauer Pont, L. *et al.* Developing blockbuster drugs: both nature and  
nurture. *Nat Rev Drug Discov* **20**, 421-422, doi:10.1038/d41573-020-00061-9  
(2021).
- 169 Sugidachi, A., Asai, F., Ogawa, T., Inoue, T. & Koike, H. The in vivo  
pharmacological profile of CS-747, a novel antiplatelet agent with platelet ADP  
receptor antagonist properties. *British Journal of Pharmacology* **129**, 1439-  
1446, doi:<https://doi.org/10.1038/sj.bjp.0703237> (2000).
- 170 Wiviott, S. D. *et al.* Prasugrel versus Clopidogrel in Patients with Acute  
Coronary Syndromes. *New England Journal of Medicine* **357**, 2001-2015,  
doi:10.1056/NEJMoa0706482 (2007).
- 171 Shan, J. & Sun, H. The discovery and development of prasugrel. *Expert Opinion  
on Drug Discovery* **8**, 897-905, doi:10.1517/17460441.2013.793668 (2013).
- 172 Ferri, N., Corsini, A. & Bellosta, S. Pharmacology of the new P2Y<sub>12</sub> receptor  
inhibitors: insights on pharmacokinetic and pharmacodynamic properties. *Drugs*  
**73**, 1681-1709, doi:10.1007/s40265-013-0126-z (2013).
- 173 Reinhart, K. M., White, C. M. & Baker, W. L. Prasugrel: a critical comparison  
with clopidogrel. *Pharmacotherapy* **29**, 1441-1451,  
doi:10.1592/phco.29.12.1441 (2009).
- 174 Norgard, N. B. & Abu-Fadel, M. Comparison of prasugrel and clopidogrel in  
patients with acute coronary syndrome undergoing percutaneous coronary  
intervention. *Vasc Health Risk Manag* **5**, 873-882, doi:10.2147/vhrm.s5699  
(2009).
- 175 Mizrahi, E. *et al.* Impact of Switching From Prasugrel to Clopidogrel Shortly  
After a Percutaneous Coronary Intervention Without a Loading Dose of  
Clopidogrel. *J Invasive Cardiol* **27**, 543-546 (2015).
- 176 Wallentin, L. *et al.* Ticagrelor versus Clopidogrel in Patients with Acute  
Coronary Syndromes. *New England Journal of Medicine* **361**, 1045-1057,  
doi:10.1056/NEJMoa0904327 (2009).
- 177 Krishnamurthy, A. *et al.* Real-world comparison of clopidogrel, prasugrel and  
ticagrelor in patients undergoing primary percutaneous coronary intervention.  
*Open Heart* **6**, e000951, doi:10.1136/openhrt-2018-000951 (2019).
- 178 Ohno, Y. *et al.* Repetitive stent thrombosis in a patient who had resistance to  
both clopidogrel and prasugrel. *Journal of Cardiology Cases* **13**, 139-142,  
doi:<https://doi.org/10.1016/j.jccase.2016.01.001> (2016).

- 179 Qureshi, Z. & Hobson, A. R. Clopidogrel "resistance": where are we now? *Cardiovasc Ther* **31**, 3-11, doi:10.1111/j.1755-5922.2011.00296.x (2013).
- 180 Nguyen, T. A., Diodati, J. G. & Pharand, C. Resistance to clopidogrel: A review of the evidence. *Journal of the American College of Cardiology* **45**, 1157-1164, doi:<https://doi.org/10.1016/j.jacc.2005.01.034> (2005).
- 181 Michelson, A. D. P2Y<sub>12</sub> antagonism: promises and challenges. *Arterioscler Thromb Vasc Biol* **28**, s33-38, doi:10.1161/atvbaha.107.160689 (2008).
- 182 Baqi, Y., Atzler, K., Köse, M., Glänzel, M. & Müller, C. E. High-Affinity, Non-Nucleotide-Derived Competitive Antagonists of Platelet P2Y<sub>12</sub> Receptors. *Journal of Medicinal Chemistry* **52**, 3784-3793, doi:10.1021/jm9003297 (2009).
- 183 Ancrenaz, V. *et al.* Impact of genetic polymorphisms and drug-drug interactions on clopidogrel and prasugrel response variability. *Curr Drug Metab* **11**, 667-677, doi:10.2174/138920010794233521 (2010).
- 184 Macfarlane, D. E. & Mills, D. The effects of ATP on platelets: evidence against the central role of released ADP in primary aggregation. (1975).
- 185 Daniel, J. L. *et al.* Molecular Basis for ADP-induced Platelet Activation: I. Evidence for three distinct ADP receptors on human platelets \*. *Journal of Biological Chemistry* **273**, 2024-2029, doi:10.1074/jbc.273.4.2024 (1998).
- 186 Kauffenstein, G., Hechler, B., Cazenave, J.-P. & Gachet, C. Adenine triphosphate nucleotides are antagonists at the P2Y<sub>12</sub> receptor. *Journal of Thrombosis and Haemostasis* **2**, 1980-1988, doi:<https://doi.org/10.1111/j.1538-7836.2004.00926.x> (2004).
- 187 Léon, C. *et al.* Defective platelet aggregation and increased resistance to thrombosis in purinergic P2Y<sub>1</sub> receptor-null mice. *J Clin Invest* **104**, 1731-1737, doi:10.1172/jci8399 (1999).
- 188 Dobesh, P. P. & Oestreich, J. H. Ticagrelor: pharmacokinetics, pharmacodynamics, clinical efficacy, and safety. *Pharmacotherapy* **34**, 1077-1090, doi:10.1002/phar.1477 (2014).
- 189 Teng, R., Oliver, S., Hayes, M. A. & Butler, K. Absorption, Distribution, Metabolism, and Excretion of Ticagrelor in Healthy Subjects. *Drug Metabolism and Disposition* **38**, 1514, doi:10.1124/dmd.110.032250 (2010).
- 190 Cannon, C. P. *et al.* Safety, Tolerability, and Initial Efficacy of AZD6140, the First Reversible Oral Adenosine Diphosphate Receptor Antagonist, Compared With Clopidogrel, in Patients With Non-ST-Segment Elevation Acute Coronary Syndrome: Primary Results of the DISPERSE-2 Trial. *Journal of the American College of Cardiology* **50**, 1844-1851, doi:10.1016/j.jacc.2007.07.053 (2007).
- 191 Storey, R. F. *et al.* Inhibition of platelet aggregation by AZD6140, a reversible oral P2Y<sub>12</sub> receptor antagonist, compared with clopidogrel in patients with acute coronary syndromes. *J Am Coll Cardiol* **50**, 1852-1856, doi:10.1016/j.jacc.2007.07.058 (2007).
- 192 Husted, S. & van Giezen, J. J. Ticagrelor: the first reversibly binding oral P2Y<sub>12</sub> receptor antagonist. *Cardiovasc Ther* **27**, 259-274, doi:10.1111/j.1755-5922.2009.00096.x (2009).
- 193 Serebruany, V. L. & Atar, D. The PLATO trial: do you believe in magic? *European Heart Journal* **31**, 764-767, doi:10.1093/eurheartj/ehp545 (2010).
- 194 Baber, U. *et al.* Ticagrelor With or Without Aspirin After PCI: The TWILIGHT Platelet Substudy. *J Am Coll Cardiol* **75**, 578-586, doi:10.1016/j.jacc.2019.11.056 (2020).
- 195 Hoffmann, K. *et al.* Competitive mode and site of interaction of ticagrelor at the human platelet P2Y<sub>12</sub>-receptor. *Journal of Thrombosis and Haemostasis* **12**, 1898-1905, doi:<https://doi.org/10.1111/jth.12719> (2014).

- 196 Navarese, E. P. *et al.* A critical overview on ticagrelor in acute coronary  
syndromes. *Qjm* **106**, 105-115, doi:10.1093/qjmed/hcs187 (2013).
- 197 Valgimigli, M. *et al.* Selatogrel and Other P2Y<sub>12</sub> Inhibitors' Putative Off-Target  
Effects. *Journal of Cardiovascular Pharmacology* **79** (2022).
- 198 Storey, R. F. *et al.* Pharmacodynamics, pharmacokinetics, and safety of single-  
dose subcutaneous administration of selatogrel, a novel P2Y<sub>12</sub> receptor  
antagonist, in patients with chronic coronary syndromes. *European Heart  
Journal* **41**, 3132-3140, doi:10.1093/eurheartj/ehz807 (2019).
- 199 Hulot, J.-S. & Montalescot, G. Do we need a new P2Y<sub>12</sub> receptor antagonist?  
*European Heart Journal* **41**, 3141-3143, doi:10.1093/eurheartj/ehz862 (2019).
- 200 Parker, W. A. E. & Storey, R. F. Pharmacology and potential role of selatogrel,  
a subcutaneous platelet P2Y<sub>12</sub> receptor antagonist. *Expert Opin Emerg Drugs* **25**,  
1-6, doi:10.1080/14728214.2020.1729121 (2020).
- 201 JJ, V. A. N. G. *et al.* Ticagrelor binds to human P2Y<sub>12</sub> independently from ADP  
but antagonizes ADP-induced receptor signaling and platelet aggregation. *J  
Thromb Haemost* **7**, 1556-1565, doi:10.1111/j.1538-7836.2009.03527.x (2009).
- 202 Xiang, B. *et al.* The P2Y<sub>12</sub> Antagonists, 2MeSAMP and Cangrelor, Inhibit  
Platelet Activation through P2Y<sub>12</sub>/G<sub>i</sub>-Dependent Mechanism. *PLOS ONE* **7**,  
e51037, doi:10.1371/journal.pone.0051037 (2012).
- 203 Mansour, A., Bachelot-Loza, C., Nessler, N., Gaussem, P. & Gouin-Thibault, I.  
P2Y<sub>12</sub> Inhibition beyond Thrombosis: Effects on Inflammation. *Int J Mol Sci* **21**,  
doi:10.3390/ijms21041391 (2020).
- 204 Bhatt, D. L. *et al.* Effect of Platelet Inhibition with Cangrelor during PCI on  
Ischemic Events. *New England Journal of Medicine* **368**, 1303-1313,  
doi:10.1056/NEJMoa1300815 (2013).
- 205 Bach, P. *et al.* A novel series of piperazinyl-pyridine ureas as antagonists of the  
purinergic P2Y<sub>12</sub> receptor. *Bioorg Med Chem Lett* **21**, 2877-2881,  
doi:10.1016/j.bmcl.2011.03.088 (2011).
- 206 Bach, P. *et al.* Lead Optimization of Ethyl 6-Aminonicotinate Acyl  
Sulfonamides as Antagonists of the P2Y<sub>12</sub> Receptor. Separation of the  
Antithrombotic Effect and Bleeding for Candidate Drug AZD1283. *Journal of  
Medicinal Chemistry* **56**, 7015-7024, doi:10.1021/jm400820m (2013).
- 207 Kong, D. *et al.* Optimization of P2Y<sub>12</sub> Antagonist Ethyl 6-(4-  
((Benzylsulfonyl)carbamoyl)piperidin-1-yl)-5-cyano-2-methylnicotinate  
(AZD1283) Led to the Discovery of an Oral Antiplatelet Agent with Improved  
Druglike Properties. *Journal of Medicinal Chemistry* **62**, 3088-3106,  
doi:10.1021/acs.jmedchem.8b01971 (2019).
- 208 Hoffmann, K. *et al.* Interaction of New, Very Potent Non-Nucleotide  
Antagonists with Arg256 of the Human Platelet P2Y<sub>12</sub> Receptor. *Journal of  
Pharmacology and Experimental Therapeutics* **331**, 648,  
doi:10.1124/jpet.109.156687 (2009).
- 209 Zech, G. *et al.* Identification of High-Affinity P2Y<sub>12</sub> Antagonists Based on a  
Phenylpyrazole Glutamic Acid Piperazine Backbone. *Journal of Medicinal  
Chemistry* **55**, 8615-8629, doi:10.1021/jm300771j (2012).
- 210 Bryant, J. *et al.* Novel P2Y<sub>12</sub> adenosine diphosphate receptor antagonists for  
inhibition of platelet aggregation (I): In vitro effects on platelets. *Thrombosis  
Research* **122**, 523-532, doi:<https://doi.org/10.1016/j.thromres.2008.03.026>  
(2008).
- 211 Post, J. M. *et al.* Novel P2Y<sub>12</sub> adenosine diphosphate receptor antagonists for  
inhibition of platelet aggregation (II): Pharmacodynamic and pharmacokinetic  
characterization. *Thrombosis Research* **122**, 533-540,  
doi:<https://doi.org/10.1016/j.thromres.2008.04.009> (2008).

- 212 Isberg, V. *et al.* Generic GPCR residue numbers – aligning topology maps while  
minding the gaps. *Trends in Pharmacological Sciences* **36**, 22-31,  
doi:<https://doi.org/10.1016/j.tips.2014.11.001> (2015).
- 213 Ballesteros, J. A. & Weinstein, H. in *Methods in Neurosciences* Vol. 25 (ed  
Stuart C. Sealfon) 366-428 (Academic Press, 1995).
- 214 Rader, A. J. *et al.* Identification of core amino acids stabilizing rhodopsin.  
*Proceedings of the National Academy of Sciences of the United States of  
America* **101**, 7246, doi:10.1073/pnas.0401429101 (2004).
- 215 Hanson, M. A. *et al.* Crystal structure of a lipid G protein–coupled receptor.  
*Science* **335**, 851-855 (2012).
- 216 Wheatley, M. *et al.* Lifting the lid on GPCRs: the role of extracellular loops.  
*British journal of pharmacology* **165**, 1688-1703, doi:10.1111/j.1476-  
5381.2011.01629.x (2012).
- 217 Salmaso, V. & Jacobson, K. A. Purinergic Signaling: Impact of GPCR  
Structures on Rational Drug Design. *ChemMedChem* **15**, 1958-1973,  
doi:10.1002/cmdc.202000465 (2020).
- 218 Venkatakrisnan, A. J. *et al.* Molecular signatures of G-protein-coupled  
receptors. *Nature* **494**, 185-194, doi:10.1038/nature11896 (2013).
- 219 Hilger, D., Masureel, M. & Kobilka, B. K. Structure and dynamics of GPCR  
signaling complexes. *Nature Structural & Molecular Biology* **25**, 4-12,  
doi:10.1038/s41594-017-0011-7 (2018).
- 220 Hauser, A. S. *et al.* GPCR activation mechanisms across classes and  
macro/microscales. *Nature Structural & Molecular Biology* **28**, 879-888,  
doi:10.1038/s41594-021-00674-7 (2021).
- 221 Zhou, Q. *et al.* Common activation mechanism of class A GPCRs. *Elife* **8**,  
e50279, doi:10.7554/eLife.50279 (2019).
- 222 Katritch, V., Cherezov, V. & Stevens, R. C. Diversity and modularity of G  
protein-coupled receptor structures. *Trends Pharmacol Sci* **33**, 17-27,  
doi:10.1016/j.tips.2011.09.003 (2012).
- 223 Rovati, G. E., Capra, V. & Neubig, R. R. The Highly Conserved DRY Motif of  
Class A G Protein-Coupled Receptors: Beyond the Ground State. *Molecular  
Pharmacology* **71**, 959, doi:10.1124/mol.106.029470 (2007).
- 224 Chee, M. J. S. *et al.* The third intracellular loop stabilizes the inactive state of  
the neuropeptide Y1 receptor. *The Journal of biological chemistry* **283**, 33337-  
33346, doi:10.1074/jbc.M804671200 (2008).
- 225 Schulz, A. & Schöneberg, T. The structural evolution of a P2Y-like G-protein-  
coupled receptor. *J Biol Chem* **278**, 35531-35541, doi:10.1074/jbc.M303346200  
(2003).
- 226 Lecchi, A. *et al.* Inherited dysfunctional platelet P2Y<sub>12</sub> receptor mutations  
associated with bleeding disorders. *Hamostaseologie* **36**, 279-283,  
doi:10.5482/HAMO-16-03-0010 (2016).
- 227 Jones, M. L. *et al.* Diversity and impact of rare variants in genes encoding the  
platelet G protein-coupled receptors. *Thrombosis and haemostasis* **113**, 826-837  
(2015).
- 228 Rovati, G. & Capra, V. The DRY motif at work: the P2Y<sub>12</sub> receptor case.  
*Journal of Thrombosis and Haemostasis* **12**, 713-715 (2014).
- 229 Hoffmann, K., Sixel, U., Di Pasquale, F. & von Kügelgen, I. Involvement of  
basic amino acid residues in transmembrane regions 6 and 7 in agonist and  
antagonist recognition of the human platelet P2Y<sub>12</sub>-receptor. *Biochemical  
Pharmacology* **76**, 1201-1213, doi:<https://doi.org/10.1016/j.bcp.2008.08.029>  
(2008).

- 230 Ignatovica, V., Megnis, K., Lapins, M., Schiöth, H. B. & Klovins, J. Identification and analysis of functionally important amino acids in human purinergic P2Y<sub>12</sub> receptor using a *Saccharomyces cerevisiae* expression system. *FEBS J* **279**, 180-191, doi:10.1111/j.1742-4658.2011.08410.x (2012).
- 231 Storey, R. F. The P2Y<sub>12</sub> receptor as a therapeutic target in cardiovascular disease. *Platelets* **12**, 197-209, doi:10.1080/09537100120058739 (2001).
- 232 Schwartz, T. W., Frimurer, T. M., Holst, B., Rosenkilde, M. M. & Elling, C. E. Molecular mechanism of 7TM receptor activation--a global toggle switch model. *Annu Rev Pharmacol Toxicol* **46**, 481-519, doi:10.1146/annurev.pharmtox.46.120604.141218 (2006).
- 233 Avlani, V. A. *et al.* Critical role for the second extracellular loop in the binding of both orthosteric and allosteric G protein-coupled receptor ligands. *J Biol Chem* **282**, 25677-25686, doi:10.1074/jbc.M702311200 (2007).
- 234 Stierand, K., Maass, P. C. & Rarey, M. Molecular complexes at a glance: automated generation of two-dimensional complex diagrams. *Bioinformatics* **22**, 1710-1716, doi:10.1093/bioinformatics/btl150 (2006).
- 235 Fricker, P. C., Gastreich, M. & Rarey, M. Automated drawing of structural molecular formulas under constraints. *J Chem Inf Comput Sci* **44**, 1065-1078, doi:10.1021/ci049958u (2004).
- 236 Rarey, M., Kramer, B., Lengauer, T. & Klebe, G. A fast flexible docking method using an incremental construction algorithm. *J Mol Biol* **261**, 470-489, doi:10.1006/jmbi.1996.0477 (1996).
- 237 Mao, Y., Zhang, L., Jin, J., Ashby, B. & Kunapuli, S. P. Mutational analysis of residues important for ligand interaction with the human P2Y<sub>12</sub> receptor. *European journal of pharmacology* **644**, 10-16, doi:10.1016/j.ejphar.2010.06.023 (2010).
- 238 Judge, H. M., Buckland, R. J., Jakubowski, J. A. & Storey, R. F. Cangrelor inhibits the binding of the active metabolites of clopidogrel and prasugrel to P2Y<sub>12</sub> receptors in vitro. *Platelets* **27**, 191-195, doi:10.3109/09537104.2015.1069809 (2016).
- 239 Hardy, A. R. *et al.* P2Y<sub>1</sub> and P2Y<sub>12</sub> receptors for ADP desensitize by distinct kinase-dependent mechanisms. *Blood* **105**, 3552-3560, doi:10.1182/blood-2004-07-2893 (2005).
- 240 Cunningham, M. R., Nisar, S. P. & Mundell, S. J. Molecular mechanisms of platelet P2Y<sub>12</sub> receptor regulation. *Biochem Soc Trans* **41**, 225-230, doi:10.1042/bst20120295 (2013).
- 241 Mundell, S. J., Barton, J. F., Mayo-Martin, M. B., Hardy, A. R. & Poole, A. W. Rapid resensitization of purinergic receptor function in human platelets. *Journal of Thrombosis and Haemostasis* **6**, 1393-1404, doi:<https://doi.org/10.1111/j.1538-7836.2008.03039.x> (2008).
- 242 Kelly, E., Bailey, C. P. & Henderson, G. Agonist-selective mechanisms of GPCR desensitization. *British journal of pharmacology* **153 Suppl 1**, S379-S388, doi:10.1038/sj.bjp.0707604 (2008).
- 243 Algaier, I., Jakubowski, J. A., Asai, F. & Von Kügelgen, I. Interaction of the active metabolite of prasugrel, R-138727, with cysteine 97 and cysteine 175 of the human P2Y<sub>12</sub> receptor. *Journal of Thrombosis and Haemostasis* **6**, 1908-1914, doi:<https://doi.org/10.1111/j.1538-7836.2008.03136.x> (2008).
- 244 Ding, Z., Bynagari, Y. S., Mada, S. R., Jakubowski, J. A. & Kunapuli, S. P. Studies on the role of the extracellular cysteines and oligomeric structures of the P2Y<sub>12</sub> receptor when interacting with antagonists. *Journal of Thrombosis and Haemostasis* **7**, 232-234, doi:<https://doi.org/10.1111/j.1538-7836.2008.03202.x> (2009).

- 245 Ding, Z., Kim, S., Dorsam, R. T., Jin, J. & Kunapuli, S. P. Inactivation of the human P2Y<sub>12</sub> receptor by thiol reagents requires interaction with both extracellular cysteine residues, Cys17 and Cys270. *Blood* **101**, 3908-3914, doi:10.1182/blood-2002-10-3027 (2003).
- 246 Oury, C., Toth-Zsamboki, E., Vermylen, J. & Hoylaerts, M. F. The platelet ATP and ADP receptors. *Curr Pharm Des* **12**, 859-875, doi:10.2174/138161206776056029 (2006).
- 247 Ohlmann, P. *et al.* The platelet P2Y<sub>12</sub> receptor under normal and pathological conditions. Assessment with the radiolabeled selective antagonist [(3)H]PSB-0413. *Purinergic Signal* **9**, 59-66, doi:10.1007/s11302-012-9329-0 (2013).
- 248 Leelananda, S. P. & Lindert, S. Computational methods in drug discovery. *Beilstein Journal of Organic Chemistry* **12**, 2694-2718, doi:10.3762/bjoc.12.267 (2016).
- 249 Ghislat, G., Rahman, T. & Ballester, P. J. Recent progress on the prospective application of machine learning to structure-based virtual screening. *Current Opinion in Chemical Biology* **65**, 28-34, doi:<https://doi.org/10.1016/j.cbpa.2021.04.009> (2021).
- 250 Panagiotopoulos, A. A. *et al.* A simple open source bioinformatic methodology for initial exploration of GPCR ligands' agonistic/antagonistic properties. *Pharmacology Research & Perspectives* **8**, e00600, doi:<https://doi.org/10.1002/prp2.600> (2020).
- 251 Shoichet, B. K. Virtual screening of chemical libraries. *Nature* **432**, 862-865, doi:10.1038/nature03197 (2004).
- 252 Lu, S., He, X., Ni, D. & Zhang, J. Allosteric Modulator Discovery: From Serendipity to Structure-Based Design. *Journal of Medicinal Chemistry* **62**, 6405-6421, doi:10.1021/acs.jmedchem.8b01749 (2019).
- 253 Millington-Burgess, S. L., Bonna, A. M., Rahman, T. & Harper, M. T. Ethaninidithioic acid (R5421) is not a selective inhibitor of platelet phospholipid scramblase activity. *Br J Pharmacol* **177**, 4007-4020, doi:10.1111/bph.15152 (2020).
- 254 Carlsson, J. *et al.* Ligand discovery from a dopamine D3 receptor homology model and crystal structure. *Nat Chem Biol* **7**, 769-778, doi:10.1038/nchembio.662 (2011).
- 255 Gahlawat, A. *et al.* Structure-Based Virtual Screening to Discover Potential Lead Molecules for the SARS-CoV-2 Main Protease. *Journal of Chemical Information and Modeling* **60**, 5781-5793, doi:10.1021/acs.jcim.0c00546 (2020).
- 256 Callejo, G. *et al.* In silico screening of GMQ-like compounds reveals guanabenz and sephin1 as new allosteric modulators of acid-sensing ion channel 3. *Biochemical Pharmacology* **174**, 113834, doi:<https://doi.org/10.1016/j.bcp.2020.113834> (2020).
- 257 Hsu, K.-C. *et al.* Novel Class IIa-Selective Histone Deacetylase Inhibitors Discovered Using an in Silico Virtual Screening Approach. *Scientific Reports* **7**, 3228, doi:10.1038/s41598-017-03417-1 (2017).
- 258 Matsoukas, M. T. *et al.* Identification of small-molecule inhibitors of calcineurin-NFATc signaling that mimic the PxIxIT motif of calcineurin binding partners. *Sci Signal* **8**, ra63, doi:10.1126/scisignal.2005918 (2015).
- 259 Naylor, E. *et al.* Identification of a chemical probe for NAADP by virtual screening. *Nat Chem Biol* **5**, 220-226, doi:10.1038/nchembio.150 (2009).
- 260 Journigan, V. B. *et al.* Structure-Based Design of Novel Biphenyl Amide Antagonists of Human Transient Receptor Potential Cation Channel Subfamily M Member 8 Channels with Potential Implications in the Treatment of Sensory

- Neuropathies. *ACS Chemical Neuroscience* **11**, 268-290, doi:10.1021/acscchemneuro.9b00404 (2020).
- 261 Rahman, S. & Rahman, T. Unveiling some FDA-approved drugs as inhibitors of the store-operated Ca<sup>2+</sup> entry pathway. *Scientific Reports* **7**, 12881, doi:10.1038/s41598-017-13343-x (2017).
- 262 Theerawatanasirikul, S., Kuo, C. J., Phetcharat, N. & Lekcharoensuk, P. In silico and in vitro analysis of small molecules and natural compounds targeting the 3CL protease of feline infectious peritonitis virus. *Antiviral research* **174**, 104697-104697, doi:10.1016/j.antiviral.2019.104697 (2020).
- 263 Cuccioloni, M. *et al.* Structure/activity virtual screening and in vitro testing of small molecule inhibitors of 8-hydroxy-5-deazaflavin: NADPH oxidoreductase from gut methanogenic bacteria. *Scientific reports* **10**, 1-11 (2020).
- 264 Boittier, E. D. *et al.* Assessing Molecular Docking Tools to Guide Targeted Drug Discovery of CD38 Inhibitors. *International journal of molecular sciences* **21**, 5183, doi:10.3390/ijms21155183 (2020).
- 265 Scior, T. *et al.* Recognizing pitfalls in virtual screening: a critical review. *J Chem Inf Model* **52**, 867-881, doi:10.1021/ci200528d (2012).
- 266 Baldi, P. & Nasr, R. When is chemical similarity significant? The statistical distribution of chemical similarity scores and its extreme values. *Journal of chemical information and modeling* **50**, 1205-1222, doi:10.1021/ci100010v (2010).
- 267 Koutsoukas, A. *et al.* From in silico target prediction to multi-target drug design: current databases, methods and applications. *J Proteomics* **74**, 2554-2574, doi:10.1016/j.jprot.2011.05.011 (2011).
- 268 Hermann, J. C. *et al.* Structure-based activity prediction for an enzyme of unknown function. *Nature* **448**, 775-779, doi:10.1038/nature05981 (2007).
- 269 Musa, M. A., Cooperwood, J. S., Khan, M. O. & Rahman, T. In-vitro antiproliferative activity of benzopyranone derivatives in comparison with standard chemotherapeutic drugs. *Arch Pharm (Weinheim)* **344**, 102-110, doi:10.1002/ardp.201000207 (2011).
- 270 Forli, S. *et al.* Computational protein–ligand docking and virtual drug screening with the AutoDock suite. *Nature Protocols* **11**, 905-919, doi:10.1038/nprot.2016.051 (2016).
- 271 Greenhalgh, J. C., Chandran, A., Harper, M. T., Ladds, G. & Rahman, T. Proposed model of the Dictyostelium cAMP receptors bound to cAMP. *Journal of Molecular Graphics and Modelling* **100**, 107662, doi:<https://doi.org/10.1016/j.jmgm.2020.107662> (2020).
- 272 Hajbabaie, R., Harper, M. T. & Rahman, T. Establishing an Analogue Based In Silico Pipeline in the Pursuit of Novel Inhibitory Scaffolds against the SARS Coronavirus 2 Papain-Like Protease. *Molecules* **26**, doi:10.3390/molecules26041134 (2021).
- 273 Augustin, T. L., Hajbabaie, R., Harper, M. T. & Rahman, T. Novel Small-Molecule Scaffolds as Candidates against the SARS Coronavirus 2 Main Protease: A Fragment-Guided in Silico Approach. *Molecules* **25**, doi:10.3390/molecules25235501 (2020).
- 274 Sousa, S. F. *et al.* Protein-ligand docking in the new millennium--a retrospective of 10 years in the field. *Curr Med Chem* **20**, 2296-2314, doi:10.2174/0929867311320180002 (2013).
- 275 McNutt, A. T. *et al.* GNINA 1.0: molecular docking with deep learning. *Journal of Cheminformatics* **13**, 43, doi:10.1186/s13321-021-00522-2 (2021).
- 276 Ballante, F., Kooistra, A. J., Kampen, S., de Graaf, C. & Carlsson, J. Structure-Based Virtual Screening for Ligands of G Protein-Coupled Receptors: What Can

- Molecular Docking Do for You? *Pharmacol Rev* **73**, 527-565, doi:10.1124/pharmrev.120.000246 (2021).
- 277 Guedes, I. A., Pereira, F. S. S. & Dardenne, L. E. Empirical Scoring Functions for Structure-Based Virtual Screening: Applications, Critical Aspects, and Challenges. *Frontiers in Pharmacology* **9**, doi:10.3389/fphar.2018.01089 (2018).
- 278 Rahman, T. & Rahmatullah, M. Proposed structural basis of interaction of piperine and related compounds with monoamine oxidases. *Bioorg Med Chem Lett* **20**, 537-540, doi:10.1016/j.bmcl.2009.11.106 (2010).
- 279 Chattopadhyay, A. *et al.* Discovery of a small-molecule binder of the oncoprotein gankyrin that modulates gankyrin activity in the cell. *Sci Rep* **6**, 23732, doi:10.1038/srep23732 (2016).
- 280 Fischer, A., Smieško, M., Sellner, M. & Lill, M. A. Decision Making in Structure-Based Drug Discovery: Visual Inspection of Docking Results. *Journal of Medicinal Chemistry* **64**, 2489-2500, doi:10.1021/acs.jmedchem.0c02227 (2021).
- 281 Baker, D. E. & Ingram, K. T. Cangrelor. *Hosp Pharm* **50**, 922-929, doi:10.1310/hpj5010-922 (2015).
- 282 Steinhubl, S. R. *et al.* Transitioning patients from cangrelor to clopidogrel: pharmacodynamic evidence of a competitive effect. *Thromb Res* **121**, 527-534, doi:10.1016/j.thromres.2007.05.020 (2008).
- 283 Schneider, D. J., Agarwal, Z., Seecheran, N. & Gogo, P. Pharmacodynamic effects when clopidogrel is given before cangrelor discontinuation. *Journal of Interventional Cardiology* **28**, 415-419 (2015).
- 284 Leonardi, S. & Bhatt, D. L. Practical considerations for cangrelor use in patients with acute coronary syndromes. *European Heart Journal. Acute Cardiovascular Care* **8**, 39-44, doi:10.1177/2048872617707960 (2019).
- 285 Seto, A. H. in *The Interventional Cardiac Catheterization Handbook (Fourth Edition)* (eds Morton J. Kern, Paul Sorajja, & Michael J. Lim) 88-106 (Elsevier, 2018).
- 286 Franchi, F. *et al.* Platelet Inhibition With Cangrelor and Crushed Ticagrelor in Patients With ST-Segment-Elevation Myocardial Infarction Undergoing Primary Percutaneous Coronary Intervention. *Circulation* **139**, 1661-1670, doi:10.1161/CIRCULATIONAHA.118.038317 (2019).
- 287 Mohammad, M. A. *et al.* Cangrelor in combination with ticagrelor provides consistent and potent P2Y<sub>12</sub>-inhibition during and after primary percutaneous coronary intervention in real-world patients with ST-segment-elevation myocardial infarction. *Platelets* **28**, 414-416, doi:10.1080/09537104.2016.1246714 (2017).
- 288 Chan, M. V., Armstrong, P. C. & Warner, T. D. 96-well plate-based aggregometry. *Platelets* **29**, 650-655, doi:10.1080/09537104.2018.1445838 (2018).
- 289 Vinholt, P. J., Nybo, M., Nielsen, C. B. & Hvas, A.-M. Light transmission aggregometry using pre-coated microtiter plates and a Victor X5 plate reader. *PloS one* **12**, e0185675-e0185675, doi:10.1371/journal.pone.0185675 (2017).
- 290 Chan, M. V., Leadbeater, P. D., Watson, S. P. & Warner, T. D. Not all light transmission aggregation assays are created equal: qualitative differences between light transmission and 96-well plate aggregometry. *Platelets* **29**, 686-689, doi:10.1080/09537104.2018.1466388 (2018).
- 291 Chan, M. V. & Warner, T. D. Standardised optical multichannel (optimul) platelet aggregometry using high-speed shaking and fixed time point readings. *Platelets* **23**, 404-408, doi:10.3109/09537104.2011.603066 (2012).

- 292 Lordkipanidzé, M. *et al.* Characterization of multiple platelet activation pathways in patients with bleeding as a high-throughput screening option: use of 96-well Optimul assay. *Blood* **123**, e11-e22, doi:10.1182/blood-2013-08-520387 (2014).
- 293 Chan, M. V., Armstrong, P. C. J., Papalia, F., Kirkby, N. S. & Warner, T. D. Optical multichannel (optimul) platelet aggregometry in 96-well plates as an additional method of platelet reactivity testing. *Platelets* **22**, 485-494, doi:10.3109/09537104.2011.592958 (2011).
- 294 Spurgeon, B. E. J. & Naseem, K. M. High-Throughput Signaling Profiling in Blood Platelets by Multiplexed Phosphoflow Cytometry. *Methods Mol Biol* **1812**, 95-111, doi:10.1007/978-1-4939-8585-2\_6 (2018).
- 295 Spurgeon, B. E. J. & Naseem, K. M. Phosphoflow cytometry and barcoding in blood platelets: Technical and analytical considerations. *Cytometry Part B: Clinical Cytometry* **98**, 123-130, doi:<https://doi.org/10.1002/cyto.b.21851> (2020).
- 296 Krutzik, P. O. & Nolan, G. P. Fluorescent cell barcoding in flow cytometry allows high-throughput drug screening and signaling profiling. *Nature Methods* **3**, 361-368, doi:10.1038/nmeth872 (2006).
- 297 OMEGA 4.1.2.0 (OpenEye Scientific Software; Sante Fe, NM: 2021).
- 298 MarvinSketch, version 20.16 (ChemAxon Ltd; Budapest, Hungary: 2020.).
- 299 Molecular Operating Environment (MOE), 2019.01. (Chemical Computing Group; Montreal, Canada: 2020).
- 300 The Open Babel Package, version 2.3.1.
- 301 O'Boyle, N. M. *et al.* Open Babel: An open chemical toolbox. *Journal of cheminformatics* **3**, 33 (2011).
- 302 ROCS version 3.4.1.0 (OpenEye Scientific Software; Santa Fe, NM: 2020).
- 303 Forge, version 10.6 (Cresset Group; Litlington, Cambridgeshire, UK: 2020.).
- 304 Abagyan, R., Totrov, M. & Kuznetsov, D. ICM - a new method for protein modeling and design: applications to docking and structure prediction from the distorted native conformation. *Journal of computational chemistry* **15(5)** (1994).
- 305 Friesner, R. A. *et al.* Extra Precision Glide: Docking and Scoring Incorporating a Model of Hydrophobic Enclosure for Protein–Ligand Complexes. *Journal of Medicinal Chemistry* **49**, 6177-6196, doi:10.1021/jm051256o (2006).
- 306 Friesner, R. A. *et al.* Glide: A New Approach for Rapid, Accurate Docking and Scoring. 1. Method and Assessment of Docking Accuracy. *Journal of Medicinal Chemistry* **47**, 1739-1749, doi:10.1021/jm0306430 (2004).
- 307 Halgren, T. A. *et al.* Glide: a new approach for rapid, accurate docking and scoring. 2. Enrichment factors in database screening. *J Med Chem* **47**, 1750-1759, doi:10.1021/jm030644s (2004).
- 308 Glide, Schrödinger, LLC (New York, NY: 2020).
- 309 Halgren, T. A. Merck molecular force field. I. Basis, form, scope, parameterization, and performance of MMFF94. *Journal of Computational Chemistry* **17**, 490-519, doi:[https://doi.org/10.1002/\(SICI\)1096-987X\(199604\)17:5/6<490::AID-JCC1>3.0.CO;2-P](https://doi.org/10.1002/(SICI)1096-987X(199604)17:5/6<490::AID-JCC1>3.0.CO;2-P) (1996).
- 310 Dallakyan, S. & Olson, A. J. Small-molecule library screening by docking with PyRx. *Chemical biology*, 243-250 (2015).
- 311 Pettersen, E. F. *et al.* UCSF Chimera--a visualization system for exploratory research and analysis. *J Comput Chem* **25**, 1605-1612, doi:10.1002/jcc.20084 (2004).
- 312 Jones, G., Willett, P., Glen, R. C., Leach, A. R. & Taylor, R. Development and validation of a genetic algorithm for flexible docking. *J Mol Biol* **267**, 727-748, doi:10.1006/jmbi.1996.0897 (1997).

- 313 Molegro Molecular Viewer (MMV), version 7.0. (Molexus; Rodder, Denmark: 2020).
- 314 Koes, D. R. & Camacho, C. J. ZINCPharmer: pharmacophore search of the ZINC database. *Nucleic Acids Res* **40**, W409-414, doi:10.1093/nar/gks378 (2012).
- 315 Koes, D. R., Pabon, N. A., Deng, X., Phillips, M. A. & Camacho, C. J. A Teach-Discover-Treat Application of ZincPharmer: An Online Interactive Pharmacophore Modeling and Virtual Screening Tool. *PLoS One* **10**, e0134697, doi:10.1371/journal.pone.0134697 (2015).
- 316 FlowJo™ Software (Ashland, Oregon, 2021).
- 317 Microsoft Excel (2018).
- 318 Norgard, N. B. Cangrelor: a novel P2Y<sub>12</sub> receptor antagonist. *Expert Opin Investig Drugs* **18**, 1219-1230, doi:10.1517/13543780903136708 (2009).
- 319 Franchi, F., Rollini, F., Muñoz-Lozano, A., Cho, J. R. & Angiolillo, D. J. Cangrelor: a review on pharmacology and clinical trial development. *Expert Rev Cardiovasc Ther* **11**, 1279-1291, doi:10.1586/14779072.2013.837701 (2013).
- 320 van Giezen, J. J. & Humphries, R. G. Preclinical and clinical studies with selective reversible direct P2Y<sub>12</sub> antagonists. *Semin Thromb Hemost* **31**, 195-204, doi:10.1055/s-2005-869525 (2005).
- 321 Ueno, M., Ferreiro, J. L. & Angiolillo, D. J. Update on the clinical development of cangrelor. *Expert Rev Cardiovasc Ther* **8**, 1069-1077, doi:10.1586/erc.10.90 (2010).
- 322 Atherton, A., Begent, N., Blackwell, G. J. & Bakhle, Y. S. The platelet aggregometer and beyond: Gustav Born at the Royal College of Surgeons. *Platelets* **30**, 3-6, doi:10.1080/09537104.2018.1513252 (2019).
- 323 Jeong, Y.-H. *et al.* Usefulness of the VerifyNow P2Y<sub>12</sub> assay to evaluate the antiplatelet effects of ticagrelor and clopidogrel therapies. *American Heart Journal* **164**, 35-42, doi:<https://doi.org/10.1016/j.ahj.2012.03.022> (2012).
- 324 Jakubowski, J. A. *et al.* A Comparison of the VerifyNow P2Y<sub>12</sub> Point-of-Care Device and Light Transmission Aggregometry to Monitor Platelet Function with Prasugrel and Clopidogrel: An Integrated Analysis. *Journal of Cardiovascular Pharmacology* **56** (2010).
- 325 Choi, S. Y. & Kim, M. H. Comparison of factors affecting platelet reactivity in various platelet function tests. *Platelets* **30**, 631-636, doi:10.1080/09537104.2018.1499887 (2019).
- 326 Born, G. V. Aggregation of blood platelets by adenosine diphosphate and its reversal. *Nature* **194**, 927-929, doi:10.1038/194927b0 (1962).
- 327 Born, G. V. & Cross, M. J. The aggregation of blood platelets. *J Physiol* **168**, 178-195, doi:10.1113/jphysiol.1963.sp007185 (1963).
- 328 Clayton, S., Born, G. V. & Cross, M. J. Inhibition of the aggregation of blood platelets by nucleosides. *Nature* **200**, 138-139, doi:10.1038/200138a0 (1963).
- 329 Takasaki, J. *et al.* Molecular cloning of the platelet P2T<sub>AC</sub> ADP receptor: pharmacological comparison with another ADP receptor, the P2Y<sub>1</sub> receptor. *Mol Pharmacol* **60**, 432-439 (2001).
- 330 Sun, J. *et al.* Discordance Between VASP Phosphorylation and Platelet Aggregation in Defining High On-Clopidogrel Platelet Reactivity After ST-Segment Elevation Myocardial Infarction. *Clinical and Applied Thrombosis/Hemostasis* **24**, 47-54, doi:10.1177/1076029617726600 (2017).
- 331 Glenn, J. R. *et al.* 'VASPFix' for measurement of VASP phosphorylation in platelets and for monitoring effects of P2Y<sub>12</sub> antagonists. *Thromb Haemost* **111**, 539-548, doi:10.1160/th13-07-0581 (2014).

- 332 Price Matthew, J. The Pharmacodynamics of Switching Between P2Y<sub>12</sub> Receptor Antagonists\*. *JACC: Cardiovascular Interventions* **9**, 1099-1101, doi:10.1016/j.jcin.2016.04.016 (2016).
- 333 Garcia, C. *et al.* Deciphering biased inverse agonism of cangrelor and ticagrelor at P2Y<sub>12</sub> receptor. *Cell Mol Life Sci* **76**, 561-576, doi:10.1007/s00018-018-2960-3 (2019).
- 334 Roberts, T. D. *The Pharmacodynamics of the Antiplatelet Drug Ticagrelor: Mode of Action, Onset and Reversibility*, University of Bristol, (2021).
- 335 Bancroft, S. K., Khalil, J. & Mundell, S. in *British Journal of Pharmacology*. 383-383 (Wiley 111 River St, Hoboken 07030-5774, NJ USA).
- 336 Suplat, D., Krzemiński, P., Pomorski, P. & Barańska, J. P2Y<sub>1</sub> and P2Y<sub>12</sub> receptor cross-talk in calcium signalling: Evidence from nonstarved and long-term serum-deprived glioma C6 cells. *Purinergic signalling* **3**, 221-230, doi:10.1007/s11302-007-9051-5 (2007).
- 337 Hardy, A. R., Jones, M. L., Mundell, S. J. & Poole, A. W. Reciprocal cross-talk between P2Y<sub>1</sub> and P2Y<sub>12</sub> receptors at the level of calcium signaling in human platelets. *Blood* **104**, 1745-1752, doi:10.1182/blood-2004-02-0534 (2004).
- 338 Li, Y., Yin, C., Liu, P., Li, D. & Lin, J. Identification of a Different Agonist-Binding Site and Activation Mechanism of the Human P2Y<sub>1</sub> Receptor. *Scientific Reports* **7**, 13764, doi:10.1038/s41598-017-14268-1 (2017).
- 339 Aleil, B. *et al.* Flow cytometric analysis of intraplatelet VASP phosphorylation for the detection of clopidogrel resistance in patients with ischemic cardiovascular diseases. *J Thromb Haemost* **3**, 85-92, doi:10.1111/j.1538-7836.2004.01063.x (2005).
- 340 Aradi, D. *et al.* Comparison of conventional aggregometry with VASP for monitoring P2Y<sub>12</sub>-specific platelet inhibition. *Platelets* **21**, 563-570, doi:10.3109/09537104.2010.494742 (2010).
- 341 Mingant, F. *et al.* Comparison of four methods to assess high-on platelet reactivity under P2Y<sub>12</sub> receptor inhibitor. *Platelets* **29**, 257-264, doi:10.1080/09537104.2018.1453058 (2018).
- 342 Lemesle, G. *et al.* Poor agreement between light transmission aggregometry, Verify Now P2Y<sub>12</sub> and vasodilator-stimulated phosphoprotein for clopidogrel low-response assessment: a potential explanation of negative results of recent randomized trials. *Platelets* **25**, 499-505, doi:10.3109/09537104.2013.840363 (2014).
- 343 Kuliczkowski, W., Rychlik, B., Chiżyński, K., Watała, C. & Golański, J. Comparison of the VASP assay and platelet aggregometry in the evaluation of platelet P2Y<sub>12</sub> receptor blockade. *Pol Arch Med Wewn* **121**, 115-121 (2011).
- 344 Humphries, R. G., Tomlinson, W., Ingall, A. H., Cage, P. A. & Leff, P. FPL 66096: a novel, highly potent and selective antagonist at human platelet P2T-purinoceptors. *Br J Pharmacol* **113**, 1057-1063, doi:10.1111/j.1476-5381.1994.tb17100.x (1994).
- 345 Simon, J. *et al.* Activity of adenosine diphosphates and triphosphates on a P2YT-type receptor in brain capillary endothelial cells. *British Journal of Pharmacology* **132**, 173-182, doi:<https://doi.org/10.1038/sj.bjp.0703816> (2001).
- 346 Horváth, G. *et al.* Central P2Y<sub>12</sub> receptor blockade alleviates inflammatory and neuropathic pain and cytokine production in rodents. *Neurobiol Dis* **70**, 162-178, doi:10.1016/j.nbd.2014.06.011 (2014).
- 347 Bekő, K. *et al.* Contribution of platelet P2Y<sub>12</sub> receptors to chronic Complete Freund's adjuvant-induced inflammatory pain. *Journal of Thrombosis and Haemostasis* **15**, 1223-1235, doi:<https://doi.org/10.1111/jth.13684> (2017).

- 348 B elanger, J. C. *et al.* Head-to-Head Comparison of Consensus-Recommended Platelet Function Tests to Assess P2Y<sub>12</sub> Inhibition-Insights for Multi-Center Trials. *J Clin Med* **9**, doi:10.3390/jcm9020332 (2020).
- 349 Spurgeon, B. E. J., Aburima, A., Oberprieler, N. G., Task en, K. & Naseem, K. M. Multiplexed phosphospecific flow cytometry enables large-scale signaling profiling and drug screening in blood platelets. *Journal of Thrombosis and Haemostasis* **12**, 1733-1743, doi:<https://doi.org/10.1111/jth.12670> (2014).
- 350 Spurgeon, B. E. *Phosphoproteomic analysis of platelet signalling cascades by flow cytometry*, University of Hull and the University of York, (2014).
- 351 Vaiyapuri, S. & Gibbins, J. Miniaturised platelet aggregation assays using Novostar microplate reader. (BMG Labtech Appl Note 215, Rev. 04. 2011. <http://www.bmglabtech.com> ..., 2015).
- 352 Vistoli, G., Brizzolari, A., Faioni, E., Razzari, C. & Santaniello, E. Naturally occurring N6-substituted adenosines (cytokinin ribosides) are in vitro inhibitors of platelet aggregation: An in silico evaluation of their interaction with the P2Y<sub>12</sub> receptor. *Bioorganic & Medicinal Chemistry Letters* **24**, 5652-5655, doi:<https://doi.org/10.1016/j.bmcl.2014.10.080> (2014).
- 353 Falciani, M. *et al.* Effects of nebivolol on human platelet aggregation. *J Cardiovasc Pharmacol* **38**, 922-929, doi:10.1097/00005344-200112000-00014 (2001).
- 354 Salentin, S., Schreiber, S., Haupt, V. J., Adasme, M. F. & Schroeder, M. PLIP: fully automated protein-ligand interaction profiler. *Nucleic Acids Res* **43**, W443-447, doi:10.1093/nar/gkv315 (2015).
- 355 Bhalekar, S. B. & Shelke, S. N. Significant Discovery of Tetrahydrothieno[3,2-c]pyridine-2-carboxamide Analogs as Potent P2Y<sub>12</sub> Receptor Antagonists. *Chem Biodivers* **16**, e1800550, doi:10.1002/cbdv.201800550 (2019).
- 356 Ahn, Y. H. *et al.* Identification of a New Morpholine Scaffold as a P2Y<sub>12</sub> Receptor Antagonist. *Molecules (Basel, Switzerland)* **21**, 1114, doi:10.3390/molecules21091114 (2016).
- 357 Basith, S. *et al.* Exploring G Protein-Coupled Receptors (GPCRs) Ligand Space via Cheminformatics Approaches: Impact on Rational Drug Design. *Frontiers in Pharmacology* **9**, doi:10.3389/fphar.2018.00128 (2018).
- 358 Evers, A. & Klabunde, T. Structure-based Drug Discovery Using GPCR Homology Modeling: Successful Virtual Screening for Antagonists of the Alpha1A Adrenergic Receptor. *Journal of Medicinal Chemistry* **48**, 1088-1097, doi:10.1021/jm0491804 (2005).
- 359 Rodr guez, D., Gao, Z.-G., Moss, S. M., Jacobson, K. A. & Carlsson, J. Molecular Docking Screening Using Agonist-Bound GPCR Structures: Probing the A2A Adenosine Receptor. *Journal of Chemical Information and Modeling* **55**, 550-563, doi:10.1021/ci500639g (2015).
- 360 Hawkins, P. C., Skillman, A. G. & Nicholls, A. Comparison of shape-matching and docking as virtual screening tools. *Journal of medicinal chemistry* **50**, 74-82 (2007).
- 361 Gonz lez-Vera, J. A. *et al.* A new serotonin 5-HT<sub>6</sub> receptor antagonist with procognitive activity-Importance of a halogen bond interaction to stabilize the binding. *Scientific reports* **7**, 1-10 (2017).
- 362 Staro n, J. *et al.* Halogen bonding enhances activity in a series of dual 5-HT<sub>6</sub>/D2 ligands designed in a hybrid bioisostere generation/virtual screening protocol. *RSC advances* **6**, 54918-54925 (2016).
- 363 Koebel, M. R., Schmadeke, G., Posner, R. G. & Sirimulla, S. AutoDock VinaXB: implementation of XBSF, new empirical halogen bond scoring

- function, into AutoDock Vina. *Journal of Cheminformatics* **8**, 27, doi:10.1186/s13321-016-0139-1 (2016).
- 364 Kurczab, R., Kucwaj-Brysz, K. & Śliwa, P. The Significance of Halogen Bonding in Ligand-Receptor Interactions: The Lesson Learned from Molecular Dynamic Simulations of the D(4) Receptor. *Molecules (Basel, Switzerland)* **25**, 91, doi:10.3390/molecules25010091 (2019).
- 365 Duroux, R. *et al.* Design, synthesis and evaluation of 2-aryl benzoxazoles as promising hit for the A(2A) receptor. *J Enzyme Inhib Med Chem* **32**, 850-864, doi:10.1080/14756366.2017.1334648 (2017).
- 366 Zhou, M. *et al.* Discovery and computational studies of 2-phenyl-benzoxazole acetamide derivatives as promising P2Y<sub>14</sub>R antagonists with anti-gout potential. *European Journal of Medicinal Chemistry* **227**, 113933, doi:<https://doi.org/10.1016/j.ejmech.2021.113933> (2022).
- 367 Verkhivker, G. M. *et al.* Deciphering common failures in molecular docking of ligand-protein complexes. *J Comput Aided Mol Des* **14**, 731-751, doi:10.1023/a:1008158231558 (2000).
- 368 Cummings, M. D., DesJarlais, R. L., Gibbs, A. C., Mohan, V. & Jaeger, E. P. Comparison of Automated Docking Programs as Virtual Screening Tools. *Journal of Medicinal Chemistry* **48**, 962-976, doi:10.1021/jm049798d (2005).
- 369 Quiroga, R. & Villarreal, M. A. Vinardo: A Scoring Function Based on Autodock Vina Improves Scoring, Docking, and Virtual Screening. *PloS one* **11**, e0155183-e0155183, doi:10.1371/journal.pone.0155183 (2016).
- 370 Trott, O. & Olson, A. J. AutoDock Vina: improving the speed and accuracy of docking with a new scoring function, efficient optimization, and multithreading. *J Comput Chem* **31**, 455-461, doi:10.1002/jcc.21334 (2010).
- 371 Eberhardt, J., Santos-Martins, D., Tillack, A. F. & Forli, S. AutoDock Vina 1.2.0: New Docking Methods, Expanded Force Field, and Python Bindings. *Journal of Chemical Information and Modeling* **61**, 3891-3898, doi:10.1021/acs.jcim.1c00203 (2021).
- 372 Yuriev, E. & Ramsland, P. A. Latest developments in molecular docking: 2010-2011 in review. *J Mol Recognit* **26**, 215-239, doi:10.1002/jmr.2266 (2013).
- 373 Chen, Y.-C. Beware of docking! *Trends in Pharmacological Sciences* **36**, 78-95, doi:<https://doi.org/10.1016/j.tips.2014.12.001> (2015).
- 374 Singh, D., Berntsen, K. R. M., Baakman, C., Vriend, G. & Lahiri, T. A Critical Note on Symmetry Contact Artifacts and the Evaluation of the Quality of Homology Models. *Symmetry* **10**, doi:10.3390/sym10010025 (2018).
- 375 Elez, K., Bonvin, A. M. J. J. & Vangone, A. Distinguishing crystallographic from biological interfaces in protein complexes: role of intermolecular contacts and energetics for classification. *BMC Bioinformatics* **19**, 438, doi:10.1186/s12859-018-2414-9 (2018).
- 376 Luo, J., Liu, Z., Guo, Y. & Li, M. A structural dissection of large protein-protein crystal packing contacts. *Scientific Reports* **5**, 14214, doi:10.1038/srep14214 (2015).
- 377 Niedzialkowska, E. *et al.* Protein purification and crystallization artifacts: The tale usually not told. *Protein Sci* **25**, 720-733, doi:10.1002/pro.2861 (2016).
- 378 DePristo, M. A., de Bakker, P. I. W. & Blundell, T. L. Heterogeneity and Inaccuracy in Protein Structures Solved by X-Ray Crystallography. *Structure* **12**, 831-838, doi:<https://doi.org/10.1016/j.str.2004.02.031> (2004).
- 379 Pagadala, N. S., Syed, K. & Tuszynski, J. Software for molecular docking: a review. *Biophys Rev* **9**, 91-102, doi:10.1007/s12551-016-0247-1 (2017).

- 380 Shoichet, B. K. & Kuntz, I. D. Protein docking and complementarity. *Journal of Molecular Biology* **221**, 327-346, doi:[https://doi.org/10.1016/0022-2836\(91\)80222-G](https://doi.org/10.1016/0022-2836(91)80222-G) (1991).
- 381 Chen, P. *et al.* DLIGAND2: an improved knowledge-based energy function for protein-ligand interactions using the distance-scaled, finite, ideal-gas reference state. *Journal of cheminformatics* **11**, 52-52, doi:10.1186/s13321-019-0373-4 (2019).
- 382 Jeong, J., Kim, H. & Choi, J. In Silico Molecular Docking and In Vivo Validation with *Caenorhabditis elegans* to Discover Molecular Initiating Events in Adverse Outcome Pathway Framework: Case Study on Endocrine-Disrupting Chemicals with Estrogen and Androgen Receptors. *International journal of molecular sciences* **20**, 1209, doi:10.3390/ijms20051209 (2019).
- 383 Lavecchia, A. & Di Giovanni, C. Virtual screening strategies in drug discovery: a critical review. *Curr Med Chem* **20**, 2839-2860, doi:10.2174/09298673113209990001 (2013).
- 384 Böhm, H. J. The development of a simple empirical scoring function to estimate the binding constant for a protein-ligand complex of known three-dimensional structure. *J Comput Aided Mol Des* **8**, 243-256, doi:10.1007/bf00126743 (1994).
- 385 Weng, Z., Vajda, S. & Delisi, C. Prediction of protein complexes using empirical free energy functions. *Protein Sci* **5**, 614-626, doi:10.1002/pro.5560050406 (1996).
- 386 Schulz-Gasch, T. & Stahl, M. Scoring functions for protein–ligand interactions: a critical perspective. *Drug Discovery Today: Technologies* **1**, 231-239, doi:<https://doi.org/10.1016/j.ddtec.2004.08.004> (2004).
- 387 Kulharia, M., Goody, R. S. & Jackson, R. M. Information theory-based scoring function for the structure-based prediction of protein-ligand binding affinity. *J Chem Inf Model* **48**, 1990-1998, doi:10.1021/ci800125k (2008).
- 388 Huang, S.-Y. & Zou, X. Inclusion of Solvation and Entropy in the Knowledge-Based Scoring Function for Protein–Ligand Interactions. *Journal of Chemical Information and Modeling* **50**, 262-273, doi:10.1021/ci9002987 (2010).
- 389 Wang, Z. *et al.* Comprehensive evaluation of ten docking programs on a diverse set of protein-ligand complexes: the prediction accuracy of sampling power and scoring power. *Phys Chem Chem Phys* **18**, 12964-12975, doi:10.1039/c6cp01555g (2016).
- 390 Vieira, T. F. & Sousa, S. F. Comparing AutoDock and Vina in Ligand/Decoy Discrimination for Virtual Screening. *Applied Sciences* **9**, 4538 (2019).
- 391 Nguyen, N. T. *et al.* Autodock Vina Adopts More Accurate Binding Poses but Autodock4 Forms Better Binding Affinity. *Journal of Chemical Information and Modeling* **60**, 204-211, doi:10.1021/acs.jcim.9b00778 (2020).
- 392 Gaillard, T. Evaluation of AutoDock and AutoDock Vina on the CASF-2013 Benchmark. *J Chem Inf Model* **58**, 1697-1706, doi:10.1021/acs.jcim.8b00312 (2018).
- 393 Morris, G. M. *et al.* AutoDock4 and AutoDockTools4: Automated docking with selective receptor flexibility. *J Comput Chem* **30**, 2785-2791, doi:10.1002/jcc.21256 (2009).
- 394 Stierand, K. & Rarey, M. Flat and Easy: 2D Depiction of Protein-Ligand Complexes. *Mol Inform* **30**, 12-19, doi:10.1002/minf.201000167 (2011).
- 395 Vranka, C. *et al.* LogP, a yesterday's value? *Nuclear Medicine and Biology* **50**, 1-10, doi:<https://doi.org/10.1016/j.nucmedbio.2017.03.003> (2017).
- 396 Daina, A., Michielin, O. & Zoete, V. iLOGP: a simple, robust, and efficient description of n-octanol/water partition coefficient for drug design using the

- GB/SA approach. *J Chem Inf Model* **54**, 3284-3301, doi:10.1021/ci500467k (2014).
- 397 Lipinski, C. A., Lombardo, F., Dominy, B. W. & Feeney, P. J. Experimental and computational approaches to estimate solubility and permeability in drug discovery and development settings. *Advanced Drug Delivery Reviews* **23**, 3-25, doi:[https://doi.org/10.1016/S0169-409X\(96\)00423-1](https://doi.org/10.1016/S0169-409X(96)00423-1) (1997).
- 398 Lipinski, C. A. Lead-and drug-like compounds: the rule-of-five revolution. *Drug discovery today: Technologies* **1**, 337-341 (2004).
- 399 Benet, L. Z., Hosey, C. M., Ursu, O. & Oprea, T. I. BDDCS, the Rule of 5 and drugability. *Adv Drug Deliv Rev* **101**, 89-98, doi:10.1016/j.addr.2016.05.007 (2016).
- 400 Brenk, R. *et al.* Lessons learnt from assembling screening libraries for drug discovery for neglected diseases. *ChemMedChem* **3**, 435 (2008).
- 401 Silliman, C. C. *et al.* Proteomic analyses of human plasma: Venus versus Mars. *Transfusion* **52**, 417-424, doi:<https://doi.org/10.1111/j.1537-2995.2011.03316.x> (2012).
- 402 Ranucci, M. *et al.* Gender-based differences in platelet function and platelet reactivity to P2Y12 inhibitors. *PLoS One* **14**, e0225771, doi:10.1371/journal.pone.0225771 (2019).
- 403 El Kerdawy, A. M., Osman, A. A. & Zaater, M. A. Receptor-based pharmacophore modeling, virtual screening, and molecular docking studies for the discovery of novel GSK-3 $\beta$  inhibitors. *J Mol Model* **25**, 171, doi:10.1007/s00894-019-4032-5 (2019).
- 404 Hu, Y., Stumpfe, D. & Bajorath, J. Recent Advances in Scaffold Hopping. *J Med Chem* **60**, 1238-1246, doi:10.1021/acs.jmedchem.6b01437 (2017).
- 405 Grisoni, F., Merk, D., Byrne, R. & Schneider, G. Scaffold-Hopping from Synthetic Drugs by Holistic Molecular Representation. *Sci Rep* **8**, 16469, doi:10.1038/s41598-018-34677-0 (2018).
- 406 Sun, H., Tawa, G. & Wallqvist, A. Classification of scaffold-hopping approaches. *Drug discovery today* **17**, 310-324, doi:10.1016/j.drudis.2011.10.024 (2012).
- 407 Anan, K. *et al.* Discovery of NR2B-selective antagonists via scaffold hopping and pharmacokinetic profile optimization. *Bioorganic & Medicinal Chemistry Letters* **29**, 1143-1147, doi:<https://doi.org/10.1016/j.bmcl.2019.02.017> (2019).
- 408 Gimeno, A. *et al.* Prediction of Novel Inhibitors of the Main Protease (M-pro) of SARS-CoV-2 through Consensus Docking and Drug Reposition. *Int J Mol Sci* **21**, doi:10.3390/ijms21113793 (2020).
- 409 Ko, H.-H. *et al.* Structure-activity relationship studies on chalcone derivatives: potent inhibition of platelet aggregation $\dagger$ . *Journal of Pharmacy and Pharmacology* **56**, 1333-1337, doi:10.1211/0022357044247 (2010).
- 410 Jaiswal, P. K. *et al.* Non-peptide-based new class of platelet aggregation inhibitors: Design, synthesis, bioevaluation, SAR, and in silico studies. *Arch Pharm (Weinheim)* **351**, e1700349, doi:10.1002/ardp.201700349 (2018).
- 411 Xie, Z., Zhao, L., Ding, X., Kong, Y. & Li, Z. Design, synthesis and evaluation of 1,4-benzodioxine derivatives as novel platelet aggregation inhibitors. *Future Medicinal Chemistry* **10**, 367-378, doi:10.4155/fmc-2017-0161 (2018).
- 412 Ojima, I. *et al.* Design, synthesis and SAR of RGD peptide hybrids as highly efficient inhibitors of platelet aggregation. *Bioorganic & Medicinal Chemistry Letters* **5**, 1941-1946, doi:[https://doi.org/10.1016/0960-894X\(95\)00329-R](https://doi.org/10.1016/0960-894X(95)00329-R) (1995).

- 413 Dockendorff, C. *et al.* Discovery of 1,3-Diaminobenzenes as Selective Inhibitors  
of Platelet Activation at the PAR1 Receptor. *ACS Medicinal Chemistry Letters*  
**3**, 232-237, doi:10.1021/ml2002696 (2012).
- 414 Fox, S. C., Behan, M. W. & Heptinstall, S. Inhibition of ADP-induced  
intracellular Ca<sup>2+</sup> responses and platelet aggregation by the P2Y<sub>12</sub> receptor  
antagonists AR-C69931MX and clopidogrel is enhanced by prostaglandin E1.  
*Cell Calcium* **35**, 39-46, doi:10.1016/s0143-4160(03)00170-2 (2004).
- 415 Bosenman, M. F. Serendipity and Scientific Discovery. *The Journal of Creative  
Behavior* **22**, 132-138, doi:<https://doi.org/10.1002/j.2162-6057.1988.tb00674.x>  
(1988).
- 416 Ban, T. A. The role of serendipity in drug discovery. *Dialogues Clin Neurosci* **8**,  
335-344, doi:10.31887/DCNS.2006.8.3/tban (2006).
- 417 Barreiro, G. *et al.* From docking false-positive to active anti-HIV agent. *J Med  
Chem* **50**, 5324-5329, doi:10.1021/jm070683u (2007).
- 418 Jorgensen, W. L. Efficient drug lead discovery and optimization. *Acc Chem Res*  
**42**, 724-733, doi:10.1021/ar800236t (2009).
- 419 Xue, C.-B. *et al.* Design, synthesis and in vitro activities of a series of  
benzimidazole/benzoxazole glycoprotein IIb/IIIa inhibitors. *Bioorganic &  
Medicinal Chemistry Letters* **6**, 339-344, doi:[https://doi.org/10.1016/0960-  
894X\(95\)00590-P](https://doi.org/10.1016/0960-894X(95)00590-P) (1996).
- 420 Baytaş, S. *et al.* Synthesis, anti-inflammatory, antiplatelet and in silico  
evaluations of (E)-3-(3-(2, 3-dihydro-3-methyl-2-oxo-3H-benzoxazole-6-yl)-1-  
phenyl-1H-pyrazole-4-yl) acrylamides. *Turkish Journal of Chemistry* **36**, 367-  
382 (2012).
- 421 Nuhrich, A., Varache-Lembège, M., Renard, P. & Devaux, G. Synthesis and  
inhibitory effects on platelet aggregation of 3-(2-thienyl)- and 3-(1-imidazolyl)-  
1,2-benzisoxazole derivatives. *European Journal of Medicinal Chemistry* **29**,  
75-83, doi:[https://doi.org/10.1016/0223-5234\(94\)90129-5](https://doi.org/10.1016/0223-5234(94)90129-5) (1994).
- 422 Xu, Z. *et al.* A novel STAT3 inhibitor negatively modulates platelet activation  
and aggregation. *Acta Pharmacologica Sinica* **38**, 651-659,  
doi:10.1038/aps.2016.155 (2017).
- 423 Kim, S. Getting the most out of PubChem for virtual screening. *Expert Opin  
Drug Discov* **11**, 843-855, doi:10.1080/17460441.2016.1216967 (2016).
- 424 Kubota, K., Funabashi, M. & Ogura, Y. Target deconvolution from phenotype-  
based drug discovery by using chemical proteomics approaches. *Biochimica et  
Biophysica Acta (BBA) - Proteins and Proteomics* **1867**, 22-27,  
doi:<https://doi.org/10.1016/j.bbapap.2018.08.002> (2019).
- 425 Saei, A. A. *et al.* Comprehensive chemical proteomics for target deconvolution  
of the redox active drug auranofin. *Redox Biology* **32**, 101491,  
doi:<https://doi.org/10.1016/j.redox.2020.101491> (2020).
- 426 Herledan, A. *et al.* Drug Target Engagement Using Coupled Cellular Thermal  
Shift Assay—Acoustic Reverse-Phase Protein Array. *SLAS Discovery* **25**, 207-  
214, doi:<https://doi.org/10.1177/2472555219897256> (2020).
- 427 Zheng, W., Li, G. & Li, X. Affinity purification in target identification: the  
specificity challenge. *Archives of Pharmacal Research* **38**, 1661-1685,  
doi:10.1007/s12272-015-0635-2 (2015).
- 428 Henderson, M. J., Holbert, M. A., Simeonov, A. & Kallal, L. A. High-  
Throughput Cellular Thermal Shift Assays in Research and Drug Discovery.  
*SLAS Discovery* **25**, 137-147, doi:<https://doi.org/10.1177/2472555219877183>  
(2020).

- 429 Simonovsky, M. & Meyers, J. DeeplyTough: Learning Structural Comparison of Protein Binding Sites. *Journal of Chemical Information and Modeling* **60**, 2356-2366, doi:10.1021/acs.jcim.9b00554 (2020).
- 430 Hajbabaie, R., Harper, M. & Rahman, T. in *British Journal of Pharmacology*. 387-388 (Wiley 111 River St, Hoboken 07030-5774, NJ USA).
- 431 Hu, L. *et al.* Platelets Express Activated P2Y<sub>12</sub> Receptor in Patients with Diabetes. *Circulation* **136**, doi:10.1161/CIRCULATIONAHA.116.026995 (2017).
- 432 Bhattad, V. B. *et al.* Intravenous cangrelor as a peri-procedural bridge with applied uses in ischemic events. *Ann Transl Med* **7**, 408, doi:10.21037/atm.2019.07.64 (2019).
- 433 Rossini, R. *et al.* Antiplatelet Therapy with Cangrelor in Patients Undergoing Surgery after Coronary Stent Implantation: A Real-World Bridging Protocol Experience. *TH Open* **4**, e437-e445, doi:10.1055/s-0040-1721504 (2020).
- 434 Angiolillo, D. J. *et al.* International Expert Consensus on Switching Platelet P2Y<sub>12</sub> Receptor-Inhibiting Therapies. *Circulation* **136**, 1955-1975, doi:10.1161/circulationaha.117.031164 (2017).
- 435 Kunapuli, P., Gurevich, V. V. & Benovic, J. L. Phospholipid-stimulated autophosphorylation activates the G protein-coupled receptor kinase GRK5. *J Biol Chem* **269**, 10209-10212 (1994).
- 436 Dawaliby, R. *et al.* Allosteric regulation of G protein-coupled receptor activity by phospholipids. *Nat Chem Biol* **12**, 35-39, doi:10.1038/nchembio.1960 (2016).
- 437 Liu, S. *et al.* Differential activation mechanisms of lipid GPCRs by lysophosphatidic acid and sphingosine 1-phosphate. *Nature Communications* **13**, 731, doi:10.1038/s41467-022-28417-2 (2022).
- 438 Bhattarai, A., Wang, J. & Miao, Y. G-Protein-Coupled Receptor-Membrane Interactions Depend on the Receptor Activation State. *J Comput Chem* **41**, 460-471, doi:10.1002/jcc.26082 (2020).
- 439 Szlenk, C. T., Gc, J. B. & Natesan, S. Does the Lipid Bilayer Orchestrate Access and Binding of Ligands to Transmembrane Orthosteric/Allosteric Sites of G Protein-Coupled Receptors? *Mol Pharmacol* **96**, 527-541, doi:10.1124/mol.118.115113 (2019).
- 440 Dyszkiewicz-Korpanty, A., Olteanu, H., Frenkel, E. P. & Sarode, R. Clopidogrel anti-platelet effect: an evaluation by optical aggregometry, impedance aggregometry, and the platelet function analyzer (PFA-100). *Platelets* **18**, 491-496, doi:10.1080/09537100701280654 (2007).
- 441 Armstrong, P. C. *et al.* Utility of 96-well plate aggregometry and measurement of thrombi adhesion to determine aspirin and clopidogrel effectiveness. *Thromb Haemost* **102**, 772-778, doi:10.1160/th09-04-0215 (2009).
- 442 Denessen, E. J. S. *et al.* Determining the optimal storage time and temperature for performing platelet function assays and global hemostasis assays. *Platelets* **33**, 416-424, doi:10.1080/09537104.2021.1934666 (2022).
- 443 Wilson, B. H., Cole, B. J., Goodale, M. B. & Fortier, L. A. Short-Term Storage of Platelet-Rich Plasma at Room Temperature Does Not Affect Growth Factor or Catabolic Cytokine Concentration. *Am J Orthop (Belle Mead NJ)* **47**, doi:10.12788/ajo.2018.0022 (2018).
- 444 Jóhannsson, F., Yurkovich, J., Guðmundsson, S., Sigurjonsson, O. & Rolfsson, O. The temperature dependence of platelet metabolism. doi:10.1101/802660 (2019).
- 445 Mansoury, M., Hamed, M., Karmustaji, R., Al Hannan, F. & Safrany, S. T. The edge effect: A global problem. The trouble with culturing cells in 96-well plates.

- Biochemistry and Biophysics Reports* **26**, 100987,  
doi:<https://doi.org/10.1016/j.bbrep.2021.100987> (2021).
- 446 Salmon, D. M. Optimisation of platelet aggregometry utilising micotitreplate  
technology and integrated software. *Thromb Res* **84**, 213-216,  
doi:10.1016/0049-3848(96)00179-x (1996).
- 447 Born, G., Juengjaroen, K. & Michal, F. Relative activities on and uptake by  
human blood platelets of 5-hydroxytryptamine and several analogues. *British  
Journal of Pharmacology* **44**, 117 (1972).
- 448 Valdorf-Hansen, J. & Zucker, M. Effect of temperature and inhibitors on  
serotonin-14C release from human platelets. *American Journal of Physiology-  
Legacy Content* **220**, 105-111 (1971).
- 449 Maurer-Spurej, E. *et al.* Room Temperature Activates Human Blood Platelets.  
*Laboratory Investigation* **81**, 581-592, doi:10.1038/labinvest.3780267 (2001).
- 450 Flower, R. J. Of platelets and aggregometers: personal reminiscences of Gus  
Born (1921-2018). *Platelets* **29**, 749-755, doi:10.1080/09537104.2018.1533740  
(2018).
- 451 Burzynski, L. C., Pugh, N. & Clarke, M. C. H. Platelet Isolation and Activation  
Assays. *Bio Protoc* **9**, e3405, doi:10.21769/BioProtoc.3405 (2019).
- 452 Awuni, Y. & Mu, Y. Reduction of false positives in structure-based virtual  
screening when receptor plasticity is considered. *Molecules* **20**, 5152-5164,  
doi:10.3390/molecules20035152 (2015).
- 453 Deng, N. *et al.* Distinguishing binders from false positives by free energy  
calculations: fragment screening against the flap site of HIV protease. *The  
Journal of Physical Chemistry B* **119**, 976-988 (2015).
- 454 Zhang, Y. *et al.* Increased platelet activation and thrombosis in transgenic mice  
expressing constitutively active P2Y<sub>12</sub>. *J Thromb Haemost* **10**, 2149-2157,  
doi:10.1111/j.1538-7836.2012.04894.x (2012).
- 455 Kakouros, N., Rade, J., Kourliouros, A. & Resar, J. Platelet Function in Patients  
with Diabetes Mellitus: From a Theoretical to a Practical Perspective.  
*International journal of endocrinology* **2011**, 742719, doi:10.1155/2011/742719  
(2011).
- 456 Zhang, D. *et al.* Two disparate ligand-binding sites in the human P2Y<sub>1</sub> receptor.  
*Nature* **520**, 317-321, doi:10.1038/nature14287 (2015).
- 457 Teague, S. J., Davis, A. M., Leeson, P. D. & Oprea, T. The Design of Leadlike  
Combinatorial Libraries. *Angew Chem Int Ed Engl* **38**, 3743-3748,  
doi:10.1002/(sici)1521-3773(19991216)38:24<3743::Aid-anie3743>3.0.Co;2-u  
(1999).
- 458 Gao, Y., Gesenberg, C. & Zheng, W. Chapter 17 - Oral Formulations for  
Preclinical Studies: Principle, Design, and Development Considerations.  
*Developing Solid Oral Dosage Forms (Second Edition)*, 455-495,  
doi:<https://doi.org/10.1016/B978-0-12-802447-8.00017-0> (2017).
- 459 Gleeson, M. P. Generation of a set of simple, interpretable ADMET rules of  
thumb. *Journal of medicinal chemistry* **51**, 817-834 (2008).
- 460 Waring, J. F. *et al.* Identification of proteasome gene regulation in a rat model  
for HIV protease inhibitor-induced hyperlipidemia. *Archives of toxicology* **84**,  
263-270 (2010).
- 461 Efremov, R. G., Gatsogiannis, C. & Raunser, S. in *Methods in Enzymology* Vol.  
594 (ed Christine Ziegler) 1-30 (Academic Press, 2017).
- 462 Mio, K. & Sato, C. Lipid environment of membrane proteins in cryo-EM based  
structural analysis. *Biophys Rev* **10**, 307-316, doi:10.1007/s12551-017-0371-6  
(2018).

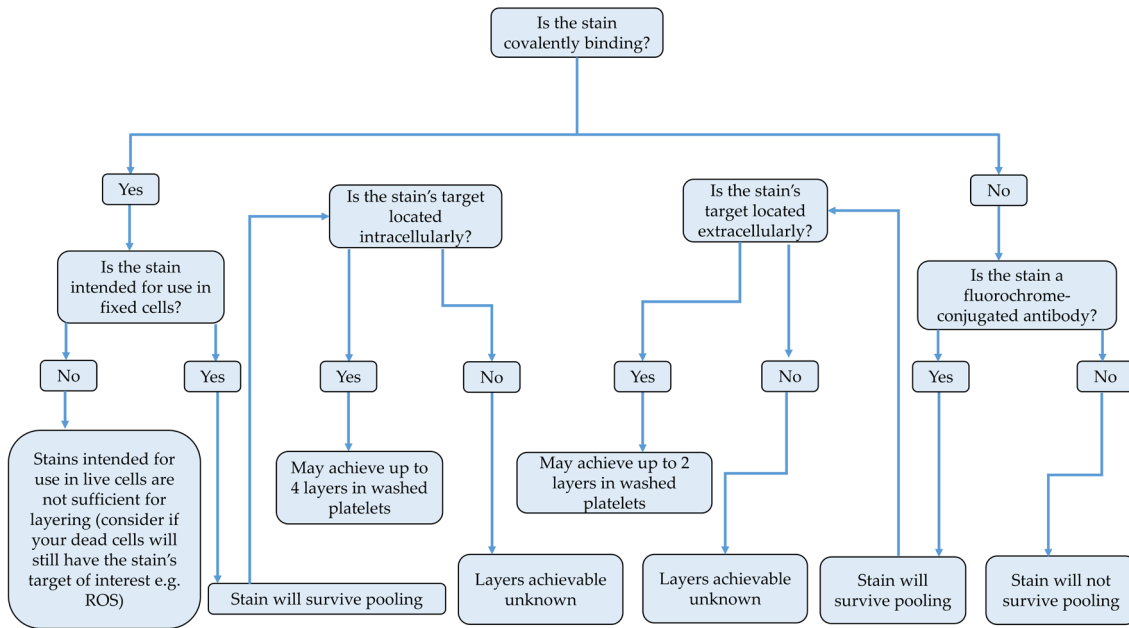
- 463 Marsden, A. J. *et al.* Inhibition of Arginine Methylation Impairs Platelet  
Function. *ACS Pharmacology & Translational Science* **4**, 1567-1577,  
doi:10.1021/acsptsci.1c00135 (2021).
- 464 Venetsanos, D. *et al.* Prasugrel versus ticagrelor in patients with myocardial  
infarction undergoing percutaneous coronary intervention. *Heart* **107**, 1145,  
doi:10.1136/heartjnl-2020-318694 (2021).
- 465 Westman, P. C., Lipinski, M. J., Torguson, R. & Waksman, R. A comparison of  
cangrelor, prasugrel, ticagrelor, and clopidogrel in patients undergoing  
percutaneous coronary intervention: A network meta-analysis. *Cardiovasc  
Revasc Med* **18**, 79-85, doi:10.1016/j.carrev.2016.10.005 (2017).
- 466 Crescence, L. *et al.* The P2Y<sub>12</sub> Receptor Antagonist Selatogrel Dissolves  
Preformed Platelet Thrombi In Vivo. *Journal of Clinical Medicine* **10**,  
doi:10.3390/jcm10225349 (2021).
- 467 Chopra, B., Dhingra, A., Kapoor, R. & Prasad, D. Synthesis and Antimicrobial  
Activity of Naphthylamine Analogs Having Azetidinone and Thiazolidinone  
Moieties. *Journal of Exploratory Research in Pharmacology* **2**, 105-112,  
doi:10.14218/JERP.2017.00005 (2017).
- 468 Taylor, K. A., Wilson, D. G. S., Harper, M. T. & Pugh, N. Extracellular chloride  
is required for efficient platelet aggregation. *Platelets* **29**, 79-83,  
doi:10.1080/09537104.2017.1332367 (2018).
- 469 Chan, H. C. S., Li, Y., Dahoun, T., Vogel, H. & Yuan, S. New Binding Sites,  
New Opportunities for GPCR Drug Discovery. *Trends in Biochemical Sciences*  
**44**, 312-330, doi:10.1016/j.tibs.2018.11.011 (2019).
- 470 Desimine, V. L. *et al.* Biased Agonism/Antagonism of Cardiovascular GPCRs  
for Heart Failure Therapy. *Int Rev Cell Mol Biol* **339**, 41-61,  
doi:10.1016/bs.ircmb.2018.02.007 (2018).
- 471 Berry, J. *et al.* An “occlusive thrombosis-on-a-chip” microfluidic device for  
investigating the effect of anti-thrombotic drugs. *Lab on a Chip* **21**, 4104-4117  
(2021).
- 472 Dejana, E., Villa, S. & de Gaetano, G. Bleeding time in rats: a comparison of  
different experimental conditions. *Thromb Haemost* **48**, 108-111 (1982).
- 473 Misra, A. *et al.* Anti-thrombotic efficacy of S007-867: Pre-clinical evaluation in  
experimental models of thrombosis in vivo and in vitro. *Biochemical  
Pharmacology* **148**, 288-297, doi:<https://doi.org/10.1016/j.bcp.2018.01.013>  
(2018).



## Appendix

### Troubleshooting tips for the pVASP assay

- Addition of BSA (1%) to wash buffer (PBS) to prevent cells sticking to the walls of tubes. Furthermore, platelets adhere to adsorbed BSA, making the pellet more visible.
- PBS as choice buffer for sharper barcode populations.
- Increasing centrifuge speed (or time) to increase pellet quality.
- Increasing the starting number of platelets, as many cells can be lost during wash and spin steps.
- During the fixing and permeabilisation stages cells are harder to pellet and most platelets are lost during these steps. Increasing wash volumes (BSA) and centrifuge speed (or time) may help with this.
- Careful aspiration of the supernatant with consideration to the position of the pellet (where the Eppendorf tube was placed in the centrifuge with the front of the lid facing the centre of the rotor, the pellet will be found at the bottom of the Eppendorf tube perpendicular from the hinge).
- Aspiration performed with 200 $\mu$ L pipette tips instead of 1000 $\mu$ L pipette tips. Prevent bubble formation by using back-pipetting. Bubbles and uneven mixing can lead to non-uniform labelling of targets, and multiple populations displaying varying levels of fluorescence, where only one population is expected.
- Using the same pipette tip during pooling of samples.
- Some aspirate may be left in the samples at sensitive stages, especially before pooling and before reading the pooled sample, to ensure no platelets are lost during pipetting.
- Solutions in DMSO 'fall' to the bottom of the tube when added to a sample and must be mixed immediately and thoroughly by pipetting to ensure homogeneity.
- Antibodies are micellar when added to a sample and must be mixed immediately and thoroughly to ensure homogeneity.
- Material of tubes used may promote cell loss. Cell loss is lesser with polypropylene material than polystyrene material.
- Filter reagents where possible, using 0.22 $\mu$ M filters, if a second unexpected population or 'debris' is observed upon reading the samples.
- FCB dyes with intracellular targets achieve more barcoding layers than those with extracellular targets.
- The FCB dye must covalently bind to its target to prevent loss of barcodes during subsequent wash and spin steps.



**Decision box flowchart for barcoding.** Showing the number of layers achievable from different stains determined from binding type, target location, and stain purpose. Further mentioned is the likelihood of a stain to survive pooling. (Note: the above flowchart is based on the results achieved from the stains tested in this work and may not apply to every stain). The barcodes successfully achieved in washed platelets may also be used in PRP with similar outcomes (results in PRP not shown). Optimisation (titration) will be required for each stain desired to be used for barcoding.